Mondragon Unibertsitatea

DOCTORAL THESIS

PARTIAL DISCHARGE-FREE ELECTRICAL MACHINE DESIGN FOR ELECTROMOBILITY DRIVES BASED ON WIDE BANDGAP SEMICONDUCTORS

LEIRE ELORZA AZPIAZU | Arrasate-Mondragón, 2025

Doctoral Dissertation

Partial Discharge-Free Electrical Machine Design for Electromobility Drives Based on Wide-Bandgap Semiconductors

Leire Elorza Azpiazu

Supervised by
Dr. Gaizka Almandoz Larralde
and
Dr. Aritz Egea Caceres

Electronics and Computer Science Department
Mondragon Unibertsitatea

July 2025

Submitted in Fulfilment of the Requirements of the

PHD PROGRAMME IN APPLIED ENGINEERING

Partial Discharge-Free Electrical Machine Design for Electromobility Drives Based on Wide-Bandgap Semiconductors

Doctoral Dissertation Presented in

Mondragon Goi Eskola Politeknikoa

Submitted in Fulfilment of the Requirements of the

PHD PROGRAMME IN APPLIED ENGINEERING

Presented by

Leire Elorza Azpiazu

Supervised by

Dr. Gaizka Almandoz Larralde

and

Dr. Aritz Egea Caceres

Electronics and Computer Science Department

Mondragon Unibertsitatea

Thesis Committee:

President: Prof. Andrea Cavallini (Alma Mater Studiorum - Università di Bologna)

Vocal: Prof. Claudia Steluta Martis (Universitatea Tehnică din Cluj-Napoca)

Secretary: Dr. Javier Poza Lobo (Mondragon Unibertsitatea)

In Arrasate, July 2025

Elektrizitatea banaiz, elektrizitatean banaiz
Lurrean idatzirik geldituko naiz
— Elektrizitatea, Zea Mays

Declaration of originality

Honen bidez nik, Leire Elorza Azpiazu, deklaratzen dut Doktorego Tesi dokumentu hau nire jatorrizko lana dela, nire kabuz landu dudana. Lan hau lantzean erabilitako iturri, erreferentzia eta literatura guztiak behar bezala aipatzen eta zerrendatzen dira, dagokion iturriari erreferentzia osoa eginez.

Hereby I, Leire Elorza Azpiazu declare, that this Doctoral Dissertation document is my original authorial work, which I have worked out by my own. All sources, references and literature used or excerpted during elaboration of this work are properly cited and listed in complete reference to the due source.

Yo Leire Elorza Azpiazu declaro que este documento de la Tesis Doctoral es original, fruto de mi trabajo personal, y que no ha sido previamente presentado para obtener otro título o calificación profesional. Las ideas, formulaciones, imágenes, ilustraciones tomadas de fuentes ajenas han sido debidamente citadas y referenciadas.

Arrasate, July 2025

Leire Elorza Azpiazu

Acknowledgements

I have always been curious about this part of any document or book because, in the end, it represents and reveals the person behind the work you are about to read. I also find it amusing that, behind documents that are usually so formal and stiff, there is often a glimpse of emotion. So, this is my little piece for those who are curious and enjoy reading everything—although you will need to understand Basque.

First of all, I would like to thank the members of the examination board for accepting the invitation. I am especially grateful to Professor Andrea Cavallini and Professor Claudia Martis for agreeing to review my thesis and for preparing a detailed report with valuable corrections. Eskerrak eman nahi dizkizuet tesi honetan parte hartu duzuen enpresa kolaboratzaileetako profesionalei, emandako konfiantzagatik eta, batez ere, eskatutako laginak une oro eskaini izanagatik.

Nola ez, eskerrik asko Gaizka eta Aritzi tesixe etteko aukerie luzatzearren eta lau urte hauetan gia lanak ettearren. Emandako aukera honi esker, guztiz ezezagune zan tematika bati gustue hartu dixot, eta pozik eta eskertute nao ikisteko oindik asko dauketen deskarga partzialan mundu hontan lanin segitzeko aukerie eukitzearren. Gia on batzuz gain, ezinbestekue izen da lankide danan laguntzie. Laneako entorno agradable bat sortziez gain, elkarri laguntzeko daon dinamikik asko erreztu dit mundu mekanikotik datorren pertsona bezela, mundu elektrikun sartzen, entenditzen eta esperimentatzen. Eindeko ensaio esperimental danake etzin izengo posible, Ainara, Jonas, Beñat, eta Markel, zuen laguntzaipe. Espero det gustoa jardun deuztela elkar lanin, eta pixket beintzet entendiuko zenutela elektroien jolas honen mundue.

Laneko entornuez gain, ezinbestekue izen da lanetik erten eta frustrazixo eta pozak konpartitzeko batemat izetie. Hortan lagunek berrezkuk izentzeate, poteotan nere tesixen inguruko esplikaixuk holako interes eta entusiasmukin aitzie asko eskertzet. Eta lasai, oindik preparaukot zoze tximista txiki hauek zer dien hobeto entenditzeko.

Horrenbeste ezinbestekon artien, familikuke ezintzenuten falta. Ama, atte, eskerrik asko ber izen deten dana emateatik, espero det bueltan ematen jakittie. Xabi, Maia, zueke nere bigarren gurasuk izentzeate. Txikitten pixket kejau ette nitzen doble bronka eukitze nittulako, baño oñ asko eskertzet zueke albun izetearren. Maia, badakit hau izengoala tesixen letukozun gauze gutxiñetako bat, bakarra ez esatearren, asike aprobetxau nahi det esker berezixek emateko, beti pentsau izen det birie iriki eta erreztu dizula,

aspekto danetan. Eta etxeko txikixeire Oihan, Alaia, Intza, eta Alize, eskerrik asko zuen poztasun eta mattesuneatik, harrigarrixe da zuek oso konsziente izeteke zenbat emateuzten. Akordatzekere, gauzek esplikatzie eta erakustie zenbat gustatze zaten konturatzen lagundu diuzte. Espero det eindeko esperimento danetatik zoze kontajiau izena, eta egunen baten hau letzebauzte, txikitteko momentu hoxekin akordako zeatela.

Eta amomak kantatzezun bezela, *ta azken orduan, isil-isilik, nere maite politari*. Eskerrik asko Hodei, urte hauetan albun eon eta aitzearren, bai txarrin eta bai onin. Emandako mattesun eta goxotasunek asko erreztu dibe tesiko bukaera honta aiatzen. Eta aipamen berezixe merezi debe tesixen zier sortu dien probleman ingurun euki dittoun txarlak, soluzixuk billatzeko birik izen dieta. Eskerrik asko.

Laburpena

Mugikortasun jasangarrirako trantsizioak ibilgailu elektrikoen garapena bizkortu du, eta banda debekatu zabaleko (WBG) bihurgailuek potentzia- eta efizientzia-dentsitate handiagoa ahalbidetzen dute. Hala ere, kommutazio azkarreko uhin-formek fidagarritasun-arazoak sortzen dituzte isolamendu-sistemetan, deskarga partzialen (PD) arriskua handituz, bereziki espiren arteko isolamenduan, eta bizitza baliagarria murriztuz.

Tesi honek WBG bihurgailuekin funtzionatzen duten eragingailuetarako isolamendu fidagarriak diseinatzeko tresnak eta jarraibideak proposatzen ditu, PDen murrizketan oinarrituta. Ikerketa hiru ildotan egituratzen da: (1) PDaren hasierako tentsioa (PDIV) baldintza adierazgarrietan estimatzea, (2) diseinu eta fabrikazioaren eragina ebaluatzea eta (3) estres termiko eta elektrikopeko iraunkortasuna aztertzea diagnostiko-markatzaileekin.

PDIVa modelatzeko, Extended Dakin's eta parallel-plate ekuazioak moldatu eta garatu dira. Garapen hauek 140 laginetan baliozkotu dira baldintza ezberdinetan, %–5,3 eta %–2,5 batez besteko errorearekin. Eredu hauek simulazioan oinarritutako metodoen zehaztasuna berdintzen dute, baina esperimentazio beharrik gabe eta kalkulu azkarragoekin. Espiren arteko isolamendurako garatuak izan arren, lurrerako sistemetan ere aplikagarriak direla erakutsi da, batez ere Extended Dakin's modeloa, parametroen doikuntzarik behar ez duelako.

Fabrikazio-prozesuen eragina enpresa industrialekin lankidetzan aztertu da. Esaterako, harilkatu mota desberdinak eta erretxinaren aplikazioa aztertu dira. PDIVaren neurketek diseinuaren ahuleziak garaiz atzematea ahalbidetu dute, azken deseinu eta produktu sendoagoak lortuz.

Zahartze-probek baieztatu dute tenperatura altuak eta WBGak sortutako estres elektrikoak iraunkortasuna murrizten dutela. Zahartze termomekanikoak ez du akats bizkorragorik eragin isotermikoarekiko, esfortzu mekanikoaren eragina material guztietan ez dela orokorra adieraziz. PDen markatzaileak, PDIV eta deskarga magnitudea, degradazioaren eta akatsaren adierazle fidagarrienak izan dira.

Emaitza hauek isolamenduaren modelatzea eta baliozkotzea motorraren garapen-prozesuan txertatzearen alde egiten dute. Etorkizunean ereduen balidazioa zabaltzea eta bobinatze-tekniken eragina espiren artean ebaluatzea proposatzen da, besteak beste.

Hitz gakoak: Isolamenduaren Diseinua, Deskarga Partzialak, PDIV Modelaketa, Isolamenduaren Iraunkortasuna, Diagnostiko Elektrikoa.

Abstract

The transition to sustainable mobility has accelerated the development of electric vehicles, with Wide-Bandgap (WBG) converters enabling greater power density and efficiency. However, their fast-switching waveforms increase the risk of Partial Discharges (PD), especially in interturn insulation, posing reliability challenges and reducing insulation lifetime.

This doctoral thesis proposes tools and guidelines to design reliable insulation systems for WBG-based drives, focusing on PD mitigation. The work follows three research lines: (1) PD Inception Voltage (PDIV) estimation under representative conditions, (2) assessment of design and manufacturing factors, and (3) evaluation of insulation endurance under thermal and electrical stress using diagnostic markers.

Novel PDIV models, based on the Extended Dakin's and parallel-plate, were validated across 140 round and rectangular wire samples under varied conditions, with mean errors of -5.3% and -2.5%. They match the accuracy of simulation-based methods but offer faster results without requiring experimentation. Even if initially developed for interturn insulation, they also proved effective for groundwall systems, notably the Extended Dakin's model, which requires no parameter fitting.

The influence of manufacturing processes was studied with industrial partners. For instance, several winding techniques and potting application benefits were analysed. PDIV measurements enabled early detection of design weaknesses, supporting robust final design and products.

Ageing tests confirmed that high temperatures and WBG-induced electrical stress reduce insulation endurance. Thermomechanical ageing did not accelerate failure beyond isothermal ageing, indicating that mechanically induced stress does not dominate across all materials. PD-based health markers, PDIV and discharge magnitude, provided the most reliable indicators of insulation degradation and imminent failure.

These results support the integration of insulation modelling and validation into machine development. Future work includes broader model validation, evaluation of interturn insulation across winding techniques, and expansion of ageing datasets, between others.

Keywords: Insulation System Design, Partial Discharge, PDIV Modelling, Insulation Endurance, Insulation Health Diagnostic.

Resumen

La transición hacia una movilidad sostenible ha acelerado el desarrollo de los vehículos eléctricos, en los que los convertidores de banda prohibida ancha (WBG) han permitido una mayor densidad de potencia y eficiencia. No obstante, su conmutación rápida ha planteado retos de fiabilidad en los sistemas de aislamiento, pudiendo reducir su vida útil al aumentar el riesgo de descargas parciales (PD).

En esta tesis doctoral se han propuesto herramientas y directrices para diseñar sistemas de aislamiento fiables en accionamientos con convertidores WBG. El trabajo se ha estructurado en tres líneas: (1) estimar el voltaje de inicio de PD (PDIV) en condiciones representativas, (2) analizar factores de diseño y fabricación y (3) evaluar la durabilidad del aislamiento bajo estrés térmico y eléctrico mediante marcadores diagnósticos.

Los modelos de PDIV desarrollados, el Extended Dakin's y parallel-plate, que se han validado en 140 muestras de hilos circulares y rectangulares sometidos a diversas condiciones, han obtenido errores promedios de -5,3% y -2,5%. Estos modelos, con cálculos más rápidos y sin requerir experimentación, han igualado la precisión de los métodos por simulación. Aunque se han diseñado inicialmente para el aislamiento entre espiras, también se han mostrado eficaces para el aislamiento a tierra, destacando el modelo Extended Dakin's, que no requiere ajuste de parámetros.

La influencia de los procesos de fabricación se ha estudiado en colaboración con empresas industriales. Se han evaluado técnicas de bobinado y los beneficios de la aplicación de la resina. Las mediciones de PDIV han permitido detectar debilidades de diseño de forma temprana, contribuyendo así a diseños y productos finales más robustos.

Los ensayos de envejecimiento han confirmado que las altas temperaturas y el estrés eléctrico asociado a convertidores WBG reducen la durabilidad del aislamiento. No se ha observado un fallo acelerado del envejecimiento termomecánico respecto al isotérmico, indicando que el esfuerzo mecánico no domina en todos los materiales. Se ha demostrado que los marcadores basados en PD, son los indicadores más fiables de fallo inminente.

Los resultados respaldan la integración del modelado y validación del aislamiento en el desarrollo de máquinas. Se prevé como trabajo futuro ampliar la validación de modelos y evaluar el aislamiento entre espiras según técnicas de bobinado, entre otros.

Palabras clave: Diseño de Sistemas de Aislamiento, Descargas Parciales, Modelado de PDIV, Envejecimiento de Aislamientos, Diagnóstico de Aislamientos.

Contents

List of Figures

List of Tables

List of Acronyms

AC	Alternating Current.
AH	Absolute Humidity.
ASF	Ageing Safety Factor.
CM	Common-Mode.
CR	Corona Resistant.
CRW	Corona Resistant Wire.
DAH	Derivation Absolute Humidity.
DC	Direct Current.
DoE	Design of Experiments.
DT	Derivation Temperature.
EV	Electric Vehicle.
FCV	Fuel Cell Vehicle.
FEM	Finite Element Method.
GaN	Gallium Nitride.
GVPI	Global Vacuum Pressure Impregnation.
HEV	Hybrid Electric Vehicle.
HF	High Frequency.
HV	High Voltage.
IC	Insulation Capacitance.
ICE	Internal Combustion Engine.
ICEM	International Conference on Electrical Machines.
IGBT	Insulated Gate Bipolar Transistor.
IM	Induction Machine.

LF	Low Frequency.
NMN	Nomex-Mylar-Nomex.
OF	Overshoot Factor.
PAI	Polyamide-imide.
PAICR	Polyamide-imide Corona Resistant.
PC	Parallel Conductor.
PD	Partial Discharge.
PDEV	Partial Discharge Extinction Voltage.
PDIV	Partial Discharge Inception Voltage.
PDSF	Partial Discharge Safety Factor.
PE	Polyether.
PEEK	Polyetheretherketone.
PEI	Polyester-imide.
PI	Polyimide.
PMBLDCM	Permanent Magnet Brushless DC Machine.
PMSM	Permanent Magnet Synchronous Machine.
PRPD	Phase Resolved Partial Discharge.
PWM	Pulse Width Modulation.
RH	Relative Humidity.
RPDIV	Repetitive Partial Discharge Inception Voltage.
SEM	Scanning Electron Microscope.
SI	International System of Units.
Si	Silicon.
SiC	Silicon Carbide.
SRM	Switched Reluctance Machine.
SW	Stardard Wire.
TP	Twisted Pair.
TSF	Temperature Safety Factor.
VAH	Validation Absolute Humidity.
VT	Validation Temperature.
WBG	Wide-Bandgap.

List of Symbols

α	Townsend's first ionisation coefficient.
$\alpha_{\mathbf{T}}$	Temperature coefficient.
$\alpha_{\mathbf{TExp}}$	Linear thermal expansion coefficient.
$\bar{\alpha}$	Effective ionisation coefficient.
γ	Townsend's secondary ionisation coefficient.
γ_+	Secondary electron emission coefficient due to positive ions.
$\gamma_{\mathbf{FE}}$	Ion-enhanced field secondary electron emission coefficient.
$\gamma_{\mathbf{ph}}$	Secondary electron emission coefficient from photoelectric effect at the cathode.
$\bar{\gamma}$	Effective secondary electron emission coefficient.
$\varepsilon_{\mathbf{r\,0}}$	Relative permittivity of vacuum.
$\varepsilon_{\mathbf{r\,eq}}$	Equivalent relative permittivity.
$\varepsilon_{\mathbf{r\,x}}$	Relative permittivity of the material under study.
η	Attachment coefficient.
$\eta_{\mathbf{ph}}$	Photon absorption coefficient.
λ	Free path, distance between two collisions in the direction of the electric field.
μ	Mean value.
ρ	Density.
ϕ_+	Positive onset phase.
ϕ_-	Negative onset phase.
A	Ionisation constant specific to a gas.

B	Ionisation constant specific to a gas.
C_0	Capacitance of vacuum.
C_{eq}	Equivalent capacitance.
C_p	Parallel capacitance.
C_x	Capacitance of the material under study.
D	Field emission onset threshold.
Du	Duty.
d	Gap distance.
d_e	Length of the constant electric field path.
d_s	Horizontal straight distance between conductors.
d_x	Distance between the edges of the material under study.
E	Electric field.
E_x	Electric field in the material under study.
e	Strain.
f	Frequency.
f_r	Resonance frequency.
h	Height of the copper in rectangular conductors.
I	Current.
K_{Sch}	Schumann's constant.
k_d	Expected electron impact ionisation frequency.
L	Inductance.
l	Length of the coated section for the grounding electrode.
N_{cr}	Critical number of electrons at the head of an avalanche.
n	Number of electrons at a given distance from the cathode.
n^-	Oxygen ion density.
n_+	Number of electrons released from the cathode due to positive ions bombardment.
n_0	Primary free electron.
P	Pressure.
Q	Electric charge.
Q_x	Electric charge in the material under study.

R	Resistance.
$r_{\mathbf{inner}}$	Radius of the copper surface in round conductors.
$r_{\mathbf{outer}}$	Radius of the insulated surface in round conductors.
$r_{\mathbf{s}}$	Electron generation rate from the surface.
$r_{\mathbf{v}}$	Electron generation rate from the air gap.
S	Area of a condenser.
$S_{\mathbf{cr}}$	Critical surface volume.
T	Temperature.
$T_{\mathbf{g}}$	Glass transition temperature.
t	Time.
$t_{\mathbf{0}}$	Electron generation starting time.
$t_{\mathbf{B}}$	Time to breakdown.
$t_{\mathbf{f}}$	Formative time lag.
$t_{\mathbf{ins}}$	Insulation thickness.
$t_{\mathbf{n}}$	Non-conduction time.
$t_{\mathbf{r}}$	Rise time.
$t_{\mathbf{s}}$	Statistical time lag.
$t_{\mathbf{w}}$	Pulse width.
V	Voltage.
$V_{\mathbf{B}}$	Breakdown voltage.
$V_{\mathbf{cr}}$	Critical air gap volume.
$V_{\mathbf{DC}}$	DC voltage.
$V_{\mathbf{inc}}$	Inception voltage.
$V_{\mathbf{p}}$	Peak voltage.
$V_{\mathbf{pp}}$	Peak-peak voltage.
$V_{\mathbf{rms}}$	Rms voltage.
w	Width of the copper in rectangular conductors.
x	Distance from the cathode.
Z	Impedance.
$\varnothing_{\mathbf{copper}}$	Copper nominal diameter.

Chapter 1

Introduction

This first chapter provides a brief introduction to the framework of the thesis. First, the research topic and its primary challenges are presented. Then, the main objective and partial objectives are defined, and several hypotheses are established. Additionally, the published articles and congress proceedings are demoed. Ultimately, this chapter concludes with a comprehensive overview of the dissertation structure, summarising the content of each chapter.

1.1 Motivation

Nowadays, most interurban and urban mobility worldwide relies on Internal Combustion Engine (ICE) vehicles. However, growing social awareness of climate change and urban pollution has placed greenhouse gas emissions from the transport sector centre stage. Several national and international agencies committed to combating climate change have imposed significant restrictions on ICE mobility, aiming to transition towards a zero-emissions scenario. For instance, the European Union has set a clear target of reducing emissions by 55% by 2030 and achieving 100% reduction by 2035 for new vehicles (European Green Deal [1]). This has encouraged major transport companies to invest in and develop cleaner and more efficient energy technologies.

An advantage of electric machines is their higher efficiency compared to ICEs (based on fossil fuels). In practice, light-duty petrol engines transfer only 45% of the power generated by fuel combustion to the engine crankshaft [2]. In contrast, electric machines for Electric Vehicles (EVs) can achieve up to 96% efficiency in converting electrical energy into mechanical [3]. Therefore, EVs require less energy consumption than ICE vehicles to deliver the same mechanical output. This aspect, along with the fact that EVs produce zero emissions in their use, serves as a compelling advantage in their favour.

The core component of an EV is the electric drive, which consists of a power converter and an electric machine that drives the wheels of the vehicle. The power converter supplies electrical energy to the machine, modulating the voltage in frequency and amplitude to achieve variable speed operation. Maximising the autonomy is crucial and one of the major constraints of EVs, requiring high power density drives. Thus, the volume and weight of the traction system must be minimised while maintaining high-efficiency levels [4].

Lately, new power electronic technologies based on Wide-Bandgap (WBG) materials, such as Gallium Nitride (GaN) and Silicon Carbide (SiC), have enabled the development of more compact converters due to their high switching frequency and efficiency [5]. Additionally, these technologies allow for increased electric machine speeds. To obtain the same mechanical power, the torque requirement is reduced as the speed is increased, leading to more compact machine designs. Consequently, using electric machines fed by WBG converters reduces the size and weight of both the power converter and the electric machine, maximising the autonomy of EVs [6].

In counterpart, this kind of converter introduces new challenges in ensuring the reliability of electric machines, particularly concerning the insulation system. WBG devices can generate short rise and fall time voltage pulses, resulting in higher $\mathrm{d}v/\mathrm{d}t$ than conventional Silicon (Si) converters. Several studies indicate that high $\mathrm{d}v/\mathrm{d}t$ voltage pulses can lead to unequal voltage distribution within the machine windings [7, 8]. Moreover, high $\mathrm{d}v/\mathrm{d}t$ can create overshoots at machine terminals due to the reflected wave phenomenon, potentially reaching up to twice the Direct Current (DC)-link voltage [9, 10].

Another trend in EV technology is the increase in battery charging power, raising battery and propulsion system voltages from 400 V to 800 V or even 1000 V [7]. This voltage rise directly impacts the requirements of the insulation system, compounding the challenges introduced by WBG converters in ensuring reliable insulation performance.

It is well-known that the electric field created on the machine winding by these effects may lead to Partial Discharge (PD) activity, one of the most common fault factors, on winding insulation during operation [11]. In particular, interturn winding insulation is most affected, being the weakest point of the winding insulation system [12, 13]. Hence, if voltages above the Partial Discharge Inception Voltage (PDIV) threshold are applied, PD events are likely to occur, accelerating the deterioration of the insulation and leading to premature failure [14, 15].

In addition to electrical factors, environmental factors also enhance PD activity and, consequently, insulation deterioration. Indeed, for the same application and waveform characteristics, PD events may occur or not depending on the environmental conditions, as they affect PDIV [16].

Several research studies indicate that PDIV decreases during service due to aforementioned electrical and environmental factors [17–20]. When the PDIV reaches the operation voltage, constant PD activity is likely to occur, leading to accelerated deterioration and potential insulation breakdown. Therefore, the goal of the insulation design should be to maximise PD-free service life. To achieve this, it is important to maintain a margin between the initial PDIV and the operating voltage. The larger this margin, the longer it will take to reduce the PDIV to the operation voltage. Having accurate models to estimate the initial PDIV in the design stage of the insulation system of the machine is necessary for that.

Given the reduced reliability of the insulation system due to the use of WBG-based converters, evaluating the health of the insulation system through its lifetime is also an important point to consider. Anticipating potential insulation breakdown is essential for ensuring an optimal performance and extending the lifetime of electric machines. Among various markers, the analysis of PDIV deterioration over the lifetime of the insulation system shows promise as a diagnostic marker.

For all the above, PD activity in electric machine insulation has garnered significant interest from Mondragon Unibertsitatea, which has long been involved in the modelling, design, and control of electric machines. This PhD thesis presents a step forward by focusing specifically on insulation design to prevent PD activity during operation, an aspect not previously addressed at the university. The purpose is to integrate a new insulation design phase into an existing electric machine design methodology covering the three main insulations of electric machines (interturn, phase-phase, and groundwall), emphasising interturn insulation. Three key lines of investigation are considered:

- **The study of partial discharge activity under operating conditions at the beginning of the machine lifetime (unaged condition):** This line focuses on the impact of electrical and environmental factors on PDIV and the models to estimate it under representative conditions during the design of the insulation system of electric machines.
- **The assessment of design, manufacturing, and assembly parameters affecting the reliability of the insulation system:** This line identifies design weaknesses and critical manufacturing and assembly stages where the insulation system may be compromised, in collaboration with two industrial companies.
- **The evaluation of the insulation system under several stress scenarios:** This line not only analyse the effect of most compromising stress factors on the PDIV and lifetime but also identifies markers for assessing the health of the insulation system.

1.2 Thesis Objectives and Hypotheses

The goal of every PhD is, by definition, to expand the boundaries of knowledge. Accordingly, the aim of this PhD is to contribute to the body of knowledge in the field of partial discharge free design of electric machines. Specifically, the main objective is to develop novel design tools and to establish some guidelines for the development of robust and reliable insulation systems in electromobility drives based on Wide-Bandgap converters, with particular attention to insulation behaviour under operating conditions and long-term endurance.

1.2.1 Objectives

To accomplish this goal, the following specific objectives were established:

O1. Identify the most relevant environmental and electrical variables affecting the PDIV, and analyse their influence on the initiation of PD activity.

O2. Develop models and procedures for estimating PDIV under representative operating conditions obtaining a mean error lower than 5%, with a particular focus on interturn insulation.

O3. Evaluate the design and manufacturing factors affecting the insulation system of electric machines by validating and extending the practical applicability of the proposed PDIV estimation tools, and assessing the insulation system during manufacturing and assembly processes.

O4. Identify, characterise, and assess the most critical stress factors that negatively impact the long-term endurance of insulation systems, by evaluating a set of insulation health monitoring markers.

1.2.2 Hypotheses

Based on the specific objectives, some hypotheses are formulated. Next, the main hypotheses are summarized:

These are the hypotheses related to **O1.**

H1. The use of WBG-based converters to supply the electric machines could affect the PDIV at the operating conditions.

H2. The exposure of the insulation to high humidity and temperature will worsen the PDIV at operating conditions.

These are the hypotheses related to **O2.**

H3. An accurate, fast, and directly applicable PDIV model without parameter adjustment that considers most relevant factors affecting PDIV during operation would enable estimating the PDIV at the beginning of the electric machine lifetime when simulation and experimental resources are not available.

H4. By applying these models in the preliminary design stage of the insulation system could help to make consistent decisions regarding the required insulation system and material.

These are the hypotheses related to **O3.**

H5. Different winding manufacturing techniques could affect the PD behaviour of the insulation system.

H6. The various weak points in the insulation system, whether identified during the design phase or not, could be successfully detected and addressed by consistently evaluating the PD behaviour throughout the assembly process of the electric machines.

H7. Fabrication tolerances associated with different processes can significantly influence the performance of the insulatin system, potentially reducing its reliability.

This is the hypothesis related to **O4.**

H8. The use of WBG-based converters and the high temperatures reached during operation will accelerate the ageing of the stator winding insulation system, reducing ultimately its endurance.

H9. Developing endurance models that account for the most critical stress factors can help estimate the lifespan of the insulating system under specific operating conditions, providing valuable support for insulation health diagnosis and preventive maintenance.

H10. By evaluating the insulation health during its lifetime could provide information regarding the proximity of insulation failure. This way, anticipated maintenance works could be performed, avoiding failure and ensuring reliable operation.

1.3 Brief Description of Publications and Contributions

1.3.1 Journal Articles

PUBLICATION 1: Reference [21]

Study of Partial Discharge Inception Voltage in inverter fed electric machine insulation systems

L. Elorza Azpiazu, G. Almandoz, A. Egea, G. Ugalde, X. Badiola

Appl. Sci. 2023, vol. 13, no. 4, p. 2417; doi: 10.3390/app13042417

Abstract: Social awareness of climate change has led to electric vehicles becoming increasingly important and their efficiency must be improved. Wide-Bandgap (WBG) converter fed electric machines could contribute. Nonetheless, unequal voltage distribution within the machine winding and high overshoots may bring serious issues on turn-to-turn insulation owing to Partial Discharge (PD) activity. The insulation should be exposed at a lower value than Partial Discharge Inception Voltage (PDIV) to avoid premature failure. It is crucial to consider turn-to-turn insulation PDIVduring design. This article makes a thorough evaluation of different environmental and electrical waveform characteristics affecting PDIV. Special attention is given to temperature. PDIVmodels found in the literature are reviewed. A simple analytical model to estimate the PDIVof twisted pairs depending on temperature is proposed. The performance of several models regarding temperature dependency is compared with experiments. All in all, further studies are necessary considering humidity, rise time and pulse width effect on PDIV. The proposed model shows the best compromise between computational requirements and PDIVestimation accuracy. However, new models regarding both, environmental and waveforms characteristics, are necessary to accurately estimate PDIV, where Extended Volume-Time theory seems to be a good basis.

1.3.2 Conference Proceedings

PROCEEDING 1: Reference [22]

Experimental-Based model for Turn-to-Turn PDIVPrediction Dependent on Temperature

L. Elorza Azpiazu, A. Egea, , G. Almandoz, G. Ugalde, I. Sarasola

2024 International Conference on Electrical Machines (ICEM), Sep. 2024, doi: 10.1109/ICEM60801.2024.10700559

Abstract: Turn-to-turn insulation partial discharge inception voltage (PDIV) plays a crucial role in the design of the insulation system of inverter-fed machines for the automotive sector. This paper presents a turn-to-turn PDIVestimation model as a function of temperature, insulation thickness, and its relative permittivity for round and rectangular conductors. The model addresses constraints identified in other published methodologies, in that it does not require FEM simulation, experimental results as reference data, and γ or Schuman's constant adjustment. The model was validated with over 100 experimental self-measurements and literature results. For almost half of these, the PDIVvalue was estimated with an error of less than or equal to 5%, and the 87% of the estimated values did not exceed an error of 12%. This figure is in good agreement with other literature models. The maximum error obtained was 18%, however this can be attributed to the assumption of unknown insulation thickness and ambient relative humidity condition differences during experiments. By employing the model, coil winding designers or wire manufacturers can quickly and effectively estimate turn-to-turn PDIVat the required operational temperature for round and rectangular conductors.

PROCEEDING 2: Reference [23]

Comparison of Impedance Spectroscopy and Partial Discharge Analysis as Insulation Health Diagnosis Techniques

L. Elorza Azpiazu, Y. Moreno, A. Egea, G. Almandoz, A. Angulo Rebollo

2024 International Conference on Electrical Machines (ICEM), Sep. 2024, doi: 10.1109/ICEM60801.2024.10700230

Abstract: The ageing of insulation systems in electric machines can compromise partial discharge-free designs. Regularly monitoring insulation health is crucial to prevent unexpected failures. Several authors have proposed health markers from impedance spectroscopy and partial discharge analysis. Nevertheless, no comparative study has evaluated their sensitivity as health monitoring techniques for complete windings tested until failure. This paper compares both techniques for a thermally aged electric machine winding until failure, with impedance spectrum and partial discharge measurements taken every 24 hours. Markers from impedance spectroscopy (resonance frequency, impedance above/-below resonance frequency, and capacitance) and partial discharge measurements (partial discharge inception voltage and charge) were compared considering: (1) deteriorated insulation identification, (2) sensitivity to changes in the insulation, and (3) near breakdown indication ability. While impedance spectroscopy markers varied with ageing, partial discharge analysis proved more meaningful. Regular monitoring of partial discharge inception voltage and charge can identify deteriorated insulation and prompt necessary maintenance.

1.4 Dissertation Outline

CHAPTER 2

This chapter presents the theoretical background necessary to support this PhD project. The first section summarises the role of electric machines in EVs, describing the most common machine topologies and stator winding types, as well as the main challenges introduced utilizing WBG-based converters concerning the insulation system. The second section provides a detailed description of stator winding insulation systems, including their components, materials, and key parameters. The third section focuses on the understanding of PD activity, explaining the conditions required to trigger an electron avalanche and how this may lead to PD through Townsend or Streamer mechanisms. The chapter concludes with a summary of the key insights.

CHAPTER 3

Chapter 3 defines the experimental procedures and methods used throughout the project. It includes descriptions of the various sample types, as well as the methods employed for measuring the relative permittivity, PD activity (PDIV and PD patterns), and impedance. The chapter also describes the setups used for thermal and electrical accelerated ageing tests.

CHAPTER 4

This chapter addresses PDIV estimation under operating conditions. It begins with the identification and literature-based analysis of the key parameters affecting PDIV, leading to the selection of the most relevant factors for modelling. Existing models from the literature are then reviewed in the second section, highlighting their strengths and limitations. Based on these insights, in the third section novel PDIV estimation models are developed and validated, offering comparable accuracy to the models proposed in the literature. The proposed models were further validated by their comparison with those from the literature, achieving comparable accuracy with reduced time and required resources to use them. The chapter concludes with the summary of the key findings and results.

CHAPTER 5

This chapter presents collaborative work with two industrial partners. The first collaboration, developed in the first section, investigates the influence of the needle winding technique compared to the semi-automatic method historically used in the company, focusing on groundwall PDIV and PD pattern characterisation. The second collaboration, in the second section, addresses insulation system performance during the design of a machine intended for aeronautical applications. After defining the specifications, the preliminary prototype is analysed, design weaknesses are identified, the impact of assembly steps is assessed, and the effect of the potting is analysed. This prototype is improved by reinforcing the vulnerable points. Manufacturing issues in the groundwall insulation detected during the final batch production are resolved through a combination

of PDIV estimation and experimental validation, allowing for the selection of the optimal thickness and material from multiple candidates. The section concludes with the final product validation, confirming the reliability and robustness of the design under the specified requirements.

CHAPTER 6

Chapter 6 focuses on the insulation system performance through its lifetime. It starts by analysing the two primary stress factors, thermal and electrical. The study is expanded by experimentally comparing the effects of isothermal and thermomechanical ageing on complete insulation systems, and by evaluating the combined influence of waveform characteristics on interturn insulation endurance. In addition, in the second section, thermal stress is further analysed by assessing the effectiveness of insulation health diagnostic markers based on impedance spectroscopy and PD measurements.

CHAPTER 7

This chapter tops off this PhD thesis. The chapter lists the main conclusions of the fulfilled work, and some challenges and opportunities for further research are identified.

Chapter 2

Theoretical Background

This chapter provides the theoretical foundation necessary for the understanding of the thesis. It examines the use of electric machines in EVs, focusing on the primary challenges associated with insulation systems. A summary of the various types of machines employed in these vehicles is presented, emphasising their features and benefits. Furthermore, the section introduces different stator winding configurations and analyses their associated insulation systems. Key parameters of insulation materials are also discussed to elucidate their influence on PD and how these factors affect the durability and efficiency of the electric machine. Finally, as PD originates from gas breakdown, the fundamental mechanisms underlying this phenomenon are compiled and explained.

2.1 Traction Systems for Electric Vehicles

The transition from ICE based transportation to more sustainable alternatives has been extensively explored in the literature. Among the proposed solutions are the battery-powered EV, the Hybrid Electric Vehicle (HEV) and the Fuel Cell Vehicle (FCV). Most manufacturers have focused on EV and HEV architectures due to their relative simplicity. A key distinction among these architectures lies in the energy source utilized. Despite this variation, the electric drive (comprising by a power converter and an electric machine) remains a common and crucial component across all types of energy sources. Consequently, the electric drive plays a pivotal role in the pursuit of more sustainable vehicles [24]. Figure 2.1 illustrates a schematic representation of EV architecture.

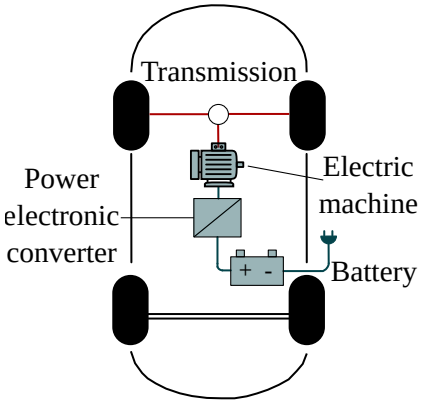

Figure 2.1: *Schematic representation of an EV architecture based on [24].*

The development of next-generation green vehicles, driven by advanced electric propulsion systems, is expected to deliver key improvements such as cost reduction, enhanced efficiency, and increased power density. Achieving these goals requires advancements in both converter and electric machine technologies [24]:

- **Cost reduction:** Achieved by using magnets with lower rare earth content and simplifying cooling systems.
- **High efficiency:** Enabled through high-frequency converters with reduced switching losses, electric machines with lower copper and iron losses, and the use of high-performance alloys.
- **High power density:** Obtained by raising machine operating speeds and implementing high-efficiency cooling strategies to boost power capability.

2.1.1 Electric Machines

As previously mentioned, the electric machine is a critical component in green vehicles, significantly influencing their efficiency, performance, and reliability. The following

lines briefly describe the main machine topologies and stator winding configurations employed in EVs, summarising their key features, advantages, and common use cases.

2.1.1.1 Machine Topologies

The electric machine is responsible for transforming electrical energy into mechanical, which generates the rotation of the wheels and finally the displacement of the EV. EVs could be equipped with either Alternating Current (AC) or DC machines. The main difference between them is the power source, which directly affects the construction of the machine. For instance, the stator of DC machines may be constructed with permanent magnets or a winding that produces a static magnetic field. On the contrary, AC machines typically have stators with multiple windings to create a rotating magnetic field.

Unlike electric machines used in the industry, the ones for EVs need to change speed, increase torque, or abruptly brake depending on the driving cycle. So, the main characteristics required for electric machines for traction applications are quick and rapid torque response, high power density, high efficiency, overload capacity, small size, reduced weight, low moment of inertia, acceptable cost, and high reliability and robustness [3].

Within these specifications, various machines have been used by EV manufacturers, such as Permanent Magnet Synchronous Machines (PMSMs), Induction Machines (IMs), Permanent Magnet Brushless DC Machines (PMBLDCMs), Switched Reluctance Machines (SRMs), or DC machines. Each of them with its advantages and limitations, Figure 2.2 summarizes the comparison of the machines regarding the operational performance, reliability, and efficiency. Based on this comparison, although DC machines are well-developed, they are no longer favoured for light vehicles given the high maintenance required by the brushes. Additionally, the minimal maintenance of IMs, PMSMs, and SRMs place the DC machines in the last place [3, 24]. These preferences are also visible in the market trend, where in the last decades, electric car manufacturers have replaced DC machines with AC machines [3].

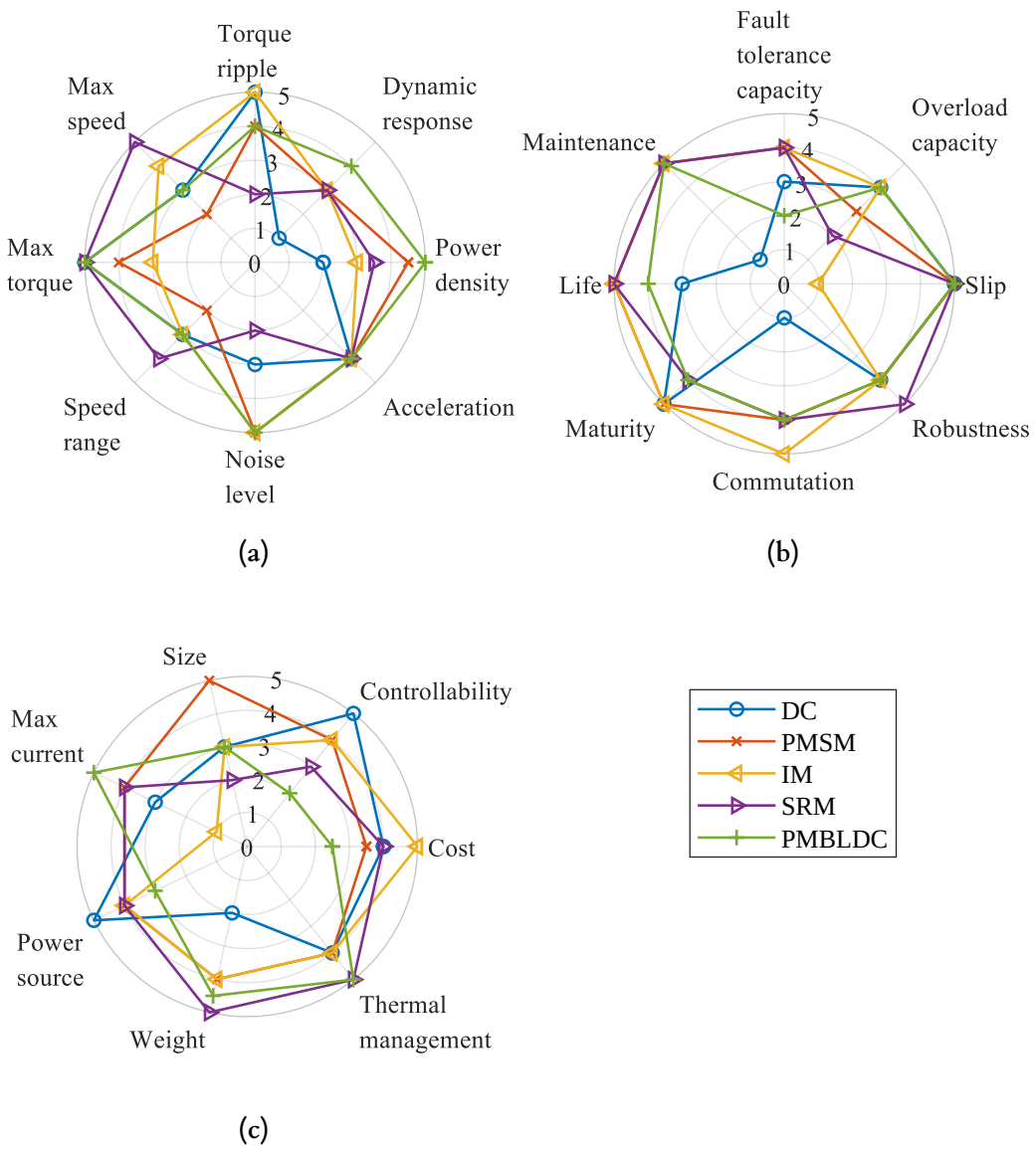

Figure 2.2: *Comparison of electric machines for EVs based on [3] considering (a) operational performance, (b) reliability, and (c) efficiency factors.*

Through the comparison between the AC machines, achieving a unique solution giving the best operational performance, reliability, and efficiency can lead to conflicting design concepts. For instance, cost reduction focuses on non-rare earth-based machines such as IMs or SRMs, which have lower power densities compared to PMSMs (rare earth-based). This makes it challenging to meet volume reduction goals. Therefore, the selection of the preferable machine for each EV should be adapted to the specific context of a given propulsion system. Factors such as required installation space, efficiency in the whole operation range, or torque vs speed characteristics should be considered for that [24].

Nonetheless, there is a clear prevalence of the use of PMSMs in EVs in the last decades [3, 24]. This highlights the importance of the increase in the power density to

enhance the autonomy of EVs. Recent advancements in less rare-earth PMSMs have contributed to both cost reductions and decreased environmental impact, one of the principal vulnerabilities of PMSMs [25].

2.1.1.2 Stator Winding Types

A common element of the different electric machine topologies is the stator, which is responsible for producing the magnetic field that generates the rotation of the rotor. The main three elements comprising the stator are the stator core, the conductors, and the insulation system.

The main role of the stator core is to provide structural support, guide the magnetic flux created by the conductors, and enhance thermal efficiency. The electric current flowing through the conductors creates the magnetic field required for the operation of the electric machines. Lastly, the insulation system is the passive component and does not play an operating function of the machine, but is still a key component. It is required as a thermal conductor, it prevents mechanical damage, and, paramount, it prevents short circuits between the conductors, or conductors and grounded elements.

Generally speaking, two main machine winding configurations are the random-wound and form-wound (Figure 2.3). The applied voltage of the machine determines the type of stator used. The former is advisable for low voltage machines (< 700 Vrms), whereas the latter is used in larger machines with operating voltage above 700 Vrms [9].

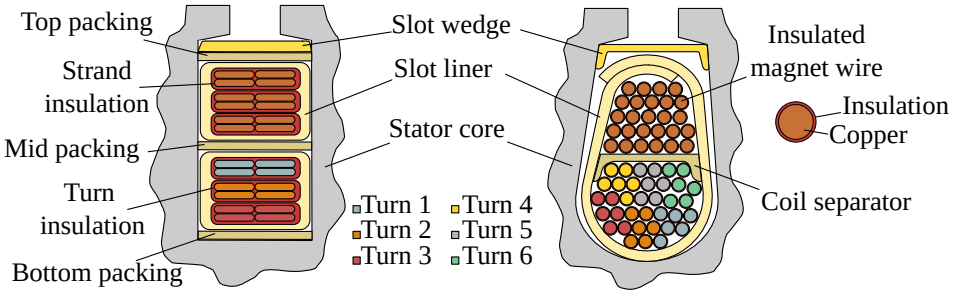

Figure 2.3: *Schematic representation of form-wound (left) and random-wound windings (right) based on [26].*

Random-wound is constructed with round insulated copper conductors (magnet wire) continuously wounded through the machine stator slot. Its main advantages are the high mechanical fixability, the consequent easy manufacturability, and cost-effectiveness. As its name suggests, the conductors are typically placed randomly inside the stator slot. Thus, as it is shown in Figure 2.3, the conductor connected to the phase terminal could be adjacent to a conductor operating at lower voltage, causing the insulation to withstand a high voltage gradient. Moreover, its efficiency is limited due to the low filling factor (in the range of 35-45%) [11].

Fabrication methods such as needle winding can be used to overcome the mentioned issues (Figure 2.4). Indeed, the arrangement of the conductors can be designed to minimize

the voltage gradient between touching conductors and increase the filling factor due to its precise and compact positioning [27, 28]. Even so, the contact between the intermediate and first turn is inevitable, and the uneven voltage distribution among the coils generated by WBG converters (explained later in Section 2.1.3.2) could increase the expected voltage difference between them.

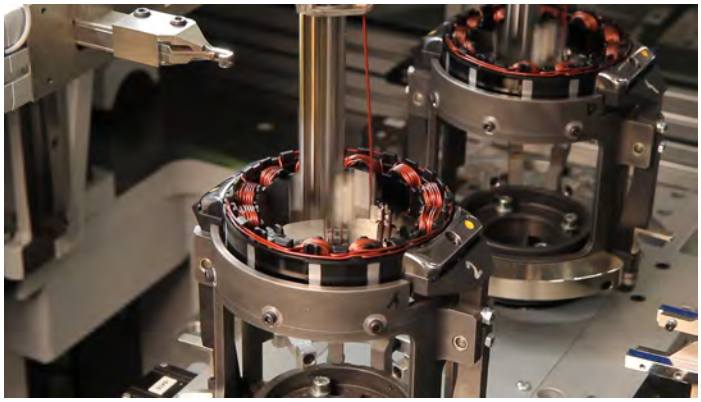

Figure 2.4: *Needle winding fabrication method for random-wound stator windings using round wire conductors. Image from [29].*

Instead of round wires, rectangular ones are used for form-wound windings and are considered a promising solution for high-power density machines [11]. Their main advantage is the maximisation of the slot filling factor, the enhanced thermal performance, and the homogeneous electrical stress distribution, which allows diminishing the difference of voltage between coils [30]. They can be easily manufactured in automatic production, being hairpin winding (Figure 2.5) and continuous multi-layer winding the most common types.

Figure 2.5: *Hairpin winding 3D model with welding points in grey. Image from [31].*

However, form-wound windings also have their limitations. On the one hand, AC losses are not negligible due to their high conductor section, and attention should be given to the losses due to skin and proximity effect at high frequencies. Further, they have limited flexibility in the number of turns in series per phase, and include a high number of bending and welding points (in the case of hairpin windings) [11, 32].

Less popular alternatives are windings constructed with litz wires. These are composed

of individually insulated thin wires twisted together. With a filling factor comparable to form-wound windings [33], they mitigate the AC losses at high-frequency operations through the division of the current between the strands, and have better mechanical flexibility than round or rectangular conductors. Even though, the complex contacting process of each individual wire renders it a less appealing option [34].

Although random-wound windings have been the preferable configuration for electric machine manufacturers in the context of EVs, form-wound windings have gained popularity and become the standard solution for high-performance EVs [35]. A clear example of this replacement is the winding configuration of the electric machine used in Tesla Model 3, where round conductors were replaced by rectangular ones in the more recent model [36, 37]. Given the predominant use of random and form-wound windings, the work developed in this thesis will be focused on round and rectangular conductors.

2.1.2 WBG-Fed Electric Machines

Together with the electric machine and battery pack, the power converter is the central component of the electric drive. It regulates the bidirectional power flow between the electric machine and battery pack and is responsible for supplying the required voltage level at the required frequency to have a variable speed.

Among other technologies, the literature extensively mentions that WBG-based converters can manage to increase the power density of the electric drive [5, 12, 24, 38–40]. New power converter technologies based on WBG materials (e.g., SiC and GaN) offer higher efficiency and power density than conventional Si devices due to their properties, such as reduced losses, high-temperature operation capability, and weight reduction. Figure 2.6 categorizes different power electronic devices based on their power versus switching frequency relationship.

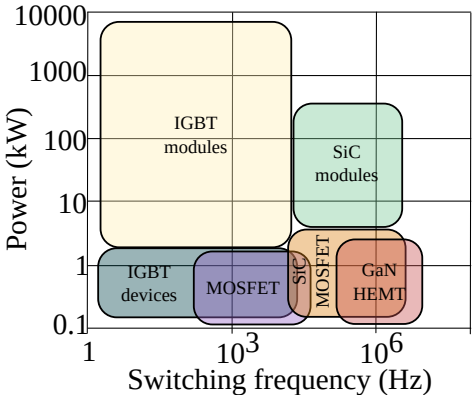

Figure 2.6: *Categorisation of power electronic devices depending on power vs switching frequency relationship based on [39].*

The high power/switching frequency relationship offered by WBG-based converters makes them ideal for automotive EVs, maximizing power density and efficiency [6, 12].

The power density of power converters is increased by reducing the weight and volume of their passive components. Additionally, high switching frequencies enable high-speed machines, which means that for the same output power, less torque is required. This presents an opportunity to reduce the size and weight of the electric machine as well [5].

2.1.3 Challenges

Despite the significant potential of WBG technology for zero-emission transportation, several challenges remain [38]. In particular, the insulation system of the electric machine winding is affected by high switching frequencies and high dv/dt [12]. These factors disturb the voltage distribution within the machine winding. Additionally, the reflected wave phenomenon can produce overshoots up to twice the DC-link voltage, depending on the cable length between the converter and the machine [9, 10].

Both effects force the insulation system of the winding to withstand higher voltage stresses than expected. Interturn insulation is particularly affected, as it is the weakest point of the insulation [12, 13]. Therefore, special attention must be paid to its design. For example, the insulation systems could be designed with a voltage margin for safety, considering non-uniform voltage distribution and high overshoots [12].

Furthermore, the latest trends in electric vehicles show a tendency to increase charging power, raising the voltage of batteries and corresponding propulsion systems from 400 V to 800 V. This higher voltage level further increases the insulation requirements to withstand the mentioned stresses [7]. These stresses may cause PD activity in conventional machine insulation, one of the most common fault factors [11], altering the scenario of winding insulation design.

2.1.3.1 Overshoot

The overshoot generated by modern converters at the machine terminals depends on several factors, including the rise time of the voltage at the converter output, the cable length between the converter and the machine, and the machine impedance. This overshoot is caused by reflected waves due to impedance mismatch. In the worst-case scenario, it may reach twice the DC-link voltage [9]. Figure 2.7 provides a schematic representation of this phenomenon.

Although this phenomenon is widely studied under typical Pulse Width Modulation (PWM) supply, shorter rise times and higher frequencies necessitate expanding the analysis to include WBG features. As illustrated in Figure 2.8, for rise times shorter than 50 ns (from SiC MOSFETs), even with cable lengths around 2 m, the overshoot can double the DC voltage at the machine terminal. Other studies have shown that for a nominal bus voltage of 400 V with a cable length of just 1 m, the overshoot at the machine terminals exceeds twice the DC bus voltage [39]. For Insulated Gate Bipolar Transistor (IGBT) fed machines with rise times around 200 ns, this overshoot occurs with cable lengths over 15 m [42].

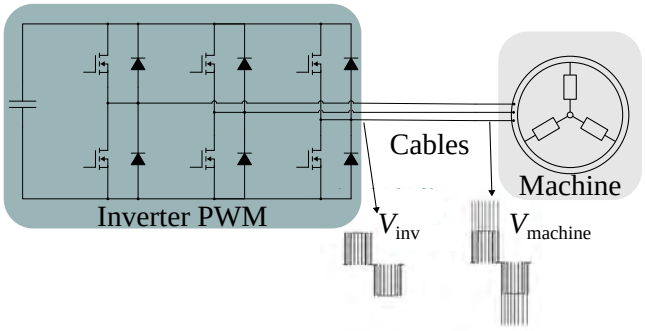

Figure 2.7: *Inverter-derived overshoot at machine terminals caused by impedance mismatch points based on [30, 41].*

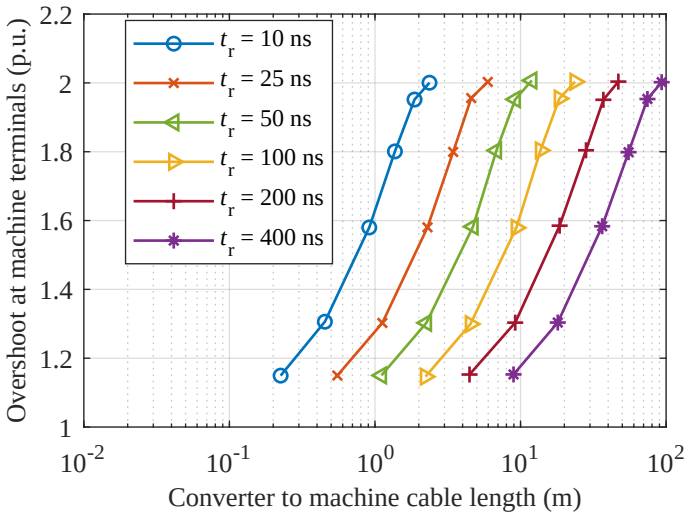

Figure 2.8: *Overshoot at machine terminals with different cable lengths for different rise times based on [42].*

Hence, it is evident that the use of short rise times can lead to significant overshoots at the machine terminals, even with short connection cables. As outlined by various authors [5, 12, 41], this can result in undesired PD triggering and premature winding ageing.

2.1.3.2 Non-Uniform Voltage Distribution

In random-wound windings, the voltage distribution along the turns of the magnet wire within a phase can be non-uniform [43]. This means a voltage gradient can exist between the first and last turn of the coil. Due to the manufacturing process of these windings, it is common to find physical contact between the first and last turn, resulting in a substantial voltage difference between adjacent turns [7, 8]. This significant voltage difference increases electrical stress on the insulation system, leading to PD activity [41].

The uneven voltage distribution is caused by parasitic capacitances, which become significant due to high-frequency components flowing through the winding, creating a

low-impedance path to ground [44]. Consequently, the enamel of two turns of the first coil of the stator withstands most of the applied voltage [8, 45].

Previous studies have analysed and experimentally validated the voltage distribution in conductors as a function of rise time. Shorter rise times increased the voltage drop along the coil [7, 8]. With a 150 ns rise time, the voltage drop was about 250 V over nearly 7 m of coil length, whereas with a 20 ns rise time, the voltage dropped to 0 V in approximately 3 m (Figure 2.9) [7]. Such electrical stresses can trigger PD, leading to premature failure of the machine insulation, particularly interturn insulation [45].

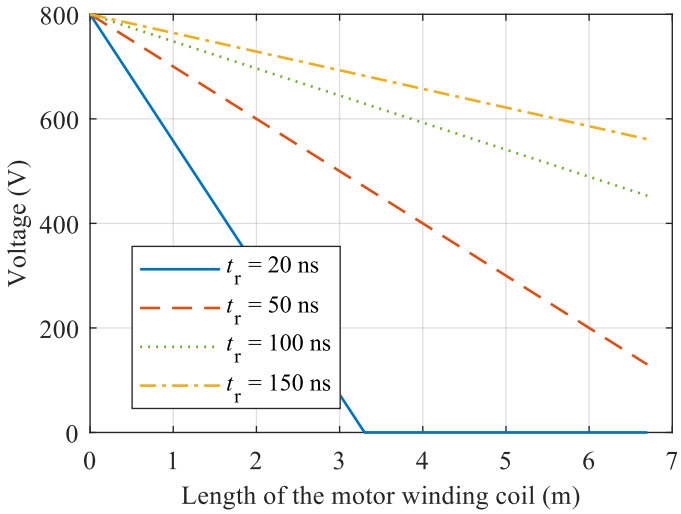

Figure 2.9: *Simulated voltage levels along the length of the machine winding coil using different rise times based on [7].*

According to [46], in hairpin windings, the uneven voltage stress distribution across the conductors within a slot is exacerbated by local temperature increases in the winding insulation. Although this thermal effect could be mitigated by optimising the cooling structure, the simultaneous presence of high local temperature and voltage stress may threaten the safety of the machine, as it facilitates the inception of PD in the interturn insulation.

2.1.3.3 Effect on Partial Discharge Activity and Machine Lifetime

As previously mentioned, one of the significant challenges associated with using WBG-based converters to power electric machines is the increased probability of PD [47]. This phenomenon arises due to the high switching frequencies and short rise times characteristic of WBG devices, which can lead to substantial electrical stresses on the machine insulation system. These stresses can trigger PD, potentially causing premature ageing and failure of the insulation, thereby impacting the overall reliability and longevity of the electric machine. Understanding and mitigating these effects is crucial for the safe and efficient operation of next-generation EVs.

PD typically occurs at weak points in the conductor where the dielectric strength is lower, making it easier to trigger PD (later in Section 2.3). In stator winding insulation, the materials used have a higher dielectric strength than air, allowing them to withstand higher voltage levels before breaking down. Consequently, PD generally occurs in the air surrounding the conductors or trapped inside voids [48].

When an electric field is applied between two electrodes, the critical voltage level at which PD conditions are met is defined as the PDIV. According to IEC 60270 [49], PDIV is the lowest applied voltage where PD is first observed when the voltage is progressively increased from a lower value where PD is not observed. For AC voltage, PDIV is usually given in rms.

Throughout the lifetime of an electric machine with a PD-free design, the PDIV value of the insulation system evolves as shown in Figure 2.10. Initially, before manufacturing and assembly, the selected insulation material has a specific PDIV. During manufacturing and assembly, PDIV decreases due to cracking and internal mechanical stresses, potentially reducing by up to 15% from the raw magnet wire to the assembled stator winding [50].

Once the machine is operational, PDIV further decreases due to electrical and environmental conditions. This reduction is depicted in green as 'No ageing' in Figure 2.10. During operation (represented in yellow as 'Ageing without PD'), ageing factors such as mechanical, electrical, and environmental stresses reduce PDIV until it equals the operating voltage, reaching a critical point [50]. Below this point (represented in red as 'Ageing with PD'), the insulation material operates under PD activity, accelerating deterioration and leading to faster failure [14, 15].

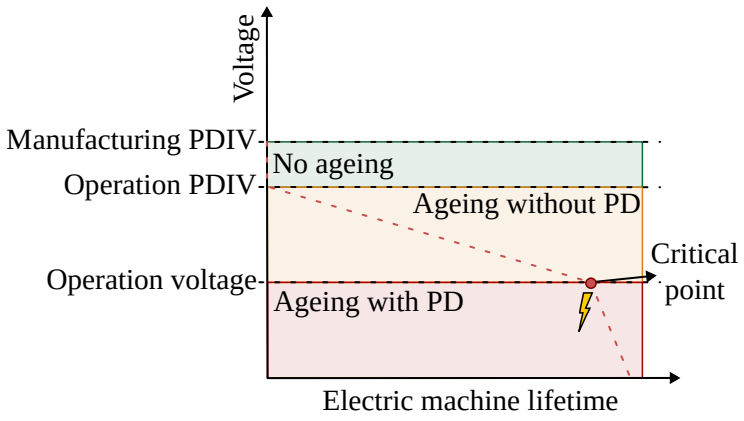

Figure 2.10: *Schematic representation of PDIV in an electric machine lifetime based on [50].*

Given this, it is crucial to design insulation systems with a safety margin between the initial PDIV and the maximum peak voltage stress applied. The larger this safety margin, the longer it will take for PDIV to decrease and reach the operating voltage level. Understanding the operational PDIV and the effect of different stresses during the lifetime can help to adapt the design of the insulation system, reducing the likelihood of unexpected insulation failures. Overall, PDIV is essential for the safe design of electric machine insulation systems.

2.2 Stator Winding Insulation System

The insulation system of the stator winding plays a critical role in the reliable operation of any electric machine. It serves three primary functions [26]:

- **Prevention of electrical short circuits:** The foremost purpose of the insulation system is to prevent electrical short circuits in the winding. A short circuit resulting from an insulation fault typically causes complete machine failure. Therefore, it is essential to ensure that the breakdown voltage of the machine significantly exceeds its operating voltage.
- **Heat dissipation:** Electrical machines experience heat generation due to current flow through the winding. According to Joule's first law, energy proportional to I^2R is produced when a current I flows through a conductor with resistance R. This heat, referred to as copper or winding losses, reduces machine efficiency and accelerates insulation degradation. Thus, effective heat dissipation through the stator core via the insulation system is crucial.
- **Prevention of mechanical damage:** Mechanical damage to the winding can result from movement caused by mechanical vibrations or Lorentz magnetic forces acting on the conductors. The insulation system helps prevent such damage.

2.2.1 Components and Materials

The properties of the components of the insulation system are the key factors in determining the machine rated voltage, life expectancy, or thermal class. Depending on the type of winding, the materials, and components of the insulation system may vary. Indeed, Type I insulation systems (generally in random-wound windings [9]) should not have PD activity during their lifetime and organic polymer materials are used. However, Type II insulation systems (usually in form-wound windings [9]) are supposed to operate under PD activity and both organic and inorganic materials are used.

Organic materials, typically derived from natural or synthetic polymers, are widely used in insulation systems due to their affordability and low processing costs, attributed to their easy machinability. These materials exhibit high breakdown strength but are not resistant to PD activity. The wide range of available materials allows for selection based on the severity of the electrical, thermal, and mechanical stresses of the application. Materials such as Polyamide-imide (PAI), Polyester-imide (PEI), Polyether (PE) or Polyimide (PI) are most often used on electric machine insulation systems [26].

In contrast, inorganic materials, which are mineral-based, offer superior thermal stability, ageing resistance, and PD activity resistance. Even so, their poor mechanical properties reduce machinability, significantly increasing the processing costs. As a result, their high cost limits their application. Among inorganic materials, mica is notably used

in electric machine insulation systems. For winding wires, a typical approach combines an organic enamel basecoat layer with an inorganic overcoat, for example, Polyamide-imide Corona Resistant (PAICR), where the standard PAI organic layer is finished with a thin Corona Resistant (CR) layer containing mica particles [26].

The components of the insulation system can be classified into three main categories: turn-turn or interturn insulation, phase-phase insulation and phase-ground or groundwall insulation (Figure 2.3) [26]:

- **Interturn insulation:** It prevents short circuits between the turns of a coil. It consists of an enamel layer on the round or rectangular copper wire. This enamel can be compounded by one or more layers (Figure 2.3). In multilayer enamels, the inner layer ensures strong adhesion to the copper (e.g., PEI), while the outer layer enhances thermal or electrical properties (e.g., PAI or PI for even higher thermal resistance).

  Common materials for interturn insulation include PAI, PEI with a PAI overcoat, PI, and PE. Conductors with these types of materials are known as conventional or Stardard Wire (SW). To improve resistance to PD deterioration, organic materials are combined with inorganic materials and applied to the wire surface. These composite materials are created by dispersing micro- or nano-sized inorganic particles within the polymer matrix. While their properties depend on the characteristics of polymer matrix and inorganic particles, they exhibit higher breakdown strength and significantly longer lifespan under PD activity than SW. Conductors using this type of insulation material are referred to as Corona Resistant Wire (CRW).

- **Phase-phase insulation:** It prevents contact between coils of different phases within the slot in double-layer windings or at the end-winding (Figure 2.3). Insulating papers are made from synthetic materials such as aramid paper or polyester fleece. Depending on the voltage, the thickness of the paper may vary from 0.1 to 0.5 mm.

- **Groundwall insulation:** If the interturn or phase-phase insulation fails, the resulting high current through the fault will destroy the next insulation component, the groundwall insulation. This separates the winding wires (round or rectangular conductors with interturn insulation) from the stator core or other grounded components (Figure 2.3). Moreover, it mechanically protects the wires from the edges of the slot. Slot liners act as separators, while wedges secure the winding in the slots and prevent conductor movement. As in phase-phase insulation, insulation paper, such as mica paper bonded with epoxy resin, is used in various thicknesses depending on the voltage class.

Finally, the entire insulation system can be reinforced with impregnation varnish or resin. This replaces air in the insulation system, improving its electrical, mechanical (by fixing the coils and reducing vibration), and thermal performance (as it is a better thermal

conductor than air). Commonly used impregnation materials include polyester-based, epoxy-based, and polyester-imide-based liquids [26]. Depending on the application, different techniques can be employed. For example, Global Vacuum Pressure Impregnation (GVPI) processes can minimize residual air content after impregnation, which is essential to prevent PD activity [26].

2.2.2 Characteristic Parameters

The characteristic parameters defining the properties of the insulation system can be categorised into mechanical (e.g., tensile and compressive strength), electrical (e.g., electric strength and insulation resistance), thermal (e.g., thermal conductivity and expansion), chemical (e.g., resistance to chemical reagents) and miscellaneous (e.g., specific gravity and transparency) properties [51]. Given the extensive number of parameters, the most relevant ones for the understanding of this work are described in the following subsections. The typical values of these parameters for several materials commonly used in electric machine insulation systems are collected in Table 2.1.

Table 2.1: *Characteristic parameters of commonly used insulating materials [51].*

Material	Electric strength (kV/mm)	Relative permittivity (ε_r) at 1 MHz (-)	Thermal class (°C)
PAI	23	3.9-5.4	200-220
PE	20-30	2.2-2.4	90
PEI	22	3.0-3.1	180-200
PI	22	3.4-3.5	240

2.2.2.1 Insulation Thickness

In addition to the material properties, the insulation capacity also depends on the thickness of the layer. Thicker interturn, phase-phase or groundwall insulation layers typically provide higher breaking voltage, PDIV, and a longer lifespan. Even so, it also hinders heat dissipation and reduces the slot filling factor, leading to increased copper losses, lower efficiency, and reduced power-to-mass ratio [12].

A wide range of insulation thicknesses is available for phase-phase and groundwall insulation papers. In contrast, interturn insulation thickness is determined by standards and classified into 'Grades', which specify the minimum and maximum allowable thickness. For round wires, Grades 1, 2 or 3 are currently specified, with thicknesses dependent on nominal conductor diameter (Table 2.2) [52]. For rectangular conductors, Grades 1 or 2 are defined, with fixed thickness ranges independent of conductor nominal dimensions (Table 2.3) [53].

Table 2.2: *Some examples of insulation Grade specifications for round copper wires [52].*

Nominal diameter (mm)	Minimum insulation thickness (µm)			Maximum insulation thickness (µm)		
	Grade 1	Grade 2	Grade 3	Grade 1	Grade 2	Grade 3
0.80	15.0	28.0	42.5	27.5	42.0	55.5
0.85	16.0	30.0	45.0	29.5	44.5	59.0
0.90	16.0	30.0	45.0	29.5	44.5	59.0
1.00	17.0	31.5	47.5	31.0	47.0	62.0

Table 2.3: *Insulation Grade specifications for rectangular copper wires [53].*

Grade	Insulation thickness (µm)		
	Minimum	Nominal	Maximum
1	30.0	42.5	55.0
2	60.0	72.5	85.0

2.2.2.2 Electric Strength

The electric strength is defined as the ratio of the maximum voltage applied without electric breakdown to the distance between the conductive parts under specified test conditions [54]. It is measured in V/m according to the International System of Units (SI).

Electrical strength depends on several factors including the insulation material and thickness, the applied voltage waveform (e.g., DC, sine wave, square wave, etc.), frequency and rate of amplitude increase (e.g., generally around 1 kV/s), and experimental conditions (e.g., temperature, humidity, and pressure) [51].

2.2.2.3 Relative Permittivity

The relative permittivity is also known as the dielectric constant and is a dimensionless measure of the ability of the material to store electrical energy in an electric field relative to the permittivity of vacuum. It quantifies the polarisation of the material in response to an applied electric field [55].

It is calculated using the capacitance ratio of a capacitor filled with the material under study (C_x) to the capacitance of the same capacitor where the material is replaced by vacuum (C_0) (equation (2.1)) [56, 57]. Considering equation (2.2), where S is the area of the capacitor and d is the distance between capacitor electrodes, and assuming the same capacitor (with equal S and d), relative permittivity of an insulation material ($\varepsilon_{r\,x}$) can also be expressed as the relationship between its absolute permittivity (ε_x) and the permittivity of vacuum ($\varepsilon_0 = 8.854 \cdot 10^{-12}\,(\frac{\mathrm{F}}{\mathrm{m}})$).

$$\varepsilon_{\mathrm{r\,x}} = \frac{C_{\mathrm{x}}}{C_0} \tag{2.1}$$

$$C_{\mathrm{x}} = \varepsilon_{\mathrm{x}} \frac{S}{d} \tag{2.2}$$

$$\varepsilon_{\mathrm{r\,x}} = \frac{\varepsilon_{\mathrm{x}}}{\varepsilon_0} \tag{2.3}$$

To better understand the significance of relative permittivity on PD activity, presume that an insulation material and air are arranged in series between two electrodes (as a parallel-plate capacitor, Figure 2.11). This configuration is equivalent to a circuit comprising two capacitors in series. For simplicity, assume that both capacitors have the same area S. The capacitance of each capacitor can then be expressed using equation (2.2), where $\varepsilon_{\mathrm{x}} = \varepsilon_{\mathrm{ins}}$ and $d = d_{\mathrm{ins}}$ for the insulation material, and $\varepsilon_{\mathrm{x}} = \varepsilon_{\mathrm{air}}$ and $d = d_{\mathrm{air}}$ for air. The equivalent capacitance for both capacitors in series can then be given by equation (2.4), considering equation (2.3).

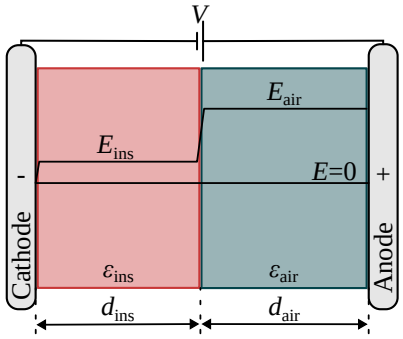

Figure 2.11: *Schematic representation of a parallel-plate capacitor composed of air and insulation material, along with the corresponding electric field distribution.*

$$\frac{1}{C_{\mathrm{eq}}} = \frac{1}{C_{\mathrm{ins}}} + \frac{1}{C_{\mathrm{air}}} \rightarrow C_{\mathrm{eq}} = \frac{S\ \varepsilon_0\ \varepsilon_{\mathrm{r\ ins}}\ \varepsilon_{\mathrm{r\ air}}}{d_{\mathrm{ins}}\ \varepsilon_{\mathrm{r\ air}} + d_{\mathrm{air}}\ \varepsilon_{\mathrm{r\ ins}}} \tag{2.4}$$

Assuming that $Q = C_{\mathrm{eq}}\ V$ (since for capacitors in series $Q = Q_{\mathrm{ins}} = Q_{\mathrm{air}}$), and the electric field is given by $E_{\mathrm{x}} = V_{\mathrm{x}}/d_{\mathrm{x}}$, the electric fields in the insulation material E_{ins} and air E_{air} can be derived using equation (2.4). They are expressed as equations (2.5) and (2.6), respectively, where V represents the applied external voltage.

$$E_{\mathrm{ins}} = \frac{V\ \varepsilon_{\mathrm{r\ air}}}{d_{\mathrm{ins}}\ \varepsilon_{\mathrm{r\ air}} + d_{\mathrm{air}}\ \varepsilon_{\mathrm{r\ ins}}} \tag{2.5}$$

$$E_{\text{air}} = \frac{V\ \varepsilon_{\text{r ins}}}{d_{\text{ins}}\ \varepsilon_{\text{r air}} + d_{\text{air}}\ \varepsilon_{\text{r ins}}} \tag{2.6}$$

From both equations (equations (2.5) and (2.6)), several conclusions can be drawn: (1) E_{air} is always higher than E_{ins}, as $\varepsilon_{\text{r ins}}$ is always greater than $\varepsilon_{\text{r air}}$, which is $\varepsilon_{\text{r air}} \approx 1$ (Figure 2.11). (2) A higher $\varepsilon_{\text{r ins}}$, reduces the drop of the electric field on the insulation, resulting in a higher E_{air}. This occurs because the polarisation efficiency of the insulating material increases with higher $\varepsilon_{\text{r ins}}$, creating an internal electric field that opposes the external field, thereby lowering the overall E_{ins} within the material. (3) A higher E_{air} raises the likelihood of PD activity. Therefore, as discussed in point (2), a higher $\varepsilon_{\text{r ins}}$ increases the probability of PD activity occurring in the air enclosed within the insulation system.

2.2.2.4 Thermal Class

The thermal class refers to the maximum temperature, in degrees Celsius, for which an insulating material or system is suitable for normal use, typically, over a lifetime of 20000 hours [54]. The detailed test procedures can be found in [58, 59]. The thermal class of the entire insulation system does not necessarily imply that all materials used have identical thermal capabilities. In general, the thermal class of the insulation system is defined by the most thermally restrictive material within it.

2.3 Partial Discharges

A widely accepted definition of PD is provided in IEC 60270 [49], where it is described as “a localized electrical discharge that only partially bridges the insulation between the conductors and which can or cannot occur adjacent to a conductor”. In simple terms, the PD is an electrical breakdown that occurs between two surfaces, where at least one is not an electrode and does not immediately lead to the complete failure of the insulator.

Although this phenomenon does not affect the whole insulation, prolonged exposure can accelerate its ageing process. Over time, this deterioration may lead to the breakdown of the stator winding insulation, ultimately causing the failure of the electric machine [60].

In electric machine insulation systems, the dielectric strength of the insulating material is approximately 100 times greater than that of air [26]. This property makes these materials highly effective in preventing electrical discharges within the machine. Nonetheless, it is common to encounter gas voids inside the insulation, particularly air. Under suitable conditions, PD can trigger in those gas-filled voids, or gas adjacent to solid insulation along a surface.

The phenomenon of PD can be categorized into four groups (Figure 2.12) [61]:

- **Internal discharge:** The PD occurs in gas-filled cavities, which may or may not be bounded by electrodes. Such cavities can result from air trapped during the manufacturing process, or delamination, which is the generation of elongated cavities due to the separation of insulation layers. The electric field component perpendicular to the discharge surface is significant in these cases.
- **Surface discharge:** It occurs on the surface of a dielectric material, where the electric field predominant component is tangential to the dielectric surface. PD at the interface between two dielectric materials is also classified as surface discharge.
- **Corona discharge:** It is a discharge in a gaseous medium originating from a metal electrode, where the electric field is highly non-uniform. In this case, no solid or liquid insulation material is involved.
- **Floating masses discharge:** This form of PD arises from metallic components that are not firmly connected to any electrode.

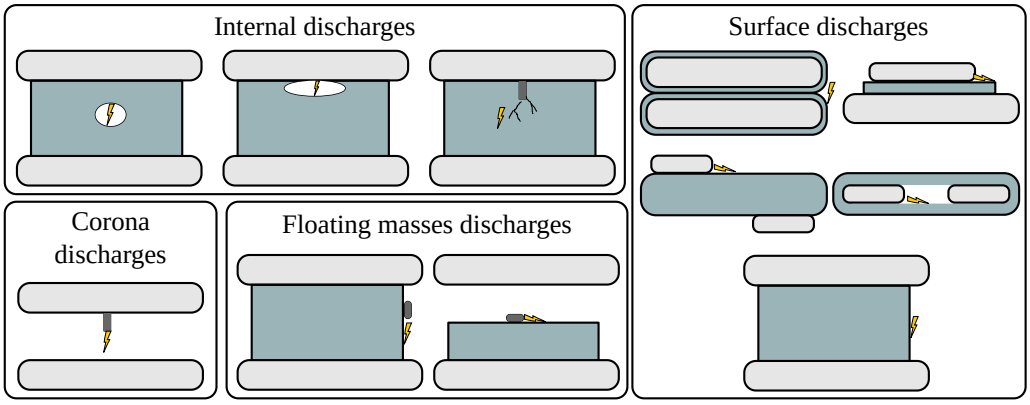

Figure 2.12: *Classification of PD activity based on [61].*

The foundation of PD can be explained through the phenomena of electrical breakdown in gases. Two classical approaches for describing gas breakdown are the Townsend mechanism and the Streamer mechanism, both of which originate from an initial phase known as the electron avalanche [62].

2.3.1 The Electron Avalanche

The primary driving the electron avalanche is impact ionisation. This process involves the creation of electrons and positive ions through collisions between a primary free electron and a neutral gas atom or molecule under the influence of an electric field. To trigger this process, two fundamental conditions must be met (1) a primary free electron must be present, and (2) the electric field strength must exceed a certain threshold value. Figure 2.13 illustrates the development of an electron avalanche via a chain reaction of impact ionising collisions [61, 62].

The electron avalanche starts with a primary free electron n_0, which may be emitted from a metal cathode [61] or the insulation surface in enamelled electrodes [63]. Under the influence of the electric field E_0, this electron accelerates and travels a free path λ, the distance between two collisions in the direction of E_0. During this motion, the electron gains kinetic energy, which can be approximated as the product of E_0 times λ. Since the pressure of the gas p is inversely proportional to λ, the ratio of E_0 to p, known as the reduced field E_0/p, directly determines the energy acquired by the electron between two ionisation collisions.

If this energy overcomes the ionisation potential of the gas, the free electron collides with a neutral particle, ejecting an outer-orbit electron and generating additional electrons and positive ions via impact ionisation. These newly created electrons n are also accelerated by E_0, leading to further collisions and ionisation, perpetuating the chain reaction [61, 62].

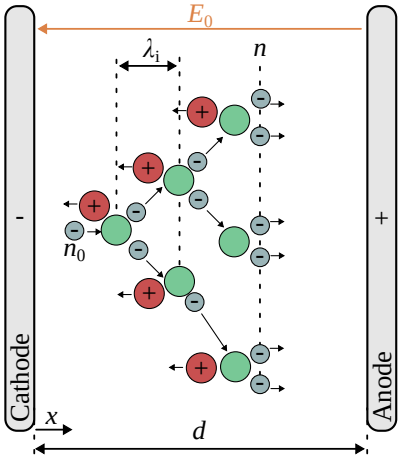

Figure 2.13: *Schematic representation of the electron avalanche multiplication process based on [62].*

The effectiveness of the electron avalanche depends on generating new free electrons and their ability to sustain the process. However, impact ionisation is not the only active mechanism during the avalanche. After an ionisation event, charged particles move under the influence of E_0. Due to their mass difference, electrons move towards the anode much faster than positive ions travel to the cathode.

This movement has several implications. First, the difference in velocity between electrons and ions causes charge separation, resulting in an electron concentration at the head of the avalanche and positive ions distribution along its tail (Figure 2.14). Second, as electrons travel, they may attach to neutral particles through attachment processes. Consequently, impact ionisation and attachment process occur simultaneously, reducing the number of free electrons available to initiate new avalanches.

Considering this coexistence, the number of effective electrons generated during the electron avalanche $\mathrm{d}n$ is expressed in equation (2.7). It depends on the number of electrons at a given distance from the cathode (n), their displacement $\mathrm{d}x$, and the effective ionisation coefficient $\bar{\alpha}$ (equation (2.8)), which is the net difference between the electrons

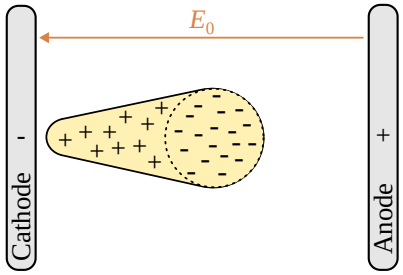

Figure 2.14: *Schematic representation of an electron avalanche based on [61].*

created by impact ionisation (given by Townsend's first ionisation coefficient, α) and those lost through attachment (given by attachment coefficient, η) [64].

$$\mathrm{d}n(x) = n(x)\ \bar{\alpha}\ \mathrm{d}x \tag{2.7}$$

$$\bar{\alpha} = \alpha - \eta \tag{2.8}$$

By integrating equation (2.7) from $x = 0$ to x with an initial number of electrons n_0 at the cathode, the total number of effective electrons at any point in the gap is given by equation (2.9).

$$n = n_0\ \mathrm{e}^{\bar{\alpha}\ x} \tag{2.9}$$

The number of electrons n depends strongly on $\bar{\alpha}$, which is influenced by the electric field and the nature of the gas. For simple gases, the relation between $\bar{\alpha}$ upon p can be described as a function of the reduced field using equation (2.10) [61].

$$\frac{\bar{\alpha}}{p} = A\ \mathrm{e}^{\left(-\frac{B}{E_0/p}\right)} \tag{2.10}$$

where A and B are ionisation constants specific to the gas, determined experimentally and available in the literature [62].

2.3.2 Townsend Mechanism and Paschen's Curve

According to Townsend's postulate, the primary electron avalanche, as described in Section 2.3.1, is insufficient to cause gas breakdown; additional secondary avalanches are required. To achieve this, the electron generation described in equation (2.9) must be augmented by other mechanisms.

To analyse how these processes occur, Townsend investigated the behaviour of the current I across a uniform electric field E_0 in a small gas gap, applying a voltage V to the electrodes. The evolution of I as a function of V, depicted in Figure 2.15 (a), shows that below V_1, the current increases proportionally with the voltage until saturation in I_0 (the saturation current). This increase results from the movement of existing charged particles generated by external natural radiation rather than the applied electric field. Beyond this region, the current remains stable until V_2, even with an increase in voltage, due to the constant rate of ion and electron production [62].

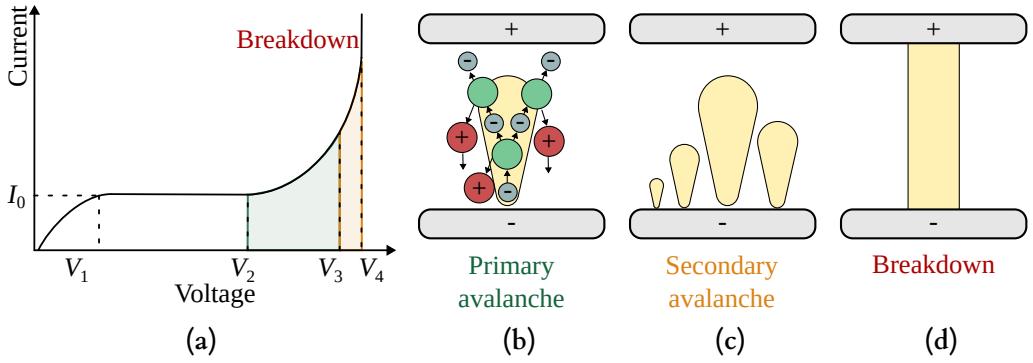

Figure 2.15: *Schematic representation of Townsend's mechanism based on [62, 65] (a) average current growth to breakdown as a function of the applied voltage, (b) primary avalanche, (c) secondary avalanche, and (d) breakdown.*

At V_2, the electric field becomes strong enough to initiate the primary electron avalanche (as detailed in Section 2.3.1) by a primary free electron emitted from the cathode (Figure 2.15 (b)). When the voltage reaches V_3, the current rises abruptly due to the secondary ionisation process (Figure 2.15 (c)).

The secondary ionisation process occurs when secondary electrons initiate new avalanches. Following the formation of primary avalanche, the positive ions created move towards the cathode. If the energy acquired by the ions during this motion (derived from E_0) surpasses the work function of the cathode, which is the energy required to release an electron from the surface of a material, new electrons are emitted from the cathode surface. The likelihood of releasing a free electron at the cathode upon impact by a positive ion is statistically represented by Townsend's secondary ionisation coefficient γ [61, 64]. Similarly to the primary avalanche, these secondary electrons trigger subsequent secondary avalanches.

Considering the initial electron count n_0 and the number of the secondary electrons released from the cathode due to positive ion bombardment n_+, the number of effective electrons n expressed using equation (2.9) can be rewritten as equation (2.11). The total number of secondary electrons n_+ is given in equation (2.12).

$$n = (n_0 + n_+)\, \mathrm{e}^{\bar{\alpha}\, x} \tag{2.11}$$

$$n_+ = \gamma \ (n - (n_0 + n_+)) \tag{2.12}$$

Based on the avalanche process illustrated in Figure 2.13 and by combining equations (2.11) and (2.12), the total number of electrons reaching the anode leads to equation (2.13).

$$n = \frac{n_0 \ \mathrm{e}^{\bar{\alpha} \ d}}{1 - \gamma \ (\mathrm{e}^{\bar{\alpha} \ d} - 1)} \tag{2.13}$$

The last step of Townsend's mechanism is held at V_4, when the breakdown condition is satisfied (Figure 2.15 (d)) [62]. This occurs when the current across the gap approaches infinity ($I \to \infty$). Since current represents the rate of charge flow, the current across the gap in the steady state is proportional to the number of electrons in a given distance of the gap. Therefore, the steady-state current measured at the anode is expressed in equation (2.14), based on equation (2.13).

$$I(x) = \frac{I_0 \ \mathrm{e}^{\bar{\alpha} \ d}}{1 - \gamma \ (\mathrm{e}^{\bar{\alpha} \ d} - 1)} \tag{2.14}$$

Therefore, the breakdown condition ($I \to \infty$) is achieved when Townsend's criterion is satisfied (equation (2.15)). This condition indicates that the number of positive ions resulting from the initial avalanche is sufficient to release the secondary electrons necessary to trigger subsequent secondary avalanches. In other words, each primary avalanche must produce at least one additional secondary avalanche, rendering the process self-sustaining.

$$\gamma \ (\mathrm{e}^{\bar{\alpha} \ d} - 1) = 1 \tag{2.15}$$

Equation (2.15) can be solved considering the relationship between $\bar{\alpha}$ and p described in equation (2.10) resulting in equation (2.16). Developing equation (2.16) and considering that the electric field is the ratio of the applied voltage upon the gap distance ($E = V/d$) results in equation (2.17), which expresses the voltage necessary to fulfil Townsend's criterion, in other words, the breakdown voltage of the gas. This equation is known as Paschen's Law [61].

$$\gamma \ (\mathrm{e}^{A \ p \ d \ \mathrm{e}^{\left(-\frac{B}{E_0/p}\right)}} - 1) = 1 \tag{2.16}$$

$$V_\mathrm{B} = B \frac{P \ d}{\ln\left(\frac{A \ P \ d}{\ln\left(1+\frac{1}{\gamma}\right)}\right)} \tag{2.17}$$

where, as forehead mentioned, A and B are ionisation constants specific to the gas (for air: $A = 12$ Torr^{-1}cm^{-1} and $B = 365$ V Torr^{-1}cm^{-1} [30]), P is the pressure, d is the gap distance and γ is the Townsend's secondary ionisation coefficient.

Figure 2.16 illustrates Paschen's curves for various gases. At the minimum point $(pd)_{V_{\text{Bmin}}}$, the number of collisions between the electrons and the neutral particles is optimal for breakdown. At low pressure, the gas density decreases, which increases the free path between collisions. This allows electrons sufficient time to gain the energy required to ionise neutral particles, thereby optimising the ionisation process. Below this minimum value ($(pd) < (pd)_{V_{\text{Bmin}}}$), the reduced pressure lowers the number of available molecules, decreasing the likelihood of collisions per unit length. Furthermore, the gap distance between electrodes becomes comparable to the average free path, leaving insufficient space to sustain an avalanche. These combined effects necessitate a higher voltage for breakdown. Conversely, for $(pd) > (pd)_{V_{\text{Bmin}}}$, an increase in pressure results in higher gas density, which shortens the free path. This reduced free path becomes too short, limiting the velocity of electrons from gaining sufficient energy to ionise neutral particles effectively [30, 32].

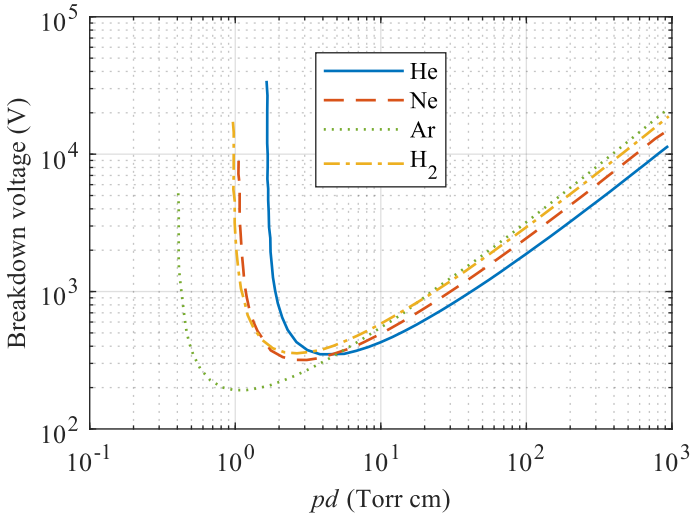

Figure 2.16: *Paschen's curves for various gases based on [30].*

Overall, the Townsend discharge mechanism is influenced by the material of the cathode and the nature of the gas. The discharge occurs after a time delay, as the positive ions must reach the cathode to promote new avalanches. This theory applies to short gap distances and uniform electric fields between electrodes, and it assumes that the generated charged particles do not alter the electric field. Furthermore, it is well established that atmospheric conditions, including temperature, pressure, and humidity, impact the breakdown voltage of the gas. Consequently, Paschen's equation, as defined in equation (2.17), does not yield accurate predictions under varying atmospheric conditions, as it was originally formulated for standard atmospheric conditions.

To account for these environmental influences, two primary corrections have been

introduced to Paschen's equation (2.17), specifically addressing temperature and pressure variations. The first, known as the Peek correction, adjusts gas density based on the ideal gas law under constant volume conditions. This correction modifies the gas density from reference conditions to new pressure and temperature values, as expressed in equation (2.18) (where pressure is in Pa and temperature in K). As a result, Paschen's equation (equation (2.17)) is adjusted following equation (2.19) [66, 67].

$$\rho = \frac{P_{\text{new}}}{P_{\text{ref}}} \frac{T_{\text{ref}}}{T_{\text{new}}} \tag{2.18}$$

$$V_{\text{B}}(P_{\text{new}}, T_{\text{new}}) = \rho \, V_{\text{B}}(P_{\text{ref}}, T_{\text{ref}}) \tag{2.19}$$

The second approach, known as the Dunbar correction, is based on Gay-Lussac's Law. This method derives an equivalent pressure P_{eq} by treating the surrounding gas as an ideal gas, calculated using equation (2.20) (where pressure is in Pa and temperature in K). Paschen's equation (2.17) is then solved using this adjusted pressure value [66, 67].

$$P_{\text{eq}} = P_{\text{ref}} \frac{T_{\text{ref}}}{T_{\text{new}}} \tag{2.20}$$

Studies as [66, 67] indicate that the Dunbar correction provides a better fit to experimental data compared to the Peek correction when temperature varies at atmospheric pressure. However, neither approach remains fully reliable when temperature and pressure variations occur simultaneously.

2.3.3 Streamer Mechanism and Schumann's Criteria

When the separation between electrodes exceeds a few centimetres (2 cm according to [68]), the timescale of the breakdown process becomes too short for positive ions to reach the cathode. Furthermore, the breakdown voltage becomes independent of the material and finish of the cathode surface. This behaviour is attributed to the distortion of the initial electric field E_0 by the dipole formed in the primary avalanche (Figure 2.14). As previously noted (Section 2.3.2), Townsend mechanism assumes that the electric field generated by charged particles is negligible compared to the applied external field, rendering it insufficient to explain breakdown phenomena in longer gaps [61, 62, 64].

The starting point for the Streamer mechanism is a primary electron avalanche, which produces electrons and positive ions. As described in Section 2.3.1, the disparity in the masses of the charged particles causes charge separation forming a dipole, as shown in Figure 2.14 [61, 62, 64]. If the charge density at the head of the avalanche becomes sufficiently large, the charge separation generates a self-induced electric field comparable in magnitude to the applied field. This modifies the original E_0 as shown in Figure 2.17.

The field is intensified at both the head and tail of the avalanche, due to the increasing field between the electrons and the anode, and between positive ions and the cathode, respectively. However, an internal field, generated by the dipole, reduces E_0 in the central region [61, 62, 64].

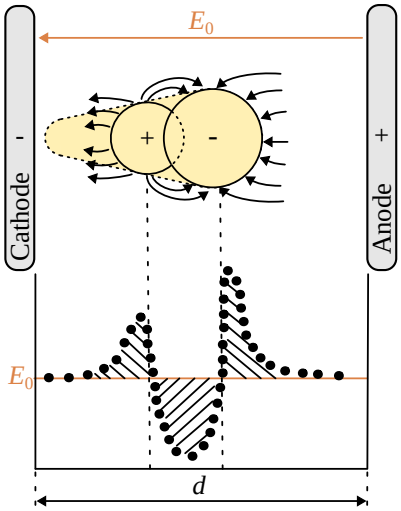

Figure 2.17: *Schematic representation of the field distortion in a gap caused by the dipole of an electron avalanche based on [64].*

The resultant weaker field E_r (Figure 2.18) encourages the recombination of electrons and positive ions in the front of the avalanche, leading to intense photon emission. These photons, in turn, generate secondary electrons via photoionisation. The newly formed electrons develop into secondary avalanches under the influence of the electric field [64].

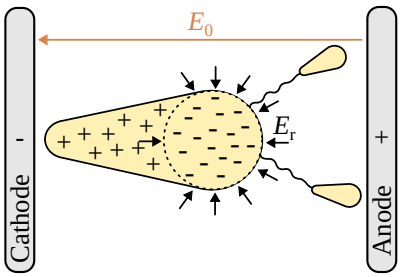

Figure 2.18: *Schematic representation of the secondary avalanche formation by photoelectrons based on [64].*

Since photons travel at the speed of light, when E_r becomes of the same magnitude as E_0 (Meek criterion), breakdown occurs rapidly. At this point, primary and secondary avalanches form a plasma channel that bridges the electrodes. This suggests that a minimum number of electrons is required to transition the primary avalanche into the Streamer mechanism. Given that the number of electrons produced in an avalanche is described by equation (2.9), the critical number of electrons at the head of an avalanche N_{cr} is given by equation (2.21) [61].

$$N_{\text{cr}} = \text{e}^{\bar{\alpha}x} \tag{2.21}$$

While in uniform fields the effective ionisation coefficient $\bar{\alpha}$ is typically assumed constant over the total gap length, it cannot be considered so in non-uniform fields. Consequently, equation (2.21) is revised as Schumann's criterion (equation (2.22)), which is further simplified in equation (2.23) [64].

$$N_{\text{cr}} = \text{e}^{\int_0^{x<d} \bar{\alpha}\, dx} \tag{2.22}$$

$$lnN_{\text{cr}} = \int_0^{x<d} \bar{\alpha}\, dx = K_{\text{Sch}} \tag{2.23}$$

where K_{Sch}, named as Schumann's constant, is a dimensionless constant often approximated as $K_{\text{Sch}} = 18 - 20 \approx \ln\left(10^8\right)$ for air. This scenario assumes an avalanche initiated by a single primary electron $n_0 = 1$ at a distance $x = 0$ from the cathode, that is to say, an avalanche starting at the cathode.

In summary, the primary avalanche transitions into the Streamer mechanism when the critical number of electrons generates a resultant electric field E_{r} of the same magnitude of E_0. This leads to new secondary avalanches driven by electrons from photoionisation, culminating in a faster breakdown process than that described by the Townsend mechanism. The Streamer theory applies to longer gap distances and considers non-uniform electric fields between electrodes.

2.3.4 Breakdown Under Impulse Voltages

The gas breakdown phenomena described in the previous sections (Sections 2.3.1-2.3.3) occur when the applied external voltage increases gradually, as in the case of 50-60 Hz AC. However, if the voltage is applied as impulses (i.e. unipolar rectangular impulse voltage), a higher and more variable V_{B} is required for the gas to breakdown under the same electrode configuration. This behaviour is primarily influenced by two factors [61, 64]:

- **Unavailability of a free electron:** When the minimum voltage for breakdown inception V_{inc} is reached, a primary free electron may not be present to trigger the avalanche. This is governed by the statistical time lag t_{s}, which represents the time between the application of the inception voltage and the availability of a primary electron. The value of t_{s} depends on the gap size, the mechanism producing primary elections (e.g. ultraviolet light irradiation), and the level of overshoot (the difference between the applied external voltage and V_{inc}). A higher overshoot significantly reduces t_{s}.

- **Development of the breakdown mechanism:** A formative time lag t_f is needed to complete the breakdown process once the primary electron avalanche begins. The duration of t_f depends on the specific breakdown mechanism. As mentioned earlier, the time required to form secondary avalanches leading to breakdown is longer for breakdowns governed by the Townsend mechanism than the Streamer mechanism. This is because the Townsend mechanism relies on secondary electrons generated at the cathode, whereas the Streamer mechanism involves photoionisation within the gas, which requires shorter time intervals. Consequently, t_f is shorter for the Streamer mechanism. Similar to t_s, the overshoot also decreases t_f.

When an impulse voltage $V(t)$ with peak value V_p exceeding V_{inc} and rise time of microsecond rage is applied across the electrodes, there is a probability, though not certainty, of gas breakdown (Figure 2.19). For breakdown to occur, the discharge must develop within the interval of overshoot ($V(t) - V_{inc}$). This requires the total time lag t ($t = t_s + t_f$) to be shorter than the available time interval $t_2 - t_1$. If this condition is not satisfied, the breakdown voltage V_B will increase, as higher overshoot extends $t_2 - t_1$ eventually fulfilling the breakdown condition. Similarly, as both t_s and t_f decrease with increasing overshoot, a higher overshoot results in a shorter time to breakdown t_B [64].

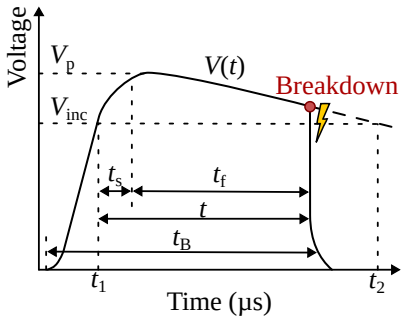

Figure 2.19: *Schematic representation of the breakdown under impulse voltages based on [64].*

Under 'static' conditions (e.g. 50-60 Hz), where the voltage increases gradually, the time available $t_2 - t_1$ is longer than that in impulse voltages (assuming the same V_p and V_{inc}). Since the breakdown condition is met when $t < t_2 - t_1$, there is a higher likelihood of fulfilling it [61].

2.4 Concluding Remarks

This chapter has outlined the theoretical background for inverter-fed machines, with a particular focus on traction systems in EV. The utilisation of WBG inverters to power electric machines significantly increases the likelihood of PD activity due to the overshoot generated on the machine terminals and the uneven voltage distribution along the stator turns.

In the stator winding insulation, PD activity generally occurs in the air surrounding the insulation or within trapped voids. It is triggered when the voltage reaches the PDIV, which is the threshold voltage for PD condition. Over the lifetime of the machine, mechanical, electrical, and environmental stresses can reduce the PDIV. If the PDIV decreases to the level of the operational voltage, PD activity accelerates ageing and hastens failure. Consequently, the PDIV is a critical factor in ensuring the safe design of electric machine insulation systems.

Random-wound and form-wound winding configurations are the most prevalent, with the insulation system comprising interturn, phase-phase, and groundwall insulation. Among the insulation characteristic parameters, the relative permittivity of the material has a significant impact on PD activity, as it directly affects the electric field magnitude in the air. Higher insulation relative permittivity values increase the air electric field magnitude, thereby raising the probability of PD occurrence.

Finally, the breakdown of gases, and therefore PD, is initiated by a primary avalanche resulting from a free primary electron. This avalanche gives rise to secondary avalanches through Townsend or Streamer mechanisms, depending on the gap distance and uniformity of the electric field. When impulse voltages are applied, the delay in forming the free primary electron (statistical time lag) and the development of the breakdown from secondary avalanches (formative time lag) can increase the breakdown voltage compared to the levels required for 50-60 Hz AC voltages, where gradual voltage increase minimises the impact of these time lags on the breakdown voltage.

Chapter 3

Experimental Procedures and Methods

This section outlines the experimental procedures adopted in this research, ensuring clarity and reproducibility. It begins by presenting the samples used, specifying their application in subsequent sections. Next, the measurement techniques are detailed, including relative permittivity assessment, PD measurements (PDIV and PD pattern analysis), and impedance spectrum evaluation. Finally, the setups for accelerated ageing tests, both thermal and electrical, are described.

3.1 Samples

This study incorporates different sample types, including Twisted Pairs (TPs) (two twisted round conductors), Parallel Conductors (PCs) (two rectangular conductors placed in parallel), and complete machine stators. This section provides a detailed description of all samples used, categorising them according to their application in Chapters 4, 5, and 6.

3.1.1 Samples for Chapter 4

In accordance with IEC 60034-18-41 [9], TPs are suitable for evaluating interturn insulation in random-wound windings, while PCs are used for form-wound windings. Hence, experimental results from both sample types were utilised in the work presented in Chapter 4. Grade 2 enamel circular wires complying with IEC 60317-0-1 [52] were used to prepare TPs as defined in IEC 60172 [69]. Similarly, PCs were prepared using rectangular conductors in accordance with IEC 60172 [69]. A partner company supplied all samples.

Table 3.1 sets out the specifications of the tested samples for PCs, and TPs. The copper dimensions and the insulation thickness (t_{ins}) of PC samples were provided by the manufacturer, while the average t_{ins} for Grade 2 wires defined in [52] was employed for TPs. Additionally, the table indicates the sections of the document where the sample results have been applied. The relative permittivity values used in Section 4.3.2.1 were set according to manufacturer specifications at 20 °C, 100 °C, and 180 °C, measured at 1 kHz (Table 3.2). However, relative permittivity values at temperatures below 100 °C for varying humidity levels were not provided.

To develop the model described in Section 4.3.2.2, it was necessary to measure the relative permittivity at different temperature and humidity conditions. These measurements were conducted following the procedure detailed in Section 3.2 for the samples listed in Table 3.1 (excluding TP3 and TP4), with results summarised in Figure 3.1. Generally, higher absolute humidity correlates with increased relative permittivity. As reported by [70], high humidity levels can raise permittivity due to water absorption, given that water has a significantly higher relative permittivity ($\varepsilon_{\text{r water}} \approx 80$) than most insulation materials. Furthermore, materials containing PAI (Figure 3.1 (a)-(d)) exhibit a stronger humidity-induced permittivity increase compared to PI (Figure 3.1 (e)). This could be attributed to the higher moisture absorption capacity of PAI relative to PI.

Table 3.1: *Sample specifications given by the partner company for results presented in Chapter 4.*

Sample name	Copper dimensions* (mm)	Insulation thickness (µm)	Base coat, %	Over coat, %	Used in Section
PC1	3.450×1.700	70.5	PAI, 100	-	4.1.4, 4.3.2.1, 4.3.2.2
PC2	3.450×1.700	83.5	PAI, 100	-	4.1.4, 4.3.2.1, 4.3.2.2
PC3	3.450×1.700	116.3	PAI, 100	-	4.1.4, 4.3.2.1, 4.3.2.2
PC4	3.215×1.540	63.0	PI, 100	-	4.1.4, 4.3.2.1, 4.3.2.2
PC5	3.215×1.540	91.5	PI, 100	-	4.1.4, 4.3.2.1, 4.3.2.2
PC6	3.215× 1.540	100.0	PI, 100	-	4.1.4, 4.3.2.1, 4.3.2.2
PC7	3.450×1.700	68.6	PAI, 60	PAICR, 40	4.1.4, 4.3.2.1, 4.3.2.2
PC8	3.450×1.700	82.1	PAI, 60	PAICR, 40	4.1.4, 4.3.2.1, 4.3.2.2
PC9	3.450×1.700	106.3	PAI, 60	PAICR, 40	4.1.4, 4.3.2.1, 4.3.2.2
PC10	3.450×1.700	67.0	PAI, 65	PI, 35	4.1.4, 4.3.2.1, 4.3.2.2
PC11	3.450×1.700	84.4	PAI, 65	PI, 35	4.1.4, 4.3.2.1, 4.3.2.2
TP1	0.800	35.0	PE, 72	PAI, 28	4.1.1.2, 4.3.2.1, 4.3.2.2
TP2	0.900	37.0	PI, 100	-	4.1.1.2, 4.3.1, 4.3.2.1, 4.3.2.2
TP3	0.800	35.0	PEI, 72	PAI, 28	4.3.2.1
TP4	0.800	35.0	PEI, 72	PAI, 28	4.3.2.1

* ⌀ for TPs and height × width for PCs

Table 3.2: *Relative permittivity values provided by the partner company at 20 °C, 100 °C, and 180 °C measured at 1 kHz.*

Temperature	PAI	PAI+PAICR	PE+PAI	PEI+PAI	PAI+PI	PI
20 °C	4.424	4.451	4.258	3.956	3.845	3.093
100 °C	4.390	4.401	4.167	3.889	3.773	2.991
180 °C	4.213	4.169	4.375	3.731	3.635	2.897

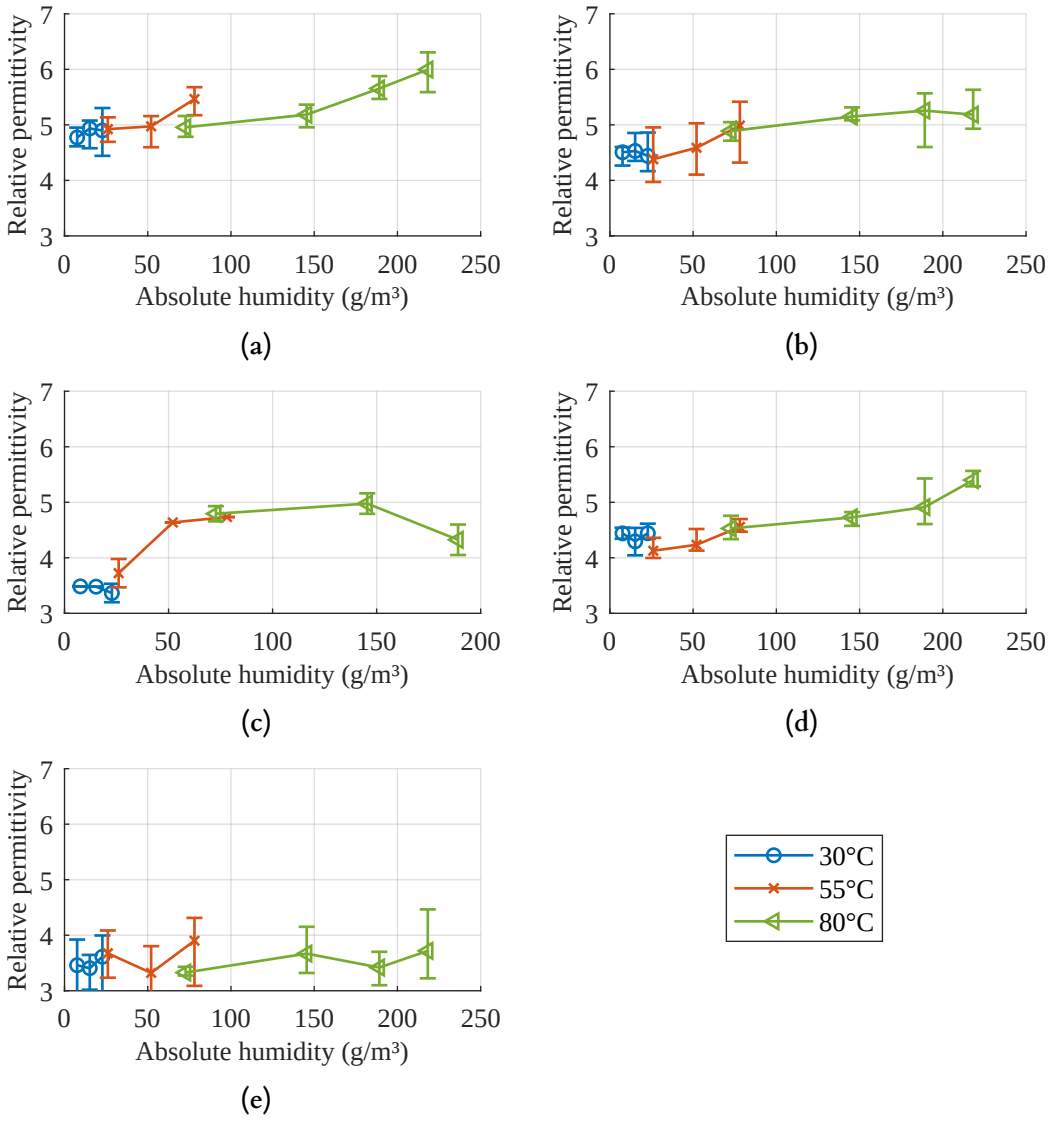

Figure 3.1: *Average relative permittivity of several materials (with error bars indicating maximum and minimum measurements) depending on absolute humidity at 30, 55, and 80 °C and 25, 50, 65 and 75% RH for PC1-11 and TP1-2 (Table 3.1) (a) PAI, (b) PAI+PAICR, (c) PEI+PAI, (d) PAI+PI, and (e) PI.*

3.1.2 Samples for Chapter 5

In Chapter 5, the work developed in collaboration with two industrial companies is presented.

3.1.2.1 Samples for Section 5.1

The collaboration with the first company focused on the comparison of different winding methods, using complete stators for the analysis. The winding conductor was a Grade 2 enamelled circular wire with a diameter of 1.35 mm. Its insulation comprised a PEI basecoat and PAI overcoat, with a thermal class of 200 °C. TRIPLEX F-20.08 insulating paper, 0.3 mm thick, was used as groundwall insulation in the active part of the stator. On the end-winding region, a 2.5 mm thick cap made of 30% fibreglass-reinforced polyamide (PA66-FG30) separated the winding from the stator core.

Two different machines were analysed, differing only in the manufacturing process of the winding. The machine type, referred to as semi-automatic, was produced using the standard manufacturing technique of the company. In this process, 4 coils are assembled by an automatic machine outside the stator and then inserted inside the stator slots. Once all coils are in place, the phases are welded.

In contrast, the machine referred to as needle was manufactured using needle winding (Section 2.2). In this method, the winding is carried out directly within the stator. A needle places the wire in the appropriate location, forming each phase continuously from start to finish without separations between the coils of the same phase. This process stretches the wire, which may affect the insulation thickness depending on the applied tension. In the current samples, data on the degree of stretching is not available. The wires are routed between coils of the same phase. Each phase has its routing channel, avoiding contact and ensuring sufficient distance between phases. These samples were specifically used in Section 5.1.

3.1.2.2 Samples for Section 5.2

The collaboration with the second company consisted of assessing the design of an aeronautic application machine. The machine had three phases connected in delta. Even though a complete description of the machine cannot be given in this document, the key parameters to understand the work developed are the following:

- **Winding manufacturing:** The machine was constructed with a random-wound winding using needle winding manufacturing. The different coils of the same phase were routed separately, ensuring a distance as large as possible between the different phases.
- **Winding wire:** A 0.3 mm diameter circular PI enamelled wire of Grade 2 was used for the winding.

- **Groundwall insulation:** The groundwall insulation consisted of two caps, each one mounted from one side of the stator, with an overlapping region on the centre of the stator length. The caps were 0.70, 0.85 or 1.00 mm thick and were manufactured by 3D printing using TR300 (Phrozen) or Nylon 12.
- **Potting:** The machines were potted with XE 663 DK50/11 from Demak. The potting process was done by preheating the sample at 60 °C, applying the potting in a partial vacuum (around 10 mbar) at 55 °C, and curing for 2 h at 60 °C at atmospheric pressure conditions. This process was done in external facilities.
- **Thermistors:** Having two thermistors between the winding coils was required. These were the model HEL-705 from Honeywell.

Due to some issues with the manufacturing process of the groundwall insulation caps, another type of sample, manufactured by the company and presented on the left side of Figure 3.2, was used to evaluate the different cap materials and thicknesses in Section 5.2.3.3. These samples are named as cap sample in the document. They were 0.70, 0.85, or 1.00 mm thick, manufactured by 3D printing using TR300 (Phrozen) or Nylon 12, and winded with the same wire used in the machine. The samples were inserted into an electrode connected to GND, while the wire was connected to the High Voltage (HV) terminal. Figure 3.2 shows the sample before (left) and after (right) placement in the GND electrode.

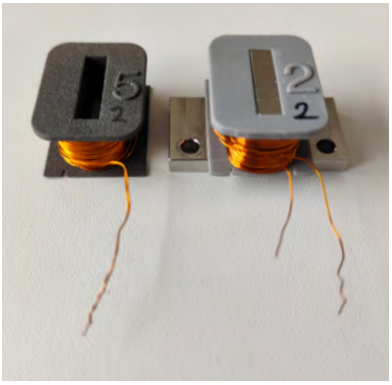

Figure 3.2: *Cap samples without (left) and with GND electrode (right) prepared to evaluate the cap insulation thickness and material during the assessment of the final definition of the groundwall insulation.*

3.1.3 Samples for Chapter 6

A complete stator winding from a 3-phase concentrated winding machine, designed specifically for lift-door actuation and supplied by a partner company, was employed to thermally age the entire insulation system (Figure 3.3). The winding conductor was a Grade 2 enamelled circular wire with a diameter of 0.335 mm. Its insulation comprised a PEI basecoat and PAI overcoat, with a thermal class of 200 °C. As the needle manufacturing

was used, in this specific coil configuration, the 3 phases were next to each other in the routing, as depicted in Figure 3.3 (a) (top view). Thus, the enamel simultaneously acted as phase-phase and interturn insulation. Besides, the groundwall insulation separating the winding from the stator core consisted of PA66-FG30 0.7 mm cap, with a softening temperature of 230 °C. It was composed of two pieces, each one mounted from one side of the stator. The pieces did not touch each other in the centre of the teeth, generating an air gap of 0.5 mm in the axial middle point of the core (Figure 3.3 (b)). These samples were specifically used in Sections 6.1.1 and 6.2.2.

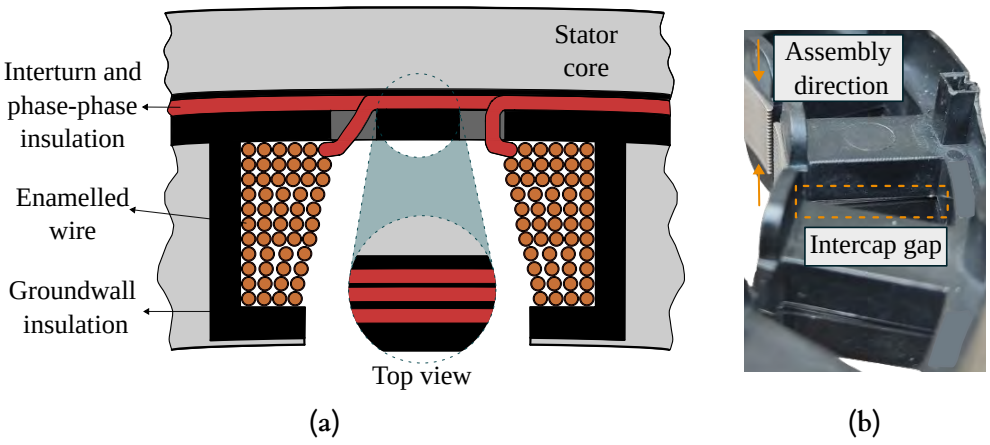

Figure 3.3: *Sample used for thermal ageing experiments (a) simplified schematic representation of the cross-section of the stator insulation system, and (b) detail of the groundwall insulation caps.*

For electrical ageing tests, TPs were prepared according to IEC 60172 [69]. Grade 1 enamelled circular wires complying with IEC 60317-0-1 [52] were employed, with 0.5 mm nominal copper diameter. Two enamelled materials were tested, a non-CR PEI (named as SW) with an average insulation thickness of 33 µm, and a CR PEI (named as CRW) with an average insulation thickness of 34.5 µm. The characteristics of the samples were given by the manufacturer. The peak-peak PDIV of the SW was 1332 V and of the CRW 1287 V (average of 74 and 64 samples respectively, measured as described later in Section 3.3.1). These samples were specifically used in Section 6.1.2.

3.2 Relative Permittivity Measurements

The relative permittivity was determined by measuring the capacitance of the conductors following the methodology outlined in [71]. For this purpose, one conductor of each TP and PC sample listed in Table 3.1 (excluding TP3 and TP4) was coated along a 10 cm section with a conductive layer (841AR-55ML from MG Chemicals), while the insulation at the conductor ends was removed.

Once prepared, the samples were placed inside a climate chamber (CCK series from Dycometal) on an electrically insulating structure. They were connected to the capacitance measurement equipment, a Bode 100 from Omicron [72], using high-temperature

Silicable NVS cables (rated up to 350 °C) from Omerin (Figure 3.4). The Bode 100 was calibrated to account for the influence of the extension cables. The bare copper end of each sample was connected to one terminal of the equipment, while the other terminal was attached to the conductive coating for measurement. Capacitance values were recorded over a frequency range from 20 Hz to 10 MHz, with values below 100 Hz discarded due to excessive noise. The capacitance at 1 kHz was considered for relative permittivity calculation, as the measured capacitance remained stable across the frequency range, making it equivalent to the value at 50 Hz.

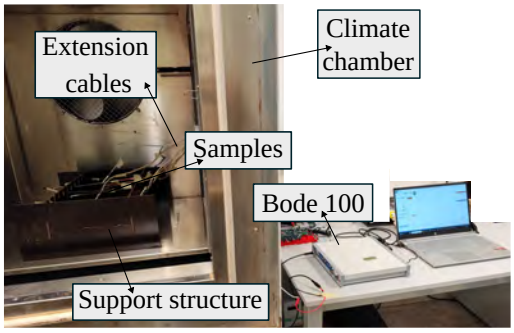

Figure 3.4: *Experimental setup for capacitance measurements for relative permittivity calculation.*

Measurements were conducted at different temperatures (30, 55, and 80 °C) and Relative Humidity (RH) levels (25, 50, 65, and 75%), with data collected 30 minutes after stabilizing the environmental conditions. As noted in [70], relative permittivity responds quickly to changes in RH and stabilizes once the target humidity is reached.

The relative permittivity of round wire samples was calculated using equation (3.1), as described in [71]. For rectangular wire samples, equation (3.1) was not applicable. Instead, the rectangular conductors were modelled as four parallel-plate capacitances in parallel (one capacitance for each face of the rectangular conductor), and the relative permittivity was determined using equation (3.2).

$$\varepsilon_{\mathrm{r\ ins}} = \frac{C}{2\,\pi\,\varepsilon_0\,l} \ln\left(\frac{r_{\mathrm{inner}}}{r_{\mathrm{outer}}}\right) \tag{3.1}$$

$$\varepsilon_{\mathrm{r\ ins}} = \frac{C\,t_{\mathrm{ins}}}{2\,\varepsilon_0\,l\,(w+h)} \tag{3.2}$$

where $\varepsilon_0 = 8.854 \cdot 10^{-12}\ (\frac{\mathrm{F}}{\mathrm{m}})$ is the permittivity of vacuum, l is the coated section length (10 cm), r_{inner} and r_{outer} are the inner (copper) and outer (copper and insulation) radii of the wire conductor, t_{ins} is the insulation thickness, and w and h are the width and height of the copper for rectangular conductors.

To validate equation (3.2), Finite Element Method (FEM) simulations were conducted to simulate the capacitance of the rectangular conductors using the relative permittivity

obtained from the measured capacitance. The difference between simulated and measured capacitance was below 3%, confirming the accuracy of equation (3.2).

After determining the relative permittivity of each sample, the value assigned to each material under specific environmental conditions was taken as the average of all samples of that material at the same condition.

3.3 Partial Discharge Measurements

3.3.1 Partial Discharge Inception Voltage Measurements

PDIV measurements were used in Sections 4.1.1.2, 4.1.4, 4.3, 5.1, 5.2, 6.1.1, and 6.2.2. The setup consisted of the commercial PDIV measurement equipment LT400W from EDC (Electrical Dynamic Company, Milan, Italy)(IEC 60270 [49]) and an industrial oven with temperature control (Memmert UF110plus). The samples were placed on a structure manufactured with electrical insulating material. Silicable NVS cables from Omerin (maximum temperature of 350 °C) were used as extensors to connect the LT400W connectors and the samples (Figure 3.5).

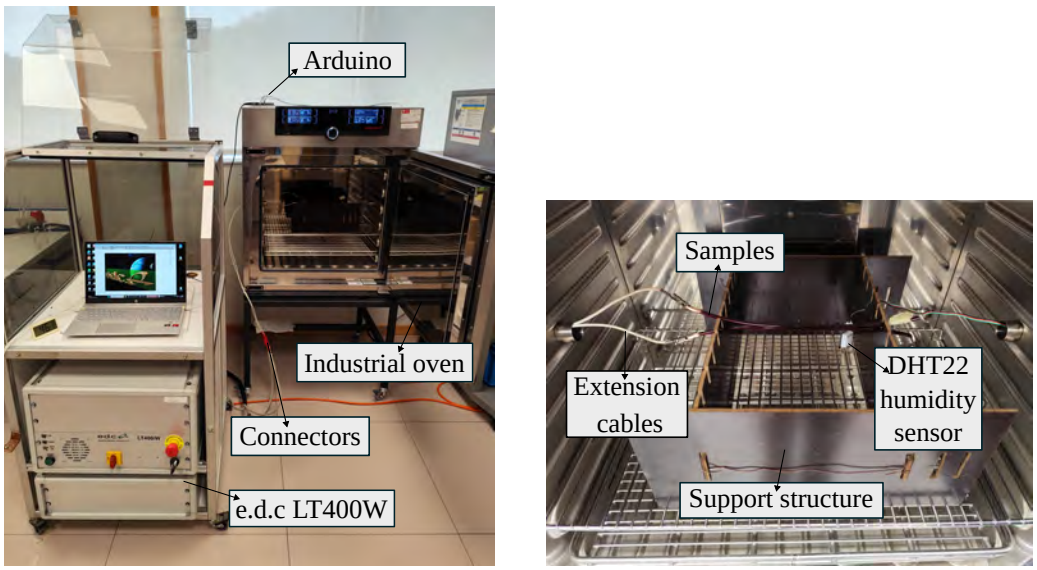

Figure 3.5: *Experimental setup for PDIV measurements (a) complete system, and (b) interior of the oven.*

To obtain the PDIV value, a 50 Hz sinusoidal waveform was used, and the voltage was increased from 0 V, in 10 V/s increments until PD was detected. The minimum PD charge was defined at 0.05 nC to avoid background noise, as explained in [21]. Hence, the PDIV was defined as the first voltage level where a PD with a charge equal or greater than 0.05 nC was detected. It must be noted that, in the majority of the measurements, this value was achieved already in the first PD detected. Then, the test voltage was increased

by between 10-50 V to ensure the PD activity remained constant and later decreased to 0 V. Each sample was measured three consecutive times with an interval of 60 s between each measurement, and the average was calculated. In preliminary measurements, it was seen that this time interval was enough to obtain stable values, avoiding memory effect.

According to the connections, for the measurements of TPs or PCs, one side of the sample was connected to the HV connector and the other to the grounded one (GND) from LT400W, and the average of three samples for each sample type and condition was taken [20]. Similarly, for the cap samples presented in Figure 3.2 (the one with GND terminal), the wire was connected to the HV, and the electrode to GND.

For complete stator measurements, different connections were used for phase-phase and groundwall insulation, as described in IEC 60034-18-41 [9]. For phase-phase measurements (Figure 3.6 (a)), one phase was connected to the HV terminal and the other two to GND, performing all possible configurations. For groundwall insulation measurements, three phases were connected to the HV connector, whereas the stator core and the thermistors (if applicable) were set to GND (Figure 3.6 (b)).

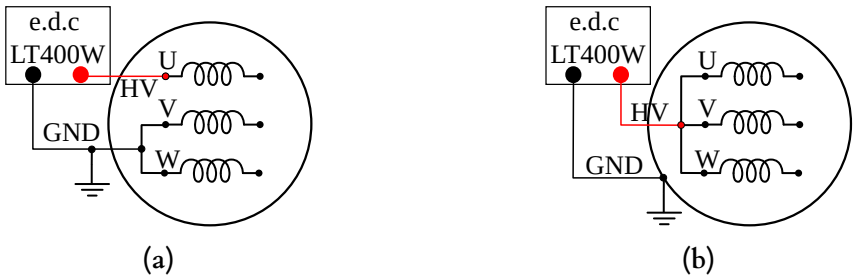

Figure 3.6: *Schematic representation of the connections for PDIV measurements in stator insulation systems (a) phase-phase, and (b) groundwall.*

Ambient temperature PDIV measurements were done outside the oven, directly connecting the samples to the equipment terminals, without using extension cables. It has been verified that the extension cables do not imply differences in the PDIV measurements, correlating negligible differences between ambient temperature measurements with and without extensions.

For high-temperature measurements (Sections 4.1.1.2, 4.1.4, and 4.3.2.1), before proceeding with the measurement, the samples were conditioned for at least 10 min after reaching the desired temperature. In the case of ambient temperature measurements presented in Sections 4.1.1.2, 4.1.4, and 4.3.2.1, the RH range was between 50-66%. At temperatures above 100 °C, the RH can be considered negligible. As noted in [73], when the RH inside of an oven is not actively controlled, it remains below 1% at temperatures above 100 °C.

To assess PDIV at different temperatures (30, 55, and 80 °C) and RH levels (25, 50, 65 and 75%) (Sections 4.3.2.2), RH was adjusted using moisture absorbers for low humidity conditions at 30 °C (RH = 25%), and by adding water inside the oven to increase the humidity. The RH was monitored using a DHT22 humidity and temperature sensor

connected to an Arduino. Measurements were conducted 30 min after stabilizing the desired conditions, following the recommendations of [70]. This way, a RH level ±5% was obtained.

3.3.2 Partial Discharge Pattern Measurements

PD patterns were obtained through HiPot tests, which consist of applying a 50 Hz AC voltage for a specified duration. The applied voltage must exceed the PDIV to initiate and observe PDs. The main objective of analysing these patterns is to identify the nature of the discharges, such as internal voids, surface discharges, or other phenomena.

The same equipment and connections used for the PDIV measurements were employed for the HiPot tests (see Section 3.3.1). The equipment provides only the data corresponding to the most critical 200 ms of each test. Therefore, to gather a representative dataset, 12 consecutive test cycles of 5 seconds each were conducted. Test of 5 s were selected to ensure enough time for increasing the voltage and activate PDs. The data from all cycles was used to generate the PD pattern at each specific voltage level. These measurements were specifically used in Section 5.1.3.

3.4 Impedance Spectrum Measurements

Impedance measurements were conducted using the arrangement depicted in Figure 3.7. The Common-Mode (CM) impedance was measured by applying a sinusoidal voltage with frequencies ranging from 1000 Hz to 50 MHz to the tested specimen with the commercial impedance measurement equipment Bode 100 from Omicron [72]. Applying a known voltage and measuring the current, Bode 100 provides the value of the impedance (Z), phase angle, and parallel capacitance (C_p, the equivalent phase-to-ground capacitance). All measurements were taken under room conditions between 13 and 19 °C. These measurements were used in Section 6.2.2.

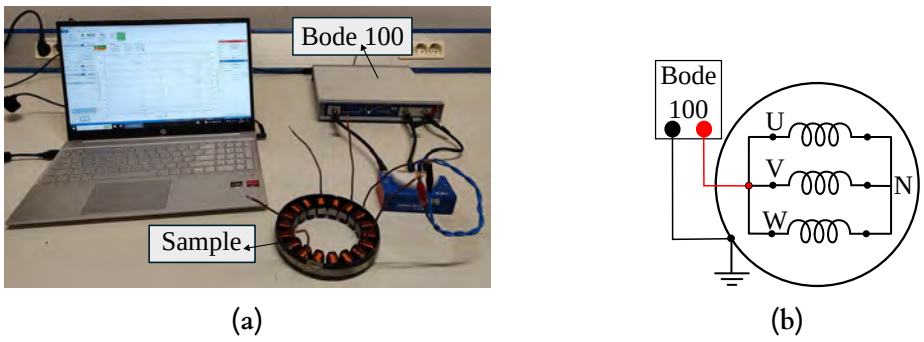

Figure 3.7: *(a) Experimental setup for CM impedance measurements, and (b) schematic representation of the CM impedance measurement connection.*

3.5 Accelerated Ageing

Accelerated ageing experiments were performed using two distinct stress factors: thermal and electrical. These tests were employed to evaluate the effects of ageing on the insulation system, as detailed subsequently in Section 6.

3.5.1 Accelerated Thermal Ageing

Complete stators described in Section 3.1.3 were employed to perform thermal ageing of the entire insulation system. Two ageing approaches were utilised: exposure to a constant temperature (isothermal ageing) and repeated thermal cycles (thermomechanical ageing).

Test parameters were defined considering the temperature limitations of the insulation materials used in the electrical machine. The softening temperature of the groundwall insulation was 230 °C, whereas the winding wire insulation had a thermal class of 200 °C. Consequently, maximum test temperatures of 230 °C and 260 °C were selected, representing the maximum operating limit of the groundwall insulation material and an over-stress condition 30 °C above it. Additionally, for thermomechanical ageing, the fastest possible thermal cycling rate within the power source limitations was chosen, as it represents the most severe thermal stress according to [74]. Preliminary testing set this cycling rate at 4°C/s. Table 3.3 summarises the test parameters and the number of samples tested for each experiment.

Table 3.3: *Definition of test parameters for isothermal and thermomechanical ageing.*

Ageing type	T_{min} (°C)	T_{max} (°C)	T_{rms} (°C)	ΔT (°C/s)	Number of samples
Isothermal	-	230	-	0	1
	-	260	-	0	2
Thermomechanical	200	230	215.2	4	1
	230	260	230.7	4	2

Figure 3.8 depicts the experimental setup. The specimens were heated by the Joule effect using a programmable DC power supply, controlled by a LabVIEW®-based program through a USB connection. The suitable DC current value was applied to achieve the required ageing temperature. Real-time monitoring of the applied current and voltage allowed the winding temperature to be estimated continuously based on changes in electrical resistance (note that this temperature is an average of the winding). The temperature of the 3 phases was also recorded with K type thermocouples and a PicoLog data logger device. Ageing campaigns were performed in an environmentally controlled room, i.e., the ambient temperature was maintained constant. In thermomechanical

ageing tests, a constant forced airflow was used exclusively during the cooling periods, to accelerate it.

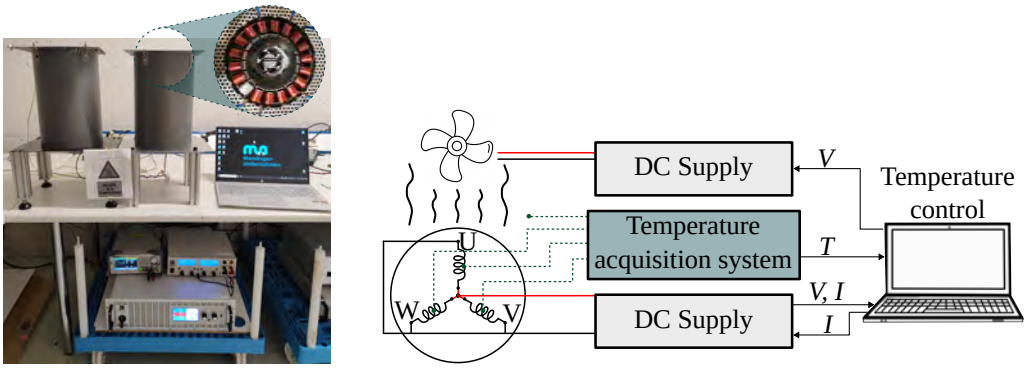

Figure 3.8: *Thermal ageing experimental setup (a) real, and (b) schematic representation. (T: temperature, V: voltage, I: current).*

A control programme was developed in LabVIEW® to regulate the temperature of the samples accurately. The system employs a Proportional-Integral (PI) controller to maintain the set point defined for each ageing process. At the start of the test, the initial sample temperature (T_0) was recorded using the thermocouples, and the initial resistance (R_0) was determined by dividing the first applied voltage by the measured current. Subsequently, the programme continuously monitored the voltage and current values to compute the instantaneous resistance (R) and estimate the corresponding temperature (T) using equation (3.3), where α_{T} represents the temperature coefficient ($0.00382\ ^{\circ}\mathrm{C}^{-1}$ for copper [75]). Based on these calculations, the controller adjusted the applied current to ensure precise temperature tracking. Throughout the test, the ambient temperature was recorded.

$$T = T_0 + \frac{\frac{R}{R_0} - 1}{\alpha_{\mathrm{T}}} \tag{3.3}$$

Every 24 hours, the samples were disconnected from the DC supply and restored to room temperature using uncontrolled air-forced cooling. Once the sample reached room temperature, the thermocouples were removed, and impedance and PDIV measurements were conducted according to the procedures outlined in Section 3.4 and 3.3.1 respectively. This procedure was repeated until the samples failed, at the moment when PDIV measurement performed a discharge current higher than 20 mA. For example, if a sample failed during the PDIV measurements after 240 h of ageing, the time to failure was defined as 240 h.

3.5.2 Accelerated Electrical Ageing

TPs described in Section 3.1.3 were used to conduct the electrical ageing tests. Based on the literature review presented in Section 6.1.2, the combined influence of rise time (t_{r}),

pulse conduction time (or pulse width, t_w) and non-conduction time (t_{nc}) was identified as particularly relevant. These variables were defined as depicted in Figure 3.9, being $t_{nc} = \frac{1}{f} - t_w$.

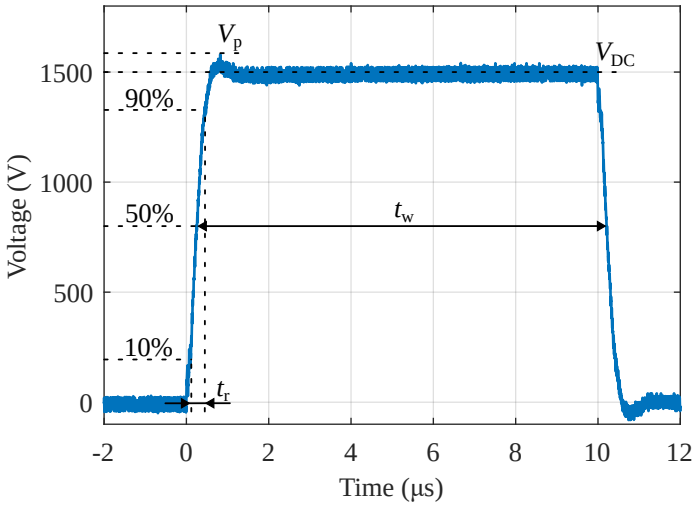

Figure 3.9: *Definition of the rise time (t_r), pulse width (t_w), peak voltage (V_p), and DC voltage (V_{DC}) of electrical ageing tests waveforms.*

In [51] the use of Design of Experiments (DoE) methodology to investigate the individual and combined influence of multiple factors on insulation endurance was recommended, due to its efficiency and scalability. Accordingly, a full factorial design with three factors at two levels was implemented. Table 3.4 summarises the tested levels for each variable. The selected rise time values present typical levels for SiC (low), and conventional Si (high) converters [76]. Conduction and non-conduction times were chosen to include balanced conditions, as well as cases where either conduction or non-conduction time dominated.

Table 3.4: *Definition of the electrical ageing test variables for the three factors and two levels DoE.*

Level	t_r (ns)	t_w (µs)	t_{nc} (µs)
Low	21	2	2
High	458	10	18

To accelerate the tests, a unipolar positive waveform with peak voltage of 1500 V was applied, which exceeded the measured PDIV of the samples under sinusoidal voltage (Section 3.1.3), assumed equivalent to impulse voltage for TPs [9]. Frequency and duty cycle were adjusted to achieve the required conduction and non-conduction times. The corresponding frequency and duty settings for each test point are summarised in Figure 3.10. Endurance was evaluated based on the number of cycles to failure. As later discussed in Section 6.1.2, this metric is expected to be independent of frequency within the range used (above 35 kHz).

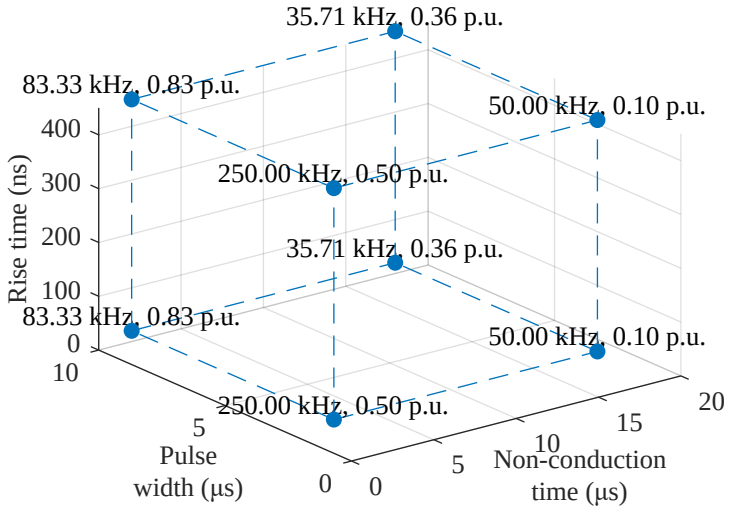

Figure 3.10: *Electrical ageing test conditions, with specific frequency (kHz) and duty (p.u) specified in each testing point.*

The experimental setup, illustrated in Figure 3.11, consisted of two main sections: power and control. In the power section, a BNC PVX-4150 high-voltage pulse generator was used to apply voltage pulses to the samples. This generator receives a square wave signal from a SIGLENT SDG 1032X signal generator, with the voltage amplitude set using a DSC DP15H-05PH DC power supply. Frequency and duty cycle were controlled via the signal generator. The voltage applied to the sample was monitored at the sample terminals using a Sapphire Instruments SI-9010A differential voltage probe and a Tektronix TDS5054B oscilloscope. The rise time could not be directly controlled by the high-voltage pulse generator, instead, an external resistor was required to increase it. Therefore, for low rise time tests, the generator was directly connected to the sample. For the high rise time tests, a 2.3 KΩ resistor was added in series between the generator and the sample.

The control section was implemented using a National Instruments ELVIS III board and a custom LabVIEW® programme to monitor and measure time to failure. Two timers were used, one internal to LabVIEW® and one external, but only the LabVIEW® timer was used for reporting due to its higher precision (up to 0.0001s). The method for detecting breakdown varied depending on the rise time condition.

For low rise time tests, the absence of the series resistor meant that breakdown triggered the overcurrent protection of the generator, automatically disabling the output. The ELVIS III system monitored the generator output voltage in real-time, and when a drop to zero in the average voltage was detected, the LabVIEW® timer was stopped.

In high rise time tests, the series resistor prevented overcurrent protection from activating, so the generator output remained enabled after breakdown. To avoid this, breakdown was detected by the voltage measured at the sample terminals. When the average voltage drop to zero was observed, the timer was stopped and a signal was sent to

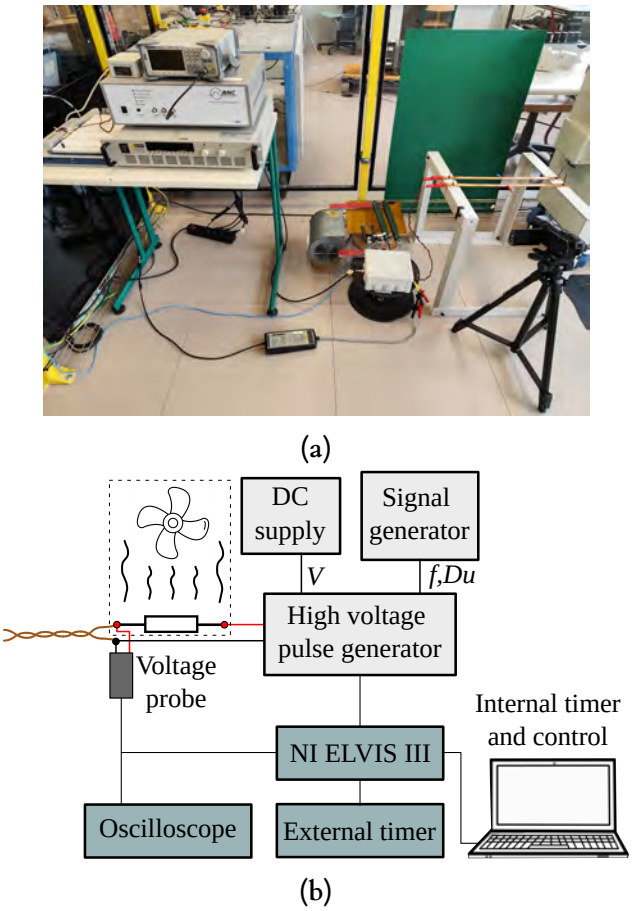

Figure 3.11: *Electrical ageing experimental setup (a) real, and (b) schematic representation. (V: voltage, f: frequency, Du: duty).*

disable the generator output from LabVIEW®.

The test system was capable of generating unipolar positive pulses with a peak-peak voltage of 1500 V, minimum rise time of 21 ns ± 2 ns with up to 13% overshoot (maximum peak-peak voltage of 1700 V) and a maximum rise time of 458 ns ± 29 ns with less than 5% overshoot (Figure 3.12). The system supported frequencies up to 250 MHz and required pulse widths and non-conduction times ±0.01µs.

All experiments were performed under room conditions in a climate-controlled laboratory. Four samples were individually tested per condition, which corresponds to the minimum number required to obtain consistent results, as recommended in [77]. The results were analysed in terms of cycles to failure, using the Weibull distribution, a widely adopted statistical method for endurance testing, whose application is extensively described in [30, 32, 51].

Throughout the tests, due to the lack of equipment to correctly detect and measure PD activity avoiding the noise of the pulse generator, PD activity was visually recorded with a video camera to verify PD activity and confirm the moment of breakdown. Figure 3.13 presents some examples of the recorded PD activity and failure moment.

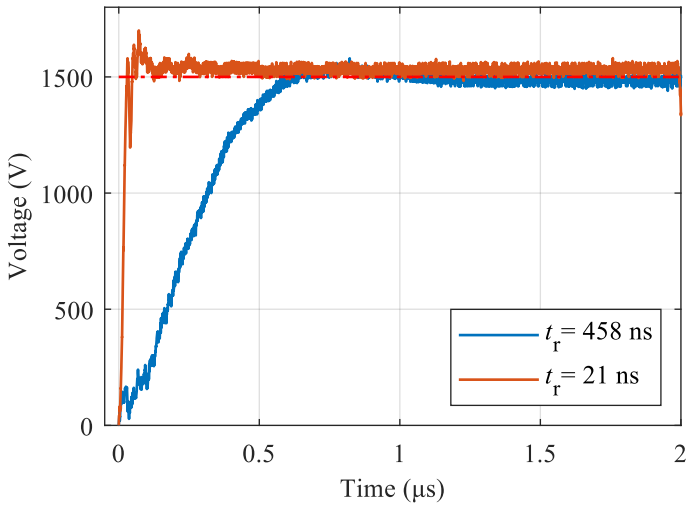

Figure 3.12: *Rising edges of the applied pulse voltages with the maximum overshoot obtained at both analysed rise time levels during the electrical ageing tests.*

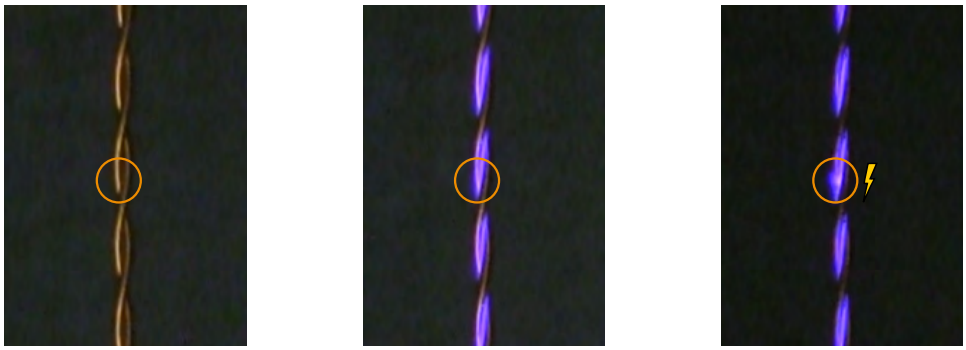

Figure 3.13: *Images recorded by the video camera during the electrical ageing test of one sample at* $t_r = 21$ ns, $t_c = 10$ µs, *and* $t_{nc} = 18$ µs, *where the breakdown point is marked with the circle (a) before starting the test, (b) during the test under PD activity, and (c) at the breakdown instant.*

Chapter 4

Partial Discharge Inception Voltage at Operating Conditions

Given the critical role of PDIV in ensuring insulation system reliability, this section examines how it is influenced by various operating conditions. Here, operating conditions are understood as the circumstances under which the machine operates in service without exhibiting ageing effects.

First, the most significant operation parameters are identified based on a comprehensive literature review and extended by analysis based on own experiments. Then, existing models for PDIV estimation are evaluated, considering their strengths and limitations. Subsequently, contributions to PDIV modelling are presented in detail. Finally, the proposed models are validated through a comparative study with various models reported in the literature. The results obtained with the developed models were as accurate as those from literature, while offering considerably faster computation. This chapter is supported by a published article [21] and a conference proceeding [22] derived from this research.

4.1 Assessment on the Parameters Affecting Partial Discharge Inception Voltage

The theoretical explanations from Section 2.3 clearly showed that the electron generation required to initiate the breakdown condition of gas is highly influenced by several factors. For instance, the pressure strongly influences the length of the free paths required by the electrons to move, gain velocity and energy, and give rise to concatenated electron avalanches and the breakdown. Impulse voltages also showed that could delay the primary electron generation and the formative time to complete the breakdown process.

As PD activity is described by the gas breakdown (e.g. the air within trapped voids in the insulation) and this breakdown may be affected by environmental or electrical parameters, these factors also directly influence PD activity, and consequently, the PDIV. Not only the air, but also the insulation material properties may be altered by these factors.

Understanding the variables that affect PDIV is essential to understand the implications of the operating conditions on the response of the insulation system to PD activity. Thus, it is important to identify and analyse the key factors impacting PDIV, evaluate the extent of their influence, and determine whether their effects are significant or negligible. This aims to identify the parameters that must be considered in the design and modelling of PD-free electric machines, ensuring this condition under operation.

4.1.1 Environmental Conditions

Even though environmental variables including contamination or Ozone could affect the PDIV, temperature, pressure, and humidity are identified as the most influential factors [21, 51]. The following lines aim to provide further insight into how these environmental factors affect the PDIV, combining information collected from the literature with additional analysis.

4.1.1.1 Pressure

The breakdown of gases depends on the likelihood of generating sufficient electron avalanches to achieve breakdown. As detailed in Section 2.3.2, the pressure plays a significant role in influencing the breakdown voltage of the gas. At high pressures, the free path is too short, preventing electrons from gaining sufficient energy to ionise neutral particles, thereby increasing the breakdown voltage. Conversely, at lower pressures, the free path is sufficiently long to allow electrons to accumulate the required energy for effective ionisation, facilitating the breakdown. However, if the pressure is too low, the reduction in air density decreases the number of available molecules, reducing the probability of collisions per unit length and hindering the breakdown process. Therefore, the breakdown voltage of the gas exhibits a characteristic U shape as a function of pressure (Figure 2.16).

Since PDIV represents the minimum applied voltage at which the voltage across the air gap equals the breakdown voltage of the air, its behaviour mirrors that of the gas breakdown. This was experimentally confirmed in [76], where the PDIV of TPs was measured using a 50 Hz sinusoidal waveform. Starting at 5 mbar, the authors observed a decrease in PDIV until a minimum was reached between 50–70 mbar. Beyond this point, PDIV increased linearly with pressure, forming the aforementioned *U* shape. This linear trend at pressures above 70 mbar was similarly observed in [78] for pressures ranging from 100–1013 mbar, and in [79] for 200–1000 mbar.

The results from these studies [76, 78, 79] are compared in Figure 4.1. PDIV values are normalised to 1000/1013 mbar and plotted for pressures ranging from 5–1013 mbar. Notably, the characteristic *U* shape is only visible in [76], as the minimum PDIV occurs at approximately 50–70 mbar, while the studies in [78, 79] focused on pressures above this range.

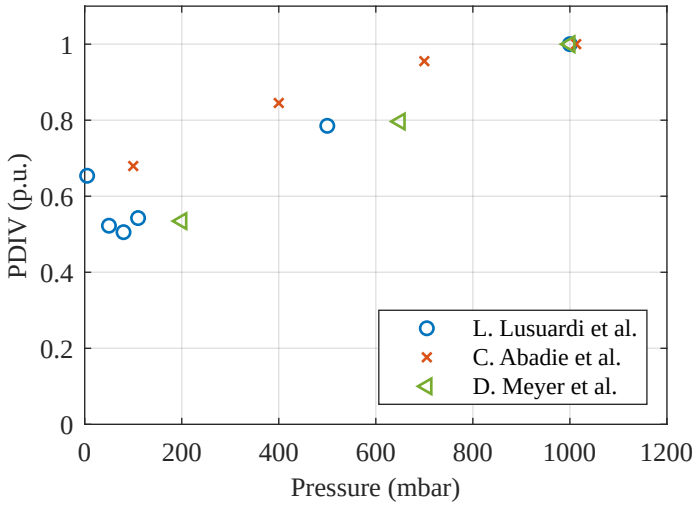

Figure 4.1: *Comparison of bibliographic results on the dependence of PDIV on pressure (L. Lusuardi et al. [76], Abadie et al. [78], and D. Meyer et al. [79]).*

It is worth noting that for PDIV measurements at low pressure, as the voltage is increased, the waiting time between consecutive voltage levels is critical for accurate results. At low pressures, the generation of the initial electron required to trigger PD is delayed because the average time between consecutive ionisations is longer than at ambient pressure [32]. Based on extensive experiments, suggested waiting times for different pressure levels under sinusoidal voltage waveforms are provided in [32] (Table 4.1).

4.1.1.2 Temperature

Temperature also plays a crucial role in the ionisation process required for PD initiation. As the temperature rises, the reduced gas density increases the average free path of electrons, and their kinetic energy also grows. These conditions make the ionisation phenomena

Table 4.1: *Waiting times between consecutive voltage levels during PDIV measurements as a function of pressure, suggested in [32].*

Pressure (mbar)	Waiting time
1013	30 s
507	60 s
111	5 min
82	8 min
50	10 min
25	20 min

more likely, reducing the air breakdown strength and subsequently lowering the PDIV. This trend has been observed in multiple studies [76, 80–82].

In addition to influencing air breakdown strength, temperature affects the relative permittivity of insulation materials, which impacts the electric field within the air gap (Section 2.2.2). As the relative permittivity of the insulating materials increases, the air electric field also rises, further influencing PDIV behaviour.

The comparison between estimated and experimental PDIV results presented in [81] for temperatures between 25-230 °C highlights the combined effects of temperature on air density and material permittivity. The findings revealed that higher temperatures decrease PDIV, due to effective changes in air density. Nonetheless, accounting for the temperature dependence of relative permittivity significantly improved model accuracy (Figure 4.2). This was demonstrated using materials like PAI and Polyetheretherketone (PEEK), which exhibit distinct permittivity-temperature relationships (increasing relative permittivity with temperature). These results align with those of [83].

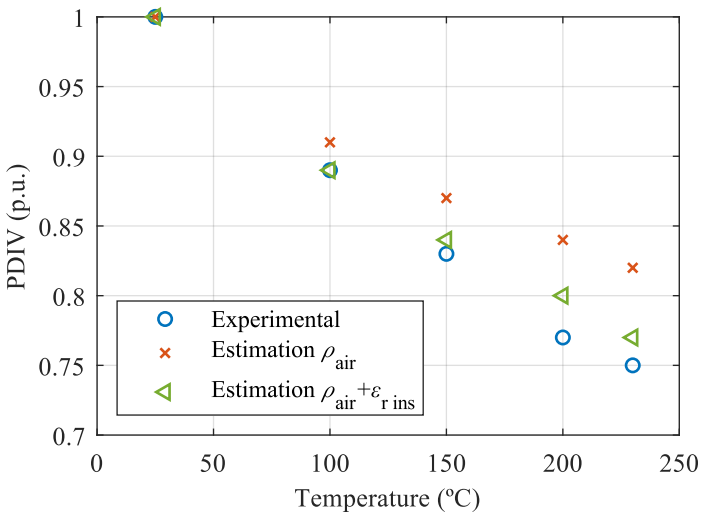

Figure 4.2: *Bibliographic experimental and estimated PDIV results depending on temperature (PAI, sample B, in D. Muto et al. [81]).*

In contrast, [76] reported negligible dependency of PAI permittivity on temperature within the 25–140 °C range, which is below its glass transition temperature (275 °C). Therefore, the effect of the relative permittivity on PDIV was minimal. For materials with lower glass temperatures, however, the influence of temperature on relative permittivity could be more pronounced [76].

It is important to note that the evolution of relative permittivity on the temperature depends on the material. In cases where permittivity decreases with temperature, its effect on PDIV may counteract the influence of air density changes, resulting in a more complex behaviour.

To assess this opposing effect, samples TP1 and TP2 were analysed (Section 3.1.1). TP1 (PE+PAI) exhibited an initial decrease followed by an increase in permittivity, with a total variation of 16% across the temperature range, whereas TP2 (PI) showed a consistent decrease with a more stable permittivity variation 7% (relative permittivity values were provided by the manufacturer, Section 3.1.1). To distinguish the contributions of air density and permittivity separately, two models subsequently discussed in Section 4.2, were applied: the Dakin's equation (Section 4.2.1.1), which accounts solely for permittivity variations, and Lusuardi's equation (Section 4.2.1.3), which just considers air density changes. To apply Lusuardi's equation, room temperature measurements of TP1 (610 Vrms) and TP2 (625 Vrms) served as references. Additionally, the PDIV values predicted by both models were compared to experimental measurements over a temperature range of 20–260 °C. All experimental data were obtained following the procedure outlined in Section 3.3.1.

Figure 4.3 illustrated the influence of permittivity and air density on PDIV as temperature increases. The normalized trends in Figure 4.3 (a) indicate that air density is consistently more affected than permittivity across the entire temperature range. Consequently, as shown in Figure 4.3 (b), Lusuardi's model aligns more closely with experimental results than Dakin's equation. This confirms that air breakdown strength is the dominant factor influencing PDIV with temperature, regardless of permittivity variations. Although permittivity changes can counteract the reduction in air breakdown strength, experimental results reinforce that air density remains the primary determinant. For instance, at 180 °C, the relative permittivity of sample TP2 would need to decrease by approximately 25% to neutralize the air density effect. Such a variation is uncommon for insulation materials typically used in enamelled wires, as reflected in the permittivity values of the samples studied in this work (Section 3.1.1).

4.1.1.3 Humidity

The influence of RH on PD behaviour is intricate due to the multiple factors it affects indirectly. When moisture levels are tied to temperature variations, the exact mechanisms by which water vapour impacts PDIV remain ambiguous. Furthermore, findings in the literature present inconsistencies, making it difficult to establish a clear relationship between temperature, humidity, and PDIV.

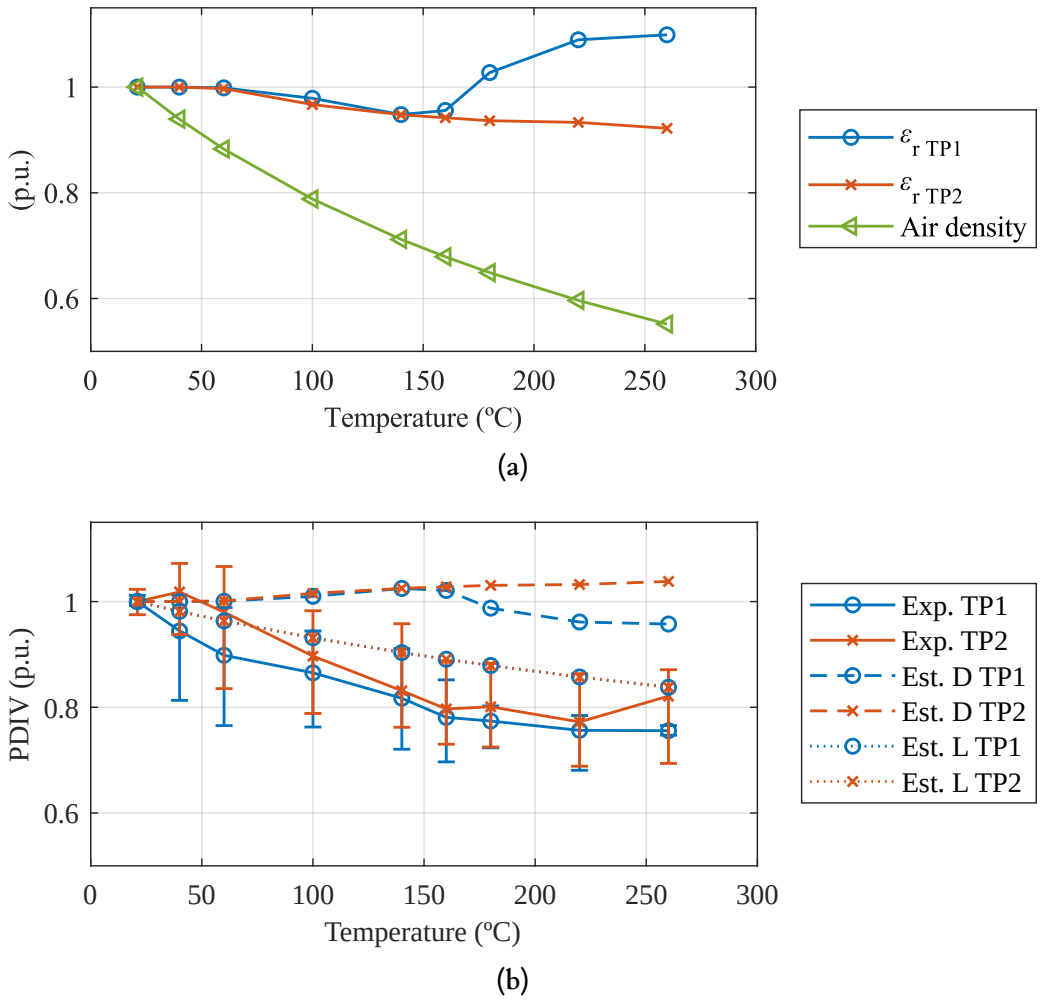

Figure 4.3: *Effect of the temperature in a range of 20-260 °C on (a) air density and relative permittivity (provided by the manufacturer) of TP1 and TP2, and (b) the comparison of experimental results (Exp.), Dakin's model estimation (Est. D), and Lusuardi's model estimation (Est. L) of PDIV for TP1 and TP2.*

Nevertheless, the main ways in which humidity influences PDIV can be categorised into three key aspects: (1) changes in the properties of insulation materials, (2) modifications to chemicals kinetic in air, and (3) alterations in the surface characteristics of conductors.

- **Changes in the properties of insulation materials:** As discussed in Section 2.2.2, the relative permittivity of the insulation material plays a crucial role in PD activity. Exposure to high humidity levels can lead to increased permittivity due to water absorption [70, 73, 84, 85]. Given that water has a significantly higher relative permittivity ($\varepsilon_{r\ water} \approx 80$) than most insulation materials, moisture uptake can immediately raise the effective permittivity of the insulation once a certain RH level is reached [70]. This increases the electric field in the air gap, reducing PDIV, as

experimentally confirmed in [85].

However, the reduction in PDIV cannot be solely attributed to permittivity changes. Several studies indicate that the contribution of relative permittivity variation depends on the insulation material. In [86–88] the effect of permittivity was deemed negligible for PEI+PAI insulation, as these materials exhibited minimal permittivity variation, contrary to the variations observed experimentally in Figure 3.1 in Section 3.1.1.

Moreover, due to the slow rate of water absorption in insulation materials and the reduced permittivity of water at elevated temperatures (78.3 at 25 °C and 66.8 at 60 °C [87]), the impact of moisture uptake on PDIV remains limited according to [88]. This contrasts with the rapid permittivity change observed in [70] for both conventional and nanocomposite PEI. Hence, it can be concluded that the influence of the relative permittivity on the reduction of PDIV varies depending on the specific properties of the insulation material and its response to environmental conditions. Nevertheless, its effect appears to be limited and must be accompanied by other mechanisms to fully explain the effect of humidity on PDIV.

- **Modifications to chemicals kinetic in air:** The initiation of PD is highly dependent on the interactions between free electrons and gas molecules (Section 2.3). The presence of moisture modifies these interactions in various ways.

  The increase in humidity enhances the production of initial free electrons [73, 84, 88, 89]. Experiments in [73] showed that the ionisation energy required for electron emission from a wet insulation surface is lower than for a dry one. This reduction in work function facilitates electron emission at lower fields, accelerating the initiation of discharge by reducing the time lag to trigger the air breakdown and lowering PDIV.

  A higher concentration of water vapour also facilitates electrical breakdown by lowering the ionisation energy of air molecules, thereby increasing the ionisation rate, and, consequently, the effective ionisation coefficient (α and $\bar{\alpha}$ respectively on equation (2.8)) [86, 90, 91]. This increase was reported beyond 45% RH at 30 °C in [91]. However, [92] reported that humidity has only a minor influence on the ionisation coefficient, attributing this to the relatively low proportion of water molecules compared to other atmospheric gases. Additionally, [88] suggested that the observed reduction in PDIV with increasing humidity cannot be solely attributed to the rise in the effective ionisation coefficient, indicating that other contributing factors must also be considered.

  At elevated temperatures, increased humidity influences the ionisation process by enhancing electron attachment (η on equation (2.8)) [70, 85]. In [93], a rise in negative ion density was observed with increasing Absolute Humidity (AH), particularly within the range of $4 - 16$ gm^{-3}. According to [87], the attachment coefficient remains secondary to the increase in air ionisation until the water content surpasses a critical threshold, which occurs at high RH levels combined with

elevated temperatures. Once this limit is exceeded (200 gm^{-3} in [87]), the effect of water vapour on the effective ionisation coefficient shifts considerably, leading to substantial reduction (equation (2.8)). This phenomenon, validated by simulations in [87] using Schumann's Streamer inception criterion, demonstrates that beyond a specific humidity level, the predominance of attachment over ionisation lowers the effective ionisation coefficient, ultimately increasing PDIV.

In summary, at low temperature (corresponding to low AH levels), an increase in RH enhances the production of initial electrons and promotes the ionisation process, thereby increasing the effective ionisation coefficient and facilitating the air breakdown, reducing the PDIV. At elevated temperatures, as RH increases and surpasses a certain AH threshold, electron attachment processes become more dominant, reducing the effective ionisation coefficient and hindering gas breakdown, ultimately increasing the PDIV. Equally, other contributing factors must also be considered to understand the effect of humidity on PDIV.

- **Alterations in the surface characteristics of conductors:** Moisture accumulated on the insulation surface can form a semi-conductive layer, altering surface resistivity. In [81], bare hand contaminated wires exhibited reduced PDIV with increase in humidity, though this effect disappeared after cleaning with pure water. However, more recent research [32, 88] suggests that humidity-related PDIV variations persist even when contamination was excluded.

  Experimental studies in [32, 86] confirmed that both temperature and humidity affected surface conductivity by increasing molecular mobility and water molecule availability. This leads to the formation of a semi-conductive film, which was further confirmed in [94] through Scanning Electron Microscope (SEM) imaging. The presence of this layer alters the electric field distribution in the air gap, thereby impacting PDIV.

  Findings in [95] indicated that the effect on PDIV depends on where the film is formed. If the conductive layer develops at the contact interface, the electric field redistributes, resulting in a rise in PDIV. Conversely, if it forms away from the contact point, the field concentrates at the contact region, reducing PDIV. Figure 4.4 provides a schematic representation of this behaviour. While [95] attributed the formation of this film to prior PD activity, which increases the hydrophilicity of the polymer surface in the affected regions, a rise in RH can also contribute to this effect. The threshold RH at which the transition between different types of semi-conductive layers occurs was experimentally determined in [94] using tanδ and Insulation Capacitance (IC) measurements across various temperatures (Table 4.2).

  As stated in [88], the predominant influence of humidity on PDIV is more likely attributed to its impact on surface conductivity rather than alterations in the insulation material properties or modifications in the chemical kinetics of the surrounding air.

After consolidating the various factors influencing PDIV due to ambient humidity,

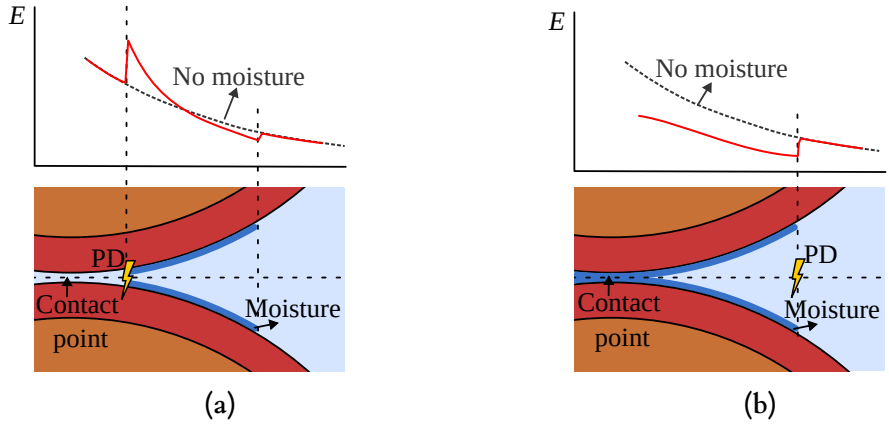

Figure 4.4: *Schematic representation of the effect of the semi-conductive film on the distribution of the electric field in the air gap and PD location based on [95] for 50 Hz (a) no moisture in the contact point, and (b) moisture in the contact point.*

Table 4.2: *Semi-conductive film formation threshold RH (%) for several temperatures [94].*

Temperature	30 °C	60 °C	90 °C
No water film formation	30–60	30–60	30–45
Water film formation (no in the contact point)	75	75	60
Water film formation (in the contact point)	90	90	75–90

Figure 4.5 compiles experimental data from multiple studies, categorised into three temperature ranges, each exhibiting distinct RH effects as discussed in [87].

For the lowest temperature range (20–30 °C, Figure 4.5 (a)), most references reported a decline in PDIV with increasing RH [70, 73, 84, 86, 87]. This reduction is linked to higher relative permittivity in the insulation material [70, 84], increased availability of initial electrons [73, 84], and an enhanced ionisation coefficient [86, 90]. [96] demonstrated that this effect persisted across different voltage frequencies. Even so, at higher frequencies, the reduction in PDIV became less pronounced. This was explained by the shift in governing mechanisms: at low frequencies, PD occurrence is primarily dictated by the availability of initial electrons, whereas at high frequencies, charge accumulation (memory effect, later in Section 4.1.2.1) becomes more dominant. At elevated humidity levels, the reduction in charged particle density, which plays a role in the memory effect, is less significant. Consequently, the influence of charge accumulation on PD activity weakens under humid conditions at higher frequencies.

Contrary to previous studies, [94] observed a trend where PDIV initially decreases but then rises after exceeding a critical RH, even at low temperatures. This behaviour was attributed to changes in surface conductivity caused by the semi-conductive film. However, [87] suggests that at these temperatures, surface conductivity plays a secondary role compared to ionisation effects, keeping PDIV on a downward trend.

In the mid-temperature range (40–60 °C, Figure 4.5 (b)), the general trend remains

similar, though the reduction in PDIV becomes less pronounced beyond 50 °C. This is attributed to a greater influence of surface conductivity due to the increased water content as AH rises with temperature [87]. Nonetheless, the dominance of ionisation over surface conductivity still results in an overall decrease in PDIV. In [94], the previously observed increasing tendency was again present. Likewise, [70] noted a slight increase in PDIV with RH, which was linked to a rise in the attachment coefficient beyond 50 °C. Contrariwise, [87] determined that this effect becomes significant only at elevated temperatures, such as 90 °C.

At the highest temperature range (70-90 °C, Figure 4.5 (c)), the typical reduction in PDIV at lower temperatures reverses, leading to an increase with higher RH [70, 86, 87]. This shift is due to the stronger attachment coefficient [87] and greater surface conductivity [86, 87], as the semi-conductive film extends to the contact region [95]. Some studies still continue to report a decreasing PDIV [73, 84], where findings are linked to increased relative permittivity [84] (even negligible variation reported in [86, 87] for the same material), and enhanced initial electron generation [73]. Interestingly, the studies reporting a sustained PDIV reduction at elevated temperatures employ surge [73] and bipolar rectangular waveforms [84] (with an overshoot factor of 1.22), whereas the majority of other investigations used sinusoidal excitation.

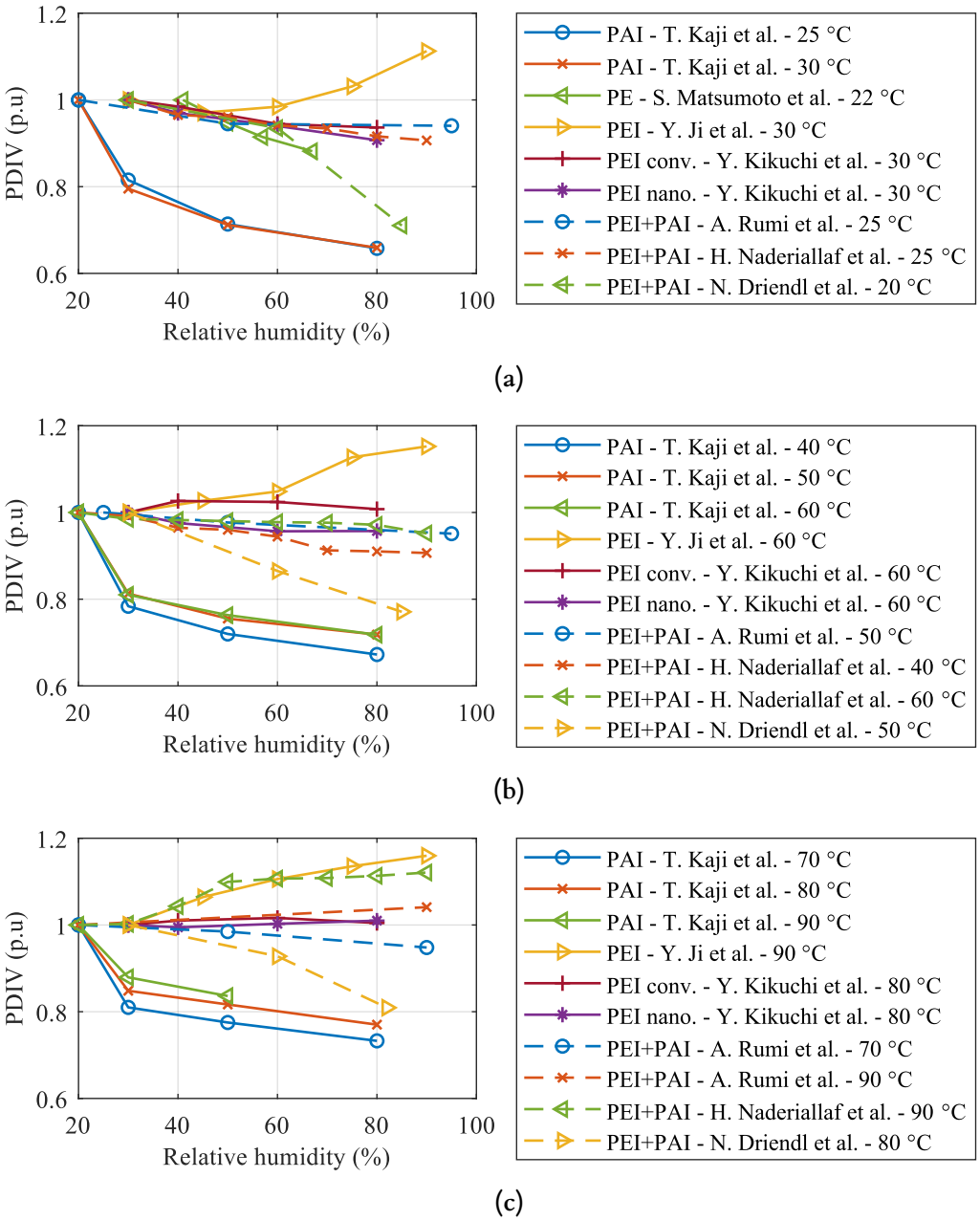

Figure 4.5: *Bibliographic results on the dependence of PDIV among RH at (a) 20-30 °C (b) 40-60 °C, and (c) 70-90 °C (T. Kaji et al. [73], S. Matsumoto et al. [97], Y. Ji et al. [94], Y. Kikuchi et al. [70], A. Rumi et al. [86], H. Naderiallaf et al. [87], and N. Driendl et al. [84]).*

4.1.2 Electrical Factors

Section 2.3.4 introduced the possible implications that impulse voltages may have on gas breakdown. The following sections analyse the potential effects of the main variables of the input voltage waveform on the PDIV, drawing on information from the literature.

4.1.2.1 Waveform Shape and Polarity

The influence of waveform shape on PDIV measurements has been widely studied, particularly in TPs. In these studies, PDIV was determined by gradually increasing the applied voltage at a constant rate until partial discharge activity was detected. Experimental observations in [98] indicated that only the peak-peak voltage of the applied waveform significantly affects PDIV, while the waveform shape (such as sinusoidal, unipolar pulse, or bipolar pulse with 50% duty) does not directly impact. Similar conclusions were obtained in [76], where the study highlights that using impulse voltages with overshoot can lead to inaccuracies in PDIV determination. Figure 4.6 illustrates this effect, where the peak voltage surpasses the inception voltage (V_{inc}), enabling PD initiation at any point within the overshoot interval (in red) if a free electron is available to trigger the avalanche.

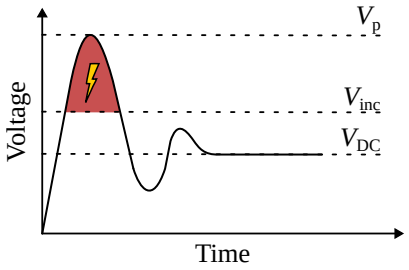

Figure 4.6: *Schematic representation of PD inception using impulse voltages with overshoot based on [76].*

Two distinct sources of error arise in PDIV measurements with these types of waveforms (Figure 4.6). When PDIV is defined based on the peak voltage, the recorded value may exceed the actual inception voltage, leading to an overestimation. Conversely, if PDIV is determined using the DC component, the measured value may be underestimated, as the DC voltage remains below the actual inception voltage. The magnitude of this error increases with larger overshoot amplitudes. Although this effect can also be observed in sinusoidal waveforms, it is generally negligible at conventional power system frequencies (50/60 Hz) due to the lower rate of voltage change [76]. Similar conclusions were drawn in [98, 99], where no significant differences were found between PDIV measurements using sinusoidal and repetitive impulse waveforms.

In addition to waveform shape, the polarity and type of applied voltage also may influence PDIV. A comparative analysis in [98] found that PDIV measured with unipolar square waveforms was approximately twice as high as the one recorded with bipolar square waveforms. This suggests that PDIV is predominantly determined by the peak-peak voltage rather than waveform shape when the measurement is conducted with a low voltage amplitude ramp rate and low dv/dt, i.e., at high rise times. Although subsequent studies reported a difference of nearly 20% between unipolar and bipolar peak-peak PDIV values in 40 ns–1 µs rise time range [100], more recent research confirmed the negligible influence of unipolar or bipolar pulses [99]. Furthermore, in [100], polarity effects on PDIV were investigated under unipolar excitation, concluding that positive or negative polarity had little influence due to the symmetric geometry of TPs. PDIV measurements

using sinusoidal and impulse voltage waveforms are also assumed to be equivalent for TPs in IEC 60034-18-41 [9].

Although PDIV generally remains unaffected by waveform shape and polarity, it is noteworthy that the application of voltage, even below PDIV, can lead to significant charge accumulation within the insulation bulk and on its surface. This effect is particularly evident when the voltage supply includes a DC component, such as in unipolar waveforms or bipolar waveforms at very low frequencies (< 10 Hz), especially for short exposure durations (below one hour) [98].

As explained in [98], surface charges are presented on the surface of the insulation and typically exhibit a polarity opposite to that of the adjacent electrode (heterocharge), thereby reducing the air gap local electric field compared to a charge-free condition. In contrast, charges accumulated within the bulk of the insulation generally share the polarity of the injecting electrode (homocharge), enhancing the electric field on it.

Experimental studies in [98] demonstrated that charge accumulation can affect the PDIV of TPs following exposure to unipolar voltage at 0.5PDIV (polling voltage). Figure 4.7 illustrates these findings through a schematic representation of the phenomenon, distinguishing between the electric field distribution without charge accumulation (dotted line) and with accumulated charges (solid line).

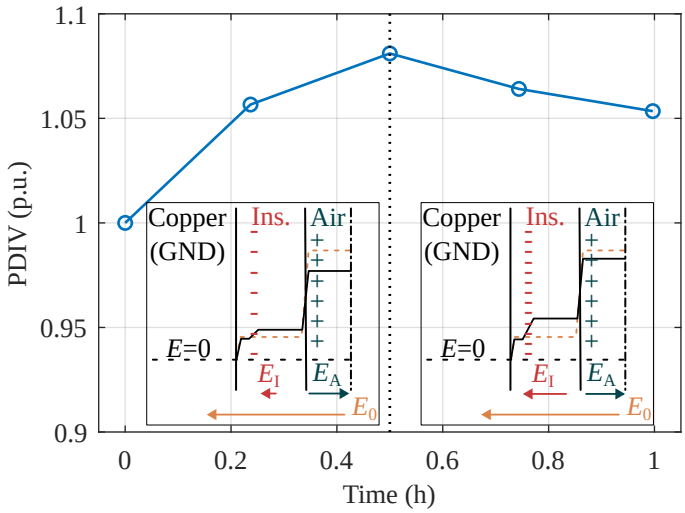

Figure 4.7: *Bibliographic results from [98] for PDIV depending on the electrical exposure time with schematic representation of surface (left) and bulk (right) charge accumulation predominance.*

During these experiments, an initial increase in PDIV was observed, approximately 1.05 times higher after 12 minutes of exposure [98] (Figure 4.7). This was attributed to the dominant influence of surface charge accumulation, which induces an opposing internal electric field, effectively lowering the net field in the air gap and increasing the PDIV. However, with prolonged exposure, bulk charge accumulation became predominant. In this case, the stored charge reinforced the electric field in the air gap, leading to a reduction in the measured PDIV [98]. Conversely, when bipolar waveforms with frequencies above

10 Hz were applied, this effect was not observed, and only negligible charge accumulation occurred in both the insulation bulk and surface, at least over relatively short durations [98].

This phenomenon, referred to as the memory effect, may occur when unipolar voltages are applied for a sufficient duration (at levels below PDIV) or when PD activity has previously been present [101]. It has been shown to influence PDIV in successive measurements [82, 102] and when the measurement is conducted after a prior electrical stress [98, 101].

4.1.2.2 Switching Frequency

In general, researchers concur that the influence of switching frequency on PDIV is insignificant [76, 86, 90, 97, 103–105]. Researchers in [76, 86] state that for a square waveform for a fixed rise time of 8 ns, PDIV remains unaffected within a frequency range of 10–100 kHz, provided that the permittivity of the insulating material remains constant. If permittivity is frequency-dependent, a critical frequency threshold exists, beyond which dipole orientation no longer occurs. This results in a dielectric loss peak and a subsequent reduction in real permittivity, potentially increasing PDIV [86]. Additionally, dielectric losses contribute to heating, which lowers air density in the proximity and, consequently, reduces PDIV. Therefore, when both the fundamental frequency and the harmonic content of the applied waveform exceed the critical threshold, PDIV may be influenced by the switching frequency.

A similar explanation was presented in [103], where it was observed that PDIV increases slightly, by approximately 6%, within a frequency range of 1–10 kHz for a square waveform with a fixed rise time of 100 ns and different duty cycles (0.2, 0.5 and 0.8). Despite the slight increase, the authors concluded that the frequency influence on PDIV was negligible. In [97], measurements conducted on sinusoidal waveforms within a 20-200 kHz frequency range also showed no significant variation in PDIV.

Although frequency does not show an evident effect on PDIV, several studies indicate that it plays a role in affecting PDIV in repetitive waveform conditions, commonly referred to as Repetitive Partial Discharge Inception Voltage (RPDIV). Researchers in [106, 107] suggested that at higher frequencies (2-2000 Hz), residual charge from previous discharges accumulates due to reduced relaxation time (i.e., 2-1000 ms [108]), facilitating electron extraction and allowing the following discharge to occur at lower voltage levels (i.e. reducing RPDIV) due to the reduction in the required time lag (Section 2.3) [109].

The accumulation of free electrons due to residual charge mainly occurs during consecutive discharges within the same half-cycle [110]. As RPDIV relies on the occurrence of multiple PD events within the same half-cycle, its behaviour aligns with this definition. Indeed, a reduced difference between PDIV and RPDIV at high frequencies (up to 2.5 kHz) was observed in [108], supporting this explanation. This effect was further demonstrated in [104], where PD patterns at 100 Hz and 1 kHz revealed that higher

frequencies promoted charge build-up, leading to increased PD magnitudes. At lower frequencies, PD magnitudes remained lower, especially in the positive voltage flank, due to the absence of charge accumulation.

Further investigations [79, 111] indicated that, within a frequency range of 5–200 kHz, RPDIV decreased with increasing switching frequency before stabilising near 75–100 kHz. Beyond 10 kHz, the memory effect is fully stabilised, having a consistent influence, and thus was excluded as a contributing factor to the RPDIV reduction observed between 20–75 kHz. Two primary aspects were investigated to clarify this trend: insulation permittivity and waveform oscillations. Measurements of permittivity across different frequencies revealed no substantial correlation with RPDIV. Instead, an examination of the instantaneous frequency spectrum of the applied pulse indicated that the dominant frequency component corresponds to the overshoot, which remains unaffected by switching frequency variations. Consequently, RPDIV was found to be influenced not by shifts in applied voltage frequency but by changes in the average overshoot amplitude. As the switching frequency increased, the average overshoot amplitude rose, while the peak voltage value remained unchanged. In other words, the overshoot exhibited several oscillations before settling to the DC component. More oscillations may heighten the probability of PD initiation in voltage ramp tests, which are commonly used to determine RPDIV [111].

4.1.2.3 Rise Time

There is no consensus in the literature regarding the influence of rise time on PDIV. Two primary perspectives emerge: one suggests that PDIV remains unaffected by rise time but is influenced by overshoot and its characteristics, which are more pronounced at shorter rise times. The other asserts that PDIV decreases with a reduction in rise time in the absence of significant overshoot.

Regarding the first perspective, multiple studies have determined that rise time does not directly affect PDIV; rather, the overshoot associated with shorter rise times is the key factor [76, 86, 90, 91, 104, 112]. As a result, discrepancies arise depending on whether PDIV is defined using the DC voltage level or the peak voltage, as illustrated previously in Figure 4.6.

Certainly, [76] found a negligible difference in PDIV (both peak and DC) when comparing a short-rise time bipolar square waveform (150 ns rise time, 1% overshoot) with a sinusoidal 50 Hz waveform. Similarly, [112] demonstrated that voltage overshoot artificially increased the (R)PDIV. When compensating for this effect by evaluating the DC voltage, all investigated rise times (130–2000 ns) yielded comparable results, indicating that the actual inception voltage of PD aligns more closely with the DC voltage than the peak voltage. In line with these findings, [91] reported that peak PDIV remained largely unchanged across rise times ranging from 30 to 200 ns, with a 2.5% overshoot, and a pulse width of 200 µs.

A summary of results from various studies comparing PDIV values based on peak and

DC voltage plotted against rise time and overshoot percentage is presented in Figure 4.8. The values are normalised to the longest rise time used in each study, which corresponds to the lowest overshoot.

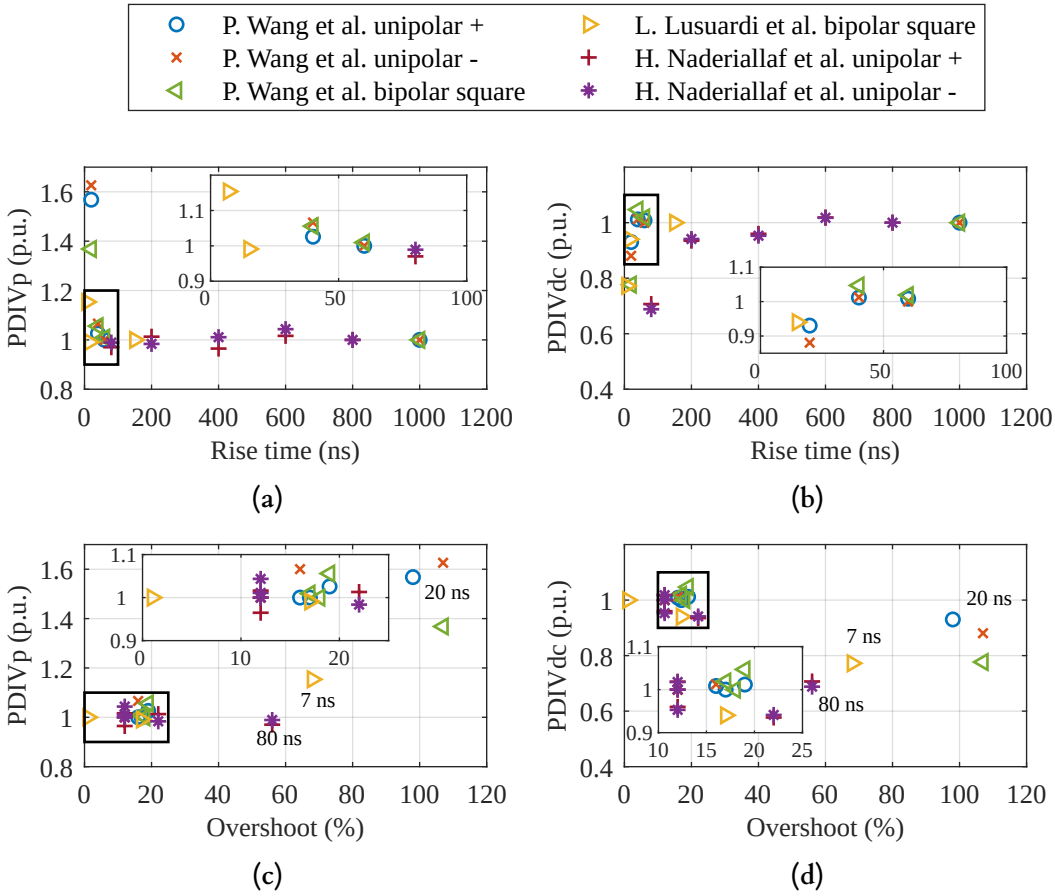

Figure 4.8: *Bibliographic results of (a) peak PDIV vs rise time, (b) DC PDIV vs rise time, (c) peak PDIV vs overshoot, and (d) DC PDIV vs overshoot (P. Wang et al. [100], L. Lusuardi et al. [76], and H. Naderiallaf et al. [90]).*

Figure 4.8 (a) indicates that for rise times exceeding 20 ns, the peak PDIV remains relatively constant regardless of waveform shape or polarity (bipolar or unipolar, both positive and negative). However, for shorter rise times, an increasing trend is observed. Some studies place this transition point below 20 ns [100], while others identify it below 15 ns [76]. Figure 4.8 (b) shows that DC PDIV follows a similar pattern but with a decreasing trend. The shift from a stable to a rising or falling PDIV is associated with an increase in overshoot [76]. Figure 4.8 (c) and (d) illustrate the relationship between PDIV and overshoot, demonstrating that for low overshoot levels, both peak and DC PDIV remain largely unaffected. However, as overshoot increases (corresponding to rise times of 7 ns [76], 20 ns [100], and 80 ns [90]) PDIV deviates more significantly. Moreover, above 60% overshoot, larger overshoot values have a strong influence on the peak PDIV, whereas shorter overshoots tend to have a greater effect on the DC PDIV.

Figure 4.9 summarises the correlation between peak and DC PDIV as a function of

overshoot, revealing a linear relationship. The disparity between peak and DC PDIV expands as overshoot increases.

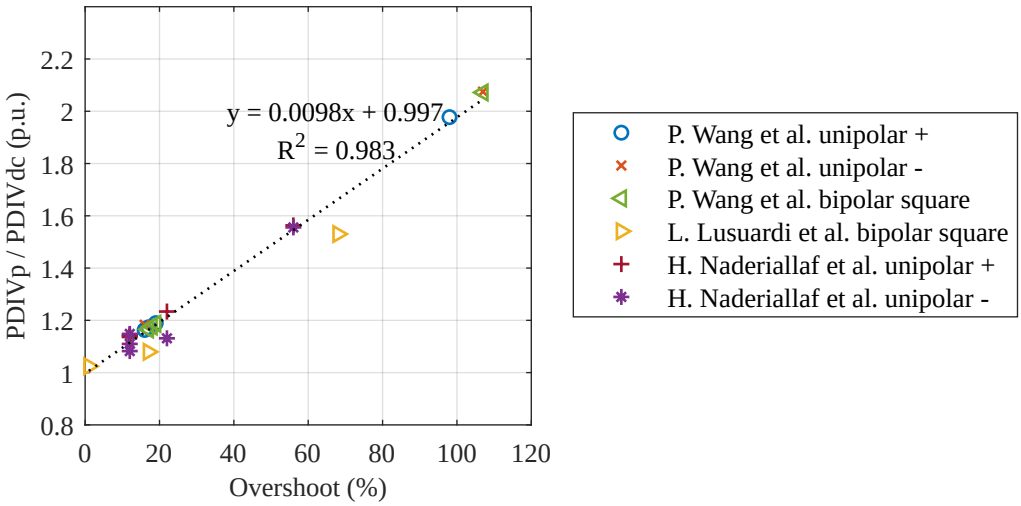

Figure 4.9: *Relationship between peak and DC PDIV as a function of the voltage overshoot based on bibliographic results (P. Wang et al. [100], L. Lusuardi et al. [76], and H. Naderiallaf et al. [90]).*

The second perspective was investigated by studies that isolated the effect of rise time by minimising overshoot ($< 5\%$ [102, 103] and $< 10\%$ [113]) in a pulse width range of 10–1000 µs. In [103], peak-peak PDIV was found to be 28% lower when measured under a unipolar square waveform with a 150 ns rise time compared to a 60 Hz sinusoidal waveform, with a further 21% reduction when the rise time decreased from 150 ns to 60 ns. A similar trend was reported in [102], where DC PDIV declined by 23–38% as the rise time of unipolar waveform was shortened from 1000 ns to 150 ns. However, the effect was less pronounced in the 100–150 ns range. The same behaviour was identified in [113] for rise times between 100–800 ns.

In [102], this reduction in PDIV was attributed to the fact that the critical number of electrons N_{cr} (defined by Schumann's criterion, Section 2.3.3) required for PD initiation remains unchanged across different rise times. When the pulse width is fixed, a shorter rise time enables electron generation to start sooner, as long as the applied voltage exceeds the inception threshold.

A schematic representation in Figure 4.10 illustrates this behaviour for a fixed pulse width, defined as the interval between the midpoints (50%) of the pulse magnitude [102], comparing two rise times. When the rise time is shorter, the inception voltage V_{inc} is reached sooner, allowing electron generation to begin earlier (t_{0s}). This provides sufficient time for electrons to accumulate N_{cr} and initiate PD activity. In contrast, for longer rise times, electron generation begins later (t_{0l}) and proceeds at a slower rate. Consequently, by the time N_{cr} is reached, the applied voltage may already have fallen below the inception level, preventing PD initiation (as explained in Section 2.3.4). As a result, PDIV is set at a

higher voltage.

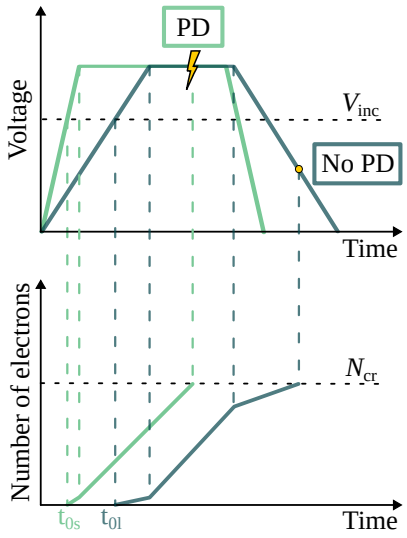

Figure 4.10: *Schematic representation of the influence of the rise time on the PD inception for a fixed pulse width, defined as the interval between the midpoints (50%) of the pulse magnitude. It is assumed that the effective ionisation process ($\bar{\alpha} > 0$) starts at t_0 when $V = V_{inc}$. Based on the explanations provided in [102].*

It is worth mentioning that these studies reported the decreasing PDIV trend independently of the pulse width, which ranged from 2–800 µs in [102] and 10–1000 µs in [113]. According to [91], long pulse widths (i.e. 200 µs) should guarantee sufficient time for electron accumulation, suggesting that rise time would not play an important role in PDIV.

Additionally, [102] suggests that space charge accumulation at different rise times may alter the local electric field, influencing the electron generation rate. [87] expands on this by noting that as dv/dt increases, the available time for surface charge dissipation is reduced, which accelerates the collection of electrons, ultimately leading to a lower PDIV. This conclusion was drawn after experimentally observing a decline in peak-peak PDIV as the rise time decreased from 800 ns to 80 ns. Even so, it is important to highlight the significant difference in the overshoot between both waveforms, with the average overshoot being higher at 80 ns. This factor could be responsible for the acceleration of electron generation [111].

Although the impact of rise time on PDIV has been quantitatively assessed in [102], the underlying mechanisms explaining why even minor variations in rise time (despite being significantly shorter than the pulse width) can result in substantial differences in PDIV remained unclear. This uncertainty is likely due to the stochastic nature of PD processes and the influence of space charge distribution on the rate of initial electron generation [102]. Indeed, [63] reported an increase in PDIV with the decrease in rise time (contrary to [102]), attributing this to a reduced supply of initiating electrons at shorter rise times, which are predominantly produced at the insulation surface. When comparing waveforms with rise times of 800 ns and 3000 ns (both with 60% overshoot),

more initiating electrons were provided for the 3000 ns rise time, leading to a lower PDIV.

4.1.2.4 Pulse Width

In general, studies suggest that an increased pulse width promotes the formation of new electrons. When the inception voltage is reached, a longer pulse duration allows more time for a sufficient number of electrons to accumulate, facilitating PD activity [106]. However, the role of pulse width in defining PDIV remains a subject of debate.

Some researchers propose that PDIV is unaffected by pulse width, provided the rise time is sufficiently long [104]. For instance, [104] observed no noticeable change in PDIV for unipolar 50 Hz pulses with a rise time of 300 ns across a pulse width range of 0.5–50 µs. Similarly, [90] reported an almost constant PDIV with only a slight increase as pulse width expanded from 40 to 100 µs (duty rate 10–25%) in unipolar waveforms (positive and negative) at 2.5 kHz and a rise time of 160 ns. These minor differences were largely attributed to measurement uncertainties. At lower pulse widths, results exhibited greater variance due to the increased influence of firing electron delays.

Conversely, [102] reported that PDIV was dependent on pulse width when measured using a unipolar waveform of 1000 ns rise time. In this case, PDIV decreased as pulse width increased from 2 to 800 µs, approximately following an inverse power law. The explanation provided was that, for a given rise time, N_{cr} remains unchanged across different pulse widths. When the pulse is longer, electrons continue to accumulate within this extended period (as long as the applied voltage exceeds the inception threshold), reducing the voltage required to reach N_{cr} for PD occurrence (Figure 4.11). Consequently, the larger the pulse width, the lower the PDIV. A similar trend was observed in [113].

The same authors [102] also noted a similar trend in the 100–150 ns rise time range, consistent with findings for longer rise times. Accordingly, [114] reported a decrease in PDIV with increasing pulse width from 1.2 to 8.8 µs for rise times of 70 ns using bipolar waveforms (50 kHz). Beyond the previously discussed reasoning, which associates this effect to the time required to reach N_{cr}, [114] further connected it to a delayed in the initial electron generation, influenced by the statistical time lag t_s (Section 2.3.4), and a slower transfer of the electric field to the enamel surface and the air gap due to polarisation processes in solid insulations. Figure 4.12 compares ideal instantaneous polarisation and the actual dielectric response for pulses significantly shorter than or comparable to the dielectric relaxation time (τ, in the order of a few ns, is considerably lower than the analysed pulse widths), assuming a Debye relaxation model [114]. Only when pulse duration exceeds approximately three times τ does the field approach the ideal condition. The authors in [114] suggested that the delay in electron availability is a more plausible cause, as this effect can persist for durations as long as 5 µs.

In contrast, for 70 ns rise time, [115] reported an increase in PDIV as pulse width expanded from 1000 to 9000 µs in unipolar 100 Hz waveforms. This resulted from the

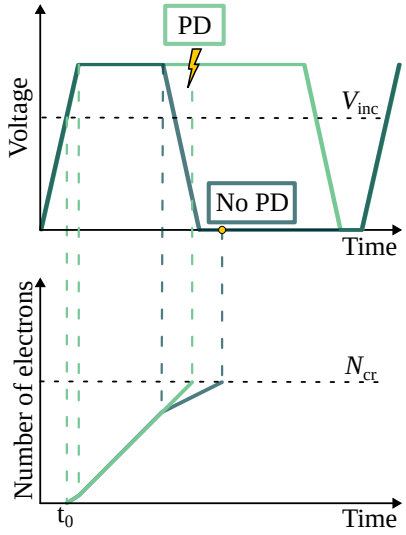

Figure 4.11: *Schematic representation of the influence of the pulse width on the PD inception for a fixed rise time. It is assumed that the effective ionisation process ($\bar{\alpha} > 0$) starts at t_0 when $V = V_{inc}$. Based on the explanations provided in [102].*

.

reduction in non-conduction duration per cycle, which affects surface charge redistribution. For instance, a 1000 µs pulse width corresponded to a 9000 µs non-conduction interval, whereas a 9000 µs pulse width left only 1000 µs for charge dissipation. When the non-conducting duration is brief relative to pulse width, charge redistribution remains incomplete. This leads to residual surface charge accumulation (heterocharge), with the consecutive reduction in the air electric field. As a result, the PDIV increased, as discussed in Figure 4.7 (Section 4.1.2.1).

Experiments repeated with 1 kHz waveform, using pulse widths of 100, 500, 900, and 960 µs with corresponding non-conduction durations of 900, 500, 100, and 40 µs, confirmed that a longer non-conduction duration relative to the conduction period (e.g. pulse width 100 µs and non-conduction duration 900 µs) results in a lower PDIV [115]. Additionally, when the non-conduction duration was equal to or shorter than the pulse width (500, 100, and 40 µs non-conduction durations for 500, 900, and 960 µs pulse widths), the dissipation rate was too low to significantly influence PDIV [115].

One of the key differences between [115] and [114], which reported opposing effects of pulse width at a rise time of 70 ns, lies in the type of voltage waveform employed: the former uses unipolar pulses, while the latter applies bipolar pulses. As explained in Section 4.1.2.1, bipolar waveforms are less likely to result in charge accumulation, and thus the effect described by [115] would not be expected.

Another observation in Section 4.1.2.1 was that the influence of charge accumulation under unipolar excitation is typically limited to prolonged exposure periods in the absence of prior PD activity, which would be the case of a PDIV measurement. Therefore, the assumption of significant charge accumulation during PDIV measurements in [115] could be questioned. Particularly, the important measurement variability in [115] should be

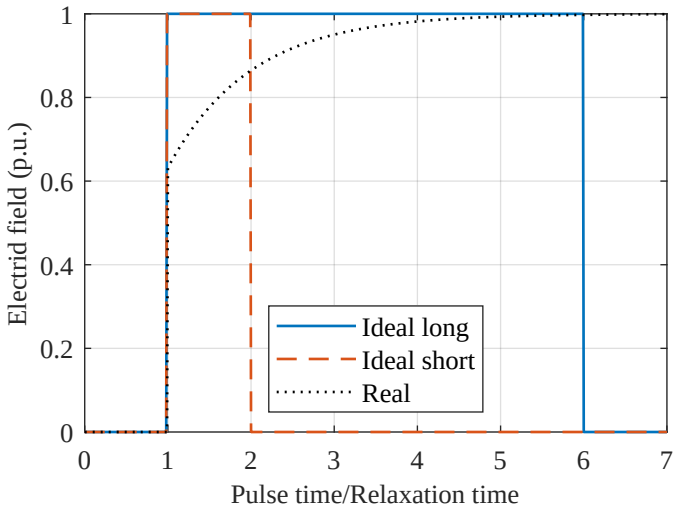

Figure 4.12: *Electric field in a selected point in the air gap between the twisted wires with ideally fast polarisation and real polarisation trend for pulses shorter or comparable to relaxation time τ based on [114].*

noted. In fact, the mean values of PDIV for each pulse width fall within the error margins of others, with each point exhibiting a variability of more than ±50 V, and the maximum difference between pulse widths being only around 125 V. This variability could be attributed to the relatively large voltage step size (50 V) used during testing.

Indeed, the effect of the non-conduction time, in terms of charge accumulation and the availability of initiating electrons, has been more commonly associated with RPDIV rather than PDIV, as discussed in [104]. In that work, charge accumulation was linked to previous PD activity. When the non-conduction duration is sufficiently long (i.e., when non-conduction duration is longer than pulse width at low duty cycles), there is enough time for the dissipation of charges generated by earlier discharges. This reduction in residual charge and starting electron availability hinders the generation of subsequent discharges, thereby increasing the RPDIV.

From the above, it can be synthesised that once the inception voltage is reached, shorter voltage application durations reduce the likelihood of initiating a PD, thereby increasing the PDIV. Conversely, longer voltage durations increase the probability of discharge inception, resulting in a lower PDIV. This effect would persist as long as the combination of rise time and pulse width provides sufficient time for electron generation after the inception voltage is reached.

4.1.3 Summary

The analysis and discussion conducted in previous sections is summarised below for each environmental and electrical factor. Table 4.3 complements this summary by offering a more direct overview. It outlines the variables and indicates whether a rise in each leads

to an increase, decrease, or negligible change in PDIV. Relevant measurement conditions are also noted.

- **Pressure:** The literature consistently reports a strong influence of pressure on PDIV, which follows a characteristic *U* shaped trend with a minimum between 50 and 70 mbar. At high pressures, the short mean free path limits ionisation, while at very low pressures, reduced molecular density decreases collision probability. Additionally, longer waiting times between voltage steps are required at low pressures to ensure accurate PDIV measurements.

- **Temperature:** Temperature primarily affects PDIV through its impact on air density. As temperature increases, air density decreases, resulting in a longer electron mean free path and higher kinetic energy. This lowers the breakdown strength and, consequently, reduces PDIV. While temperature-induced changes in insulation permittivity can partially offset this effect, experimental data confirm that air density is the dominant factor. This was validated through modelling and testing across various materials and temperatures.

- **Humidity:** The impact of humidity is complex and dependent on temperature and multiple concurrent mechanisms. In general, increasing RH tends to reduce PDIV at low to moderate temperatures due to enhanced ionisation, moisture-induced permittivity changes, and surface conductivity effects. However, at higher temperatures and humidity levels, this trend may reverse as electron attachment and conductive film formation at contact points become dominant, leading to an increase in PDIV. Consequently, the overall impact of humidity on PDIV varies with both environmental conditions and insulation material properties.

- **Waveform shape and polarity:** When peak-peak voltage is considered and measurements are conducted promptly, thereby avoiding the memory effect, waveform shape and polarity have minimal influence on PDIV. However, excessive overshoot can cause PDIV being over- or underestimated, depending on whether the peak or DC value is used. Additionally, prolonged voltage exposure (with or without PD activity) may lead to memory effects, especially under unipolar conditions, which alter the measured PDIV. Bipolar waveforms tend to minimise charge accumulation effects when operated above 10 Hz.

- **Switching frequency:** While switching frequency does not affect PDIV, which is defined by the first discharge, it does influence the RPDIV. At frequencies below 10 kHz, residual charge accumulation increases electron availability and reduces RPDIV. At higher frequencies, RPDIV keeps reducing, but it is more influenced by the average overshoot amplitude, finally stabilising at around 75–100 kHz.

- **Rise time:** Although overshoot, which is more likely with short rise times, strongly affects PDIV, the direct impact of rise time remains debated when overshoot is controlled (limited to 10%). These discrepancies persist even when the pulse width

allows sufficient time for electron generation. Nevertheless, most recent studies conclude that rise time does not significantly influence the PDIV under these controlled conditions.

- **Pulse width:** At longer rise times (160 ns and above), some studies reported no effect of pulse width on PDIV, while others reported a reduction. At shorter rise times, longer pulse widths typically lead to lower PDIV, as they allow more time for the necessary electron generation. Furthermore, non-conduction duration affects RPDIV by allowing or limiting the dissipation of charge from previous discharges.

Table 4.3: *Summary of the effect of the increase in the environmental and electrical variables on PDIV.*

Affecting variable	Effect on PDIV	Range	Measuring conditions	Reason	Notes	Ref.
Pressure	Decrease	5-50/70 mbar	-	$\downarrow V_{B_{air}}$	Range depends on air gap and material	[76, 78, 79]
	Increase	100-1013 mbar	-	$\uparrow V_{B_{air}}$		
Temperature	Decrease	25-230 °C	-	$\downarrow V_{B_{air}}$ and $\varepsilon_{r\,ins}$ change	Important to consider the $\varepsilon_{r\,ins} - T$ relation	[76, 80, 81, 116]
Humidity	Decrease	30-75%	$40 \leq T \leq 60$ °C	Semi-cond. film on non-contact point	-	[94]
		20-95%	$T \leq 30$ °C	$\uparrow \varepsilon_{r\,ins}$, n_0, and $\bar{\alpha}$	-	[86, 87]
			$40\,°C \leq T \leq 60$ °C	$\uparrow \bar{\alpha} > \uparrow$ surface cond.	-	[86, 87]
			$20\,°C \leq T$	$\uparrow \varepsilon_{r\,ins}$ and n_0	Surge/bipolar pulses	[73, 84]
	Increase	75-90%	$30\,°C \leq T \leq 60$ °C	Semi-cond. film on contact point	-	[94]
		30-90%	$70\,°C \leq T$	$\uparrow \eta$ and semi-cond. film on contact point	-	[86, 87]
	Negligible	50-95%	$T = 25$ °C & Pure water washing	Bare-hand contaminants dependency	-	[81]
Waveform and polarity	Negligible	Sinusoidal	No overshoot	Defined by V_{pp}	↑ PDIV after prolonged V/PD exposition, or consecutive measurements	[76, 98, 99]
		Bipolar square				[98, 99]
		Unipolar +/-				[76, 99, 100]
Switching frequency	Decrease*	2-10000 Hz	-	↑ space charge, $\downarrow t_B$	-	[104, 106, 107]
		10–75 kHz	-	↑ average overshoot	-	[79, 111]
	Negligible	1–200 kHz	-	No memory effect on detection of first PD	If $\varepsilon_{r\,ins}$ independent on frequency	[76, 86, 90, 97, 103–105]
		75-200 kHz*	-	-	-	[79, 111]
Rise time	Increase	60–1000 ns	No overshoot $t_w = 2 - 1000$ µs	$\downarrow$ time for electron generation	-	[102, 103]
	Negligible	7–1000 ns	Overshoot $t_w = 2 - 1000$ µs	Differences from overshoot rather than t_r	-	[76, 86, 90, 100, 104, 112]
		30–200 ns	No overshoot $t_w = 200$ µs		Compared to 60 Hz sine	[76, 86, 91]
Pulse width	Decrease	1.8-1000 µs.	$t_r = 70$–1000 ns	↑ time for electron generation	Change frequency and duty rate	[102, 113, 114]
	Increase	900-9000 µs	$t_r = 70$ ns	↑ t_{nc}, charges partially dispersed	Same frequency, change of duty rate	[115]
	Negligible	0.5-100 µs	$t_r \geq 160$ ns	N_{cr} during rising	Same frequency, change of duty rate	[90, 104]
		100-960 µs	$t_r = 70$ ns	$\downarrow t_{nc}$, no charge dispersion		[115]

* for RPDIV

4.1.4 Definition of the Environmental Parameters for Inclusion in PDIV Modelling and Assessment of Sinusoidal Waveforms for Model Definition and Validation

As previously stated, in addition to understanding how environmental and electrical factors affect the PDIV, this analysis aimed to identify which variables must be included in the estimation of PDIV during the insulation system design phase.

Starting with the environmental factors, the three analysed factors (pressure, temperature, and humidity) were all shown to influence PDIV. Thus, they should all be considered in PDIV estimation models. However, their impact may vary depending on the specific application. For instance, in the context of EV insulation system design, pressure may be of secondary importance compared to temperature or humidity.

Temperature must always be considered. The high temperature experienced in windings due to copper losses subject both the insulation system and the surrounding air to elevated conditions. In EV machines, winding temperature can reach up to 180 °C [117]. In the same context, humid environments may also affect, depending on the operating location of the vehicle and the temperatures reached in service.

Regarding the electrical factors, there remains a lack of consensus on whether rise time or pulse width significantly affects the PDIV, and if so, how. In particular, the suitability of sinusoidal voltage waveforms for evaluating interturn insulation in converter-fed machines has been questioned in some studies [103]. These concerns are mainly from the influence of rise time [102, 103], which could render sinusoidal measurements unreliable.

However, as previously mentioned, most studies conclude that PDIV is largely independent of rise time. The observed differences are generally attributed to the increased overshoot associated with shorter rise times [76, 86, 91, 104, 112], indicating that only the peak voltage applied to the interturn insulation is critical.

In this context, [76] affirmed that sinusoidal waveforms are valid for assessing insulation systems, even when these are fed by inverters. As highlighted in Section 4.1.2.1, IEC 60034-18-41 [9] also assumes equivalence between PDIV measurements using sinusoidal and impulse voltage waveforms for interturn insulation when evaluating TPs, as well as for phase-phase and phase-ground insulations when testing motorettes or complete windings.

Since sinusoidal waveforms were the primary method for PDIV measurement in this study, confirming their validity for insulation system design in converter-fed machines was essential. For this purpose, sinusoidal PDIV measurements (Section 3.3.1) for samples PC1-PC5 and PC7-PC11 (Section 3.1), were compared with results from a partner company. The partner measured the same samples under unipolar negative pulses with a 300 ns rise time, 100 µs pulse width, and 500 Hz switching frequency with an overshoot of approximately 20%. At least 10 samples were measured and averaged to obtain a PDIV for each sample type.

Figure 4.13 compares PDIV values obtained with sinusoidal and unipolar negative pulse waveforms at 20 °C and 180 °C. The average values along with the maximum and minimum measurements with error bars are displayed. As shown in Figure 4.13 (a), at 20 °C the difference between both measurement methods remains below 10%, which is within the maximum variability observed for unipolar measurements (22% for TP10 between the maximum and minimum). Furthermore, the mean sinusoidal PDIV values generally fall within the range of unipolar pulse measurements. Similar trends are observed at 180 °C (Figure 4.13 (b)).

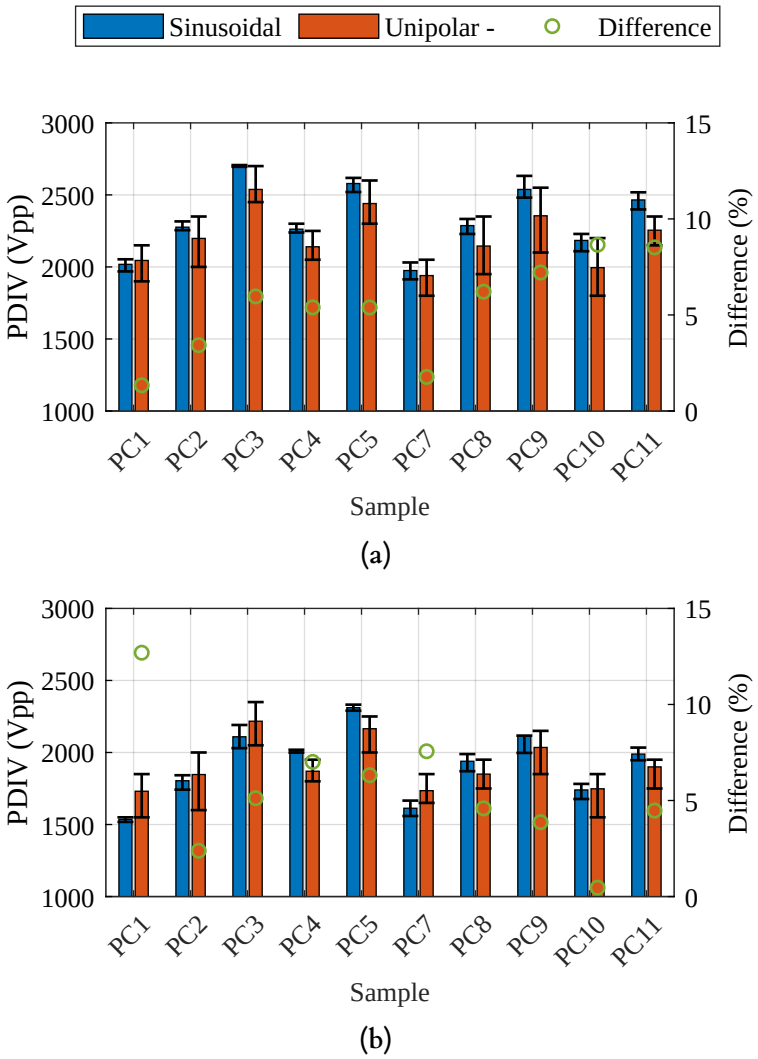

Figure 4.13: *Comparison of experimental PDIV values for PC1-PC5, PC7-PC11 samples performed with sinusoidal voltage (own measurements) and unipolar negative voltage (partner company measurements) at (a) 20 °C, and (b) 180 °C.*

This comparison rules out a significant influence of waveform shape, polarity, rise time, or pulse width on PDIV. It is worth noting that the rise time resembles the output of conventional Si converters, rather than that of SiC converters. This may also explain the absence of pulse width effect, as most literature indicates that these are negligible

when rise time exceeds 160 ns (Section 4.1.2.4). Consequently, in agreement with [76], it could be concluded that sinusoidal and unipolar pulse waveforms yield comparable PDIV results.

On the top of that, [118] stated that using 50 Hz sinusoidal measurements provide conservative PDIV values. This is particularly relevant because, in impulse waveforms, PDIV could be overestimated if peak-peak voltage is considered, especially in the presence of high overshoots, as discussed in Section 4.1.2.1. Indeed, sinusoidal waveforms are widely used for the comparison and validation of various PDIV models [81, 90, 119–122]. The observed similarities in experimental measurements (Figure 4.13) further support the validity of the developed models presented later in Section 4.3, ensuring a conservative approach to insulation system design.

All in all, pressure, temperature, and humidity should be considered in PDIV estimation models. Depending on the specific application, pressure may be a secondary factor. Finally, the use of sinusoidal waveforms for model validation is justified, as they provide comparable results and are widely adopted in the literature.

4.2 Literature Overview of Estimation Models for Partial Discharge Inception Voltage

To maximise the longevity of PD-free operation, PDIV must be carefully considered during the initial design phase of the insulation system. As previously discussed in Section 2, interturn insulation is the most vulnerable part of the system, making it the most likely site for PD activity. Therefore, ensuring a PD-free insulation design requires the development of accurate models for estimating PDIV. Most of the models identified in the literature are focusing on interturn PDIV, yet some research extends the models to the groundwall or phase-phase insulations.

Various modelling approaches have been proposed in the literature, which can be broadly classified into two categories: analytical equations and FEM simulation based. Among these models, some rely on Paschen's Law and others on Schumann's criterion to describe the mechanisms to develop the PD. Despite a minor number of models consider electrical waveform variables, most of them are limited to the environmental variables.

4.2.1 Analytical Models

4.2.1.1 Dakin's Equation

Dakin et al. [123] conducted extensive PDIV measurements across various insulating materials and thicknesses, proposing an empirical equation (4.1) that correlates insulation thickness and relative permittivity (reduced coating thickness, $t_{\text{ins}}/\varepsilon_{\text{r ins}}$).

$$\text{PDIV} = 163 \left(\frac{t_{\text{ins}}}{\varepsilon_{\text{r ins}}} \right)^{0.46} \tag{4.1}$$

where PDIV is given in V_{rms}, t_{ins} is the total insulation thickness in µm and $\varepsilon_{\text{r ins}}$ is the relative permittivity of the insulation. In the case of TPs or PCs, t_{ins} is twice the enamel thickness, considering that each conductor is coated with an enamel layer. When different enamel materials are used, the equivalent permittivity ($\varepsilon_{\text{r ins eq}}$) should be used, calculated as in equation (4.2) [68].

$$\varepsilon_{\text{r ins eq}} = \left(\sum_{i=1}^{N} \frac{t_{\text{ins}_i}}{t_{\text{ins}}} \varepsilon_{\text{r ins}_i}^{-1} \right)^{-1} \tag{4.2}$$

Although widely applicable to different insulation thicknesses and permittivity values, this equation does not incorporate the influence of environmental factors such as temperature, which can significantly impact PDIV.

A similar approach based on the t_{ins} and $\varepsilon_{\text{r ins}}$ was adopted in SAE AS50881H [124] for selecting appropriate insulation parameters in circular wires used in aerospace applications. In this sense, instead of providing a fixed equation, the standard presents a series of curves covering multiple temperature and pressure conditions to determine the required insulation properties for a given PDIV. Given the increasing adoption of rectangular conductors in modern electric machines (Section 2), accounting for their specific characteristics is essential for developing a generalised predictive model, which is not covered by the mentioned standard.

4.2.1.2 Parallel-Plate Capacitor Equation

This PDIV prediction model presented for TPs is based on two established equations and is used, for instance, in [119] and [68] at standard ambient conditions. The model simplifies a TP configuration by representing it as several parallel-plate capacitors (Figure 4.14), where two copper conductors are separated by an enamel-air-enamel layer. This approach assumes that the enamel thickness (in µm) is significantly smaller than the conductor diameter (in mm), allowing the curvature of the wire to be disregarded. Consequently, the series capacitor insulation model from [125], expressed in equation (4.3) is applied. Additionally, since PDIV is the minimum voltage at which the voltage across the air gap equals the breakdown voltage of air, as defined by Paschen's Law (Section 2.3.2, equation (2.17)), the model determines PDIV as the lowest total voltage $V_{\text{air}} = V_{\text{B}}$ for varying air gap sizes (equation (4.4)).

$$V = \left(\frac{V_{\text{air}}}{d_{\text{air}}} \right) \left(d_{\text{air}} + \frac{t_{\text{ins}_1}}{\varepsilon_{\text{r ins}_1}} + \frac{t_{\text{ins}_2}}{\varepsilon_{\text{r ins}_2}} + \ldots \right) \tag{4.3}$$

$$\text{PDIV} = min\left[\left(\frac{V_\text{B}}{d_\text{air}}\right)\left(d_\text{air} + \frac{t_{\text{ins}_1}}{\varepsilon_{\text{r ins}_1}} + \frac{t_{\text{ins}_2}}{\varepsilon_{\text{r ins}_2}} + ...\right)\right] \tag{4.4}$$

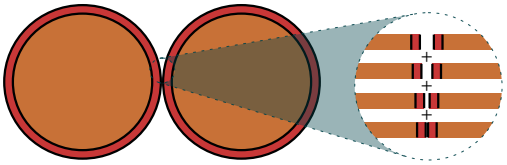

Figure 4.14: *Simplified representation of the twisted pair configuration as an array of parallel-plate capacitors.*

where V is the voltage between conductors, V_air is the voltage across the air gap, d_air is the thickness of the air gap, V_B is the air breakdown voltage as defined in equation (2.17), and t_{ins_i} and $\varepsilon_{\text{r ins}_i}$ denotes the thickness and the relative permittivity of each insulation layer, respectively.

Since Paschen's Law formed the basis of equation (4.4), its limitations discussed in Section 2.3.2 regarding the ambient conditions are inherent to this model. Indeed, based on the information available to the author, the effect of those conditions on the air breakdown was not considered when this model was applied previously in the literature.

4.2.1.3 Lusuardi's Equation, Estimation Based on Reference PDIV

Based on experimental PDIV measurements at varying pressure levels using 50 Hz AC, L. Lusuardi et al. [76] developed an analytical model to estimate PDIV under different pressure and temperature levels. Initially, an empirical equation was derived through linear regression, correlating PDIV values with the logarithm of pressure (in bar). Given that ionisation is governed by the mean free path, which is inversely related to the number density of gas molecules per cubic meter, the results were later expressed in terms of number density. Since this parameter depends on both pressure and temperature, equation (4.5) was formulated normalised to reference conditions.

$$\frac{\text{PDIV}_{P_\text{new},T_\text{new}}}{\text{PDIV}_\text{ref}} = 1 + 0.299\ \ln\left(\frac{P_\text{new}}{P_\text{ref}}\frac{T_\text{ref}}{T_\text{new}}\right) + 0.0446\ \ln\left(\frac{P_\text{new}}{P_\text{ref}}\frac{T_\text{ref}}{T_\text{new}}\right)^2 \tag{4.5}$$

where $\text{PDIV}_{P_\text{new},T_\text{new}}$ represents the estimated PDIV at a given pressure and temperature, while PDIV_ref corresponds to the measured PDIV under reference conditions. P_ref and T_ref indicate the reference pressure and temperature, whereas P_new and T_new are the conditions at which PDIV is being estimated (pressure in Pa, temperature in K).

This model was developed because Paschen's curve did not accurately capture the observed PDIV dependence on pressure. Nonetheless, the author acknowledged its limitations, particularly when relative permittivity exhibits a strong dependency on temperature.

4.2.1.4 Färber's Equation

R. Färber et al. [68] proposed a PDIV model for TPs based on the parallel-plate equation, incorporating the reduced coating thickness ($t_{\text{ins}}/\varepsilon_{\text{r ins}}$) within Townsend's breakdown theory under standard atmospheric conditions and negligible overshoot. The model presents a simplified equation (4.6) (PDIV is in V and t_{ins} in µm) achieving a relative error below 1.3% for $t_{\text{ins}}/\varepsilon_{\text{r ins}}$ in the 4-50 µm range.

$$\text{PDIV} = 4.64\ 10^{2} + 4.66\ 10^{1}\frac{t_{\text{ins}}}{\varepsilon_{\text{r ins}}} - 6.16\ 10^{-1}\left(\frac{t_{\text{ins}}}{\varepsilon_{\text{r ins}}}\right)^{2} + 5.08\ 10^{-1}\left(\frac{t_{\text{ins}}}{\varepsilon_{\text{r ins}}}\right)^{3} \tag{4.6}$$

A key contribution of this work is the parametrisation of the effective secondary electron emission coefficient ($\bar{\gamma}$), which accounts for both cathode-driven secondary electrons and those produced via photo-ionisation (as defined in Section 2.3.2) in the gas bulk. The proposed expression (equation (4.7)) integrates ion and photon feedback, considering the ion-enhanced field emission of secondary electrons. The model also introduces an effective ionisation coefficient ($\bar{\alpha}$, equation (4.8)) dependent on the applied electric field. Although environmental conditions are not explicitly accounted for, the same author applied a fixed value of $\bar{\gamma} = 0.0025$, corresponding to a gap distance range from 20 µm to 1 mm for metallic electrodes under atmospheric conditions (obtained from equation (4.7)), to estimate the PDIV of TP at varying humidity levels.

$$\bar{\gamma} = \gamma_{+} + \gamma_{\text{ph}}\frac{1}{1-\frac{\eta_{\text{ph}}}{\bar{\alpha}}}\text{e}^{-\eta_{\text{ph}}d_{\text{air}}} + \gamma_{\text{FE}}\text{e}^{-\frac{D}{E}} \tag{4.7}$$

$$\bar{\alpha} = 910\cdot 10^{3}\text{e}^{-\frac{E_{\text{th}}}{E}} + 23\cdot 10^{-6}E - 6338\cdot 10^{3}\text{e}^{-\frac{E-E_{\text{crit}}}{E''_{\text{th}}}} \tag{4.8}$$

In the previous equations, γ_{+} represents the secondary electron emission coefficient due to positive ions (assumed 0 for large gaps), γ_{ph} corresponds to the secondary electron emission coefficient from photoelectric effect at the cathode ($1.5\cdot 10^{-3}$), while γ_{FE} accounts for ion-enhanced field emission (0.9). The photon absorption coefficient is denoted as η_{ph} (800 m^{-1}), and $\bar{\alpha}$ (equation (4.8)) represents the effective ionisation coefficient (m^{-1}). The gap length is given by d_{air} (m), while D is the field emission onset threshold ($178\cdot 10^{6}$ V m^{-1}), and E denotes the electric field (V m^{-1}). The threshold electric field value below which ionic space charge enhances the ionisation yield of secondary avalanches is E_{th} ($25.5\cdot 10^{6}$ V m^{-1}), whereas E_{crit} ($2.42\cdot 10^{6}$ V m^{-1}) defines the minimum electric field required for $\bar{\alpha} > 0$ ($E''_{\text{th}} = 50\cdot 10^{6}$ V m^{-1}). All values correspond to standard atmospheric conditions.

The study further suggests that the transition from Townsend to Streamer breakdown occurs gradually, around a 2 cm gap length, where cathode-driven secondary emission becomes ineffective. When $\eta_{\text{ph}} \geq \bar{\alpha}$, photon feedback is suppressed, shifting the dominant

secondary process from cathode-driven emission to gas ionisation. With the increasing gap width, photo-ionisation within the gas bulk gains relevance, promoting the single-avalanche Streamer mechanism. The feasibility of electron generation from polymers is also highlighted, as their work function (4-5.5 eV) is comparable to that of metallic electrodes (4-5 eV for copper). Other aspects, such as the use of the straight-line distance between wires and the applicability of Townsend's mechanism in non-uniform or quasi-uniform fields, are also examined. The findings indicate that these considerations are suitable for PDIV estimation in TPs.

As the author concludes, while temperature effects can be incorporated by adjusting parameters such as $\varepsilon_{\mathrm{r\ ins}}$, the model has yet to be extended to varying temperature, pressure, and humidity conditions. Additionally, it assumes discharges under negligible overshoot, limiting its applicability in more dynamic electrical environments.

4.2.1.5 Wei's Equation, Estimation Considering Rise Time and Pulse Width

Based on Extended Volume-Time theory, explained later in Section 4.2.2.3, Wei et al. [102] developed a model to estimate PDIV for a single pulse, incorporating rise time and pulse width. By approximating the initial electron generation probability (equation (4.9)) as the cumulative PD probability $Prob$, they determined this probability from experimental PDIV values and the time delay between the applied voltage reaching inception and PD occurrence (Figure 4.10).

$$Prob = 1 - e^{-A(t-t_0)} \tag{4.9}$$

$$Prob = 1 - e^{-A\left(t-\frac{V_{\mathrm{inc}}t_{\mathrm{r}}}{0.8V}\right)} \tag{4.10}$$

where A represents the effective electron contribution from the air volume and enamel surface, while t_0 corresponds to the ionisation initiation time. Under consistent environmental conditions, t_0 aligns with the moment when the applied voltage (V) equals the inception voltage (V_{inc}). The rise time (t_{r}) is defined between 10% and 90% of the V, thus, 0.8 factor is introduced. Consequently, equation (4.9) is rewritten as (4.10).

To facilitate the determination of the parameter A, equation (4.11) was proposed, using equation (4.10) alongside experimental PDIV values (when the probability is 50%), and delay time data, where V, t_{r} are in kV and ns, respectively.

$$A = 1.038\ V^{7.542}\ 211.4\ t_{\mathrm{r}}^{(-1.149)} \tag{4.11}$$

Since the critical number of electrons necessary to trigger PD was relatively stable regardless of pulse width and rise time, equation (4.12) was formulated (t_{w} in µs). Hence,

the number of critical electrons N_{cr} can be described by the equation (4.12). As the term $\frac{V_{inc}t_r}{0.8V}$ is negligible compared to the pulse width, combining equations (4.11) and (4.12), PDIV can then be written as equation (4.13). For simplification, an alternative formulation was proposed in equation (4.14).

$$N_{cr} = A\left(t_w - \frac{V_{inc}t_r}{0.8V}\right) \tag{4.12}$$

$$\text{PDIV} = \left(\frac{N_{cr}}{1.038 \cdot 211.4}\right)^{\frac{1}{7.542}} t_w^{-\frac{1}{7.542}} t_r^{-\frac{-1.149}{7.542}} \tag{4.13}$$

$$\text{PDIV} = \text{PDIV}_{t_w=100\mu s, t_r=120ns}\left(\frac{t_w}{100}\right)^{(-0.1142)}\left(\frac{t_r}{120}\right)^{0.01818} \tag{4.14}$$

This model is valid under conditions without overshoot in the applied waveform or space charge accumulation. The authors noted that space charge distribution varies with rise time, influencing the electron generation rate. Moreover, as the model was developed for a specific enamel material at room temperature, its constants may require recalibration for different insulation materials and temperature conditions.

4.2.2 FEM Simulation-Based Models

All methods that involve FEM analysis to determine electric field distribution between two insulated wires (round or rectangular) use geometries defined in Figure 4.15. Generally, the most critical situation of interturn insulation, where one conductor is subjected to high voltage (HV, defined as peak voltage) and the other to 0 V (GND), without impregnation, is considered in these simulations. In this setup, $\varnothing_{copper}$ represents the nominal diameter of the conductor for round conductors, whereas w_{copper} and h_{copper} define the nominal width and height of the rectangular conductors. t_{ins} is the insulation thickness, d_0 is the minimum separation between wires, d_s is the straight horizontal distance between conductors, and d_e is the length of the constant electric field path. The voltage distribution across the air gap is then computed over the defined gap distance (either d_s or d_e).

4.2.2.1 Using Paschen's Law

For PDIV estimations using FEM combined with Paschen's Law, simulations are conducted for varying voltage levels. The computed voltage distribution across the air gap is compared against Paschen's curve (Figure 4.16). If the FEM-derived voltage curve ($V - d$) intersects Paschen's curve, PD activity is expected. If no intersection occurs, PD

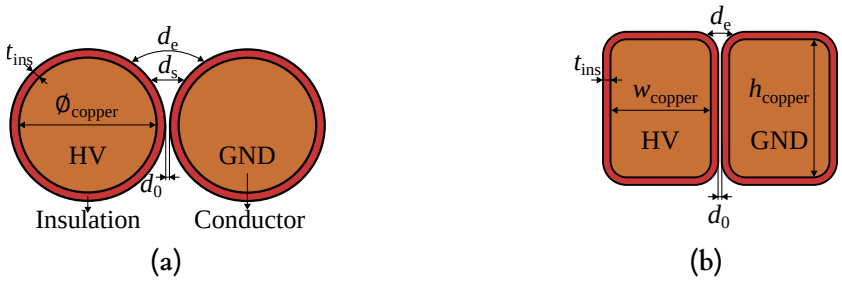

Figure 4.15: *Simplified geometries of interturn insulation used in FEM simulations for (a) round conductors, and (b) rectangular conductors.*

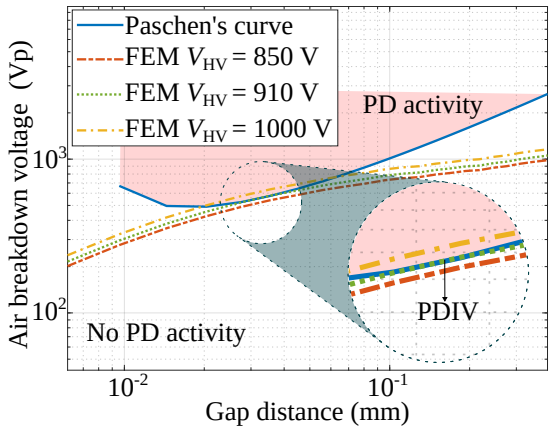

Figure 4.16: *Schematic representation of FEM-based PDIV estimation using Paschen's curve.*

does not initiate. Consequently, PDIV is defined at the voltage level where the FEM $V - d$ is tangential to Paschen's curve, as shown in Figure 4.16.

Some researchers have extended their models by incorporating permittivity variations and temperature corrections to improve accuracy. [81] implemented such modifications by adjusting temperature-dependent air breakdown voltage (correcting Paschen's curve) and insulation relative permittivity. To represent the influence of humidity, [94] included a 2 µm water film on the enamel surface in the FEM model.

A key discrepancy among models lies in defining the air gap distance d_s or d_e to get the $V - d$ curve obtained from FEM. Some studies [81, 120, 126, 127] defined d_{air} as the straight-line separation between conductor surfaces (d_s on Figure 4.15), yielding errors of 2-5%. Others, [122, 128] argued that the electric field path length (d_e on Figure 4.15) better represents the electron trajectory, estimating the effective gap distance through the polynomial fitting of the FEM-computed constant electric field lines distribution. Even so, the difference between the d_e and d_s length is generally below 1% for low distances, while increases to about 7% for distances higher than 50 µm [120].

Another critical factor in PDIV estimation is Townsend's secondary ionisation coefficient (γ in Paschen's equation (2.17)). While $\gamma = 0.01$ is commonly used for metallic electrodes [129], polymeric enamelled TPs require adjustment for improved agreements with experimental data. For instance, [119] found that $\gamma = 0.001$ provided the best fit for

measurements on PEI+PAI enamel combinations.

To refine γ estimation, [126] proposed an interactive approach by obtaining the $V-d$ curve from FEM when experimentally measured PDIV was applied in HV conductor (using d_s) and adjusting γ until the Paschen's curve matched the FEM-derived $V-d$ curve. This method yielded in $\gamma = 0.0006$ for PAI overcoat samples (the average considering several insulation thicknesses), with negligible variation across different conductor diameters. A similar strategy was adopted in [122], where constant electric field lines d_e were used, leading to an estimation of $\gamma = 0.0078$ for several enamel materials based on the average of multiple wire diameters and permittivity values. In a different approach, [129] integrated FEM-calculated electric field lines and scalar potential into a self-developed software to interpolate γ within a range of 10^{-6} to 10^{-2} based on experimental PDIV values. Table 4.4 collects the γ values established in the literature for several materials.

Table 4.4: *γ values proposed in the literature for FEM simulation based PDIV estimation using Paschen's Law.*

Material	T (°C)	γ (-)	Ref.
G	25–150	0.0078	[122]
PEI+PAI	25	0.001	[119]
PAI	25	0.0006	[126]
PI	25–200	0.00065	[129]
Metallic electrodes and polymers	25	0.0025	[68]

Generalised for several materials (G)

Considering the potential temperature dependence on γ, [122] reported a decreasing trend with rising temperature (100–150 °C), though variations in insulation material and manufacturer were more influential. Conversely, [129] observed a slight increase in γ with temperature. Even so, using γ values approximated at 20 °C for higher temperatures (up to 200 °C) led to negligible differences in PDIV, aligning with the findings of [122]. As noted by [68], the observed temperature dependence may, at least in part, be misattributed to variations in γ. This does not necessarily mean that γ cannot inherently vary with e.g. temperature, but rather that fundamental physical mechanisms, such as changes in the $\varepsilon_{\mathrm{r\,ins}}$ with temperature, are not always fully accounted for.

Although this methodology can consider temperature, pressure, and humidity, its main challenges include the higher computational cost compared to analytical models and the necessity of experimental results for the γ adjustment, particularly for different insulation materials.

4.2.2.2 Using Schumann's Criterion

Although Paschen's Law has been widely used for PDIV estimation with accurate results [119, 126–128], some studies indicate that the Streamer inception mechanism

provides a more realistic representation of PD behaviour [121]. The primary limitation arises from the non-uniform field distribution in TPs, which challenges the applicability of Townsend's mechanism. Additionally, the insulating layer covering TP electrodes makes secondary electron emission from the cathode (γ) highly improbable, according to [121]. Consequently, Townsend's discharge mechanism, and thus Paschen's Law (Section 2.3.2) are deemed inadequate for PDIV prediction and should be substituted with the Streamer inception mechanism and Schumann's criterion [121] (Section 2.3.3).

Accordingly, Lusuardi et al. [121] developed a methodology integrating FEM simulations with Schumann's criterion to estimate PDIV under various temperature conditions. As explained in Section 2.3.3, PD occurs when the electron population along a field line meets the Schumann's constant K_{Sch}. While typically set between 18 and 20 for air, similar to γ, K_{Sch} must be adjusted for PDIV estimation [121].

To determine an optimal value, an iterative approach was applied, analogous to γ adjustments. Instead of fitting the Paschen's curve to the FEM-derived $V - d$ curve, the integral in equation (2.23) was evaluated, progressively reducing K_{Sch} from 18 until at least one field line (FEM-derived applying experimental PDIV value) satisfied $\int_0^{d_e} \bar{\alpha} dx \geq K_{\text{Sch}}$. Gas ionisation parameters were incorporated as a function of the specific electric field, resulting in an average K_{Sch} of 5.98 across different wire diameters and enamel permittivities, with a maximum PDIV estimation error of 9% at 25 and 150 °C [121].

Building on this methodology, [130] examined the influence of different waveforms and pressures on K_{Sch} in rectangular conductors. Their results show that K_{Sch} remained largely stable across a pressure range of 10–1013 mbar when the same waveform was applied. The obtained K_{Sch} values, summarised in Table 4.5, led to a maximum PDIV estimation error of 4%. Furthermore, in a separate study [131], the same authors proposed an equation for K_{Sch} as a function of pressure, varying based on the statistical method used to define PDIV. For instance, distinct equations were established for the mean PDIV and the 10^{th} percentile of the two-parameter Weibull distribution (B10). Additionally, [132] reported that K_{Sch} remains constant within a temperature range of 20–120 °C. Further research by the same authors investigated the combined effects of temperature and humidity, introducing additional equations for K_{Sch} and achieving PDIV estimation errors below 7% [87].

The study [133] extended this methodology to phase-phase and groundwall insulations for different materials, using FEM models illustrated in Figure 4.17. Their study confirmed that, while K_{Sch} was independent of the insulation thickness, was dependent on the insulation material and type. The reported K_{Sch} values, summarised in Table 4.5, resulted in a maximum PDIV estimation error of 1.48% at ambient temperature and 10.49% at 180 °C.

To assess the accuracy of using Paschen's Law or Schumann's criterion for PDIV estimation, [30] conducted a comparative analysis combining each criterion with FEM simulations, as outlined in [122] and [121], respectively. At room temperature, Paschen's Law presented a lower prediction error (2.36%) compared to Schumann's criterion (4.19%).

Table 4.5: *K_{Sch} values proposed in the literature for FEM simulation based PDIV estimation using Schumann's criterion.*

Insulation	Material	T (ºC)	RH (%)	P (mbar)	Waveform	K_{Sch} (-)	Ref.
Interturn (TP)	G	25-150	-	-	AC-50 Hz	5.98*	[121]
Interturn (PC)	PAI	25	14-60	10-1013	AC-50 Hz	5.43*	[130]
	PAI	25	14-60	10-1013	Bipolar	5.67*	[130]
	PAI	25	14-60	10-1013	Unipolar	9.4*	[130]
Interturn (TP)	PEI+PAI	25	30-90	-	AC-50 Hz	$-1.5RH + 5.85$*	[87]
	PEI+PAI	40	20-90	-		$-1.34RH + 5.95$*	[87]
	PEI+PAI	60	20-90	-		$-0.43RH + 5.86$*	[87]
	PEI+PAI		20-40	-		$1.62RH + 5.88$*	[87]
	PEI+PAI	90	40-50	-		$-34.08RH + 20.16$*	[87]
	PEI+PAI		50-90	-		$1.10RH + 2.55$*	[87]
	PEI+PAI	40	13	100-1000		$-0.003P + 9.0432$*	[131]
	PEI+PAI					$-0.0021P + 7.9754$**	[131]
Interturn (PC)	PI-FEP	25	-	-	AC-50 Hz	4.76	[133]
Phase-phase	Nomex and NMN	25	-	-	AC-50 Hz	4.76	[133]
	Kapton	25	-	-		8.65	[133]
Phase-ground	Nomex and NMN	25	-	-	AC-50 Hz	3.58	[133]
	Kapton	25	-	-		7.79	[133]

Generalised for several materials (G); Nomex-Mylar-Nomex (NMN); * Obtained from B10 PDIV; ** Obtained from mean PDIV.

However, at 150 ºC, the error difference was negligible, with reported values of 7.05% and 7.16%, respectively. In humid environments, which neither model accounted for, the error increased to 15%, suggesting that external uncertainties introduce greater deviations than the choice of criterion.

This method faces similar challenges to those encountered with the FEM approach using Paschen's Law, including high computational costs and the need for experimental data to adjust K_{Sch} for different material and environmental conditions.

4.2.2.3 Using Volume-Time Theory

Both, analytical and FEM-based models previously explained adopt a deterministic approach, assuming that PD occurs when specific conditions are met. However, this assumption does not always hold when overshoot is presented, as the time for which the applied voltage remains above the inception level is crucial for the availability of electrons. If the duration of the overshoot is too brief, the probability of having available electrons is low, even if the applied voltage exceeds the inception threshold (as discussed in Sections 2.3.4 and 4.1). To address this limitation, probabilistic PDIV estimation models incorporate both, electron availability probability and the inception voltage condition, analysing the applied voltage evolution over time. Within this framework, Volume-Time theory estimates discharge inception by considering the temporal and spatial variation of

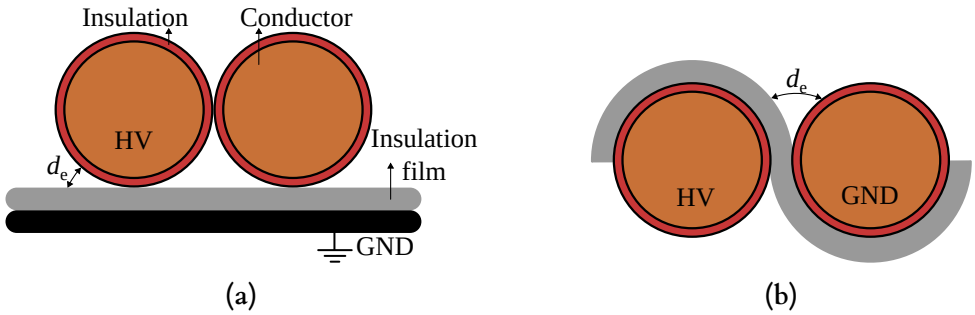

Figure 4.17: *Simplified geometries used in FEM simulations proposed in [133] for (a) groundwall insulation, and (b) phase-phase insulation.*

the electric field in the air gap.

Expanding upon this concept, [63] introduced the Extended Volume-Time theory, which, in addition to electron detachment within the air gap, also considers electron availability (*Prob*), which is computed as in equation (4.15), with PDIV defined at the 50% probability threshold.

$$Prob(t) = 1 - e^{\int (R_V(t) + R_S(t))\mathrm{d}t} \tag{4.15}$$

$$R_V(t) = \int_{V_{cr}} r_V \left(1 - \frac{\eta}{\alpha}\right) \mathrm{d}V \tag{4.16}$$

$$R_S(t) = \int_{S_{cr}} r_S \left(1 - \frac{\eta}{\alpha}\right) \mathrm{d}S \tag{4.17}$$

where $R_V(t)$ represents the contribution from the air gap (equation (4.16)), and $R_S(t)$ accounts for initial electrons on the enamel surface (equation (4.17)). The parameters α and η denote the electron impact ionisation and attachment coefficients. The variables V_{cr} and S_{cr} define the critical air gap volume and enamel surface area, while r_V (equation (4.18)) and r_S (equation (4.19)) are the respective electron generation rates.

$$r_V = k_d \, n^- \tag{4.18}$$

$$r_S = a \, E^2 \, e^{-\frac{b}{E}} \tag{4.19}$$

where n^- is the oxygen ion density, assumed constant in space and time, and k_d is the expected electron impact ionisation frequency, dependent on the electric field strength. The constants a and b are experimentally derived based on Fowler-Nordheim's equation [134].

While r_V stabilises with increasing field strength, r_S exhibits a sharp rise, highlighting the significant role of the enamel surface in electron generation [63].

The determination of V_{cr} and S_{cr} requires FEM analysis, where Schumann's criterion must be satisfied (equation (2.23)). However, the study does not specify the definition of Schumann's constant, a crucial parameter, as highlighted in Section 4.2.2.2. Both, V_{cr} and S_{cr} increase with stronger electric fields.

This model enables PDIV estimation for waveforms with overshoot, and different rise time and pulse width configuration, making it particularly relevant for interturn insulation exposed to high overshoots derived from WBG-converter signals. However, its applicability under varying environmental conditions, such as the temperature effects, remains unexplored.

4.2.3 Summary of PDIV Estimation Models

To ensure reliable insulation design in electric machines and prevent PD activity over their lifetime, PDIV prediction models must consider key influencing factors. Section 4.1 highlights stronger evidence that environmental conditions (temperature, humidity, and pressure) have a more significant impact on PDIV than waveform parameters. The standard further indicates that measurements using sinusoidal signals are equivalent to those obtained with impulse waveforms for common insulation samples such as TPs and motorettes, widely used in insulation system evaluation [9]. It was also shown in Section 4.1.4 that in the comparison of sinusoidal and unipolar negative rectangular waveform, the difference generally lies below the 10%, even with an estimated overshoot of 20% for the unipolar waveform. Taking this into account, while some models incorporate rise time, pulse width, or overshoot consideration in PDIV predictions, most focus on sinusoidal waveforms. Indeed, if the operation overshoot voltage does not overcome the PDIV of the designed insulation, PD activity should be uncommon.

Most PDIV estimation models are developed for TPs or PCs, which are commonly used in electric vehicle windings. As discussed in previous sections and summarised in Table 4.6, these models integrate environmental factors such as pressure, temperature, and humidity and are either analytical or rely on FEM electrostatic analysis combined with Paschen's or Schumann's criteria. While these methods provide accurate PDIV predictions under varying temperatures and humidity (with pressure variations being less critical for EV applications), they have notable limitations:

- **Estimation of γ or K_{Sch}:** These constants are key parameters in air breakdown and depend on the assumed PD inception mechanism. In Townsend's breakdown model, γ represents the secondary electron coefficient, which influences the density of secondary electron avalanches. In the Streamer mechanism, K_{Sch} defines the critical number of electrons required to initiate PD.

  Despite their significance, no universal agreement exists regarding their values for PDIV estimation [68, 122, 126]. Although [68] parametrises γ and demonstrates

that a value of 0.0025 (derived from metallic surfaces) can accurately estimate PDIV between polymer surfaces in gap distances ranging from 20 µm to 1 mm under standard conditions, most studies conclude that these constants require adjustment for each specific material or even manufacturer [126]. Consequently, various methodologies exist for their estimation, primarily relying on experimental calibration [121, 122, 126].

- **Computational cost:** When FEM simulations are used, PDIV estimation can be computationally expensive, regardless of whether Paschen's or Schumann's criteria is applied.
- **Dependence on experimental data:** Many models require experimental measurements, which may be challenging if appropriate equipment is unavailable. This dependency complicates parameter adjustments (e.g., γ or Schumann's constant) and the estimation of PDIV under various environmental conditions, as required in Lusuardi's model [76].

Table 4.6: *Summary of PDIV estimation models proposed in the literature.*

Model	Used data	Considered variables					Pros	Cons	Ref.
		T	*P*	*HR*	t_r	t_w			
Dakin	$\varepsilon_{r\,ins}$ and t_{ins}	✓*	x	x	x	x	Simple and ↓ computational cost	Room conditions	[81, 119, 123, 135]
Parallel plate	$\varepsilon_{r\,ins}$, t_{ins}, A, B, γ, and d_{air}	x	x	x	x	x	Simple and ↓ computational cost	Room conditions. Difficult to define γ	[119]
Lusuardi	T_{ref}, P_{ref}, and $PDIV_{ref}$	✓**	✓	x	x	x	Simple and ↓ computational cost	Not valid for high $\varepsilon_{r\,ins}$ change with T. Necessity of an experimental ref. PDIV	[76]
Färber	$\varepsilon_{r\,ins}$ and t_{ins}	✓*	x	x	x	x	Simple and ↓ computational cost	Room conditions	[68]
Wei	$\varepsilon_{r\,ins}$, t_{ins}, and $PDIV_{ref}$	x	x	x	✓	✓	Simple and ↓ computational cost	Room conditions. Necessity of an experimental ref. PDIV	[102]
FEM Paschen's straight lines	$\varepsilon_{r\,ins}$, t_{ins}, A, B, γ, and d_{air}	✓	✓	✓	x	x	Apparently more accurate than analytical models	↑ computational cost. Difficult to define γ	[81, 120, 126, 127]
FEM Paschen's E lines	$\varepsilon_{r\,ins}$, t_{ins}, A, B, γ, and d_{air}	✓	✓	x	x	x	Apparently more accurate than analytical models	↑↑ computational cost. Difficult to define γ	[122]
FEM Schumann's E lines	$\varepsilon_{r\,ins}$, t_{ins}, $\bar{\alpha}$, K_{Sch}, and d_{air}	✓	✓	✓	x	x	Apparently more accurate than analytical models	↑↑ computational cost. Difficult to define K_{Sch}	[87, 121, 130–133]
Extended Volume-Time theory	$\varepsilon_{r\,ins}$, t_{ins}, d_{air}, $R_V(t)$, and $R_S(t)$	x	x	x	✓	✓	Independent of overshoot. Temperature and pressure correction can be implemented	↑↑ computational cost. Difficult to define K_{Sch}	[63, 102, 136]

* Only consider change in $\varepsilon_{r\,ins}$; ** Only consider change in air properties; $\varepsilon_{r\,ins}$: relative permittivity; t_{ins}: insulation thickness; A: experimental constant for Paschen's curve (for air 11.25 $Pa^{-1}m^{-1}$) , B: experimental constant for Paschen's curve (for air 11.25273.75 $VPa^{-1}m^{-1}$), γ: Townsend's secondary electron emission coefficient, d_{air}: path followed by the electronic avalanche, T_{ref}: temperature for a reference PDIV measurement, P_{ref}: pressure for a reference PDIV measurement, $PDIV_{ref}$: reference PDIV measurement, $\bar{\alpha}$: effective ionisation coefficient of the anode, K_{Sch}: Schumann's criterion constant, $R_V(t)$: air gap volume initial electrons, $R_S(t)$: enamel surface initial electrons

4.3 Contributions to the Estimation of Partial Discharge Inception Voltage

Considering the limitations identified in the literature review, the objective of the contributions to interturn PDIV estimation models was to develop a model that provides accurate predictions within a reduced computational time while avoiding the need for fitting the model to specific samples. These approaches aimed to enable a direct PDIV estimation without requiring extensive experimental calibration or parameter adjustments, enhancing its applicability to a wide range of insulation systems. Special attention was given to temperature and humidity, as pressure is not a critical parameter for EV applications.

In the development of the work described in the following section, several datasets were required. Each datasets contains experimental PDIV results for different insulation materials and thicknesses, and measurement environmental conditions. In total, four datasets were used. Two of them, referred to as Derivation Temperature (DT) and Derivation Absolute Humidity (DAH), were employed to develop the Extended Dakin's equations (presented later in Section 4.3.2). The other two, referred to as Validation Temperature (VT) and Validation Absolute Humidity (VAH), were used for validating the Extended Dakin's equation and for comparing different models for PDIV estimation (described in Section 4.3.3).

Importantly, the datasets used for equation development were not included in the model validation or comparison to prevent bias in favour of the Extended Dakin's model, thereby ensuring a fair and objective evaluation. A summary of each dataset is provided in Table 4.7, including the dataset name, number of data points, references to where the samples and PDIV results are detailed in the document, and the specific section and purpose for which each dataset was used.

Table 4.7: *Description of the datasets employed in the contribution to the estimation of PDIV.*

Name	Size	Description in	Utilisation in
DT	45	Section 3.1.1 and Appendix A.1.1	Extended Dakin's temperature model derivation in Section 4.3.2.1
DAH	117	Section 3.1.1 and Appendix A.2.1	Extended Dakin's absolute humidity model derivation in Section 4.3.2.2
VT	127	Appendix A.1.2	Extended Dakin's temperature model validation in Section 4.3.2.1 and PDIV estimation model comparison in Section 4.3.3
VAH	118	Appendix A.2.2	Extended Dakin's absolute humidity model validation in Section 4.3.2.2 and PDIV estimation model comparison in Section 4.3.3

4.3.1 Extended Parallel-Plate Equation

The parallel-plate equation has been used to estimate PDIV under standard environmental conditions in studies such as [119] and [68]. It seems to be a good candidate for predicting PDIV with good accuracy while avoiding heavy FEM simulations. However, as discussed in Section 4.2.1.2, the application of Paschen's curve limits its accuracy when extended environmental conditions are considered. This limitation could potentially be addressed using the Peek (equation (2.19)) or Dunbar (equation (2.20)) corrections, as outlined in Section 2.3.2 for gas breakdown. To the best of the author's knowledge, these corrections have not previously been validated in the context of the parallel-plate equation. Applying these modifications, equation (4.4) leads to equation (4.20) with Peek correction, and to equation (4.21) with Dunbar correction.

$$\mathrm{PDIV} = min\left[\frac{\frac{P_{\mathrm{new}}}{P_{\mathrm{ref}}}\frac{T_{\mathrm{ref}}}{T_{\mathrm{new}}}B\frac{P_{\mathrm{ref}}\,d_{\mathrm{air}}}{\ln\left(\frac{AP_{\mathrm{ref}}\,d_{\mathrm{air}}}{\ln\left(1+\frac{1}{\gamma}\right)}\right)}}{d_{\mathrm{air}}}\left(d_{\mathrm{air}}+\frac{t_{\mathrm{ins}_1}}{\varepsilon_{\mathrm{r\ ins}_1}}+\frac{t_{\mathrm{ins}_2}}{\varepsilon_{\mathrm{r\ ins}_2}}+\ldots\right)\right] \tag{4.20}$$

$$\mathrm{PDIV} = min\left[\frac{B\frac{P_{\mathrm{ref}}\frac{T_{\mathrm{ref}}}{T_{\mathrm{new}}}\,d_{\mathrm{air}}}{\ln\left(\frac{AP_{\mathrm{ref}}\frac{T_{\mathrm{ref}}}{T_{\mathrm{new}}}\,d_{\mathrm{air}}}{\ln\left(1+\frac{1}{\gamma}\right)}\right)}}{d_{\mathrm{air}}}\left(d_{\mathrm{air}}+\frac{t_{\mathrm{ins}_1}}{\varepsilon_{\mathrm{r\ ins}_1}}+\frac{t_{\mathrm{ins}_2}}{\varepsilon_{\mathrm{r\ ins}_2}}+\ldots\right)\right] \tag{4.21}$$

Figure 4.18 compares the experimental results obtained for sample TP2 (Section 3.1), measured between 20–260 °C as described in Section 3.3.1, with the PDIV estimations obtained using the Extended parallel-plate model with Dunbar (equation (4.21)) and Peek (equation (4.20)) corrections. Given that TP2 is insulated with PI enamel, $\gamma = 0.00065$ was used, as proposed in [129] for this material. The results indicate that applying Dunbar correction leads to a maximum error of 12%, while Peek correction results in significantly higher deviations, with a maximum error of 30%. The superior accuracy of Dunbar correction over Peek has also been reported in [66, 67] for gas breakdown.

These findings demonstrate that incorporating Dunbar correction (equation (4.21)) into the parallel-plate model (equation (4.4)) allows for a reasonable estimation of PDIV across different temperatures. Moreover, the accuracy achieved is comparable to that reported in [122] for PDIV estimation using FEM-based models, which yielded a maximum error of 11%. However, applying this model to other materials may require a different γ value, which poses a limitation due to the challenges in accurately defining this parameter [126].

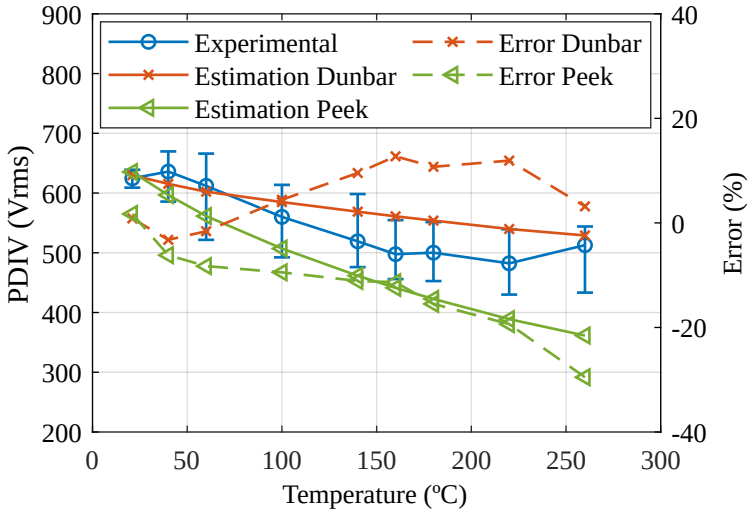

Figure 4.18: *Comparison of experimental measurements and Extended parallel-plate estimation using Dunbar and Peek corrections for sample TP2 considering* $\gamma = 0.00065$ *(proposed for PI in [129]).*

4.3.2 Extended Dakin's Equations

As previously stated, given the constraints of most existing models, there is a clear need for a simplified approach capable of estimating PDIV across different environmental conditions without requiring FEM simulations or experimental calibration. The Extended parallel-plate equation discussed in Section 4.3.1 has demonstrated good accuracy while avoiding FEM simulations, thereby reducing computation time. However, it still faces the limitation of requiring an appropriate definition of γ to ensure accurate predictions.

As discussed in Section 4.2.1.1, the Dakin's equation [123] is among the simplest models in the literature that does not require fitting to a specific sample, though its applicability is limited to standard environmental conditions. A similar approach is employed in SAE AS50881H [124] for circular wires in aerospace applications, with multiple curves accounting for different temperature and pressure conditions. However, its applicability to rectangular conductors remains unknown.

Building on the straightforward estimation of PDIV using t_{ins} and $\varepsilon_{\text{r ins}}$, and considering the growing use of rectangular conductors in electric vehicles [81], the following section presents novel PDIV models. These models incorporate temperature, humidity, t_{ins}, and $\varepsilon_{\text{r ins}}$ for both round and rectangular wires, eliminating the need for FEM simulations or experimental calibration.

4.3.2.1 Temperature Consideration

To develop the Extended Dakin's temperature model, DT dataset was used (Table 4.7), which collects PDIV measurements as described in Section 3.3.1 developed at 20, 100,

and 180 °C for the samples from Table 3.1 (Section 3.1.1). Figure 4.19 illustrates the experimental PDIV values as a function of the $t_{ins}/\varepsilon_{r\,ins}$ ratio at 20, 100, and 180 °C, showing the average value along with the maximum and minimum variations. All results are also collected in Appendix A.

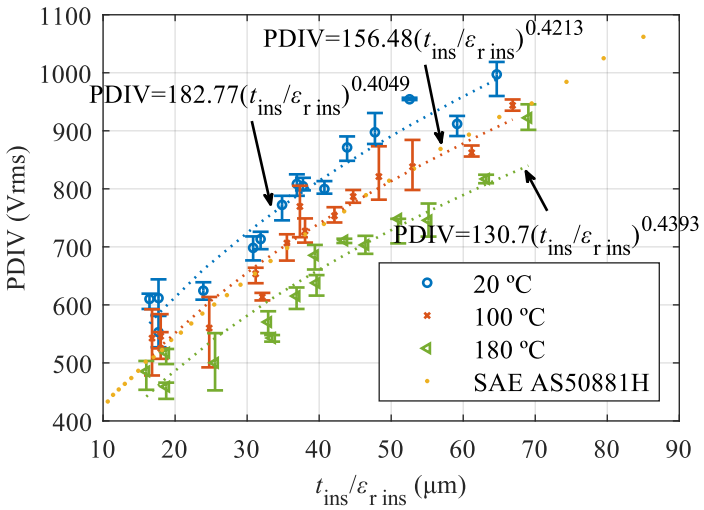

Figure 4.19: *Experimental results of PDIV evolution depending on $t_{ins}/\varepsilon_{r\,ins}$ for DT dataset at 20, 100, and 180 °C, and sea level 100 °C curve from SAE AS50881H [124].*

As widely reported in the literature (Section 4.1.1.2), PDIV decreases with increasing temperature due to the reduction in air breakdown voltage [70, 81, 121, 122, 137]. This trend persists even when the relative permittivity of the insulation decreases with temperature, which could theoretically increase PDIV. As discussed in Section 4.1.1.2, the influence of temperature on air properties outweighs its effect on $\varepsilon_{r\,ins}$. Consequently, PDIV remains primarily dependent on air breakdown strength, leading to a consistent decrease with rising temperature, regardless of variations in the relative permittivity of the material.

In agreement with previous studies, the experimental PDIV results presented in Figure 4.19 also decrease as the insulation thickness-to-relative permittivity ratio decreases [81, 119, 123]. Additionally, the 100 °C PDIV values obtained for both TPs and PCs align with the sea-level 100 °C curve from SAE AS50881H [124], which was originally developed for round wires. This suggests that the $t_{ins}/\varepsilon_{r\,ins}$ ratio could serve as a reliable predictor for PDIV, regardless of conductor geometry.

To further refine the analysis, the obtained PDIV values were fitted to power-law curves for each tested temperature. The equations derived from these fits are presented in Figure 4.19, and the corresponding constants (K_1 and K_2), along with the coefficient of determination (R^2), are summarized in Table 4.8. The lowest obtained R^2 value was 0.92 for the 180 °C curve, indicating a strong correlation.

The next step involved examining the dependence of constants K_1 and K_2 on temperature. Both exhibited linear relationships, as described by equations (4.22) and (4.23),

Table 4.8: *K_1 and K_2 constants, and coefficient of determination (R^2) of the curves presented in Figure 4.19.*

Temperature (°C)	K_1	K_2	R^2
20	182.77	0.4049	0.95
100	156.48	0.4213	0.95
180	130.70	0.4393	0.92

with high correlation values (R^2 = 1 and 0.99, respectively).

$$K_1 = -0.33\,T + 189.19 \tag{4.22}$$

$$K_2 = 0.0002\,T + 0.4004 \tag{4.23}$$

Integrating these relationships into the PDIV formulation, the generalized Extended Dakin's temperature model presented in equation (4.24) was developed to estimate PDIV as a function of temperature, insulation thickness, and relative permittivity for both round and rectangular conductors.

$$\text{PDIV} = (-0.33\,T + 189.19)\left(\frac{t_{\text{ins}}}{\varepsilon_{\text{r ins}}}\right)^{0.0002\,T+0.4004} \tag{4.24}$$

where PDIV is given in Vrms, T in °C, t_{ins} in µm, and $\varepsilon_{\text{r ins}}$ represents the relative permittivity of the insulation. For TPs or PCs, t_{ins} corresponds to twice the insulation thickness of a single conductor. For multi-layer insulations, the equivalent permittivity ($\varepsilon_{\text{r ins eq}}$) should be used, calculated as in equation (4.2).

The proposed model was validated with the VT dataset, which has 127 PDIV experimental values, derived from both direct measurements (60 PDIV tests conducted as in Section 3.3.1, requiring approximately 120 hours) and published data [70, 81, 122]. These validation cases encompassed various wire geometries, enamel materials, and temperatures ranging from 20 to 240 °C. The insulation properties, measurement conditions, experimental PDIV values, and the corresponding model predictions using equation (4.24) are detailed in the Appendix A.

Figure 4.20 presents the error distribution between the model predictions and experimental results from VT dataset, distinguishing between TP (Figure 4.20 (a)) and PC (Figure 4.20 (b)). Notably, since the data from [81] were reported as PDIV ratios relative to 25 °C, the model validation was also conducted in these terms (Appendix A, Table A.3).

The model estimates PDIV with an error below 10% (dotted lines) for most TPs (Figure 4.20 (a)) and PCs (Figure 4.20 (b)) measurements from VT dataset. While the

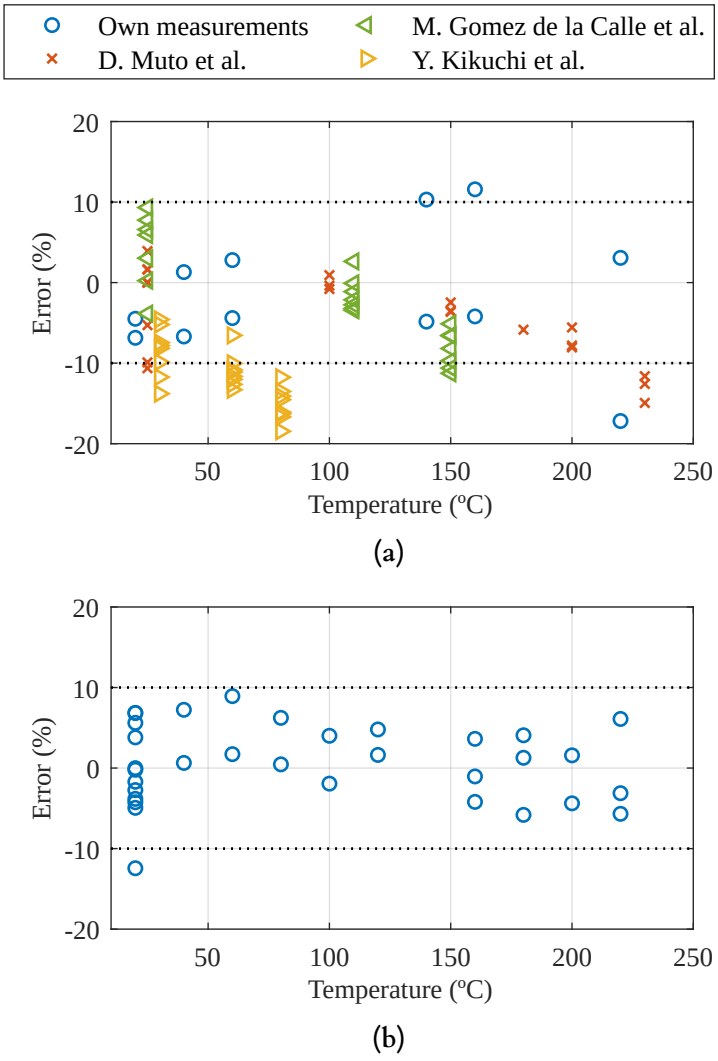

Figure 4.20: *Error obtained with the proposed Extended Dakin's temperature model compared to experimental results and published data from VT dataset for (a) TPs, and (b) PCs (D. Muto et al [81], M. Gomez de la Calle et al. [122], and Y. Kikuchi et al. [70]).*

error slightly increases at higher temperatures for TPs, it remains consistent for PCs. The largest deviation (18%) was observed in comparisons with results from [70] at high temperatures (60-80 °C) and RH (80%), likely due to moisture effects and the assumption of an average insulation thickness.

- **Assumed average t_{ins} value:** Since [70] did not provide specific insulation thickness values, the present study used the average thickness for Grade 2 insulation in its estimations.
- **Effect of moisture:** As outlined in Section 4.1.1.3, humidity influences PDIV not only by altering the relative permittivity but also by affecting air chemical kinetics and modifying surface characteristics. In [70], experiments were conducted at 30-80% RH for temperatures below 100 °C. While the estimation accounted for

RH effects on insulation permittivity using the values provided in [70], the model was developed under RH conditions of 50-66% (at 20 °C), without incorporating the impact of extreme moisture levels. This discrepancy could explain the increased model error observed at temperatures below 100 °C.

The absolute error distribution for the model is summarised in Table 4.9. Among the 127 validated PDIV measurements, 46% had an error of 5% or less, while 30% fell within 5-10%, and 20% within 10-15%. Only 4% exhibited an error exceeding 15%, with the maximum error reaching 18%.

Table 4.9: *Distribution of the absolute error of the Extended Dakin's temperature model for VT dataset.*

Absolute error range	Validated measurements	
	Amount	%
Error $\leq$ 5%	59	46
5% $<$ Error $\leq$ 10%	38	30
10% $<$ Error $\leq$ 15%	25	20
15% $<$ Error $\leq$ 18%	5	4
18% $<$ Error	0	0
Total	127	100

Existing PDIV models reported errors between 1-12%. For instance, the analytic model in [76] had a maximum error of 10%. Most FEM-based models estimate PDIV with errors between 6-12% [81, 87, 121, 122, 137, 138]. However, many of these models required tuning parameters such as γ or K_{Sch} based on experimental data [87, 121, 122, 137] or rely on experimental reference PDIV values [76]. In contrast, the proposed model achieved an absolute error of 12% or lower for 87% of the cases without adjusting any variables to experimental data, even when applied to non-exact values (such as the assumed t_{ins} for the data from [70]) and in an RH range of 30-80% (despite being developed for RH levels of 50-66%).

Overall, the model effectively estimates PDIV for round and rectangular conductors based on temperature, t_{ins}, and $\varepsilon_{\mathrm{r\,ins}}$, without requiring FEM simulations or reference experimental values, limitations present in many published models. Further work is needed to extend its applicability to a wider range of ambient conditions, such as pressure and humidity. However, the model can already be integrated with existing approaches to enhance its predictive capabilities. For example, PDIV at different pressures could be estimated using the present model to determine the reference PDIV required by Lusuardi's model [76]. Combining both models enables PDIV estimation at 25 °C across a pressure range of 25-1013 mbar with an absolute error of 7% (at 50 mbar) compared to experimental data from [76], assuming a 31 µm insulation thickness and a relative permittivity of 3.956 for a TP made from Grade 2 round wire with PEI+PAI insulation. The Extended Dakin's temperature model was published in a conference proceeding

resented on International Conference on Electrical Machines (ICEM) 2024 [22].

4.3.2.2 Absolute Humidity Consideration

To improve PDIV estimation at temperatures below 100 °C, where the Extended Dakin's temperature model presented in Section 4.3.2.1 may have higher errors due to the absence of humidity considerations, an alternative approach was developed for different temperature and RH levels. A new dataset (DAH) was created conducting new PDIV measurements, as described in Section 3.3.1, at 30, 55, and 80 °C with RH levels of 25, 50, 65 (at 80 °C), and 75% (at 30 and 55 °C) for the samples listed in Section 3.1.1 (excluding TP3 and TP4).

To simplify the environmental condition representation in the model and combine temperature and RH into a single variable, AH was used as described in equation (4.25) (kg/m^3) [139], where P_{sat} is the saturation vapour pressure (in Pa), RH is the RH (in %), R_{w} is the specific gas constant for water vapour (461.5 J/(kg K)) and T the temperature (in K). The P_{sat} (in Pa) was calculated following Buck equation (equation (4.26)), being T the temperature (in °C) [140].

$$AH = \frac{P_{\text{sat}}\, RH}{100\, R_{\text{w}}\, T} \tag{4.25}$$

$$P_{\text{sat}} = 611.21\, e^{\left(18.678 - \frac{T}{234.5}\right)\left(\frac{T}{257.14+T}\right)} \tag{4.26}$$

The experimental results from DAH dataset, plotted as a function of the $t_{\text{ins}}/\varepsilon_{\text{r ins}}$ ratio, are shown in Figure 4.21 (a) at 30 °C, Figure 4.21 (b) at 55 °C, and Figure 4.21 (c) at 80 °C, and collected in tables in Appendix A. The data generally aligns with the trends observed in the literature regarding the effect of RH on PDIV (Section 4.1.1.3). At the lower temperature (30 °C), higher humidity levels reduce PDIV. As temperature increases (55 °C), this reduction is less pronounced, while at elevated temperatures (80 °C), PDIV remains relatively unaffected at the highest humidity level 65%. Extending experimental measurements to higher temperatures was not feasible due to resource limitations. However, if the observed trend continues, it can be hypothesised that at 90 °C, higher humidity levels may lead to an increase in PDIV, consistent with the observations in [86, 87, 94].

Following the methodology used in Section 4.3.2.1, equations were derived for the curves illustrated in Figure 4.21. The R^2, and K_3 and K_4 constants as functions of AH are presented in Figure 4.22. The minimum R^2 value obtained was 0.83, indicating a good fit. The fitted linear equations for K_3 and K_4 had R^2 values of 0.64 and 0.8, respectively, excluding 7.59 g/m^3 to improve the fitting (red points).

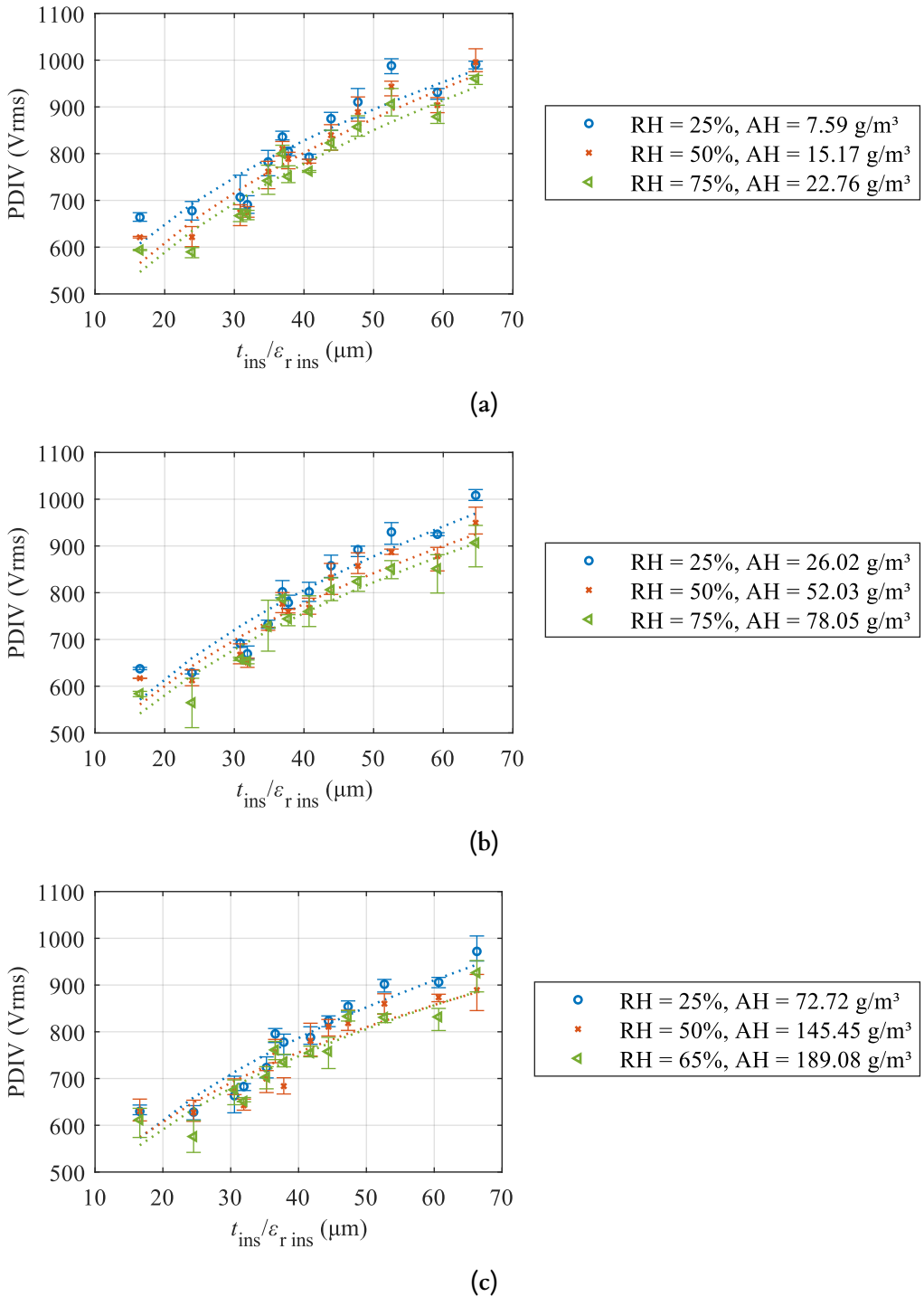

Figure 4.21: *Experimental results of PDIV evolution depending on $t_{ins}/\varepsilon_{r\ ins}$ for DAH dataset at 25, 50, 65 and 75% RH levels at (a) 30 °C, (b) 55 °C, and (c) 80 °C.*

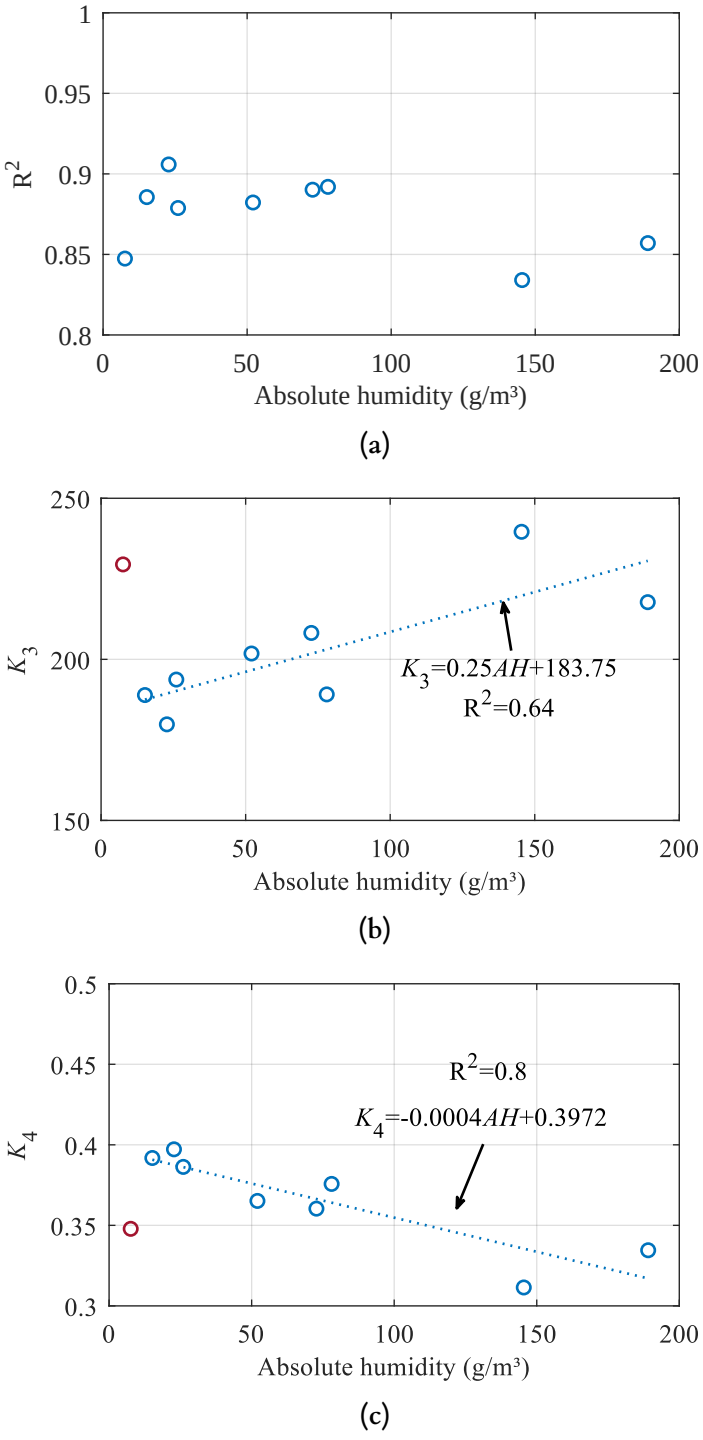

Figure 4.22: *Fitting parameters of the curves shown in Figure 4.21 (a) coefficient of determination (R^2), (b) constant K_3, and (c) constant K_4.*

Using the equations presented in Figure 4.22 for constants K_3 and K_4, the final PDIV equation incorporating AH is given by equation (4.27). Similar to the Extended Dakin's temperature model, PDIV is expressed in Vrms, AH in g/m^3, t_{ins} in µm, and $\varepsilon_{r\,ins}$ is unitless. For TPs or PCs, t_{ins} is equal to twice the insulation thickness of a single conductor.

In the case of multi-layer insulations, the equivalent relative permittivity ($\varepsilon_{\text{r ins eq}}$) should be used, calculated as in equation (4.2).

$$\text{PDIV} = (0.25\ AH + 183.75)\left(\frac{t_{\text{ins}}}{\varepsilon_{\text{r ins}}}\right)^{-0.0004\ AH+0.3972} \tag{4.27}$$

To assess whether the omission of RH contributed to the higher generalised error observed in the Extended Dakin's temperature model presented in Section 4.3.2.1, a direct comparison was made using the experimental results from Y. Kikuchi et al. [70] (Table A.5 in Appendix A). As reported in Figure 4.23, the error obtained with the Extended Dakin's absolute humidity model was lower than that of the Extended Dakin's temperature, confirming that neglecting humidity, particularly at high AH levels (i.e. elevated temperature and RH), was a key factor in the observed discrepancies, as discussed in Section 4.3.2.1. Specifically, the maximum error decreased from 18% in the Extended Dakin's temperature model to 14% using the Extended Dakin's absolute humidity model, while the mean error was reduced from 11% to 8%.

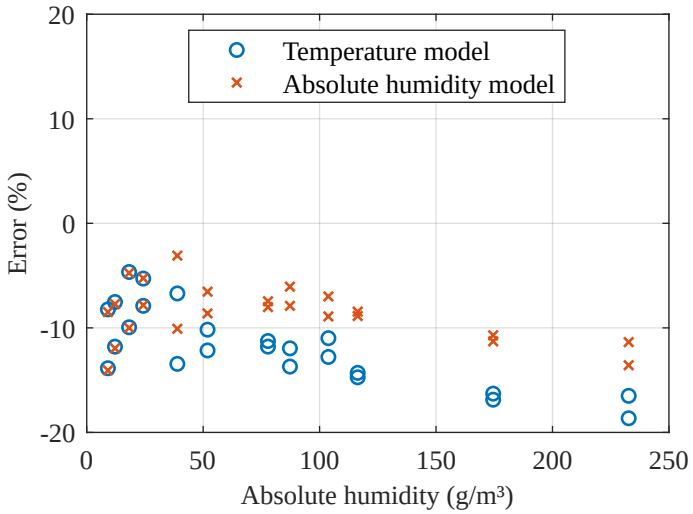

Figure 4.23: *Error obtained with the proposed Extended Dakin's temperature and Extended Dakin's absolute humidity models compared to experimental results published in Y. Kikuchi et al. [70].*

To further validate the model, it was tested against VAH dataset, which is compounded of 118 PDIV experimental values obtained from both this study and bibliographic sources, all measured at temperatures below 100 °C and within a RH range of 4-98%. Similar to the validation of the Extended Dakin's temperature model (Section 4.3.2.1), the dataset included various wire geometries, enamel materials, humidity levels, and temperatures. The specifications for each validation sample fron VAH are provided in Appendix A. Figure 4.24 illustrates the error distribution between the Extended Dakin's absolute humidity model predictions and the experimental PDIV results from VAH, distinguishing between TPs (Figure 4.24 (a)) and PCs (Figure 4.24 (b)).

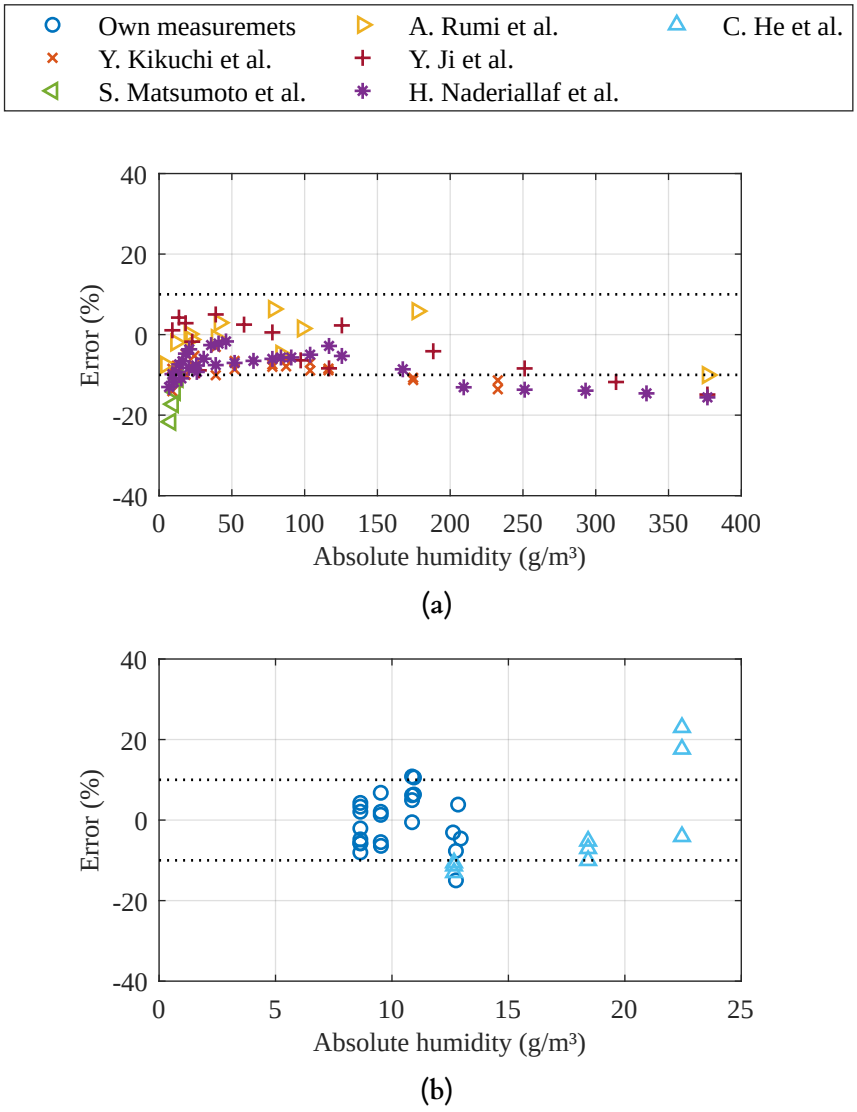

Figure 4.24: *Error obtained with the proposed Extended Dakin's absolute humidity model compared to experimental results and published data from VAH dataset for (a) TPs, and (b) PCs (Y. Kikuchi et al. [70], S. Matsumoto et al. [97], A. Rumi et al. [86], Y. Ji et al. [94], H. Naderiallaf et al. [87], and C. He et al. [141]).*

Overall, the model estimates PDIV with an error below 10% for most measurements, with a slight increase in the error at AH levels exceeding 200 g/m^3. This may be attributed to the fact that the model was developed using experimental data with a maximum AH of 189 g/m^3. Extending the dataset to higher values, such as measurements at 90 °C and 90% RH, could improve accuracy. It is important to note that, except for Y. Kikuchi et al., the relative permittivity was considered remained constant across environmental conditions due to the lack of specific values for each case. Additionally, in several validated samples, the relative permittivity was assumed from Table 3.2, as literature sources did not provide this information. All assumptions are specified in Appendix A. The largest deviation observed was 23% in comparison with C. He et al. [141].

The absolute error distribution for the Extended Dakin's absolute humidity model is presented in Table 4.10. Of the 118 validated PDIV measurements from VAH dataset, 31% had an error of 5% or less, 42% fell within 5–10% range, and 22% were between 10–15%. Only 5% of the cases showed an error exceeding 15%, with the maximum error reaching 23%. The obtained average error was of 7.5%. As previously mentioned, existing models in the literature typically report maximum errors around 12%, often requiring FEM simulations and experimental calibration. In contrast, 86% (102 out of 118 samples) of the estimations in this study remained within a 12% error margin without any parameter adjustments. These results demostrate the effectiveness of the model in estimating the PDIV for round and rectangular conductors by incorporating AH (accounting for temperature and RH) along with t_{ins}, and $\varepsilon_{\text{r ins}}$. Unlike many existing models, it does not require FEM simulations or reference experimental values.

Table 4.10: *Distribution of the absolute error of the Extended Dakin's absolute humidity model for VAH dataset.*

Absolute error range	Validated measurements	
	Amount	%
Error $\leq$ 5%	37	31
5% $<$ Error $\leq$ 10%	50	42
10% $<$ Error $\leq$ 15%	26	22
15% $<$ Error $\leq$ 20%	3	3
20% $<$ Error $\leq$ 23%	2	2
23% $<$ Error	0	0
Total	118	100

4.3.2.3 Combination of Temperature and Absolute Humidity Models

Both the Extended Dakin's temperature and absolute humidity models have demonstrated reliable PDIV predictions within their respective validation ranges. However, a unified approach capable of estimating PDIV across the full range of validated temperature (20–250 °C) and RH (4–98%) is desirable. To assess this, both models were tested against VT and VAH datasets.

Figure 4.25 presents the error between experimental results and predicted PDIV values. In Figure 4.25 (a), which corresponds to VT dataset (Tables A.2–A.5 from Appendix A), the prediction error of the absolute humidity model increases significantly above 100 °C, leading to inaccurate estimations. Below 100 °C, the absolute humidity model provides slightly lower prediction errors. However, it is important to note that in this dataset, the RH range is limited, except for the data from Y. Kikuchi et al. [70], where the absolute humidity model has already been shown to yield better predictions.

To further evaluate prediction accuracy at temperatures below 100 °C with varying humidity levels, Figure 4.25 (b) displays the prediction errors for both models using VAH

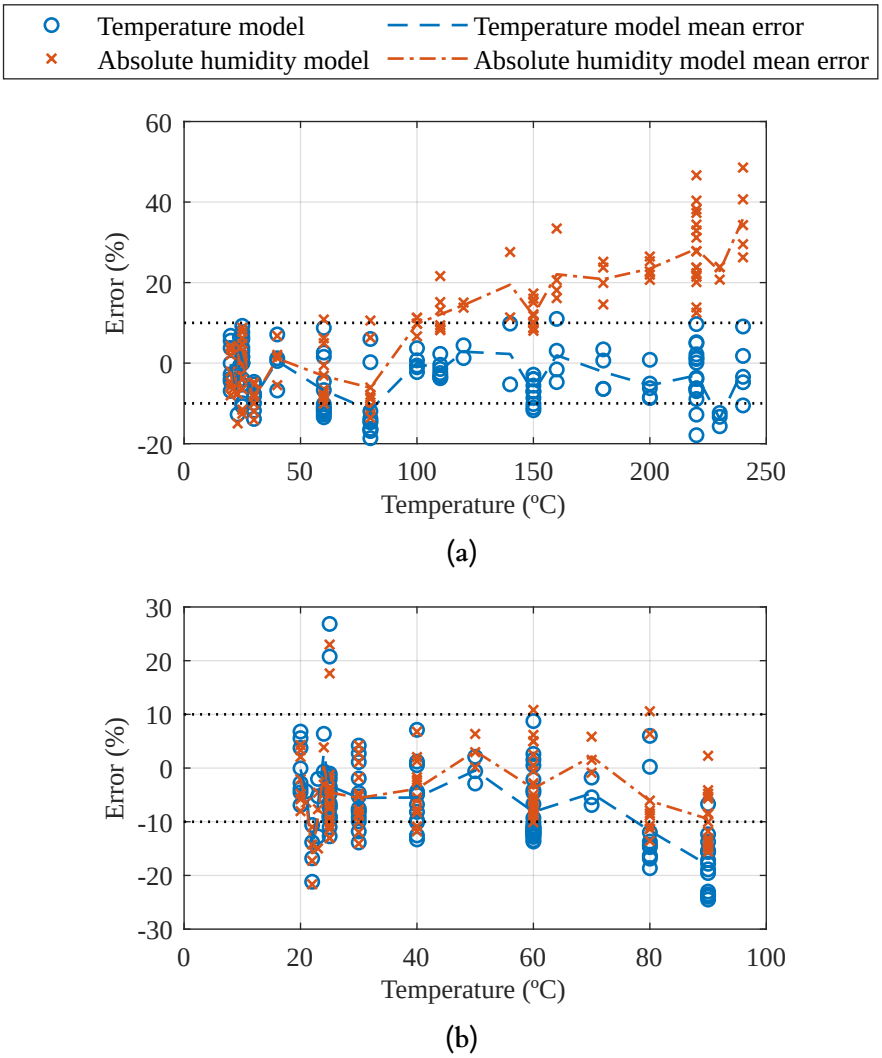

Figure 4.25: *Error obtained with the proposed Extended Dakin's temperature and absolute humidity models compared to experimental results and published data from (a) VT dataset, and (b) VAH dataset.*

dataset (Tables A.9–A.14 from Appendix A). At ambient temperature (low AH levels), both models perform similarly. However, as temperature and, therefore, AH levels increase, the absolute humidity model provides more accurate results.

To minimize prediction errors, the Extended Dakin's absolute humidity model (equation (4.27)) should be used for temperatures below 100 °C, while the Extended Dakin's temperature model (equation (4.24)) should be applied at temperatures of 100 °C or higher.

4.3.3 Comparison of Partial Discharge Inception Voltage Modelling Techniques

Several models for PDIV estimation under varying environmental conditions were compared, focusing on prediction accuracy and estimation time. Direct implementation was prioritized, avoiding model fitting and experimental calibration. Therefore, the Extended Dakin's and Extended parallel-plate models, discussed in Sections 4.3.2 and 4.3.1, respectively, were evaluated alongside the FEM+Paschen's and FEM+Schumann's criterion models. These two FEM-based models were selected from Table 4.6 as they enable direct PDIV estimation under different environmental conditions. Lusuardi's model [76] was excluded as it requires experimental measurements for implementation.

The models were applied to predict the PDIV of the VT and VAH datasets, detailed in Appendix A. To avoid redundancy, VAH1–24 (Table A.9) were excluded, having been accounted for in VT1–24. Samples VT104–127 (Table A.5) were included in the VAH dataset as VAH25–48. PC samples from own measurements (Table A.2) and C. He et al. [141] were not included in FEM-based models due to missing geometric parameters. However, as the Extended Dakin's (Section 4.3.2) and Extended parallel-plate (Appendix B) models demonstrated reliable performance for PC samples, their exclusion does not impact the general conclusions. In total, 140 samples were used for model comparison, implemented as follows:

- **Extended Dakin's model:** Applied using the Extended Dakin's absolute humidity model (equation (4.27)) for temperatures below 100 °C and the Extended Dakin's temperature model (equation (4.24)) for 100 °C or higher (Section 4.3.2).
- **Extended parallel-plate model:** Implemented using Dunbar's correction for Paschen's curve (equation (2.20)), as described in Section 4.3.1. To ensure direct application, literature-based γ values were used. Among the four tested approaches (Appendix B.1), the best results were achieved with $\gamma = 0.0025$ (proposed in [68]) for temperatures below 100 °C and $\gamma = 0.0078$ (proposed in [122]) for 100 °C or higher.
- **FEM+Paschen's Law model:** Implemented following Appendix B.2, considering only constant electric field lines for consistency with Schumann's criterion. $\gamma = 0.0025$ (proposed in [68]) was used for temperatures below 100 °C, while $\gamma = 0.0078$ (proposed in [122]) was used for 100 °C or higher.
- **FEM+Schumann's criterion model:** Implemented as detailed in Appendix B.2, using the best-performing K_{Sch} value, $K_{\text{Sch}} = 5.98$ proposed in [121], for model comparison.

Figure 4.26 presents the error distributions for each model, with key metrics summarized in Table 4.11 and detailed results in Appendix B.3. Figure 4.26 (a) illustrates results for the VT dataset (Appendix A.1), where most samples are above 100 °C, with a stable

RH of approximately 50% for those below 100 °C. Figure 4.26 (b) shows results for the VAH dataset (Appendix A.2), where all samples are below 100 °C with varying humidity levels. Figure 4.26 (c) combines both datasets.

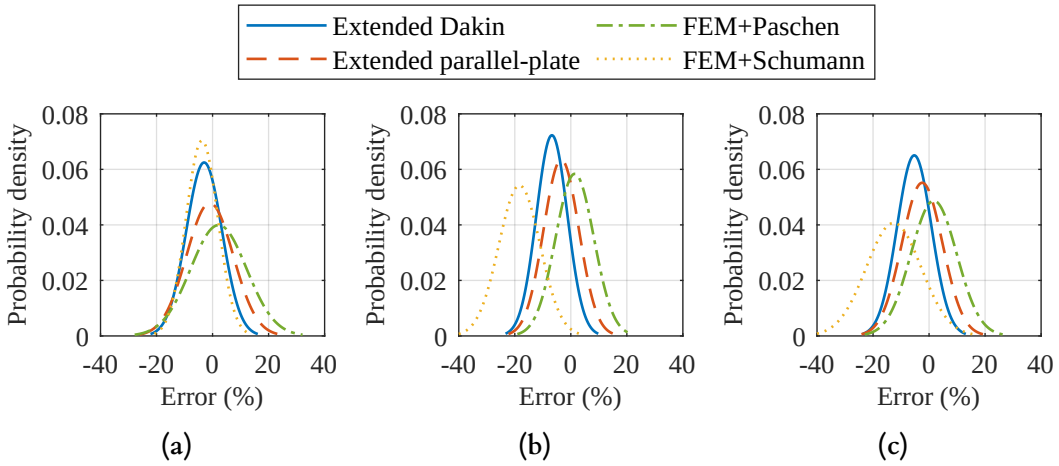

Figure 4.26: *Comparison of the error distributions for PDIV prediction with different models (a) using only VT dataset, (b) using only VAH dataset, and (c) combining both datasets.*

Table 4.11: *Mean (μ), standard deviation (σ), and maximum absolute error obtained in the prediction of PDIV using several models for VT dataset, VAH dataset, and the combination of both datasets (%).*

Model	VT dataset			VAH dataset			Combination		
	μ	σ	Max. error	μ	σ	Max. error	μ	σ	Max. error
Extended Dakin's	-3.0	6.4	17.9	-6.7	5.5	21.6	-5.3	6.3	21.6
Extended parallel-plate	-1.0	8.3	21.3	-3.4	6.3	15.5	-2.5	7.2	21.3
FEM+Paschen's Law	2.2	10.0	26.1	1.4	6.8	16.2	1.7	8.2	26.1
FEM+Schumann's criterion	-3.8	5.7	16.1	-18.3	7.4	38.6	-12.6	9.8	38.6

For the VT dataset (Figure 4.26 (a)), all models achieved similar mean absolute errors (1–3.8%). The FEM+Schumann's model had the lowest maximum error and dispersion, followed by the Extended Dakin's model. In the VAH dataset (Figure 4.26 (b)), the FEM+Schumann's model exhibited higher mean and maximum errors than the other models, including the Extended parallel-plate and FEM+Paschen's models, which do not explicitly account for humidity. This discrepancy suggests a possible error in the implementation of humidity effects within the FEM+Schumann's model, which could not be identified. Among the other three models, the mean absolute error remained between 1.4–6.7%, with the Extended Dakin's model exhibiting the least dispersion. The

maximum error for the Extended Dakin's model (21.6%) was slightly higher than that of the other two models (15.5–16.2%).

Considering both VT and VAH (Figure 4.26 (c)), excluding FEM+Schumann's, the mean absolute error for the remaining models ranged between 1.7–5.3%, with the lowest dispersion observed for the Extended Dakin's model. The maximum errors for the Extended Dakin's and Extended parallel-plate models were approximately 21%, while FEM+Paschen's reached 26%. These results indicate that analytical models can achieve prediction accuracy comparable to that of FEM-based models.

Another key aspect of the comparison was the evaluation of the time required for PDIV prediction across all samples. Table 4.12 presents the time required to estimate PDIV for the 140 samples considered in Figure 4.26 using each model. FEM simulation time refers to the duration required by the software Altair FLUX® to simulate the geometry described in Appendix B.2 and export the results. Model application time represents the time taken by MATLAB® to execute each model. This encompasses applying the corresponding equations in the Extended Dakin's and Extended parallel-plate models, obtaining the constant electric field line values and lengths for FEM+Paschen's and FEM+Schumann's models, performing the comparison with Paschen's curve in FEM+Paschen's model, and extracting ionisation parameters from BOLSIG- while evaluating Schumann's criterion in FEM+Schumann's model.

Table 4.12: *PDIV prediction time required by each model for the estimation of 140 samples used in the comparison of the models (h:min:s).*

Model	FEM simulation time	Model application time	Total time	Time per sample (s)
Extended Dakin's	0	00:00:00.04	00:00:00.04	0.25 $10^{-}3$
Extended parallel-plate	0	00:00:00.05	00:00:00.05	0.34 $10^{-}3$
FEM+Paschen's Law	04:01:17.68	00:16:02.87	04:17:20.55	110.29
FEM+Schumann's criterion	04:01:17.68	02:02:07.09	06:03:24.77	155.75

Although both analytical models required comparable computational time, FEM-based models demanded significantly longer processing times. This difference is particularly evident in the FEM+Schumann's model, where the additional step of retrieving ionisation data from BOLSIG- further increases computation time. The efficiency advantage of analytical models highlights their suitability for practical applications requiring rapid PDIV estimation.

All in all, the Extended Dakin's and Extended parallel-plate models proposed in this work provide PDIV predictions for interturn insulation (considering both round and rectangular conductors) with accuracy comparable to simulation-based models while

significantly reducing computational time. The Extended Dakin's model achieved this accuracy without any parameter adaptation for specific samples, relying solely on sample specifications and environmental conditions. The Extended parallel-plate model, on the other hand, demonstrated strong predictive capability using literature-defined γ values, yielding results as accurate as the FEM+Paschen's model when the same γ values were used. Another important observation is that both Extended Dakin's and Extended parallel-plate models generally underestimate PDIV values, providing a conservative prediction that enhances insulation design safety.

Although some studies suggest using γ as a fitting parameter for specific samples and conditions to further reduce error (Section 4.2.2.1), this approach would require experimental data. Additionally, finer meshing or increasing grid points in FEM simulations could improve the accuracy of FEM+Paschen's and FEM+Schumann's models, but at the cost of significantly increased computational time. Given that the applied mesh and grid parameters already produced accurate predictions in the comparison with [30] (Appendix B.2), further refinement may not be necessary.

This does not imply that FEM-based models are not valuable. They remain essential for gaining more in-depth insight into PD mechanisms and assessing the influence of various factors. For instance, [87] employs the FEM+Schumann's criterion model to examine the combined effects of temperature and humidity on PDIV. Moreover, FEM-based approaches may be better suited for estimating groundwall or phase-phase PDIV [133], which has not yet been totally validated using the Extended Dakin's or Extended parallel-plate models. Nevertheless, the Extended Dakin's model shows promising potential for application to groundwall insulation PDIV estimation, as it is discussed later in Chapter 5.

4.4 Concluding Remarks

In this chapter a comprehensive assessment of the environmental and electrical factors influencing PDIV, along with models for predicting PDIV under operating conditions required to design PD-free insulation systems, with a focus on interturn insulation, was presented.

Among the environmental variables, temperature, humidity, and pressure were identified as key contributors to PDIV variation. Temperature was confirmed as the dominant factor, consistently reducing PDIV due to its effect on air density, while humidity showed a dual influence depending on the thermal environment. Pressure followed a characteristic U shaped dependency, although its practical relevance may be limited in atmospheric-pressure systems. These findings reinforce the importance of incorporating environmental factors into PDIV estimation during insulation system design.

In terms of electrical parameters, waveform shape, polarity, rise time, and pulse width were shown to have a limited impact on PDIV under controlled conditions. Sinusoidal waveforms, despite concerns raised in earlier studies, yielded comparable results to unipo-

lar pulses when overshoot was constrained, thereby validating their use for insulation evaluation. This confirmation is especially relevant in view of international standards such as IEC 60034-18-41 [9], which assumes equivalence between impulse and sinusoidal PDIV measurements for TP evaluation. Consequently, sinusoidal excitation remains a valid and conservative approach for model development and testing of interturn insulation in inverter-fed machines.

In this context, several analytical and simulation-based models for PDIV prediction were reviewed, each with specific strengths and limitations. These include the need for fitting parameters like γ or K_{Sch}, high computational costs (in simulation-based models), or reliance on experimental data. To address these issues, the Extended parallel-plate and Extended Dakin's models were developed and validated in this work. Both provided predictive mean accuracy of around 5%, comparable to FEM-based models, across a temperature range of 20-250 °C and RH range of 4-98%, while requiring significantly fewer resources. The Extended Dakin's model, in particular, derived reliable results without parameter fitting, offering a practical and conservative tool for insulation system design. FEM-based models remain valuable for in-depth analysis of PD mechanisms.

Depending on the intended application, the Extended Dakin's model offers significant advantages. It provides valuable support for coil winding designers and wire manufacturers using round or rectangular insulated conductors, enabling them to select optimal insulation materials based on predicted PDIV values. By applying this model, they can determine the PDIV value for the required operating temperatures and humidity levels with reasonable accuracy, eliminating the need for extensive FEM simulations or labour-intensive experiments. Last but not least, it can also be extended to incorporate pressure effects by using its predicted value as the reference PDIV in the approach proposed by Lusuardi's model.

Chapter 5

Effect of Design and Manufacturing Factors on the Insulation System

The reliability of the insulation system of electric machines is strongly influenced by its design and manufacturing processes. To assess potential vulnerabilities and enhance performances, this research has been supported by collaborative projects with two industrial partners, each offering distinct perspectives on insulation system evaluation.

In collaboration with the first company, the study was focused on evaluating the effects of transitioning from semi-automatic winding techniques to needle winding technology. The primary aim was to identify potential weaknesses in the insulation system resulting from this manufacturing shift, ensuring that electrical integrity was preserved under operational conditions.

The second partnership involved a systematic evaluation of the insulation system during the machine design. This ongoing analysis enabled active engagement in material selection and the early detection of design-related vulnerabilities, ultimately contributing to the development of an optimised and robust machine configuration.

These industrial collaborations have not only enriched the research with practical insights but also provided valuable support to the surrounding companies. The outcomes of these partnerships are presented in this chapter, detailing the methodologies, key findings, and proposed improvements.

5.1 Effect of the Needle Winding Manufacturing Process on the Integrity of the Insulation System Considering Partial Discharge Analysis

The following section outlines the outcomes of a joint investigation with an industrial partner, aimed at evaluating the potential implications of adopting needle winding technology in electric machine manufacturing. As described earlier in Section 3.1.2, needle winding constructs the coils directly within the stator by guiding a needle through the slots to place the wire in its designated position. This process inevitably stretches the wire, which may result in a slight reduction of its nominal diameter and insulation thickness.

The central aim of this study was to determine whether this change in manufacturing method could compromise insulation reliability. Although the semi-automatic machine has never exhibited PD activity during its operation, suggesting the insulation system is properly designed, the mechanical stress introduced by the needle winding process may reduce the insulation thickness, thereby lowering dielectric strength. This could also cause micro-cracks or tears in the insulation, increasing the likelihood of PD.

The PDIV and PD patterns were used as the primary indicators to assess insulation integrity. Although the most notable effects were expected in the interturn insulation, the absence of equipment for impulse-based interturn PDIV testing on complete machines, as outlined in IEC 60034-18-41 [9], constrained the study. Nonetheless, as this machine is powered by Si-based converter and not by WBG-based ones, the expected non-uniform voltage distribution and overshoot are limited (Section 2.1.3.3).

5.1.1 Definition of the Required Partial Discharge Inception Voltage Value

Before comparing the two winding technologies, the required PDIV values for phase-phase and groundwall insulations were established based on the electrical and thermal stresses applied to the insulation system, following the guidelines of IEC 60034-18-41 [9]. As both types of machines work under the same operation conditions, with the following analysis it was possible to ensure the safety functioning during their lifetime.

The machine operated with a two-level converter, featuring a voltage rise time of 0.3 µs and a DC bus voltage of $V_{DC} = 565$ V. The expected peak voltage at the machine terminals was approximately 645 V, resulting in an overshoot factor of 1.14. This was determined experimentally in [142]. According to Table 5.1, this corresponds to a moderate stress category.

Following the calculation example provided in [9], the maximum peak-peak operating voltage for phase-phase and groundwall was estimated considering $V_{DC} = 565$ V and a moderate stress category, which applies a multiplier of 3.0 (Table 5.1). A service voltage variation of $\pm$ 10% was also considered, adding a safety factor of 1.1.

To define the required minimum PDIV value, other several enhancement factors

Table 5.1: *Stress categories for Type I insulation systems based on a 2-level converter [9].*

Stress category	Overshoot Factor (OF)	Impulse rise time (μs)	Phase-phase Vpp max in units of V_{DC}
A - Benign	$OF \leq 1.1$	0.3	2.2
B - Moderate	$1.1 < OF \leq 1.5$		3.0
C - Severe	$1.5 < OF \leq 2.0$		4.0
D - Extreme	$2.0 < OF \leq 2.5$		5.0

apart from the electrical ones were applied, which are adopted regardless of whether the test voltage is sinusoidal or impulse-based. These enhancement factors are the following ones [9]:

- **Partial Discharge Safety Factor (PDSF):** A safety factor of 1.25 accounts for the hysteresis effect, where Partial Discharge Extinction Voltage (PDEV) is typically 25% below PDIV. This is applicable when PD activity is initiated by a transient overshoot exceeding the normal peak voltage.
- **Temperature Safety Factor (TSF):** Temperature-induced reductions in PDIV during operation are considered. For phase-phase, PDIV may decrease by up to 30%, while for groundwall the reduction may reach 10%, due to the cooling effect of the stator slot. Values of TSF=1.3 and TSF=1.1 were used for phase-phase and groundwall, respectively, considering the most restrictive performance.
- **Ageing Safety Factor (ASF):** This factor considers thermal ageing effects. It ranges from 1 to 1.2 depending on the proximity to the insulation class temperature. Since the current machine works significantly below the insulation class temperature, TSF=1 was selected.

Based on these conditions, the required PDIV values were calculated as follows:

$$V_{\text{phase-phase}} = 565 \cdot 3.0 \cdot 1.1 \cdot 1.25 \cdot 1.3 \cdot 1 = 3030 \text{ Vpp} \tag{5.1}$$

$$V_{\text{groundwall}} = 0.7 \cdot 565 \cdot 3.0 \cdot 1.1 \cdot 1.25 \cdot 1.1 \cdot 1 = 1795 \text{ Vpp} \tag{5.2}$$

As previously mentioned, the semi-automatic machine has never exhibited PD activity during its operation, therefore, compliance with the minimum PDIV for both phase-phase and groundwall insulations has been ensured through extensive operational experience. Turning now to the needle machine, preliminary PDIV measurements (as defined in Section 3.3.1) showed a phase-phase PDIV of approximately 6700 Vpp, more than twice

the required value of 3030 Vpp. The groundwall PDIV was approximately 3300 Vpp, 1.8 times higher than the required 1795 Vpp. Based on these results, the needle machines were deemed to have a reliable insulation system, with no failure expected during operation.

Nevertheless, comparison with the semi-automatic machine was considered valuable to confirm that the insulation integrity of the needle was at least equivalent. As the groundwall insulation was found to be more limiting, the following analysis focused on this insulation.

5.1.2 Partial Discharge Inception Voltage Analysis

For the comparison of the needle and semi-automatic machines, three samples of each machine (see Section 3.1.2) were measured following the procedure described in Section 3.3.1. In addition to the connections from the HV terminals, the same procedure was conducted from the neutral point terminals. The ambient temperature conditions during these tests were 14–21 °C and 59–75% RH range.

Figure 5.1 collects the groundwall PDIV measurement results, representing the average of three machines per manufacturing method at each connection, with error bars indicating the maximum and minimum PDIV values recorded. As expected, no difference was observed between the measurements conducted from the HV and neutral (with *n*) terminals for both machine types, either when the phases were connected independently or collectively to HV. These findings indicate two key conclusions: first, all measurements reliably captured the groundwall PDIV, and second, there were no manufacturing imbalances among the three phases.

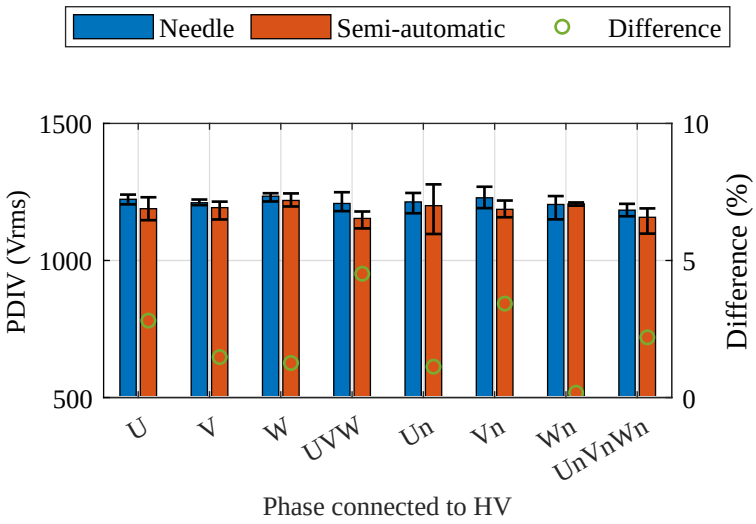

Figure 5.1: *Experimental groundwall PDIV measurement comparison between needle and semi-automatic machines.*

Comparing needle and semi-automatic results (green dots in Figure 5.1), the maximum difference between both types was 5%, observed in the UVW connection to HV. Given

the variability observed between the three measured samples, this difference is disregarded, concluding that the insulation system of the needle and semi-automatic machines is equivalent in terms of groundwall PDIV value. Yet, a more direct evaluation of interturn insulation using impulse voltages for PDIV assessment could provide more in-depth insights into potential defects arising from the needle winding method.

5.1.3 Partial Discharge Pattern Analysis

Phase Resolved Partial Discharge (PRPD), named as PD pattern, represents the PD activity occurring over a certain period, mapped onto a single voltage cycle. Figure 5.2 illustrates an example of such a pattern, defining the positive (ϕ_+) and negative (ϕ_-) onset phases as points where PD activity initiates during the positive and negative half-cycles, respectively. The corresponding phase widths, during which PD activity is active, are denoted as $\Delta\phi_+$ and $\Delta\phi_-$ [61].

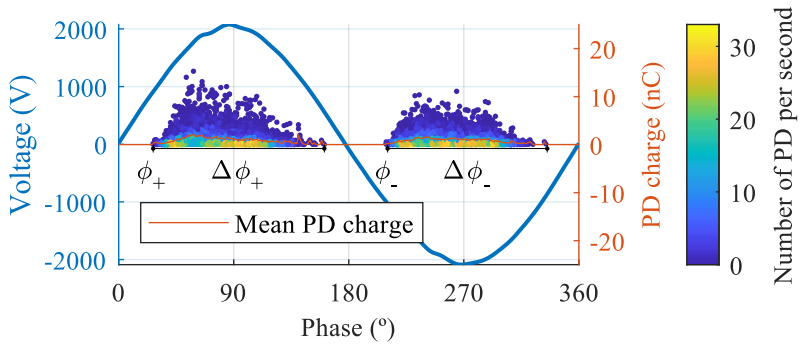

Figure 5.2: *Example of a PD pattern with the definition of the onset phase (ϕ) and the phase width where PD activity is active ($\Delta\phi$).*

To perform a meaningful analysis, it is recommended to record the PD patterns at three or four different overvoltage levels (i.e. the ratio of the applied voltage to the PDIV) [61]. Considering the limited variability of PDIV values (differing by less than 5%, see Figure 5.1) the same test voltage levels were defined for both machine types. Based on the maximum measured PDIV of 1270 Vrms, the minimum HiPot test (described in Section 3.3.2) voltage was set at 1300 Vrms, ensuring consistent and sufficient PD activity across all machines. To assess the evolution of the patterns under varying electric stress levels, tests were conducted at 1300, 1400, 1500, 1600, and 1700 Vrms.

The HiPot tests used to acquire the PD patterns followed the specifications outlined in Section 3.3.2. All measurements were conducted under ambient conditions of 13-21 °C and RH between 59-78%. Given the negligible difference in PDIV results between configurations where one or all phases were connected to HV, the following analysis only presents the measurements in which all three phases were connected (UVW), as this provides clearer insight. Nevertheless, similar conclusions apply to the alternative configurations.

Beginning with the semi-automatic machines (sample 1 in Figure 5.3, and samples 2 and 3 in Appendix C), the PD pattern is centred around the voltage peak and exhibits symmetry between the positive and negative half-cycles. As the applied voltage increases, a slight advancement in the onset of the pattern is observed, shifting from approximately 45° to 30° and widening the active phase range. However, this last change is not particularly pronounced. Higher test voltages also consistently resulted in increased maximum discharge values.

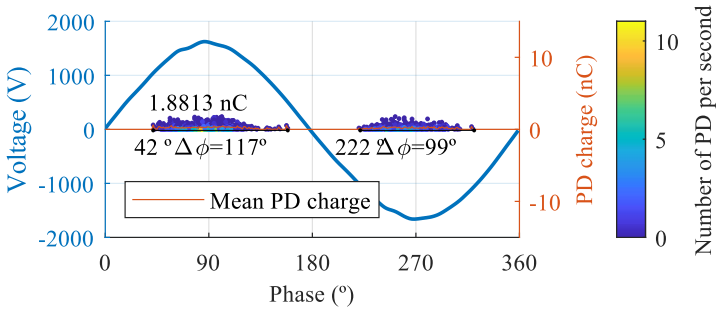

(a)

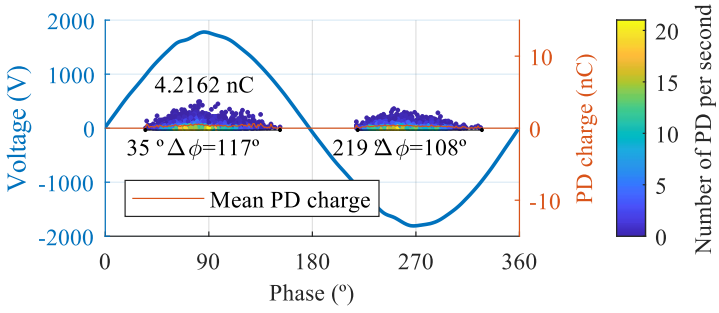

(b)

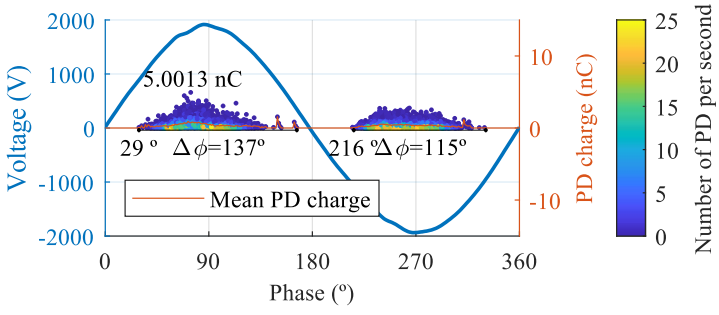

(c)

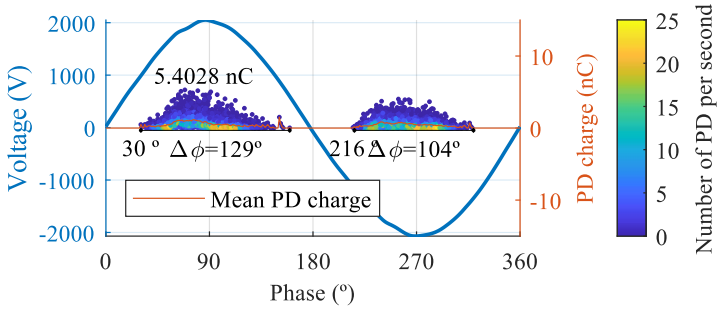

(d)

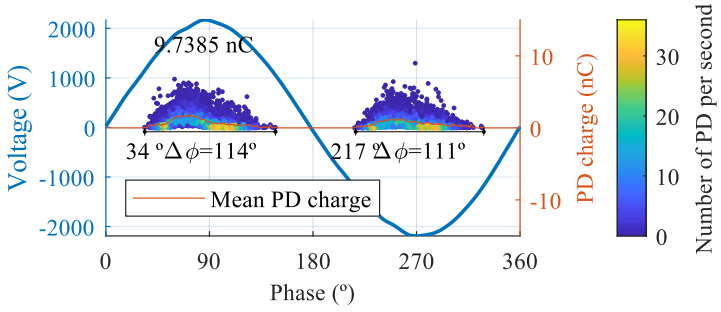

(e)

Figure 5.3: *Groundwall insulation PD patterns (UVW to HV, stator to GND) of semi-automatic machine sample 1 (a) 1300 Vrms, (b) 1400 Vrms, (c) 1500 Vrms, (d) 1600 Vrms, and (e) 1700 Vrms.*

Across all three tested machines, no significant variation was observed. All exhibit discharge magnitudes of 1–3 nC at 1300 Vrms, increasing to 9–10 nC at 1700 Vrms. At lower voltages (1300–1400 Vrms), the pattern shape is generally more oval, gradually transitioning to a triangular shape at 1700 Vrms. This evolution suggests a change in the discharge mechanism, from internal voids within the insulation system involving the groundwall insulation, to air gaps between the enamelled wire and the insulation paper or between the paper and the stator core. Figure 5.4 provides reference patterns for both discharge types.

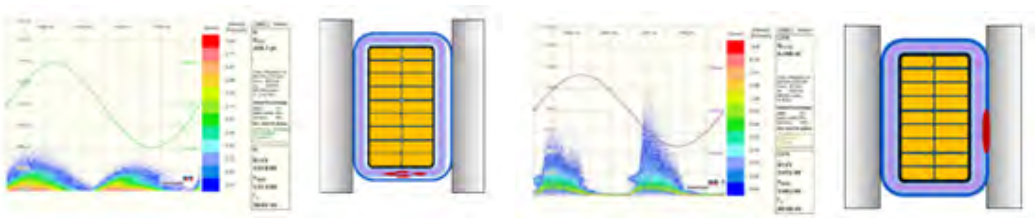

(a) (b)

Figure 5.4: *Examples of PD patterns of the insulation system of electric machines, PD occurring (a) in air bubbles inside the wire enamel, and (b) between the enamelled wire and the paper/stator core. Images from [143].*

The observations are reinforced by the mean PD charge pattern shown in Figure 5.5, where the response is consistent across all semi-automatic machines. As previously mentioned, a transition from oval to triangular shape can be noted as test voltage increases.

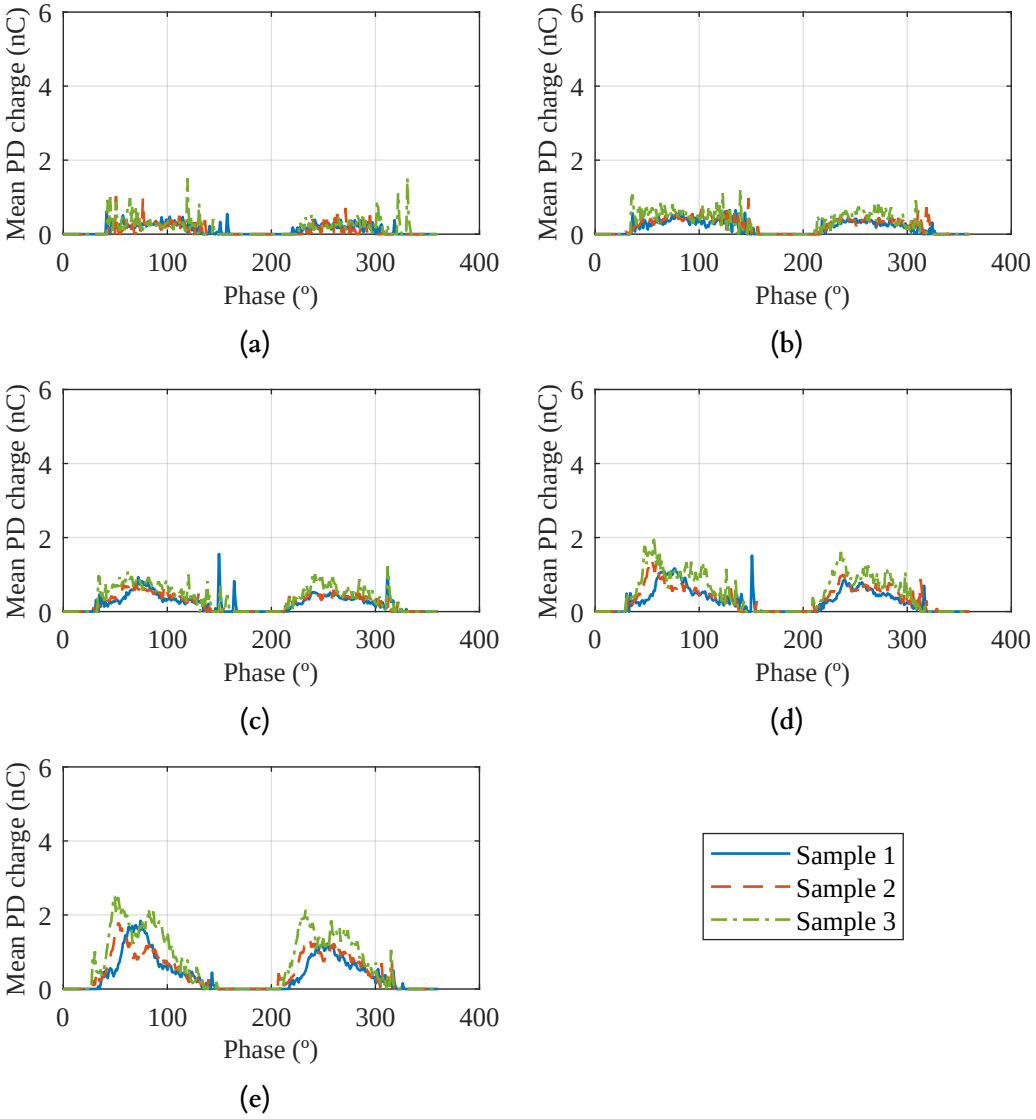

Figure 5.5: *Groundwall insulation mean PD charge value (UVW to HV, stator to GND) of semi-automatic machine sample 1, 2, and 3 (a) 1300 Vrms, (b) 1400 Vrms, (c) 1500 Vrms, (d) 1600 Vrms, and (e) 1700 Vrms.*

A similar behaviour is observed in the needle machine (sample 1 in Figure 5.6 and samples 2 and 3 in Appendix C). Like the semi-automatic machine, the PD patterns are centred around the voltage peak and exhibit symmetry across the voltage cycles. With increasing voltage, the onset of the discharges shifts earlier (from around 45° to 25°), and the active phase width increases from about 90° to 140°. This increase is more pronounced than in the semi-automatic machines. The pattern shape evolves similarly to the semi-automatic machine, from an oval to a triangular form, with higher test voltages yielding

larger discharge magnitudes (which are larger than in the semi-automatic machine). This trend is consistent across the three needle machines, as reflected in the mean charge distribution shown in Figure 5.7.

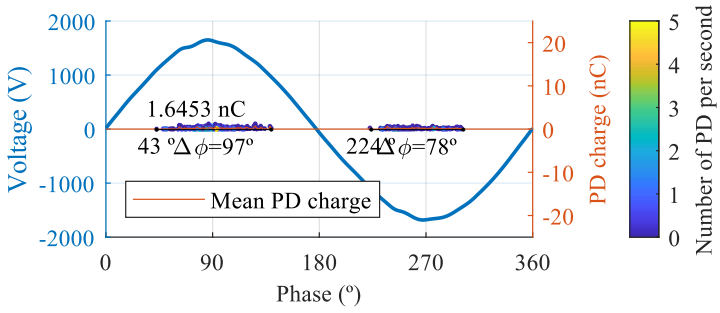

(a)

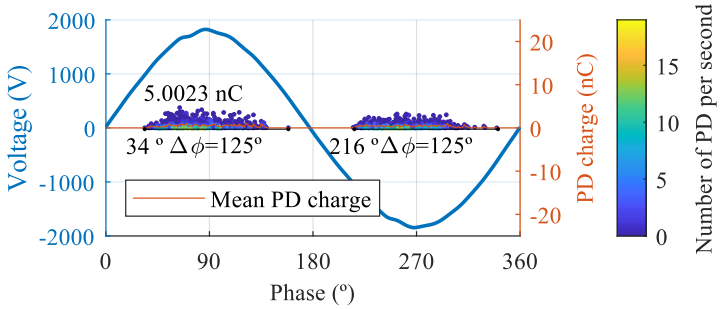

(b)

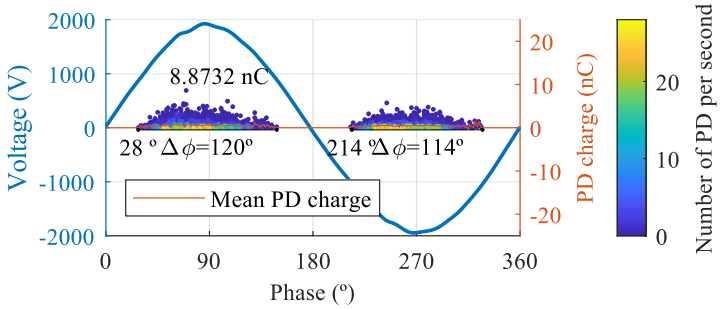

(c)

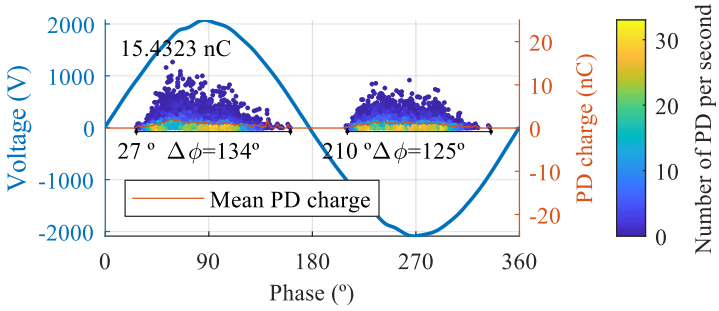

(d)

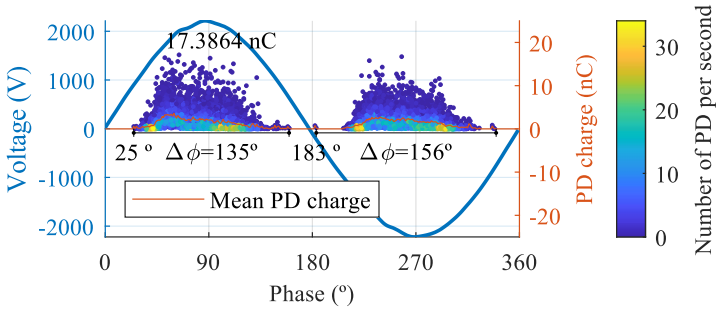

(e)

Figure 5.6: *Groundwall insulation PD patterns (UVW to HV, stator to GND) of needle machine sample 1 (a) 1300 Vrms, (b) 1400 Vrms, (c) 1500 Vrms, (d) 1600 Vrms, and (e) 1700 Vrms.*

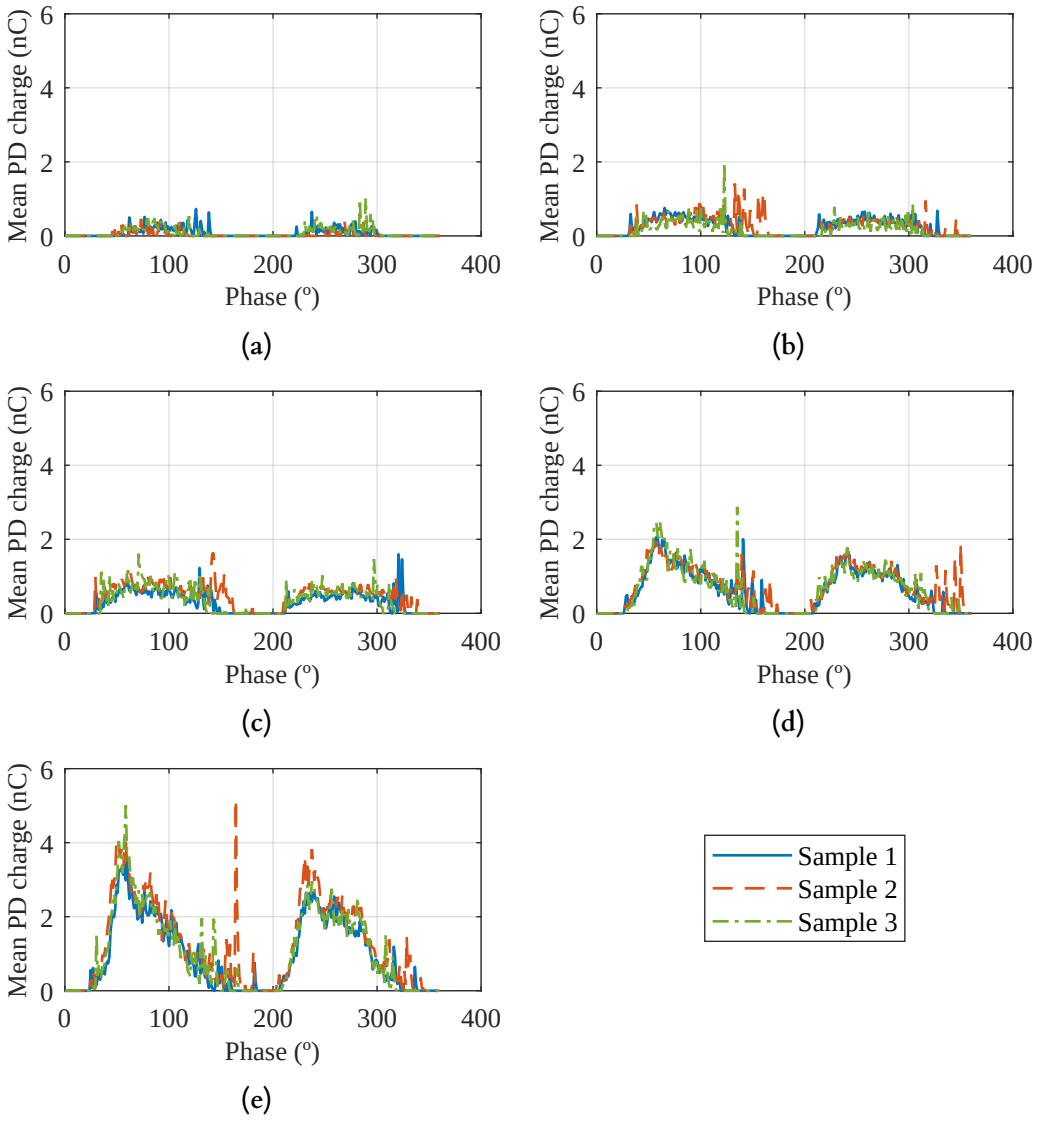

Figure 5.7: *Groundwall insulation mean PD charge value (UVW to HV, stator to GND) of needle machine sample 1, 2, and 3 (a) 1300 Vrms, (b) 1400 Vrms, (c) 1500 Vrms, (d) 1600 Vrms, and (e) 1700 Vrms.*

Figure 5.8 compares the average of the mean PD charge of the three samples per type across voltage levels. At lower voltages (1300–1500 Vrms), no substantial differences are observed. However, at higher voltages (1600–1700 Vrms), samples produced using needle machines exhibited both higher discharge magnitudes and broader phase widths. This difference emerged despite both machine types having comparable PDIV values. These results may initially seem unexpected, as under equal overvoltage conditions, one might anticipate similar apparent charge values.

Although the cause of the observed difference in charge was not further analysed, one possible explanation is that the apparent charge may have been distorted due to resonances in the path between the PD source and the detection system. According to

[144], depending on the winding design and the measurement arrangement, resonance phenomena within the frequency range of the PD measuring device may occur, potentially influencing the measured PD values. It is therefore possible that such a resonance was excited in one machine but not in the other. Unfortunately, no information was available on the frequency range of the measurement device used, although this aspect should be investigated further.

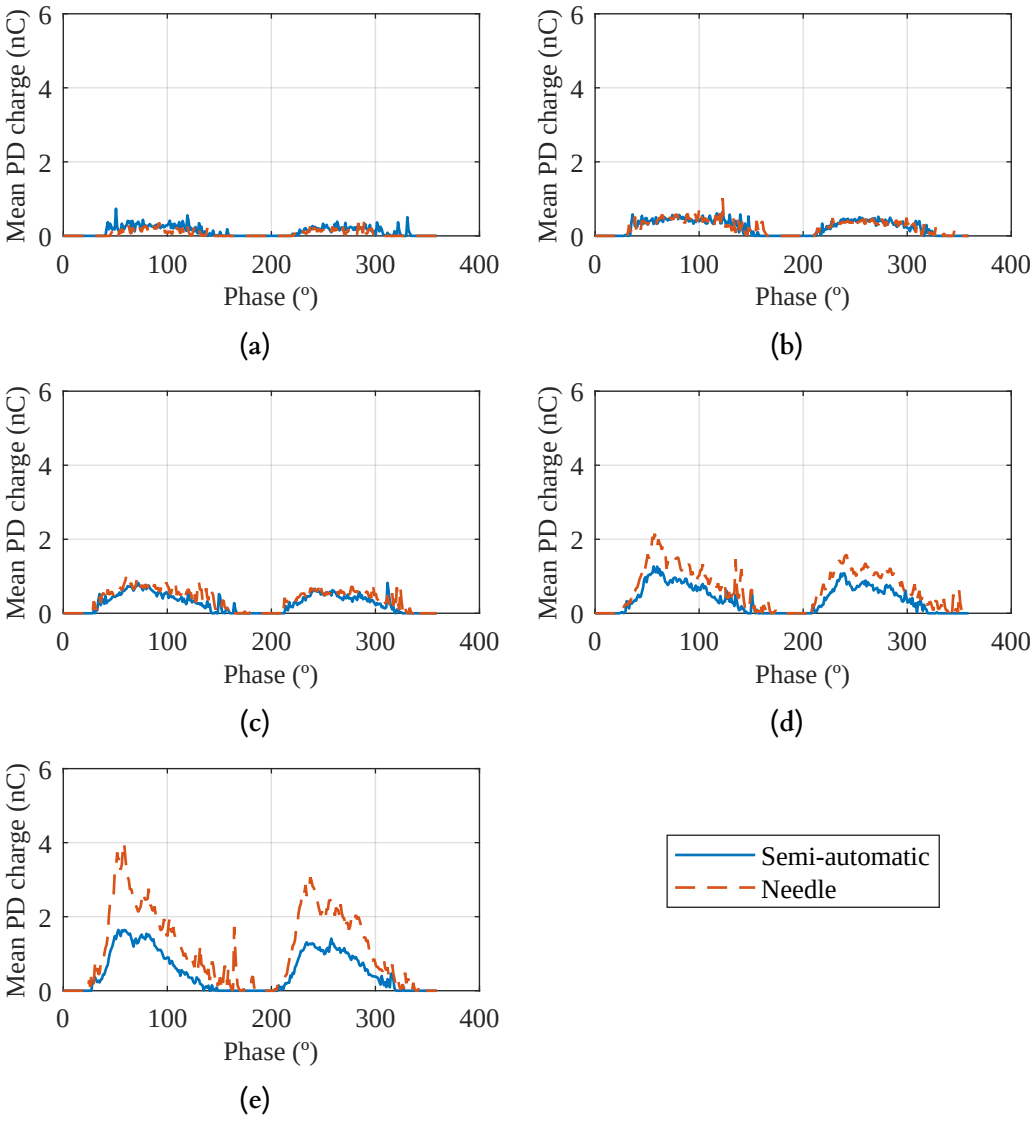

Figure 5.8: *Comparison of the average value of the mean PD charge of the three samples of semi-automatic and needle machines for groundwall insulation (UVW to HV, stator to GND) (a) 1300 Vrms, (b) 1400 Vrms, (c) 1500 Vrms, (d) 1600 Vrms, and (e) 1700 Vrms.*

In the hypothetical case that the increased PD charge observed in needle machines reflects a true increase in discharge magnitude rather than a resonance excitation, this could have practical implications. If the operating voltage approaches the PDIV, the more intense discharge activity could result accelerate insulation degradation. Nonetheless,

further analysis is necessary to confirm the origin of the differences in measured PD charge.

5.1.4 Concluding Remarks

The measurements and analysis conducted to compare semi-automatic and needle machines allow several conclusions to be drawn. Firstly, the similarity between the PDIV values measured for all groundwall configurations, along with the low variability among the three machines of each type (in both PDIV measurements and the PD patterns) demonstrates consistent manufacturing quality and repeatability for both winding techniques.

In addition, the PDIV differs below 5% between semi-automatic and needle machines, indicating that the insulation system was not evidently compromised during the needle-winding process. Thus, the needle machines are expected to maintain the same PD-free operational performance historically demonstrated by the semi-automatic machines.

The symmetry and overall shape of the PD patterns obtained from both machine types were equivalent, suggesting that both are subjected to the same type of PD activity. At low voltages, the patters are consistent with discharges occurring in air pockets, while at higher test voltages, the triangular pattern that is commonly associated with groundwall insulation (such as discharge between the insulating paper and the enamelled wire) becomes more pronounced in both cases.

Nevertheless, the needle machine exhibited higher discharge magnitudes at elevated test voltages (1600–1700 Vrms). The reason for this behaviour remains unclear. A more detailed analysis of the frequency response of the PD measurement system, as well as a review of the manufacturing process, including the applied stretching force during winding, potential reductions in insulation thickness, and the formation of micro-defects, could help clarify these findings. Additionally, PD testing with impulse voltages could provide further evidence of such defects. If a genuine increase in PD charge is confirmed in needle machines, then, in the unlikely event of PD activity during service, these machines may be more susceptible to accelerated insulation degradation. To validate this hypothesis and investigate the underlying mechanisms, a dedicated electrical ageing test comparing both machine types would be required.

In summary, for the current study, the insulation system of the needle machine is expected to be as reliable as that of the semi-automatically manufactured one. Further investigations into interturn insulation, including potential insulation thickness reduction and PD analysis, could offer additional insights into possible differences. However, given the present power supply technology, this insulation is not considered as critical as it would be under WBG-based converter operation.

5.2 Assessment on the Insulation System Definition During the Design of a Machine for Aeronautic Application

The second collaboration with an industrial partner, presented in the following section, focused on evaluating the insulation system during the design phase of a machine intended for aeronautic applications. This involved a systematic assessment throughout the design process, enabling active participation in material selection and early detection of design-related weaknesses. This continuous evaluation supported the development of a robust and optimised machine configuration.

To assess the insulation integrity, PDIV analysis together with HiPot measurements were carried out. The requirements were set by the company, and specifically targeted groundwall insulation. Accordingly, measurements were focused on this configuration. Nevertheless, in certain cases, phase-phase measurements were also carried out to investigate potential manufacturing issues.

5.2.1 Specifications

The company defined the specifications outlined below. Although the machine was ultimately intended for aeronautic applications, the insulation system requirements (specifically the required PDIV) were established under room conditions, approximately 20 °C and atmospheric pressure. No specific requirements were set for RH values.

The PDIV requirement applied to groundwall insulation was set at 1700 Vpp (1202 Vrms), with PDIV defined as the first voltage at which PD activity with a minimum PD charge was detected and sustained. During the design process, the minimum charge threshold used to define PDIV was revised from 0.05 nC to 0.5 nC. The specific threshold used in each case will be indicated in the following sections. PD activity was considered sustained when the minimum PD charge was also present at subsequent voltage levels.

An additional requirement specified that the groundwall insulation must withstand 2000 Vrms for 60 seconds without insulation failure. The fulfilment of this specification was ensured with HiPot tests.

5.2.2 Preliminary Prototype

The initial stage of the assessment involved a detailed review of the manufacturing process steps to identify and address potential design vulnerabilities, thereby ensuring a robust final configuration. First, possible weak points were identified, and corrective actions were taken where needed. Then, the evolution of PDIV through the manufacturing stages was evaluated. Finally, the effect of the potting was analysed. Although proper use of potting can enhance the insulation system, its primary purpose in this case was to ensure the thermal performance of the machine. All PDIV measurement results presented

in the following sections were obtained using the procedure described in Section 3.3.1 with a 0.05 nC PD charge threshold.

5.2.2.1 Weak Point Identification

The evaluation commenced after the preliminary prototype had already been designed and manufactured. This prototype consisted of a stator core, two TR300 resin 3D-printed caps (0.5 mm thick), and winding made of Grade 2 PI enamelled wire with a diameter of 0.3 mm (Section 3.1.2). During the preliminary inspection, two main critical points were identified:

- **Gap between the caps:** as specified in Section 3.1.2, the caps isolate the phases from the grounded stator core. The use of two caps, one inserted from each side, creates a 1.5 mm air gap between them (marked with rectangles in Figure 5.9 (a)). Since this space is filled with air, it presents a potential weak point with an increased likelihood of PD activity.
- **Thermistors:** Two thermistors were positioned between the winding coils due to design constraints. According to the standard IEC 60034-27-1 [144], thermistors should be connected to GND during PDIV measurements, making their insulation a potentially critical point.

To assess the first critical point, a 60 second HiPot test at 2000 Vrms was conducted on the stator before forming the delta connection and without thermistors, to verify compliance with the insulation strength requirement and to identify the weakest point by testing to failure. The test was carried out with all three phases connected to HV and the core connected to GND. While the first test passed successfully, ensuring the insulation strength requirement, two of the three phases failed in a subsequent test. It should be noted that the sample had previously undergone several PDIV and HiPot tests at lower voltage levels.

To determine the failure location, the stator was disassembled. The breakdown occurred in the air gap between the caps, affecting turns located closest to the core (i.e., the first turns of the coils, the circle in Figure 5.9 (a)). Visible discharge traces were found on the winding wire of several initial turns (Figure 5.9 (b)), and the stator core was visibly blackened in this area (Figure 5.9 (c)), particularly in the failed phases, confirming this region as a critical insulation weakness.

To assess the second critical point and confirm that no PD occurred between the winding and the thermistor, extra tests were performed in samples prepared by twisting the winding wire around the thermistor (Figure 5.10 (a)) and measuring the PDIV between the thermistor (connected to GND) and the winding wire (connected to HV). This configuration yielded a PDIV of 1330 Vrms. Although this exceeded the required specification, the same test was repeated with the thermistor enclosed in a thermoretractable

(a) (b) (c)

Figure 5.9: *Failure location identification (a) disassembling of the failed coil affecting the turns closest to the core, (b) discharge trace in the initial turns of the coil, and (c) blackened region in the stator core corresponding to the gap between the caps.*

tube to enhance insulation (Figure 5.10 (b)). This setup increased the PDIV to 1929 Vrms, 1.45 times higher than the unshielded configuration.

(a) (b)

Figure 5.10: *Winding wire twisted to the thermistor for PDIV measurements (a) without thermoretractable tube, and (b) with thermoretractable tube.*

As a result of these analyses, the final decision was to leave the gap between the caps unchanged, as it was assumed that the potting process would mitigate this potential weak point. Regarding the thermistor, since the insulation of the thermoretractable tube required minimal modifications to the production process, the company opted to implement this solution to ensure adequate thermistor insulation.

5.2.2.2 Partial Discharge Inception Voltage Evolution Through Manufacturing Stages Before Potting

After analysing potential weak points, the PDIV was evaluated throughout the manufacturing stages before potting. The process began with the stator assembled but without the delta connection (Figure 5.11 (a)). The next steps involved making the delta connection and attaching the output cables (Figure 5.11 (b)), followed by inserting the stator

into the housing (Figure 5.11 (c)), a critical stage due to the limited clearance between the routing and the housing. Finally, two shielded thermistors were installed between the winding coils (Figure 5.11 (d)).

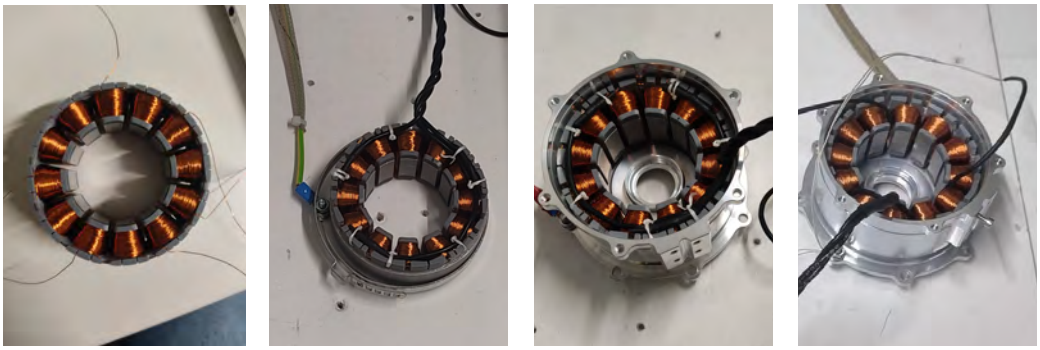

(a) (b) (c) (d)

Figure 5.11: *Preliminary prototype used to assess in the design process of an aeronautic machine in collaboration with a partner company (a) initial stator, (b) stator with delta connection and output cables, (c) stator mounted in the housing, and (d) stator mounted in the housing with the required thermistors.*

For the PDIV measurements, although the stator core was connected to GND in all cases, as specified in Section 3.3.1, the connection method differed depending on whether the stator was mounted in the housing. When the housing was not installed, a metallic flange was used to connect the GND terminal, as shown in Figure 5.11 (b). Conversely, when the stator was mounted inside the housing, the GND terminal was connected to the housing using a screw. The stator was inserted with the help of a press, ensuring direct contact between the stator and the housing. A multimeter was used to confirm that the stator was properly grounded.

Groundwall PDIV measurements for each manufacturing stage are shown in Figure 5.12. The stator data before the delta connection presents the average of three samples, while the rest correspond to one sample each (with each value being the average of three repeated measurements). All tests were carried out at 14-25 °C and 52-71% RH.

The results show consistent PDIV values among the initial stators, all exceeding the specified requirement of 1202 Vrms, which indicates a homogeneous manufacturing process. No significant PDIV variation was observed across the different manufacturing stages. The largest deviation, below 7%, occurred after inserting the stator into the housing. This was likely attributable to changes in ambient conditions rather than design-related issues, as these measurements were taken under the minimum temperature and humidity conditions. This confirmed that the clearance between the routing and housing was adequate.

Additionally, the absence of a notable difference between the configurations with and without thermistors suggests that the inclusion of the thermoretractable tube effectively improved the insulation of the thermistors. This is supported by the fact that the PDIV

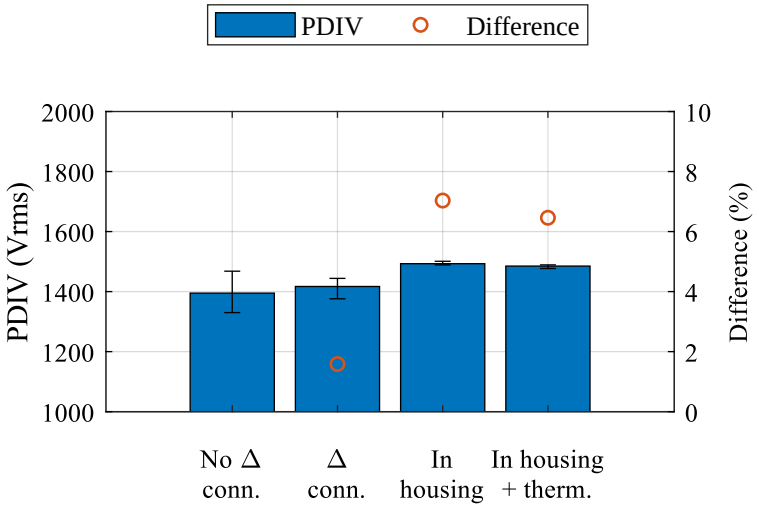

Figure 5.12: *Experimental PDIV measurement results for each manufacturing stage of the preliminary prototype.*

measured for the complete machine with shielded thermistors was higher than that obtained from the configuration with an unshielded thermistor twisted with the wire (Section 5.2.2.1).

In conclusion, the preliminary machine design met the PDIV specification at every stage before potting, being above the specified threshold by a margin of 23%.

5.2.2.3 Effect of the Potting

After confirming the groundwall PDIV compliance of the preliminary prototype and verifying the insulation integrity throughout the manufacturing stages before potting, the effect of the potting was evaluated. Although the potting was not primarily intended to enhance the insulation system, it was essential for fulfilling the thermal performance requirements of the machine. As described in Section 3.1.2, the applied potting was the XE 663 DK50/11 from Demak, and the potting was carried out on external facilities.

A preliminary potting application test was conducted by potting the stator (without housing) using external tooling to contain both the interior and the exterior parts of the machine. Figure 5.13 (a) and (b) show the configuration before and after the potting, respectively, where the thermistors are properly shielded. Visual inspection revealed a well-finished upper stator surface. In addition, a cross-section of another simultaneously potted dummy sample confirmed good impregnation through the winding, indicating effective air removal and lower PD probability.

Despite the success of the initial potting configuration, the preferred method was to perform the potting directly with the stator mounted in its housing. A preliminary batch of six samples was manufactured using this in-housing configuration (Figure 5.13 (c) and (d)). However, unlike the externally potted sample, most of the in-housing potted samples

exhibited defects such as suck backs (Figure 5.13 (d)), indicating that the potting material had drained downward during the curing process. Another indication of potential air entrapment was the absence of potting in the gap between the caps in several samples (Figure 5.14 (b)). Additionally, in some cases, winding wires were exposed at the potting surface (Figure 5.14 (c)).

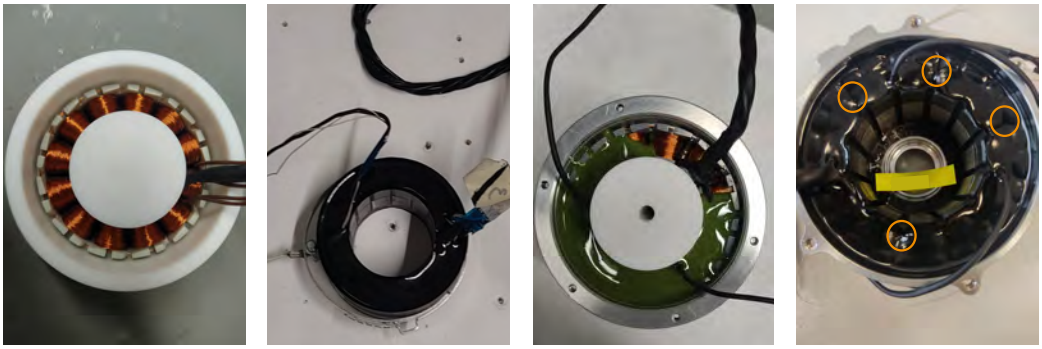

Figure 5.13: *Preliminary prototype (a) outside the housing before potting, (b) outside the housing after potting, (c) inside the housing during potting, and (d) inside the housing after potting.*

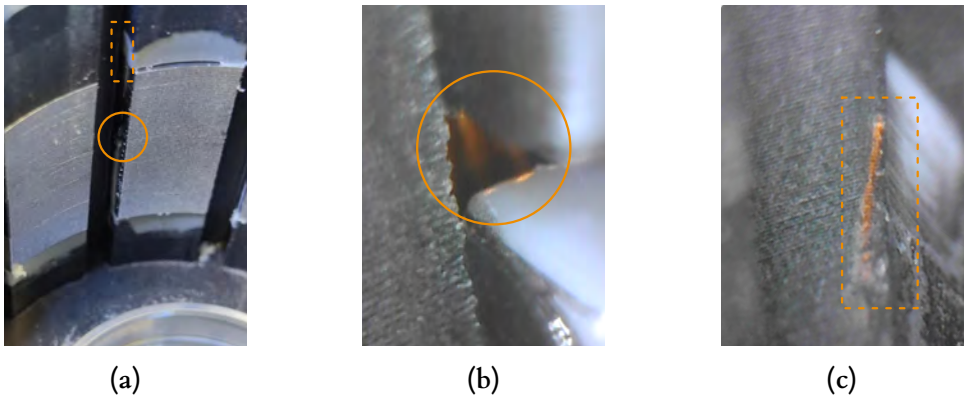

Figure 5.14: *Examples of potting defects identified in the in-housing potting process (a) failure locations, (b) lack of potting in the winding and gap between the caps, and (c) non impregnated winding wires.*

Figure 5.15 presents the comparison of PDIV values before and after potting for the outside and inside housing configurations. For the outside housing configuration, since only one sample was prepared, the figure reports the average, maximum and minimum values obtained from three repeated measurements on the same single sample. Conversely, for the in-housing process, the results show the average, maximum and minimum PDIV values (with error bars) of six samples.

Starting with the pre-potting condition, the limited difference among both configurations before potting, and the similarity with the non-potted samples presented in the previous Section 5.2.2.2 (results shown in Figure 5.12) confirms good manufacturing repeatability. When the potting is applied, for outside housing configuration, the PDIV

increases by 43%, suggesting that the process contributes positively to the insulation reliability. However, the PDIV improvement of the in-housing configuration is limited to 10%, likely due to insufficient potting in the critical gap area.

Interestingly, one of the samples of the in-housing configuration that exhibited a high PD charge (almost 8 nC) during pre-potting measurements showed a significantly reduced charge to 0.083 nC after potting. Even if PDIV improvements are modest, the lower PD charge contributes to insulation longevity by slowing down ageing in the event of discharge activity. Nonetheless, it is important to emphasise that the primary design goal was to achieve a PD-free system. Based on the defined PDIV threshold of 1202 Vrms, this condition was fulfilled even when potting defects were present, making discharge activation during operation highly unlikely.

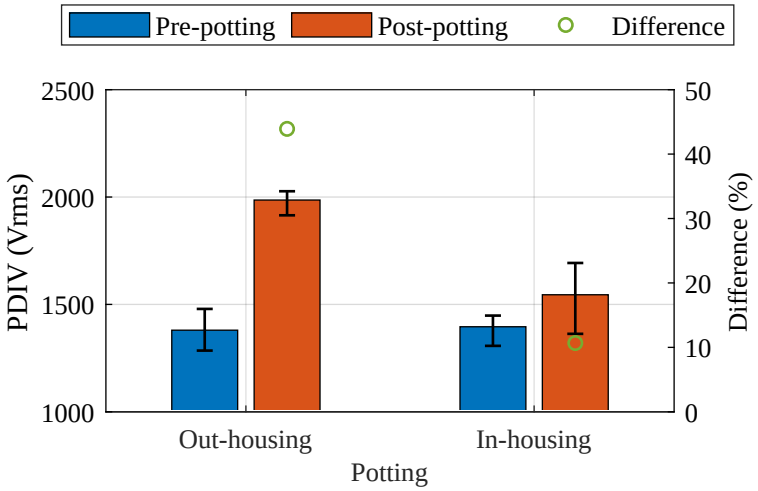

Figure 5.15: *Comparison of the PDIV obtained at pre-potting and post-potting condition with the stator potted outside the housing (out-housing) and inside the housing (in-housing).*

5.2.3 Improvement of the Preliminary Prototype

Based on the preliminary results presented in Section 5.2.2, several improvements were implemented, with particular focus on the cap design. The inter-cap gap, previously identified as a weak point, was targeted for reinforcement. Additionally, during the manufacturing of a product batch, issues with cap quality were detected due to degraded tolerances in the 3D printer used to fabricate the TR300 resin caps. All PDIV measurement results presented in the following sections were obtained using the procedure described in Section 3.3.1 with a 0.05 nC PD charge threshold.

5.2.3.1 Cap Design Modification and Stator Core Pre-Treatment Evaluation for Inter-Cap Gap Reinforcement

Given that the insulation weak point was located at the gap between the caps (where failure had previously occurred) and considering the likelihood of potting defects in this area, targeted efforts were made to reinforce this region. Different approaches were evaluated using prototypes manufactured with two alternative cap designs, both with a thickness of 0.7 mm and printed in TR300 resin. The first design preserved the 1.5 mm gap between caps, while the second introduced an overlapping configuration to eliminate the gap.

Additionally, three treatments applied before assembling the stator were also tested: no pre-treatment, varnishing the stator core, and manually applying potting on the gap or overlap area.

Figure 5.16 presents the groundwall PDIV results for each configuration (only one sample was tested per type). Overall, the overlapping design did not lead to a significant improvement in PDIV compared to the gapped design, likely due to the persistence of small air gaps between the overlapping surfaces. The use of pre-treatments, whether varnish or manual potting, resulted in a slight increase in PDIV, but not enough to justify an additional manufacturing step.

Based on these findings, the company selected the overlapping cap design without any pre-treatment for the final configuration. The final cap design for the manufacturing of the product was a 0.85 mm thick overlapping cap.

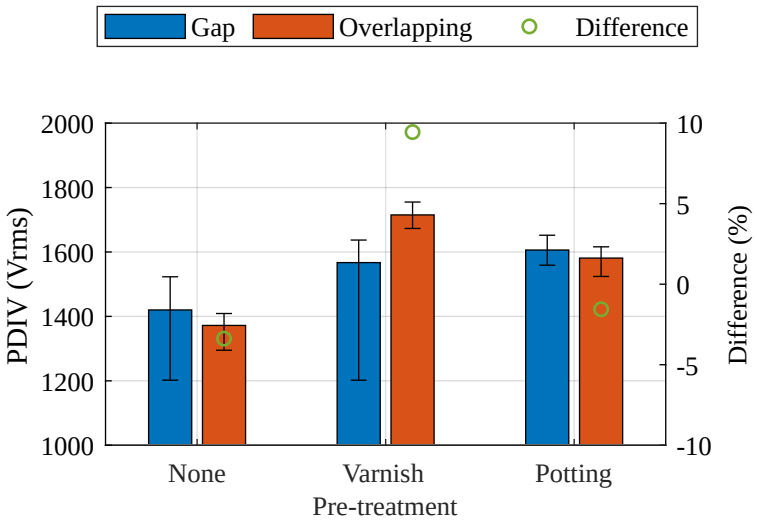

Figure 5.16: *Comparison of the PDIV obtained with different cap designs and pre-treatment application.*

5.2.3.2 Cap Manufacturing Problems

During the manufacturing of the final product batches, issues were identified in the TR300 resin 3D printing stage of the cap. Although the design was unchanged, the printer failed to meet the required cap thickness tolerances, resulting in thicker caps than intended. As a consequence, the same number of coil turns using the same winding manufacturing parameters resulted in reduced inter-coil spacing, with instances where coils made direct contact. Figure 5.17 shows a comparison between correctly separated coils (a), and coils in contact (b).

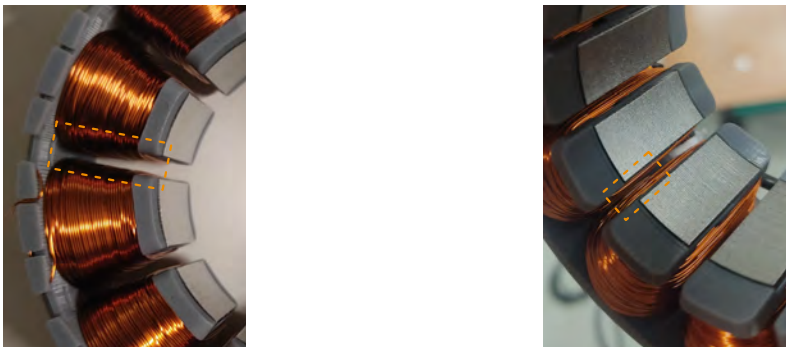

(a) (b)

Figure 5.17: *Spacing between coils after needle winding (a) correct separation, and (b) in direct contact.*

To verify the integrity of the phase-phase insulation in the cases where the coils are in direct contact, samples with the same theoretical cap thickness, but different real thicknesses were tested. Three samples were measured: one with correct spacing (no cap manufacturing issues), one with slightly reduced spacing due to a moderate cap thickness increase, and one where the coils were in contact. The measurements were performed at 20 °C and 83% RH, with one phase connected to the HV terminal and the other two to GND (as shown in Figure 3.6 (a), Section 3.3.1).

Figure 5.18 collects the resulting phase-phase PDIV values. As expected, PDIV decreased as the coil spacing was reduced. In the case where coils were touching, the measured value (656 Vrms) was similar to the theoretical PDIV of a TP made of the same material and insulation grade (565 Vrms, per equation (4.27)). These results confirm that cap manufacturing precision is critical, as excessive thickness directly compromises phase-phase insulation reliability. They also verify that the routing design effectively maintains proper phase separation under normal conditions, as the obtained phase-phase PDIV value is greater than the groundwall value for the specimen with the correct coil separation.

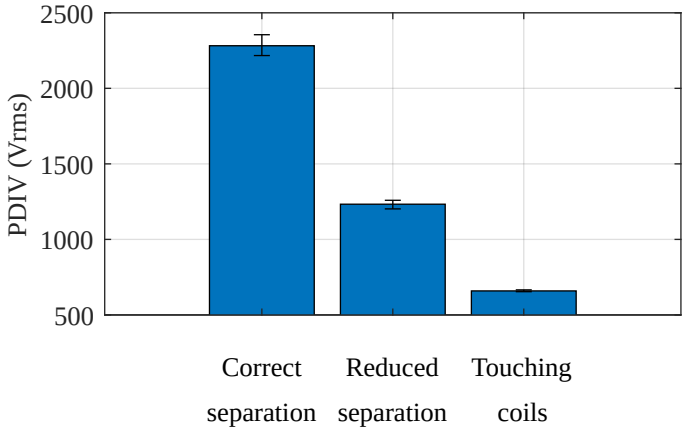

Figure 5.18: *Experimental phase-phase PDIV results when the spacing between coils is ensured (correct separation), reduced (reduced separation), and nonexistent in some parts (touching coils).*

5.2.3.3 Cap Final Material and Thickness Definition

To ensure consistent and reliable cap production and avoid coil spacing problems described in Section 5.2.3.2, the company opted to transition to Nylon 12, which allows for more precise fabrication using a different 3D printer with better tolerance control. However, concerns were raised about the higher porosity of Nylon 12 and its potential effect on insulation performance. As a result, comparative tests were conducted between TR300 resin and Nylon 12 for 0.70, 0.85, and 1.00 mm thicknesses using three samples per case (samples presented in Section 3.1.2, Figure 3.2).

Firstly, the evaluation and comparison of the materials and thicknesses was done theoretically, applying PDIV models proposed in Section 4.3.1 and Section 4.3.2. In addition to comparing the design, this was valuable for assessing the usefulness of the models to estimate groundwall insulation in addition to interturn insulation. This comparison was limited to Nylon 12 samples (with $\varepsilon_r = 3.6$, provided by the company), as permittivity data for TR300 resin was unavailable. While the theoretical thicknesses were 0.70, 0.85, and 1.00 mm in design, actual measured thicknesses (via micrometer) were 0.48, 0.67, and 0.79 mm, respectively (mean value of the three samples per thickness). The wire was the one used in the machines, a PI enamelled wire of 0.3 mm nominal diameter and Grade 2, with an average insulation thickness of 21.75 µm (Section 3.1.2) and $\varepsilon_r = 3.093$ (Table 3.2).

The Extended parallel-plate model was applied using equation (4.21), adjusting $\gamma = 0.15$ to minimise error across the tested thicknesses (this adjustment method is widely used in the literature, as stated in Section 4.2). This adjustment reduced error by more than 20% compared to the general value of $\gamma = 0.0025$ proposed in [68]. For the Extended Dakin's model, an adaptation (equation (5.3)) was used to account for multiple insulations.

$$\text{PDIV} = (0.25\ AH + 183.75)\left(\frac{t_{\text{ins}_1}}{\varepsilon_{\text{r ins}_1}} + \frac{t_{\text{ins}_2}}{\varepsilon_{\text{r ins}_2}} + \ldots\right)^{-0.0004\ AH + 0.3972} \tag{5.3}$$

Table 5.2 presents the PDIV estimations obtained with both models. As expected, higher PDIV values are estimated as the insulation thickness increases. At the minimum thickness, the Extended parallel-plate model predicts a lower value. Nonetheless, it exceeds the Extended Dakin's model at higher thicknesses. This suggests that the Extended parallel-plate model is more sensitive to insulation thickness than the Extended Dakin's model.

Considering the requirement of 1202 Vrms, all thicknesses meet this criterion. Nevertheless, the design thickness of 0.70 mm is close to the limit. Thus, a design thickness of 0.85 mm is recommended as the minimum value.

Table 5.2: *Estimated PDIV values using Extended Dakin's and Extended parallel-plate models for Nylon 12 cap samples.*

Groundwall t_{ins} (mm)		PDIV (Vrms)	
Designed	**Measured**	**Ext. Dakin's**	**Ext. parallel-plate**
0.70	0.48	1285	1249
0.85	0.67	1460	1567
1.00	0.79	1556	1759

Experimental tests were performed to validate the estimation analysis and compare both materials. Each material was tested at 20 °C and 77-80% RH by connecting the enamelled wire to the HV terminal and the metallic electrode to GND. Three samples of each material and thickness were measured. The average, maximum, and minimum PDIV values are shown in Figure 5.19. As expected, PDIV increased with insulation thickness for both materials. The 0.70 mm TR300 sample yielded results consistent with the overlapping cap configuration in Figure 5.16, with a 12% deviation probably due to the trapped air between the overlapping surfaces, indicating that such simplified samples can provide useful preliminary insights for groundwall insulation material and thickness selection.

Comparing the two materials, TR300 resin exhibited higher PDIV values within 10%, but both exceeded the minimum requirement of 1202 Vrms. However, for 0.70 mm Nylon 12 sample, audible PD activity was detected, and one sample failed after several measurements. The failure occurred at the upper corner of the cap, where the material was perforated (Figure 5.20). Based on these observations, Nylon 12 was deemed a viable alternative, provided the cap thickness was at least 0.85 mm.

Table 5.3 further compares experimental and modelled PDIV values. Both models showed good agreement with the measurements. The Extended Dakin's model had a maximum deviation of 4.6%, and the Extended parallel-plate model, with the optimised γ, had a maximum error of 11.0%. These findings align with earlier conclusions in Section 4.3.3, confirming the applicability of both models to groundwall insulation.

Although both methods are valid, the Extended Dakin's model may be preferred due to its more conservative estimates and the lack of need for empirical adjustment. These

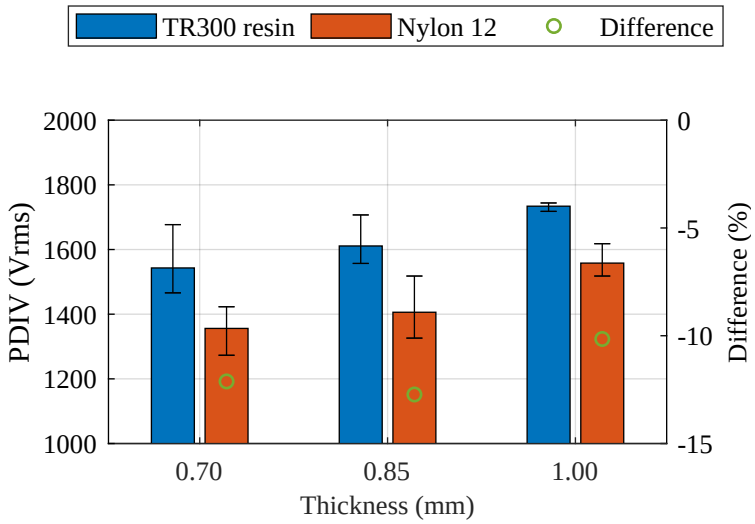

Figure 5.19: *Experimental PDIV measurement results for the cap samples with different insulation thicknesses (0.70, 0.85, and 1.00 mm) and materials (TR300 resin and Nylon 12).*

(a) (b)

Figure 5.20: *Failure location of the breakdown during PDIV measurements of 0.70 mm Nylon 12 sample (a) cap sample, and (b) electrode.*

preliminary results demonstrate the usefulness of the model in early-stage design, offering a faster alternative to more complex approaches like FEM simulations [133].

As previously discussed, cap samples can serve as valuable tools in guiding the selection of groundwall insulation thickness and materials before full prototyping. Establishing a correlation between PDIV estimations and measurements obtained from these samples can significantly support the definition of the insulation system and streamline the design process. Although further investigation, including a wider range of materials and environmental conditions, is required, these preliminary results highlight the potential of the proposed Extended Dakin's model as a fast and reliable method for early-stage insulation design decisions.

Ultimately, the company validated the Nylon 12 as the cap material, with a minimum thickness of 0.85 mm and an overlapping design. A prototype was manufactured to verify

Table 5.3: *Comparison of the experimental and modelled PDIV values using Extended Dakin's and Extended parallel-plate models for Nylon 12 cap samples.*

Groundwall t_{ins}(mm)		PDIV (Vrms)			Difference (%)	
Designed	Measured	Exp.	Ext. Dakin's	Ext. parallel-plate	Ext. Dakin's	Ext. parallel-plate
0.70	0.48	1359	1285	1249	-4.4	-11.0
0.85	0.67	1406	1460	1567	4.6	7.8
1.00	0.79	1558	1556	1759	0.5	9.1

that this configuration did not complicate the winding process and ensured sufficient coil spacing. Due to the improved manufacturing precision of the 3D printer used for Nylon 12, proper phase-phase clearance was successfully maintained.

5.2.4 Final Validation of the Design

This section presents the results of the final machine validation. Based on the developments described above, the final design incorporated a 0.85 mm thick cap with an overlapping configuration, thermistors shielded with thermoretractable tubing, and potting performed directly with the stator mounted in the housing. The samples were produced in three batches, referred to as B1, B2, and B3, and each unit was evaluated at the final manufacturing stage (post-potting) to ensure compliance with the groundwall PDIV (performed as described in Section 3.3.1) requirement of 1202 Vrms. Initially, this threshold was defined considering sustained PD activity with a minimum charge of 0.05 nC. During the manufacturing of B2, however, this limitation was revised to 0.5 nC.

Additionally, although Nylon 12 was selected as the final cap material (Section 5.2.3), all B1 samples and a portion of those from B2 and B3 were manufactured using TR300 resin.

5.2.4.1 Partial Discharge Inception Voltage Estimation due to Partial Discharge Charge Threshold Changes

As mentioned in Section 5.2.1, the PD threshold was revised from 0.05 nC to 0.5 nC during the assessment process. Unfortunately, this updated criterion could not be retroactively applied to all B1 samples after potting, as some were no longer available for testing. Furthermore, it was not possible to infer the PDIV using the 0.5 nC criterion from measurements obtained with the 0.05 nC threshold, since the discharge levels recorded in those tests did not reach 0.5 nC. Therefore, the objective of this section is to evaluate whether the PDIV values obtained under the 0.05 nC criterion can be extrapolated to the 0.5 nC threshold for the relevant samples, thus ensuring that all units from all batches

comply with the updated specification.

For the pre-potting PDIV results (using TR300 resin caps), as this stage represented an intermediate step before final machine validation, the goal was not to determine a definitive PDIV value. Instead, the aim was to verify batch-to-batch repeatability and assess whether the results obtained with the 0.05 nC threshold could predict the expected values using the 0.5 nC criterion.

In the PDIV measurements, B1 and B2 machines were tested using the 0.05 nC criterion. Table 5.4 summarises the results for both batches using TR300 resin caps. When comparing B1 to B2, the average PDIV differed by only 1.5%, confirming the repeatability between batches. Based on this observation, it was assumed that the pre-potting PDIV values of B1, if measured using the 0.5 nC threshold, would be equivalent to those of B2. Additionally, with the 0.05 nC the defined threshold (1202 Vrms) was already exceeded for B1.

Interestingly, the results for B2 were consistent with those obtained for the 0.85 mm thick TR300 resin cap sample (Figure 5.19), showing a deviation of approximately 6%. The similarities with the manufactured stator reinforced the use of the cap sample as a preliminary measurement method for the material selection and the use of, particularly, the Extended Dakin's model for the preliminary estimation of the groundwall PDIV.

Table 5.4: *Comparison of the measured pre-potting PDIV values with 0.05 PD charge threshold for batches 1 (B1) and 2 (B2) TR300 resin cap units of the final validation of the design.*

Batch	Number of samples	PD threshold (nC)	$PDIV_{mean}$ (Vrms)	$PDIV_{max}$ (Vrms)	$PDIV_{min}$ (Vrms)
B1	9	0.05	1553	1642	1377
B2	12	0.05	1529	1661	1424

After ensuring consistent performance across batches in the pre-potting stage, an equivalent PDIV value was estimated for post-potting samples that were not evaluated using the 0.5 nC threshold. For this purpose, a subset of post-potting samples from B1 and B2, all with TR300 resin caps, were compared using both the 0.05 nC and 0.5 nC criteria.

Table 5.5 presents the measured PDIV values under both definitions for tested samples. On average, the PDIV value determined using 0.5 nC threshold was approximately 1.3 times greater than that obtained using the 0.05 nC threshold. Accordingly, for B1 samples not tested at 0.5 nC, the estimated PDIV was calculated as 1.3 times the measured PDIV with the 0.05 nC criterion. This estimation was applied exclusively to post-potting results for machines with TR300 resin cap units, ensuring a consistent dataset across all manufactured units. In total, the post-potting PDIV values of 11 samples from B1 were estimated using this method, presented later in Section 5.2.4.2.

Table 5.5: *Comparison of the measured post-potting PDIV values with 0.05 and 0.5 nC PD charge threshold for batches 1 (B1) and 2 (B2) TR300 resin cap units of the final validation of the design.*

Batch	Number of samples	PD threshold (nC)	$PDIV_{mean}$ (Vrms)	$PDIV_{max}$ (Vrms)	$PDIV_{min}$ (Vrms)	$PDIV_{mean}$ difference (p.u)
B1	8	0.05	1723	2288	1254	1.3
		0.5	2280	2500	1917	
B2	14	0.05	1892	2241	1420	1.3
		0.5	2389	2500	2103	

5.2.4.2 Validation of the Final Units: Partial Discharge Inception Voltage Measurement and HiPot Tests at Ambient Temperature

As previously mentioned, samples of three batches were measured considering a consistent PD activity criterion with a minimum charge of 0.5 nC. Table 5.6 summarises the number of samples measured in each batch, distinguishing between materials and pre-potting (Pre) and post-potting (Post) conditions. As discussed in Section 5.2.4.1, some PDIV values from B1 in post-potting condition were estimated (11 of the 19 samples).

Table 5.6: *Number of samples measured per material and batch in the pre-potting (Pre) and post-potting (Post) conditions for the final validation of the design, considering a consistent PD activity with a charge equal or higher than 0.5 nC.*

Material	B1		B2		B3	
	Pre	Post	Pre	Post	Pre	Post
TR300 resin	0	19 (11/19 estimated)	12	14	24	22
Nylon 12	0	0	0	3	11	10

Starting with the pre-potting condition, measurements were conducted in ambient conditions ranging from 18-25 °C range and 56-85% RH. Table 5.7 summarises for both cap materials (TR300 resin and Nylon 12), whereas Figure 5.21 presents the probability density distribution. Despite a 2.5% difference in the mean PDIV between B2 and B3 for TR300 resin, B3 samples showed greater dispersion. Nonetheless, all results exceeded the 1202 Vrms requirement. B1 samples were not measured in 0.5 nC threshold condition in the pre-potting stage, but their PDIV was assumed equivalent to that of B2, as detailed in Section 5.2.4.1.

When comparing B3 results for the two cap materials, Nylon 12 yielded a 5.4% higher average PDIV with lower dispersion. This outcome contrasts with the trend observed in the cap sample comparison (Section 5.2.3.3), where TR300 resin performed better. However, it is important to highlight that the discharge magnitudes recorded

during PDIV testing were significantly higher for Nylon 12 cap units. In these cases, peak discharge values in samples with Nylon 12 caps exceeded 43 nC (limited by sensor range), whereas samples with TR300 resin caps remained below 3 nC. In several tests involving Nylon 12 caps, the partial discharge activity was even audible.

Table 5.7: *Groundwall mean, minimum, and maximum PDIV (Vrms) values for TR300 resin and Nylon 12 cap units in the pre-potting condition for the batches of the final validation of the design, considering a consistent PD activity with a charge equal or higher than 0.5 nC.*

Material	B1			B2			B3		
	Mean	Min	Max	Mean	Min	Max	Mean	Min	Max
TR300 resin	-	-	-	1672	1616	1773	1714	1551	1938
Nylon 12	-	-	-	-	-	-	1806	1711	1910

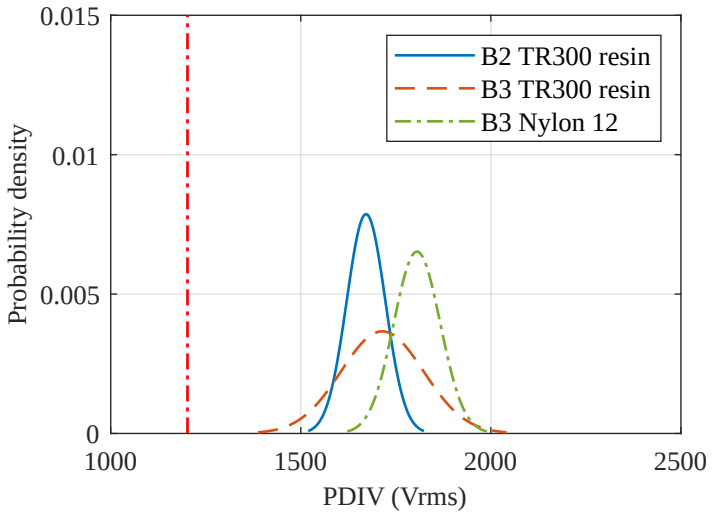

Figure 5.21: *Probability distribution of the groundwall PDIV results in the pre-potting condition of the final validation of the design, considering a consistent PD activity with a charge equal or higher than 0.5 nC for the units with caps made by TR300 resin and Nylon 12.*

It is worth noting that the PDIV measurements in the pre-potting condition also revealed two types of manufacturing defects in several machines:

- **Thermistor related issues:** Deficiencies in the thermoretractable tubing installed on the thermistors were identified (Figure 5.22 (a)), resulting in lower-than-expected PDIV values. To verify this, measurements were repeated with the thermistors disconnected from GND, resulting PDIV values in line with expectations. This confirmed that the thermistor-to-GND connection was responsible for the PDIV reduction. The failing thermistor was removed and replaced before the potting process, where a failure on the thermoretractable tube was visible.
- **Routing related issues:** Although the measured PDIV met the expected value for

a sample with TR300 resin caps, the corresponding discharge magnitudes were abnormally high (approximately 24 nC, compared to typical values below 3 nC for TR300 resin cap units). Visual inspection revealed that, in certain routing areas, the winding wire was almost in contact with the housing (Figure 5.22 (b)). After applying Kapton tape to the affected area, the discharge magnitude dropped to 2 nC. Since disconnecting the thermistor from GND did not alter the result, the issue was attributed to the routing, which was corrected before the potting stage.

(a) (b)

Figure 5.22: *Manufacturing defects revealed during the pre-potting PDIV measurements (a) broken thermoretractable tube in the thermistor, and (b) winding wire almost touching the housing in the routing.*

Following with the post-potting results obtained under environmental conditions of 18–21 °C and 63–76% RH, Table 5.8 summarises the mean, maximum, and minimum PDIV values obtained for both cap materials across the three batches. The corresponding probability density distributions are presented in Figure 5.23. A general observation is that the potting process increased the variability of the PDIV results. This increase was primarily attributed to the potting process itself, as most samples exhibited visible surface defects that may indicate the presence of internal air bubbles. Additionally, the lower variability observed in the pre-potting condition indicates that the dispersion caused by earlier manufacturing stages and the measurement procedure was more controlled.

Despite this, with TR300 resin cap units, the largest difference observed among the mean value of the three batches was 8.6%, specifically between B1 and B2. It is also worth noting that the implementation of the overlapping cap design improved the PDIV compared to the preliminary potted prototype that featured an inter-cap gap with lack of potting penetration (Figure 5.14).

Regarding the Nylon 12, the difference in mean PDIV between the two batches was 9.1%. The average PDIV value for Nylon 12 remained lower than that obtained for TR300 resin cap units. Nevertheless, the minimum PDIV value measured for all Nylon 12 samples still exceeded the defined specification threshold of 1202 Vrms, and the likelihood of obtaining a value below this requirement was found to be insignificant.

Lastly, Table 5.9 and Figure 5.24 compare the pre-potting and post-potting conditions

Table 5.8: *Groundwall mean, minimum, and maximum PDIV (Vrms) values for TR300 resin and Nylon 12 cap units in the post-potting condition for the batches of the final validation of the design, considering a consistent PD activity with a charge equal or higher than 0.5 nC.*

Material	B1			B2			B3		
	Mean	Min	Max	Mean	Min	Max	Mean	Min	Max
TR300 resin	2199	1631	2500	2389	2103	2500	2374	2061	2500
Nylon 12	-	-	-	2389	1758	1994	1690	1250	1875

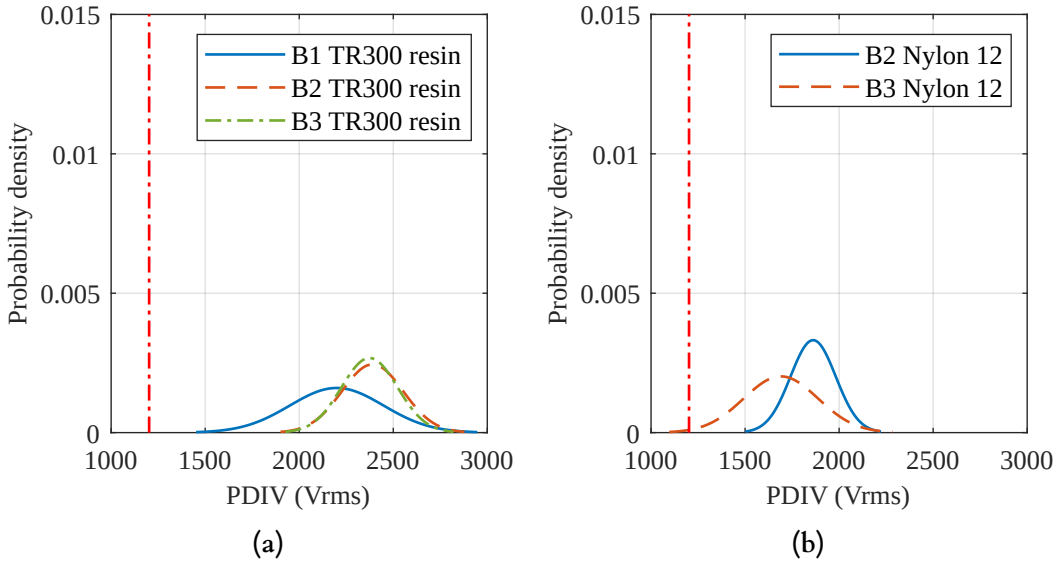

Figure 5.23: *Probability distribution of the groundwall PDIV results in the post-potting condition of the final validation of the design, considering a consistent PD activity with a charge equal or higher than 0.5 nC for the units with caps made by (a) TR300 resin, and (b) Nylon 12.*

for both cap materials, considering samples from all batches. In the pre-potting condition, the use of TR300 resin caps resulted in greater dispersion of PDIV values and a slightly lower average value, with a 5.8% reduction compared to Nylon 12 caps.

Despite the observed variability, it is important to highlight that for TR300 resin cap units, the average PDIV increased by 27% following the application of potting. This average improvement was observed even though visual defects, such as bubbles and sink marks, were present in the potting layer of some samples.

Conversely, for Nylon 12 caps, the potting process led to a 4% decrease in the mean PDIV, along with lower minimum values. This reduction in performance was also visible during visual inspection, particularly in the upper part of the machines, suggesting a lower potting quality compared to the TR300 resin samples. Indeed, due to the improved dimensional tolerances achieved with Nylon 12 caps, applying the same potting volume resulted in a lower filling level, probably leading to a higher air content within the winding region.

Table 5.9: *Groundwall mean, minimum, and maximum PDIV (Vrms) values for TR300 resin and Nylon 12 cap units in the pre-potting and post-potting conditions for the batches of the final validation of the design, considering a consistent PD activity with a charge equal or higher than 0.5 nC.*

Material	Pre-potting			Post-potting		
	Mean	Min	Max	Mean	Min	Max
TR300 resin	1700	1551	1938	2318	2103	2500
Nylon 12	1806	1711	1910	1730	1250	1994

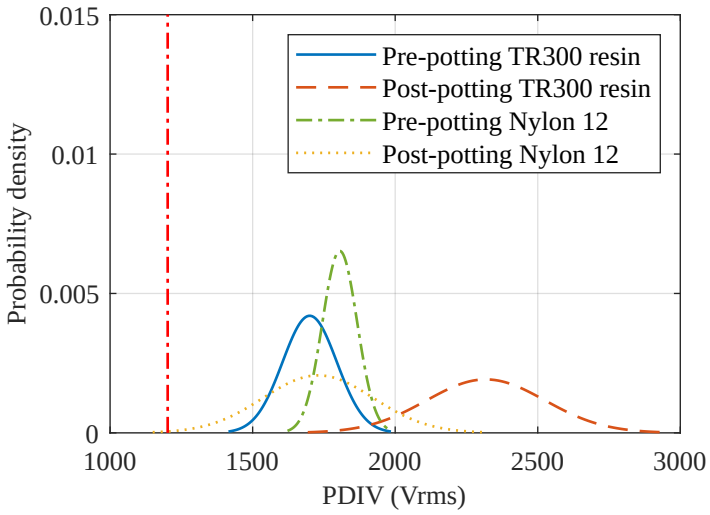

Figure 5.24: *Probability distribution of the groundwall PDIV results in the pre-potting and post-potting conditions of the final validation of the design, considering a consistent PD activity with a charge equal or higher than 0.5 nC for the units with caps made by (a) TR300 resin, and (b) Nylon 12.*

Nevertheless, a key benefit of potting in Nylon 12 samples was the significant reduction in PD activity magnitude, which reached levels comparable to those measured in TR300 resin cap samples. In other words, although potting did not improve the PDIV for Nylon 12 cap samples, it was still necessary to reduce the severity of discharge events, thus mitigating insulation ageing in the unlikely event that PD activity occurs. Notably, all measured PDIV values remained above the 1202 Vrms specification.

To verify compliance with the HiPot test requirement of withstanding 2000 Vrms for 60 seconds without failure, two post-potted samples with Nylon 12 caps and three with TR300 resin caps were subjected to a 120 second test. All samples passed without breakdown. Even more severe voltage conditions were applied multiple times to a TR300 resin cap unit, yet insulation failure could not be reached.

In summary, the impact of the potting on the insulation system was not as beneficial as initially anticipated. Even the mean value obtained in the samples with TR300 resin

caps, the variability introduced in the insulation performance of the final machine was considerable. This drawback was more pronounced in machines with Nylon 12 caps, where the PDIV values generally decreased following the potting process. Nevertheless, the minimum groundwall PDIV value still exceeded the defined specification of 1202 Vrms. Despite the considerable variability introduced by manufacturing processes (e.g., thermistor placement, routing, potting procedures) and the presence of defects like surface bubbles or suck backs in the potting, all machines fulfilled the PDIV requirement when assessed using a 0.5 nC minimum discharge charge and sustained partial discharge activity as the acceptance criteria.

Although the use of Nylon 12 generally resulted in lower insulation performance compared to TR300 resin, the company ultimately chose to adopt this material for cap manufacturing in subsequent batches. This decision was based on its improved manufacturing consistency rather than real insulation performance, particularly in achieving tighter thickness tolerances, which helps reduce the likelihood of phase-phase insulation issues.

5.2.5 Concluding Remarks

This study presents a comprehensive evaluation of the insulation system during the design of a machine for aeronautic applications, integrating PDIV analysis throughout the development process. The assessment of the preliminary prototype enabled early identification of critical insulation weaknesses, particularly the thermistor insulation and inter-cap gap. These issues were mitigated by implementing thermoretractable shielding and adopting design modifications, such as overlapping caps, both of which improved insulation performance without compromising manufacturability.

PDIV measurements conducted through the manufacturing stages demonstrated high repeatability and confirmed that no degradation occurred from the initial assembly steps to the final stage before potting. All configurations complied with the defined groundwall PDIV requirement of 1202 Vrms.

Cap design and material selection were subsequently optimised due to the dimensional inconsistencies observed in the initial batches of TR300 resin cap units. This analysis was conducted through estimation and experimental measurements using simplified cap samples. The comparison between estimated and experimental PDIV for Nylon 12 groundwall insulation validated the use of Extended Dakin's and Extended parallel-plate models as preliminary tools, showing a maximum error of 4.6% and 11%, respectively. The Extended Dakin's model was particularly advantageous, as it required no parameter adjustment for different materials.

Furthermore, similarities between the simplified cap sample and the final machine specimens before potting validated their usefulness as early-stage assessments. These findings also support the applicability of the Extended Dakin's model for estimating PDIV in groundwall insulation, as demonstrated by the consistency between modelling and

experimental results. Although TR300 resin cap units exhibited superior electrical performance, Nylon 12 was ultimately selected for production due to its improved dimensional control, which ensured consistent phase separation exceeding the groundwall insulation requirement.

The final validation of the complete machine confirmed compliance with PDIV specification across all tested units. For TR300 resin cap samples, the potting improved effectively the insulation strength, despite introducing considerable variability. For Nylon 12 cap specimens, although the potting process had a limited effect on improving insulation strength, primarily due to irregularities and possible internal voids, it significantly reduced PD magnitudes. This reduction contributes positively to insulation ageing resistance. Even the lower groundwall PDIV showed at the end stage of the product, Nylon 12 caps were selected by the company due to improved manufacturing consistency.

The final configuration, combining 0.85 mm Nylon 12 caps, overlapping geometry, shielded thermistors, and potting process, offered a reliable and manufacturable insulation solution suitable for the intended aeronautic application. This configuration successfully fulfilled the required 1202 Vrms for the groundwall PDIV in all specimens, withstanding 120 seconds at 2000 Vrms without insulation failure.

Chapter 6

Study of Insulation System Degradation and Fault

In addition to assessing PDIV under the operating conditions of electric machines and designing an effective insulation system, another key factor for ensuring long-term reliability is insulation degradation. As discussed in Section 2.1.3.3, PDIV decreases over the lifetime of the insulation due to electrical, environmental, and other stress factors. Therefore, it is essential to evaluate not only how these factors influence PDIV at initial operating conditions but also their role in insulation degradation and the associated risk of failure.

Beyond design considerations, monitoring the health of the insulation system throughout its lifetime is crucial to prevent unexpected failures and enable preventive maintenance. Regular assessment of insulation condition helps anticipate failures and supports maintenance decisions based on observed degradation trends.

In this chapter, the impact of various stress factors on insulation health and their role in potential failures is reported. Additionally, it reviews different techniques and markers for imminent failure detection and insulation health diagnosis. Part of the work presented in this chapter is supported by a conference proceeding [23].

6.1 Assessment of the Most Critical Factors Affecting Insulation Endurance

Understanding the factors that affect insulation lifespan is crucial for enhancing the reliability and longevity of electric machines. Insulation deterioration results from various operational and environmental stresses that, over time, can weaken its performance and increase the likelihood of failure (Section 2.1.3.3). Identifying these influences allows for a more robust insulation system that can better endure real conditions.

Insulation deterioration in stator windings is influenced by multiple stress factors, with the most significant categorised as TEAM stresses: Thermal, Electrical, Ambient, and Mechanical. These stresses contribute to insulation ageing and can lead to premature failure.

Ambient stress encompasses a range of environmental factors that can alter the dielectric properties of the insulation, including moisture condensation, high humidity, pressure, aggressive chemicals, oil contamination, and dirt ingress [26]. However, their effect is generally less significant than thermal or electrical factors [51]. Their main contribution lies in increasing variability in degradation trends, rather than directly accelerating ageing. For this reason, alongside mechanical factors, ambient stress is not considered in the present study. Instead, attention is given to the effects of thermal and electrical stresses, which are widely recognised as primary contributors to insulation degradation in electric machines [51].

By recognising how thermal and electrical factors contribute to degradation, it is possible to adjust design choices and operating parameters to reduce their impact. Minimising exposure to harmful conditions through informed decisions in material selection and system configuration can help extend insulation durability and improve overall machine performance, ensuring reliable machine operation.

6.1.1 Thermal Stress

Thermal stress arises from temperature fluctuations and sustained exposure to elevated temperatures, which cause material embrittlement and chemical degradation. The following sections summarise the main effects of thermal stress as reported in the literature. This review is complemented by an experimental comparison between isothermal and thermomechanical ageing, identified as the two primary thermal cycles used in accelerated thermal ageing studies. Finally, the effectiveness of thermomechanical ageing as an accelerated ageing method is evaluated.

6.1.1.1 Overview of the Effect of the Thermal Stress on Insulation Endurance

The rise in winding temperature caused by Joule losses during operation exposes the insulation system to thermal stress. When the temperature surpasses a critical limit, chem-

ical reactions, notably oxidation, induce embrittlement of the insulation, thus hastening its deterioration [26]. In general, higher ageing temperatures are associated with shorter lifetimes [51, 80, 145, 146], with the degradation rate accelerating once the ageing temperature exceeds the insulation thermal class. This implies that the impact of thermal stress becomes significantly more pronounced as the difference between ageing temperature and insulation thermal class (ΔT) increases.

In [147] researchers observed a significant reduction in breakdown time when higher temperatures were applied to the samples. For example, increasing the temperature from 235 to 255 °C reduced the time to failure by at least half (from 288 h to 72–144 h). A comparable effect was also reported by [148] for samples subjected to electrothermal ageing. When the electric ageing occurred at 100 °C, the breakdown time was reduced by 91% compared with room-temperature conditions. Although the samples experienced PD activity, this accelerated degradation was attributed primarily to changes in the chemical bonds within the insulation material rather than alterations in PD, given the similar PD characteristics throughout the temperature range studied.

Beyond insulation breakdown, several studies have explored the influence of thermal ageing on PDIV [17, 20, 90, 119, 147, 149, 150]. It is generally recognised that higher ageing temperatures cause more pronounced reductions in PDIV, particularly when temperatures exceed the insulation thermal class. This trend has been consistently observed for non-impregnated TPs or PCs [17, 20, 119, 151], impregnated TPs [152], impregnated motorettes [150], and assembled impregnated stators [147]. Some studies identified an initial sharp reduction in PDIV during the first hours of ageing, followed by a more gradual decline, fitting an inverse power law [17, 20, 150, 153]. In contrast, other investigations observed a linear decrease without a clearly defined stabilisation stage [119, 151].

The main effects of thermal stress on insulation performance are reductions in insulation thickness [119, 151] and changes in relative permittivity [119]. For instance, it was reported in [119] that insulation thickness remained mostly unchanged for the PAI overcoat across the tested ageing temperature range (180 to 220 °C), consistent with its thermal index (220 °C, thus $\Delta T = 0$ °C). PEI basecoat, however, exhibited a thickness reduction of 50% after 1650 h at 220 °C ($\Delta T = 40$ °C), although remaining stable below its thermal rating. A similar effect, with a reduction of 33% insulation thickness, was reported for PEI+PAI at 250 °C ($\Delta T = 50$ °C) after 312 h, alongside a reduction in relative permittivity [151]. As stated in Section 2.2.2, a lower relative permittivity results in a reduced electric field intensity in the air gap, thereby theoretically increasing the PDIV. However, as experimental results showed a continued decline in PDIV with ageing time [151], they concluded that the thickness reduction had a dominant impact compared to the effect of reduced permittivity.

Additionally, [119] demonstrated that PDIV of thermally aged samples could be effectively estimated using established prediction models (Section 4.2), particularly the Dakin equation, by incorporating insulation thickness and permittivity measured at various ageing stages. Similarly, the FEM+Schumann's criterion model was also successfully applied in [151] for the same purpose. Figure 6.1 summarises selected findings from these

studies, and Table 6.1 provides the corresponding experimental details.

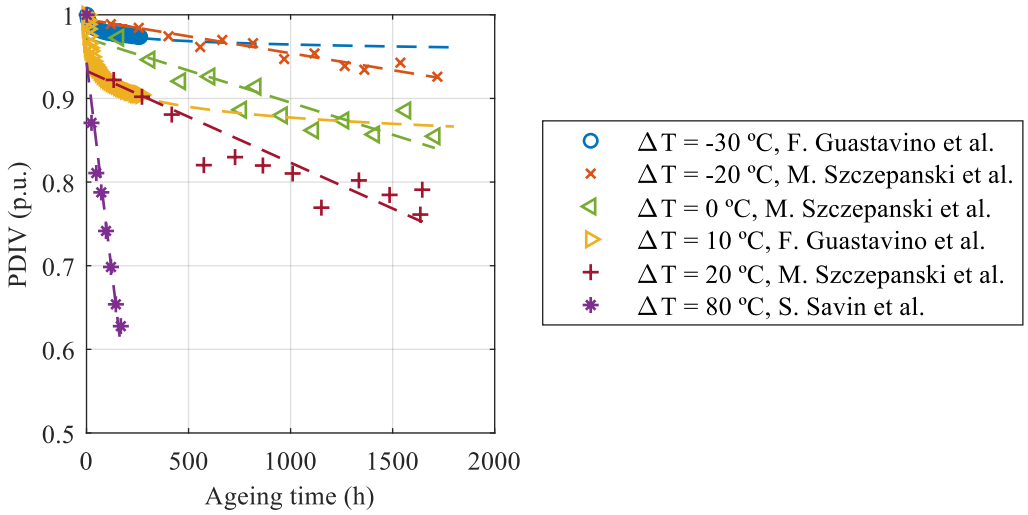

Figure 6.1: *Bibliographic results on PDIV deterioration during isothermal ageing of TPs under the conditions summarised in Table 6.1, based on the works of F. Guastavino et al. [20], M. Szczepanski et al. [119], and S. Savin et al. [17].*

Table 6.1: *Experimental specifications for isothermal ageing of TPs of the bibliographic results reported in Figure 6.1.*

Material	Copper diameter (mm)	Thermal class (°C)	Ageing temperature (°C)	ΔT (°C)	Ref.
PAI	1.23	240	210	-30	[20]
PEI+PAI	0.6	200	180	-20	[119]
PEI+PAI	0.6	200	200	0	[119]
PAI	1.23	240	250	10	[20]
PEI+PAI	0.6	200	220	20	[119]
PEI+PAI	0.85	200	280	80	[17]

While most thermal ageing studies employ constant temperatures (isothermal ageing), some researchers argue that cyclic temperature profiles should be considered, as electric machines typically operate intermittently [74]. Their findings suggest that the accelerated ageing of enamelled wire coils under cyclic temperature variations (200–260 °C) induces significant mechanical stress in the enamel due to repeated transitions between elastic and plastic behaviour, resulting in mechanical fatigue. Furthermore, the faster the thermal cycle, the more rapidly the insulation degrades. Therefore, the temperature variations introduce not only thermal stress but also mechanical stress, leading to thermomechanical ageing. According to this study, this approach, combined with PDIV studies based on B10-life assessments, provides a promising methodology for the rapid qualification and comparison of insulation materials.

Thermomechanical effects have been observed in other configurations as well. In [150], they reported greater PDIV degradation in impregnated motorettes aged from -20 to 180 °C (20% reduction of PDIV after 1100 h) compared to isothermal conditions at 180 °C (few % reduction of PDIV after 1100 h). Similarly, [154] found a significant PDIV decline in interturn insulation due to cyclic stress. Yet, consistent patterns were not established for groundwall insulation, likely due to the effect of manufacturing tolerances on the performances of insulation systems. Although the isothermal and thermomechanical ageing were not compared experimentally, [127] extended the PDIV analysis to the endurance evaluation to derive an ageing estimation model, concluding that cyclic thermal testing better replicated service conditions, producing more realistic lifetime estimates. They further noted that interturn insulation endurance was halved for every 7 °C rise.

In summary, thermal ageing significantly impacts insulation lifespan and PDIV, with degradation accelerating as the ageing temperature exceeds the thermal class of the insulation. While higher temperatures primarily lead to thickness reduction and permittivity changes, cyclic thermal stress further exacerbates insulation deterioration by introducing mechanical strain. Although studies confirm that both constant and cyclic ageing provide valuable insights, cyclic profiles more closely replicate actual operating conditions of electrical machines, offering more realistic predictions and enabling faster screening of interturn insulation materials. Most research focuses on interturn insulation when comparing isothermal or thermomechanical stress, whereas consistent conclusions for groundwall insulation remain lacking. Additionally, while many studies examine PDIV degradation, they often do not assess insulation endurance comprehensively.

6.1.1.2 Experimental Comparison Between Isothermal and Thermomechanical Ageing

Building on the preceding literature review, isothermal and thermomechanical ageing tests were experimentally conducted on the complete stator insulation system. The tested insulation system, designed for a lift-door actuator, is described in Section 3.1.3. The groundwall insulation consisted of PA66-FG30 caps, while the interturn and phase-phase insulation relied on the enamel of the winding wire. Isothermal and thermomechanical ageing were conducted as defined in Section 3.5.1 and detailed in Table 3.3. The evaluation of the degradation was done in terms of PDIV measurements and time to failure. Given that the interturn and phase-phase insulation shared the same material and thickness, it was assumed that phase-phase PDIV measurements provided an equivalent evaluation of the interturn insulation, and that the evaluation of the phase-phase PDIV during degradation would mirror that of the interturn insulation.

In total, six samples were tested (Section 3.5.1): one sample for each ageing type at a peak temperature of 230 °C, and two samples for each type at a peak temperature of 260 °C. In all tests, failure occurred in the groundwall insulation while the phase-phase, which was assumed to reflect the behaviour of the interturn insulation, remained unbroken.

Figure 6.2 shows examples of the failure locations. Although the air gap between the caps could initially be considered a weak point (rectangle of Figure 6.2 (a)), breakdowns consistently occurred at the edges of the cap (solid line circles of Figure 6.2). This was likely related to the deformation of the cap induced during the needle winding manufacturing process. As highlighted in the dashed circle of Figure 6.2 (a), mechanical strain during winding may distort the cap geometry and reduce the thickness at the corners, enhancing the local electric field and triggering breakdown during PDIV measurements (marked with solid circles). The corresponding discharge trace is visible in Figure 6.2 (b), where the stator core shows a darkened spot at the same location. A lighter discolouration is also visible in the air gap region (rectangle of Figure 6.2 (b)), indicating PD activity, though without failure.

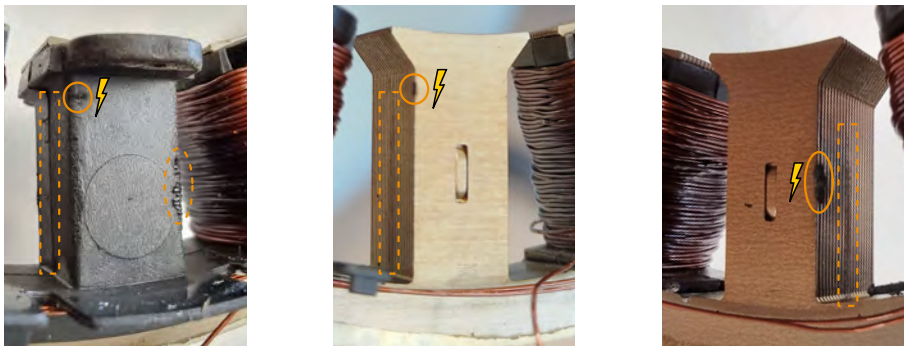

(a) (b) (c)

Figure 6.2: *Groundwall insulation breakdown locations during thermal ageing tests: (a) cap of the sample aged isothermally at 230 °C, (b) core of the sample aged isothermally at 230 °C, and (c) core of the sample aged thermomechanically between 200–230 °C.*

Table 6.2 summarises the time to failure results for each tested sample in hours. As expected, both isothermal and thermomechanical tests conducted at higher peak temperatures resulted in shorter ageing durations. For instance, considering the most conservative results (i.e., sample number 1), the sample aged at 230 °C lasted 2.5 times longer than the one aged at 260 °C. Similarly, the test conducted at 200-230 °C lasted 2.2 times as long as the one at 200-260 °C. These findings align with the general trend observed in the literature, where increased temperatures are associated with reduced insulation lifetimes.

Table 6.2: *Endurance results for isothermal and thermomechanical ageing tests, conducted on complete insulation systems using one sample at a peak temperature of 230 °C and two samples at 260 °C (h).*

Sample number	Isothermal ageing		Thermomechanical ageing	
	230 °C	260 °C	200-230 °C	200-260 °C
1	240 h	96 h	264 h	120 h
2	-	192 h	-	168 h

When comparing isothermal and thermomechanical ageing under the same peak temperature (230 °C vs. 200–230 °C, and 260 °C vs. 200–260 °C), the isothermal tests generally proved more restrictive, except sample 2 at 260 °C. At 230 °C, the thermomechanical aged sample lasted 1.1 times longer than the isothermal one, while at 260 °C, the same comparison yielded a factor of 1.25 when considering the most restrictive results (sample 1 in each case). These observations suggest that continuous exposure to elevated temperatures, such as isothermal ageing, causes more pronounced degradation than the thermal oscillations imposed during thermomechanical ageing, where the influence of mechanical stress appears to be limited for the groundwall insulation.

A comparison can also be made between tests conducted at equivalent rms temperatures. As shown in Table 3.3 in Section 3.5.1, the rms temperature of the thermomechanical ageing developed at 200–260 °C (230.7 °C) is comparable to the isothermal ageing at 230 °C. However, according to the results in Table 6.2 (considering sample number 1), the thermomechanical test failed 1.8 faster than its isothermal counterpart. This indicates that exposing the insulation system to higher temperatures during half of the cycle (230–260 °C) is sufficient to drive deterioration, even if the remaining half period is spent at lower temperature than rms value (200–230 °C). That is, equivalent rms temperatures do not necessarily reflect comparable thermal stress levels.

Figure 6.3 presents the PDIV and PD charge evolution during ageing in p.u. referenced to the non-ageing condition. It should be noted that final values correspond to the test preceding failure. For clarity, only the measurements with phase U connected to HV are shown for interturn and phase–phase insulations, as this typically yielded the lowest PDIV, although the trends were similar across all phases.

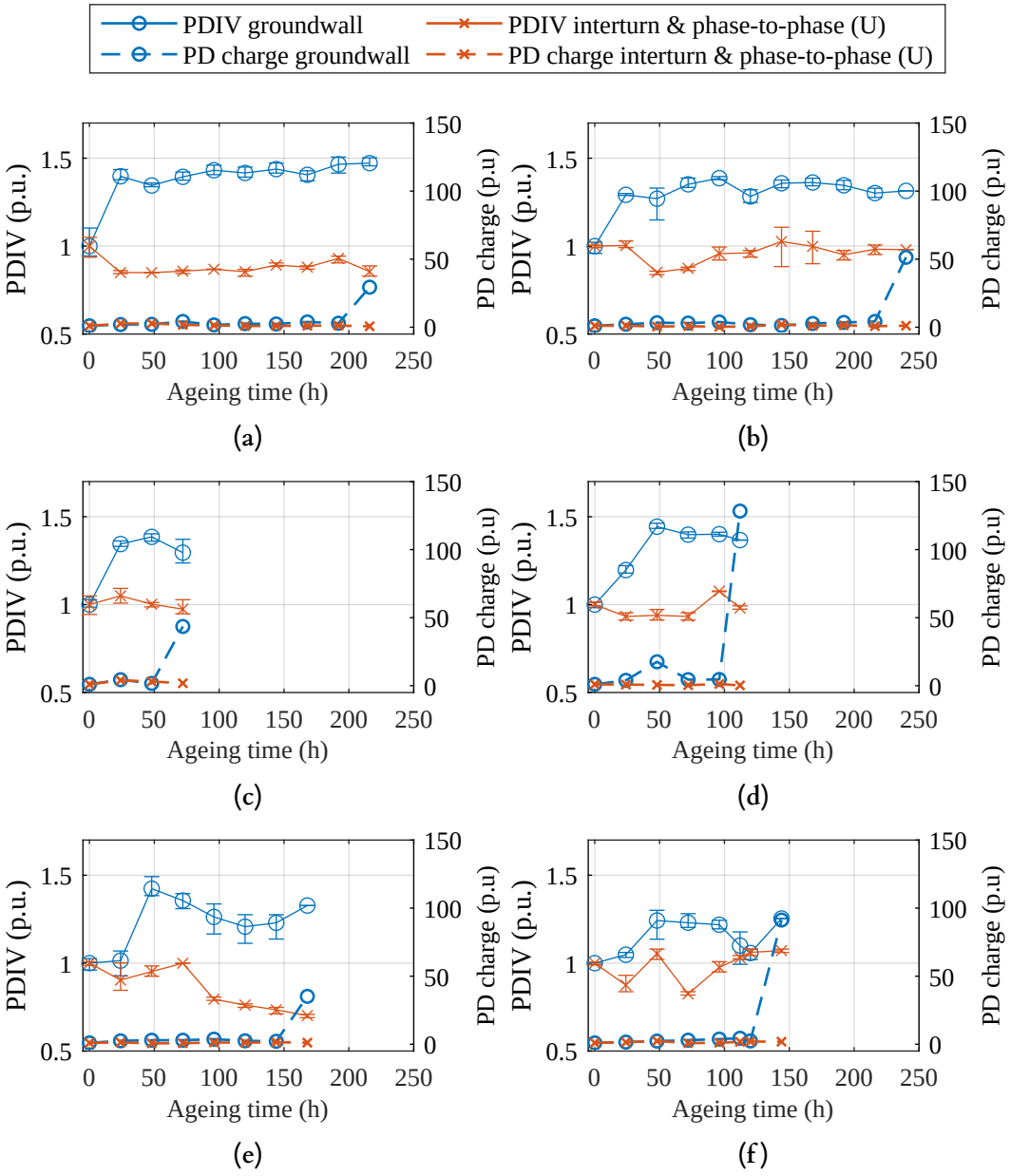

Figure 6.3: *Evolution of the PDIV of the groundwall, interturn, and phase-phase insulation during thermal ageing experiments, expressed in p.u. relative to the non-aged condition: (a) isothermal at 230 °C, (b) thermomechanical at 200–230 °C, (c) isothermal at 260 °C (sample 1), (d) thermomechanical at 200–260 °C (sample 1), (e) isothermal at 260 °C (sample 2), and (f) thermomechanical at 200–260 °C (sample 2).*

No generalised PDIV decrease was observed for the interturn and phase-phase insulation. While some cases show a clear decline (e.g., isothermal 230 °C in Figure 6.3 (a), and isothermal 260 °C sample 2 (e)), most samples developed limited or erratic evolution. Visual inspection revealed that the enamelled wire at the routing, where PDIV was measured, was less aged than in the coils (Figure 6.4). As the average winding temperature was estimated via resistance, the routing was likely exposed to lower temperatures resulting

from the greater heat dissipation of this area. Therefore, insufficient ageing at the routing could explain the lack of a generalised PDIV decrease. The PD charge neither reveals any relevant difference between the samples, where it was mainly unchanged.

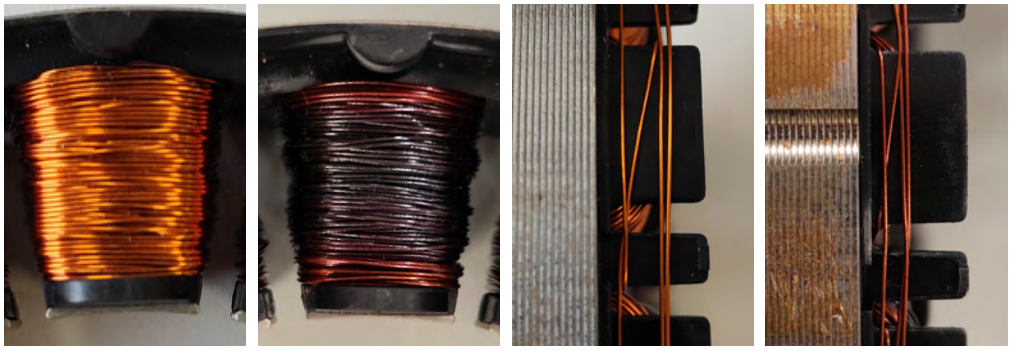

(a) (b) (c) (d)

Figure 6.4: *Comparison of the winding wire of the tested stator (a) non-aged coil, (b) coil of sample 2 subjected to thermomechanical ageing at 200-260 °C after 144 h, (c) non-aged routing, and (d) routing of sample 2 subjected to thermomechanical ageing at 200-260 °C after 144 h.*

Following with interturn and phase-phase insulation, although isothermal ageing showed a more consistent PDIV reduction compared to thermomechanical ageing (e.g., Figure 6.3 (a) vs. (b), and (e) vs. (f)), no conclusive difference can be established due to the limitations mentioned above. Thus, for analysing interturn insulation degradation, PDIV measurements using impulse voltages, applicable to the assessment of interturn insulation in complete machines [9] should be considered. With this measurement, the voltage differences between the different turns of the coil are applied. Alternatively, more suitable sample types, such as wire coils, could also be employed, as consistent results for comparing both ageing methods were reported in [74] using this sample configuration. In the present work, these alternatives could not be explored due to limited equipment availability, restricted to sinusoidal waveform PDIV measurements, and time constraints.

For the groundwall insulation, a more consistent trend was observed. In all cases, the PDIV initially increased (around 25-40%) and then remained relatively stable (with a slight decreasing tendency in some samples) until breakdown. This rise may have been due to changes in the relative permittivity of the PA66-FG30. Indeed, a reduction of at least 25% in permittivity after thermally ageing PA66 at 150 °C was reported in [155]. Another potential explanation is the curing or drying of the material during the initial ageing phase, as the samples were stored at ambient temperature and humidity before testing. The increase of the PDIV was associated with this phenomenon for other polymeric materials in [156, 157]. In addition to the PDIV, the PD charge did also show a consistent trend in all samples, showing a relatively stable value until the proximity of the failure, where the PD charge considerably increased in the measurement prior to failure.

Even when the failure occurred in the groundwall insulation, no clear evidence was found in PDIV evolution of accelerated degradation under thermomechanical ageing

compared to isothermal ageing. At 230 °C peak temperature, the initial PDIV increase was higher for isothermal ageing (Figure 6.3 (a)) than for thermomechanical ageing (Figure 6.3 (b)). At 260 °C peak temperature, the initial increases and subsequent slight decreases were similar between both conditions. Therefore, no consistent differences in PDIV trends were observed between ageing methods for groundwall insulation.

6.1.1.3 Effectiveness of Thermomechanical Ageing as an Accelerated Thermal Stress Testing Method

The absence of evident deterioration under thermomechanical ageing compared with isothermal ageing contrasts with the findings of [150], which, as far as this author is concerned, is the unique bibliographic reference comparing isothermal and thermomechanical experimental results. In [150], comparing the same ageing peak temperature, a greater reduction in PDIV was reported for interturn insulation aged between -20 and 180 °C under thermomechanical conditions than under isothermal ageing at 180 °C. Although endurance times were not provided, the more pronounced degradation observed under cyclic conditions suggests a shorter lifetime. As previously mentioned, according to [74], the mechanical stress induced by cyclic temperature ageing is attributed to periodic loading, that is, fatigue. Since no external mechanical stress was applied in [150], it is assumed that the fatigue originated from thermal expansions and contractions, i.e., strain (e).

The key differences between the present work and [150] lie in the applied thermal conditions (gradient and peak temperature) and the insulation material used. While [150] subjected interturn insulation (non-specified enamel) to a 200 °C thermal gradient (between -20 and 180 °C) until failure, the present study applied 30 °C and 60 °C gradients (between 200 and 230/260 °C) to groundwall insulation made of PA66-FG30.

Starting with the thermal conditions, differences in the applied gradients result in different material strains. For the same material, a higher strain is produced by a higher temperature gradient, as shown in equation (6.1) for the linear strain. Therefore, the temperature gradient is a key factor in the produced mechanical stress.

$$e = \alpha_{\mathrm{TExp}}\, \Delta T \tag{6.1}$$

where α_{TExp} is the linear thermal expansion coefficient of the material and ΔT is the applied temperature difference.

Assuming the wire in [150] was enamelled with PAI, PEI, or PI (commonly used for machine windings) their thermal expansion coefficients are $25-31\ 10^{-6}\ \mathrm{K}^{-1}$, $56\ 10^{-6}\ \mathrm{K}^{-1}$, and $30-60\ 10^{-6}\ \mathrm{K}^{-1}$ [158], respectively, while PA66-FG30 has a coefficient of $50\ 10^{-6}\ \mathrm{K}^{-1}$ (from 23 to 100 °C) [159]. Even though these values do not correspond to the precise temperatures used in the thermal ageing tests, and considering the upper values (more likely at elevated temperatures due to the decrease in the yield strength), a 200 °C thermal

difference would result in a linear strain of 0.62% in PAI, 1.12% in PEI, and 1.2% in PI, while 60 °C gradient will lead to 0.30% strain in PA66-FG30, presenting the lowest among them (equation (6.1)).

According to [74], a 60 °C temperature variation (200-260 °C) was sufficient to induce mechanical stress in enamelled wire coils made of PEI+PAI, resulting in estimated strains of 0.336% and 0.186% for PEI and PAI, respectively. Although not explicitly stated, additional stress could also arise from mismatches between the thermal expansion coefficients of the basecoat and overcoat materials. This effect may also be present in [150], where the winding was impregnated with PEI. Based on this analysis, the mechanical stress resulting from thermal cycles in the present conditions for PA66-FG30 could be expected to be lower than that applied in the literature.

Another relevant aspect is the applied maximum temperature. In [150], the peak temperature matched the thermal class (180 °C). As previously discussed, ageing at the thermal class temperature imposes limited stress, given that the materials are expected to endure at that value [150]. In contrast, the present study applied peak temperatures exceeding the thermal class, which could have amplified the effects of thermal stress in isothermal ageing compared to [150], resulting in faster deterioration under constant conditions.

Regarding the aged materials, the type of polymeric insulation plays a significant role, with the glass transition temperature (T_g) being a key distinguishing factor. This is defined as the temperature at which amorphous materials transition from a rigid and relatively brittle state to a more flexible one. Below T_g, the material is stiffer and less deformable due to the low molecular mobility. Above T_g, increased molecular mobility softens the material, making it more flexible and ductile and allowing partial stress relaxation [160].

In [150] a thermosetting material was apparently used (e.g. PAI), whereas in the current study, the failed insulation (groundwall) was thermoplastic. In general, T_g for thermosetting materials is significantly higher (e.g. 270-300 °C for PAI [161]) than that of thermoplastic (48 °C for PA66-FG30 [159]). Thus, in [150], the test temperature remained below T_g, whereas in the present work it exceeded it, resulting in different material behaviours.

Thermosetting materials exposed to sub-T_g conditions (glassy state) exhibit higher rigidity, which could promote the accumulation of internal stress during thermal cycling and accelerate degradation under thermomechanical regimes. Conversely, thermoplastics tested above T_g (rubbery state) benefit from increased molecular mobility, allowing partial relaxation of the internal stress. That is to say, thermomechanical tests induce greater internal mechanical stress in thermosetting materials than in thermoplastics. These differences may also explain the contrasting outcomes between the two studies.

In conclusion, considering the higher endurance of thermomechanical ageing over isothermal ageing observed in the present study, there is insufficient evidence to confirm that a significant mechanical stress was applied to the groundwall insulation during thermal cyclic experiments to overcome the continuous thermal stress imposed by isothermal

ageing. The experimental analysis conducted on the complete insulation system suggests that the effectiveness of thermomechanical ageing in accelerating insulation degradation, when applying the same peak temperature as isothermal ageing, depends on both the applied thermal conditions (temperature level and gradient) and the nature of the insulation material. Given the relevance of assessing the complete insulation system when determining the thermal class of the final machine, the present results indicate that it should not be directly assumed that thermomechanical ageing will be more restrictive than isothermal. The specific thermal and mechanical characteristics of the insulation material should be more thoroughly analysed to determine whether thermomechanical ageing can indeed accelerate degradation more effectively.

Nevertheless, when the same rms temperature was applied in both ageing processes, the higher thermal stress associated with the periods exceeding the rms value contributed to accelerated degradation under cyclic conditions. That is, although a lower temperature was applied during half of the cycle, the increased stress during the higher-temperature phase led to a faster deterioration.

In interpreting the current analysis, it must also be acknowledged that it was based on a limited number of tested samples. While these experiments enabled the formulation of initial conclusions, the number of analysed samples should be increased in future studies to validate the findings and support the conclusions. Further investigation into the thermal and mechanical properties of insulation materials at elevated temperatures would also improve the understanding of the underlying mechanisms.

6.1.2 Electrical Stress

Electrical stress primarily accelerates insulation degradation through PD activity. Over time, electron bombardment erodes the insulating material, potentially leading to premature failure if the operating voltage exceeds the PDIV [26]. In inverter-fed machines, PD has been detected at voltages as low as 440 V [26].

The following sections summarise the state of the art regarding the influence of electrical stress on the endurance of insulation systems. This review is complemented by an experimental analysis examining the combined effect of rise time, pulse width, and non-conduction duration of square pulses on the endurance of insulation systems operating under PD conditions.

6.1.2.1 Overview of the Effect of the Electrical Stress on Insulation Endurance

Multiple studies have demonstrated that key electrical parameters influencing insulation ageing due to PD activity include applied voltage level [15, 18, 146, 162–164], and various waveform characteristics, such as switching frequency [109, 146, 165], dv/dt [14, 162], rise time [166, 167], or pulse width [167].

The influence of applied voltage level on insulation lifetime has been widely modelled

as an inverse power function, demonstrating that higher voltages significantly reduce the time to breakdown, irrespective of other waveform characteristics or temperature [146, 163, 164]. In [15], this effect was attributed to increased PD magnitude and occurrence, driven by a greater difference between the PDIV and the applied voltage, leading to faster degradation. Similarly, [18] demonstrated that higher applied voltage levels accelerated the decline in PDIV over time.

The influence of waveform polarity (bipolar or unipolar) was examined in [166], which found that its influence on insulation time to failure was negligible if the repetitive impulsive voltages have similar peak-peak values, rise time (50 ns-16 μs), duty cycles (0.01-99.99%), and frequencies (3-5 kHz). Comparing square and sinusoidal waves, [166, 168] found that square wave voltages led to shorter lifetimes and fewer surges to failure, despite having the same peak-peak voltage. This behaviour was further examined in [169], where it was attributed to the higher PD magnitudes observed in unipolar voltages with identical peak-peak voltage and frequency characteristics.

Regarding switching frequency, multiple studies agree that higher frequencies reduce insulation lifetime across various rise times and voltage levels [51, 146, 165, 170]. This effect has been consistently observed for both unipolar and bipolar voltages in the range of 0.5-3 kHz [165]. Nonetheless, [146] found that while frequency (0.05-5 kHz) affects time to breakdown (Figure 6.5 (a)), the number of cycles to failure remains consistent regardless of frequency within the range of 600-2000 V (Figure 6.5 (b)). This suggests that higher frequencies accelerate failure, yet they do not inherently alter the ageing process, serving as a useful tool for accelerating endurance tests.

For higher frequencies, studies have reported an inverse power law relationship between lifetime and switching frequency from 5 to 30 kHz [51, 170], indicating that as frequency increases, its impact on time to failure diminishes. Below 10 kHz, [170] attributed this to the rise in surface temperature caused by dielectric losses at higher frequencies. Beyond 10 kHz, the reduction in lifetime was linked to a shorter space charge dissipation time between PD events, leading to charge accumulation. This process lowered the average PD magnitude while maintaining the number of PD occurrences per cycle, thereby increasing the total PD amplitude per second. The explanation for the decline in breakdown time above 10 kHz does not fully align with the discussions in Section 4.1.2.2, which highlighted higher PD magnitudes due to surface charge accumulation and the stabilisation of the memory effect above this threshold. Indeed, if the relation between the frequency and the RPDIV explained in Section 4.1.2.2 is considered, the decrease in the time to breakdown with the increase in the frequency could be attributed to the same effect of the frequency on the RPDIV. When the same ageing voltage is maintained, as frequency increases, the difference between the applied voltage and RPDIV increases, resulting in a more persistent PD activity. However, it should be noted that [170] used a needle-plate configuration, whereas Section 4.1.2.2 refers to TPs, which may exhibit different space charge dynamics due to the geometry effects.

Figure 6.6 (a) illustrates the relationship between the time to failure and the frequency, as observed in [51] for PEI+PAI TPs at 1.75 kV and 30 °C, and in [170] for PI in a

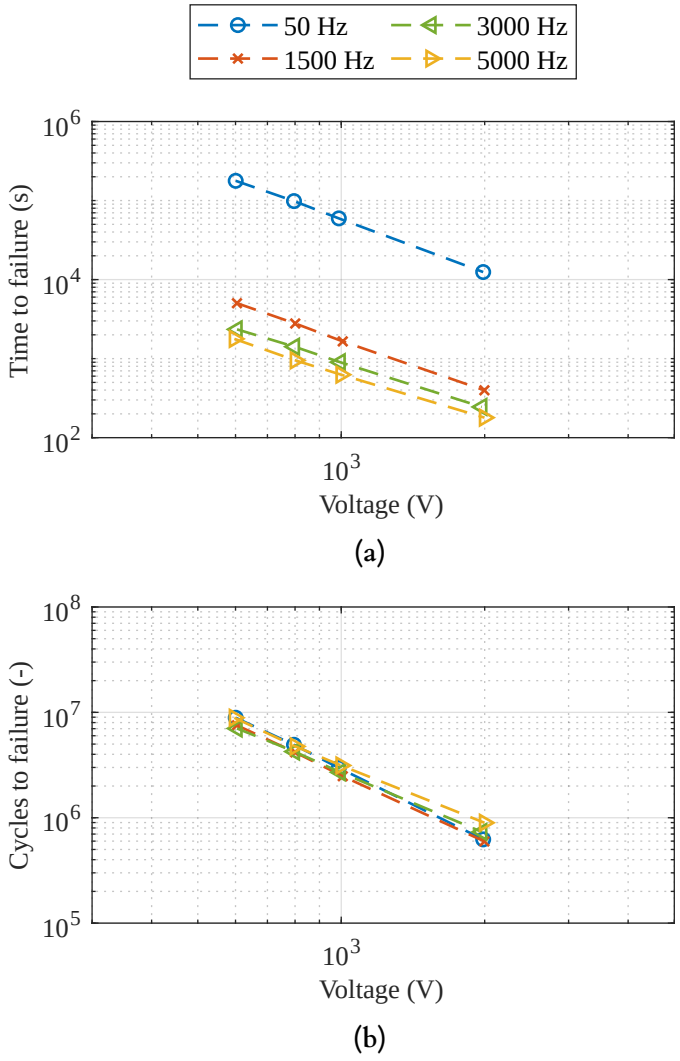

Figure 6.5: *Bibliographic results illustrating the effect of frequency on insulation failure for PI enamelled TPs aged with sinusoidal voltage at 200 °C (a) time to failure, and (b) number of cycles to failure. Based on data from [146].*

needle-plate configuration at 2.5 kV and 14.5 °C. Both studies confirmed an inverse power trend. While these experiments were conducted between 5 and 30 kHz, the fitting was extended up to 250 kHz to assess effects at higher frequencies. Beyond 35 kHz, the influence of the frequency on the time to failure loses significance, particularly for TP configuration. This could be reinforced with the lack of effect of the frequency on the RPDIV at frequencies higher than 75–100 kHz reported in [111] (Section 4.1.2.2).

Although the studies did not explicitly present results in terms of cycles to failure, this can be determined by multiplying time to failure by the corresponding frequency [166]. Figure 6.6 (b) displays the same data but in terms of cycles to failure. Unlike [146], where cycles to failure were considered constant below 5 kHz, the number of cycles to failure depends on the frequency. Beyond 35 kHz, frequency has a greater impact on cycles to failure than on time to failure, particularly in the needle-plate configuration. Despite

this, in the TP configuration, the variation remains within 5% for frequencies between 35–250 kHz.

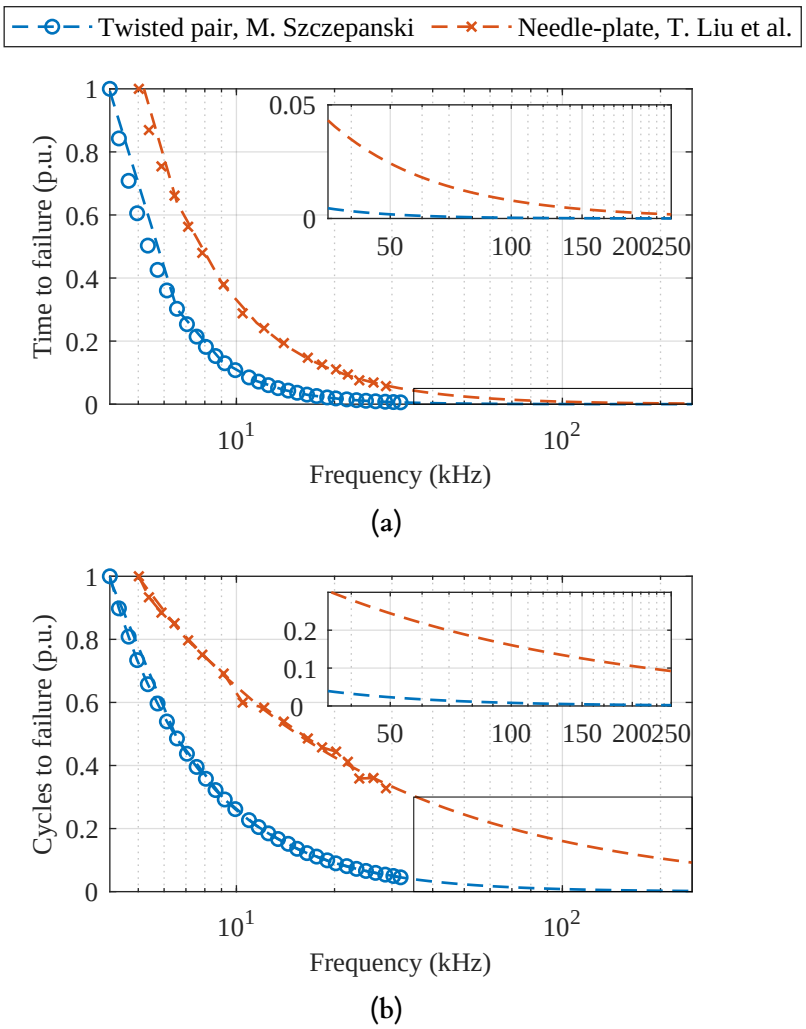

Figure 6.6: *Bibliographic results illustrating the effect of frequency on insulation failure, normalised to the lowest analysed frequency, for TP and needle-plate configurations (a) time to failure, and (b) number of cycles to failure (M. Szczepanski [51] and T. Liu et al. [170]).*

High dv/dt and the resulting overshoot associated with short rise time devices can increase the likelihood of PD, shortening insulation lifespan [14, 162]. However, this only occurs when the voltage is sufficiently high to trigger PD, meaning that SiC converters do not necessarily lead to shorter insulation lifetimes than Si converters [162].

According to [166], reducing rise times to as low as 50 ns while maintaining the peak-peak voltage and avoiding significant overshoot, shortens both the insulation lifespan and the number of cycles to failure. Despite fewer PD occurrences at shorter rise times, degradation was accelerated due to the increased PD magnitude. This was attributed to a delay in the generation of initial electrons. When the electric field becomes strong enough to trigger PD, the voltage is already significantly higher in shorter rise time conditions

at the time the first available electron initiates the discharge, leading to more energetic discharges. Consequently, it was concluded that a single PD event of large magnitude was deemed more damaging than multiple low-energy discharges. Since degradation is largely dictated by the number of electrons possessing sufficient energy to break molecular bonds, shorter rise times shift the electron energy distribution towards higher values. Further analysis down to 10 ns rise times [167] confirmed similar PD magnitude trends for waveforms within the 10–100 ns rise time range at the same peak-peak voltage (with overshoot observed at 10 and 30 ns). Nevertheless, endurance data was not provided.

As previously mentioned, endurance is closely linked to the difference between PDIV and the applied voltage. While some studies reported a reduction in PDIV with shorter rise times, its overall effect remains uncertain (Section 4.1.2.3). Indeed, authors who observed a decrease in time to failure with shorter rise times [166], also reported that PDIV remains largely unaffected for rise times longer than 20 ns (without considerable overshoot) [100]. Thus, the time to failure reduction observed in [166] was likely not due to variations in PDIV but rather to increased stress from higher discharge magnitudes.

Another relevant explanation could be that, even though the effect on the rise time is limited on PDIV, it could affect the RPDIV. As RPDIV implies a more persistent PD activity, increasing the difference between the applied voltage and the RPDIV could lead to more PD activity and therefore a reduction in lifetime. According to [108], the difference between the PDIV and the RPDIV (defined with peak values) is lower as the rise time reduces. Therefore, assuming the same peak-peak PDIV and ageing voltage (greater than the PDIV), as the rise time decreases, the RPDIV would be closer to the PDIV but further from the ageing voltage, thereby increasing the threat of higher harmfulness probability.

Further studies explored the influence of waveform characteristics beyond the rise time. [167] compared short (low duty, 0.04%) and symmetrical (50%) pulse waveforms at 4.2 kV peak-peak, 2 kHz and 110 °C (rise time not specified but could be between 10-100 ns). It was observed that shorter duty cycles (lower pulse widths) prolonged the time to breakdown and altered the PD erosion patterns. Conversely, [171] reported conflicting results with endurance tests were conducted at 50 kHz using bipolar square waveforms with 250 ns rise times and comparing 2 level (10 μs conduction) and 3 level (1.2 μs conduction) pulses at voltage levels 5% above PDIV (without overshoot). No significant differences in lifetime were observed, which was attributed to the low repetition rate and PD magnitude due to operation close to PDIV, where only a minimal field strength was sufficient to initiate discharge. Furthermore, discharges generally occurred at both rising and falling voltage transitions, further minimising differences in time to breakdown (as the same frequency was used).

Comparing [167] and [171], the key distinction lies in the applied ageing voltage: the former applied a fixed voltage irrespective of PDIV, whereas the latter used varying voltages while maintaining equivalent stress levels relative to PDIV. As discussed in [114] (Section 4.1.2.4), shorter pulse widths (shorter pulses) could result in a higher PDIV. Therefore, the extended time to failure observed in [167] for short pulses likely results

from a smaller difference between PDIV and the applied voltage, leading to reduced stress and a prolonged lifetime.

One more difference relies on the utilised pulse width and non-conduction time relationship. As discussed in Section 4.1.2.4 not only the pulse width (conduction time), but the non-conduction duration may influence the RPDIV, which in turn can influence the endurance. As far as this author is concerned, the influence of the non-conduction duration on the endurance is still unknown in the literature.

Overall, the electrical stress effect on the endurance of insulation is critically influenced by both the magnitude and the characteristics of the applied voltage. Higher voltage levels consistently shorten lifetime by increasing the difference from PDIV, thereby intensifying discharge activity. Although square waveform polarity has limited influence when other parameters are controlled, voltage waveform shape (square or sinusoidal) affects the energy and frequency of discharges. Switching frequency reduces time and cycles to failure, especially below 35 kHz, with a diminishing impact at higher frequencies. Shorter rise times and higher dv/dt induce more energetic discharges, accelerating the degradation due to higher PD charge magnitudes and reduced RPDIV. Finally, short pulses can extend lifetime when they reduce the voltage–PDIV/RPDIV difference, yet the literature lacks on the effect of the non-conduction time on the endurance, whose decrease could effectively decrease the endurance due to its similar effect on the RPDIV.

6.1.2.2 Experimental Evaluation of the Combined Effect of Rise Time, Pulse Width, and Non-Conduction Time on the Endurance

Given the insights from the literature, it becomes evident that the differences between the PDIV and RPDIV with the applied ageing voltage are crucial in determining insulation endurance. As the non-conduction duration has a strong influence on RPDIV, and given the limited research on its impact on lifetime, further investigation was warranted. Pulse width and rise time were also included due to their known influence on RPDIV. The combined effect of pulse width and non-conduction time was therefore evaluated at both low and high rise time conditions.

The study also included two insulation types, non-corona resistant wires (SW) and corona resistant wires (CRW), to compare the behaviour of systems expected to be PD-free and non-PD-free during operation. Sample descriptions are provided in Section 3.1.3.

Following the recommendations in [51], a DoE approach was adopted to assess the effect of multiple variables, both independently and in combination. Three variables were defined, each with two levels (see Table 3.4 in Section 3.5.2). The rise time levels of 21 and 458 ns represent typical values for SiC and conventional Si converters, respectively. Additionally, they were also selected to evaluate the possible different effects of the pulse width depending on the rise time level. At low rise time, the pulse width may affect both PDIV and endurance, especially when it is below 70 ns [48]. At high rise time, pulse width is not expected to affect PDIV, but can still influence RPDIV. Pulse widths of 2 and

10 µs were selected to lie below and above the 5 µs delay time associated with electron generation, resulting in a higher PDIV [48]. Non-conduction durations of 2 and 18 µs were chosen to be equal to or longer than the pulse width. Details of the test conditions and setup are provided in Section 3.5.2.

Two key assumptions were made. First, the overshoot level would not influence the endurance of the insulation. This was limited to 1.13 OF, a value close to the 1.1 benign stress category defined in [9]. Second, frequencies above 35 kHz would not significantly affect endurance due to their limited impact on RPDIV. As a result, tests used frequencies between 35 and 250 kHz with duty cycles ranging from 10% to 83%, to achieve the target pulse width and non-conduction times.

Turning now to the experimental evidence, all numerical results are presented in Appendix D. Figure 6.7 shows the effect of rise time on cycles to failure for both materials. A clear increase in cycles to failure was observed with longer rise times, regardless of the pulse width or non-conduction time. This aligns with results from [166]. The observed endurance regression may be linked to higher PD charge magnitudes or lower RPDIV at shorter rise times. These findings confirm that, even though rise time may not influence PDIV, it can significantly affect endurance. As highlighted in [166, 168], square waveforms with short rise times produce more severe ageing conditions than sinusoidal waveforms, making the latter unsuitable for evaluating insulation endurance in inverter-fed systems.

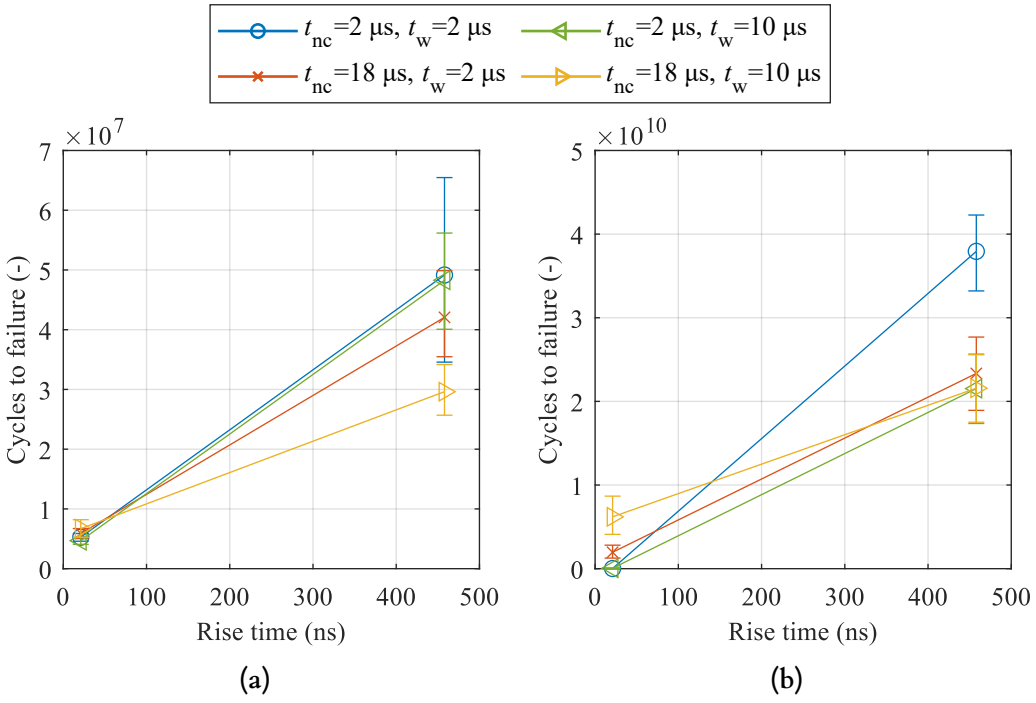

Figure 6.7: *Experimental cycles to failure results depending on the rise time of the electrical ageing tests represented by the scale parameter of the Weibull distribution (considering 63.2% probability) and confidence intervals with 90% probability (a) SW, and (b) CRW.*

Further analysis shown in Figure 6.8 proves that the effect of the pulse width on the

cycles to failure is inconsistent on both rise time levels and materials. Two distinct clusters are observed, each corresponding to a different rise time level, and this holds for both materials. At higher rise times, since the applied ageing voltage remained constant, an increase in pulse width should not affect the PDIV and reduce the RPDIV, raising the electrical stress and lowering the endurance. At low rise times, the increase in the pulse width will probably reduce both PDIV and RPDIV, resulting in a greater decrease in the endurance.

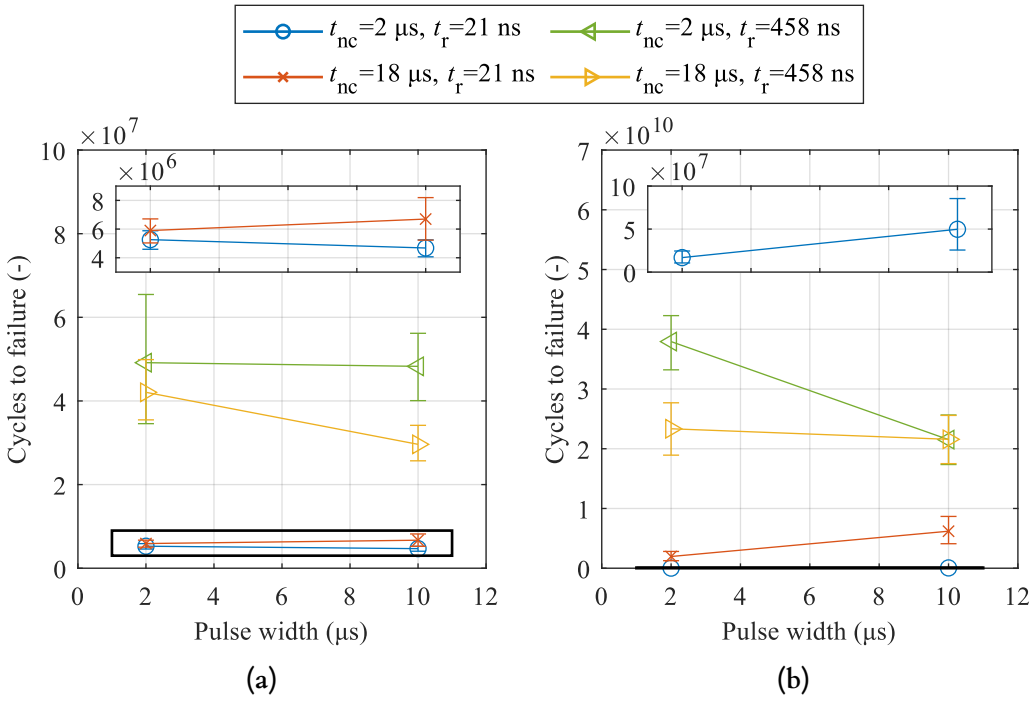

Figure 6.8: *Experimental cycles to failure results depending on the pulse width of the electrical ageing tests represented by the scale parameter of the Weibull distribution (considering 63.2% probability) and confidence intervals with 90% probability (a) SW, and (b) CRW.*

This expected trend is partially confirmed. For both SW and CRW, longer pulse widths lead to fewer cycles to failure. However, this behaviour depends on the non-conduction duration. In SW, endurance remains unaffected when the non-conduction time is short, i.e., equal to or shorter than the pulse width. In contrast, for CRW, the reverse is observed. When the non-conduction time is long, endurance is relatively stable, and a decreasing trend with increasing pulse width is only visible under short non-conduction durations.

This behaviour in CRW aligns more closely with the literature discussing the role of non-conduction time on RPDIV. As detailed in Section 4.1.2.4, longer non-conduction times reduce space charge accumulation, limit the availability of initiating electrons, and increase the RPDIV, potentially improving endurance. Hence, the negative impact of increased pulse width should be more pronounced at short non-conduction times, which is seen in CRW but not in SW.

At shorter rise times, results are less conclusive. In SW, the impact of pulse width is masked by variability, though a slight increase in cycles to failure appears with longer pulses. For CRW, endurance tends to increase with pulse width, which contradicts expected behaviour and prior studies.

These findings suggest that the effect of pulse width on insulation endurance depends on non-conduction time, rise time, and material type. Variations in charge accumulation and dissipation between SW and CRW may account for these differences. Further investigation is needed to clarify the role of space charge in each insulation material.

Following with the non-conduction time, the expected effect of its increase was an increase in the RPDIV, resulting from improved dissipation of space charges generated by prior PD activity. This would reduce the availability of initiating electrons, lowering the likelihood of discharge inception and thereby improving endurance.

Figure 6.9 presents the trends in cycles to failure as a function of non-conduction duration. At shorter rise times, the expected pattern is clearly observed: longer non-conduction durations lead to increased endurance, particularly for CRW. At higher rise times, however, an opposite effect is seen, except for CRW under long pulse width conditions, where there is a negligible difference. It could be said that the effect of the non-conduction duration depends on the rise time level.

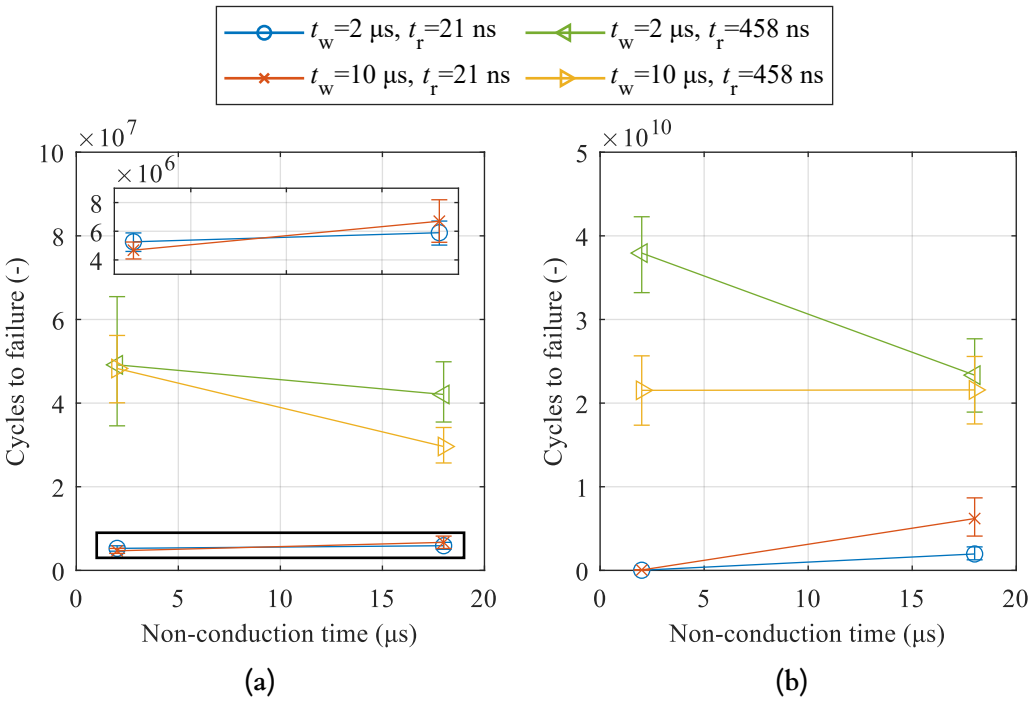

Figure 6.9: *Experimental cycles to failure results depending on the non-conduction time of the electrical ageing tests represented by the scale parameter of the Weibull distribution (considering 63.2% probability) and confidence intervals with 90% probability (a) SW, and (b) CRW.*

Overall, the reduction of rise time consistently leads to a decrease in endurance, regardless of the other parameters. In contrast, the effect of pulse width and non-conduction

duration is dependent on both the rise time and the insulation material. To identify the most critical conditions, the worst-case scenarios for each material and rise time were evaluated. Figure 6.10 summarises the minimum endurance points in red. Generally, the most severe degradation was observed at high pulse widths and short non-conduction durations, except in the case of CRW at low rise time and SW at high rise time, respectively. These findings align with the literature observations, where longer pulse widths result in earlier failures, and increased non-conduction durations improve RPDIV, thus enhancing endurance.

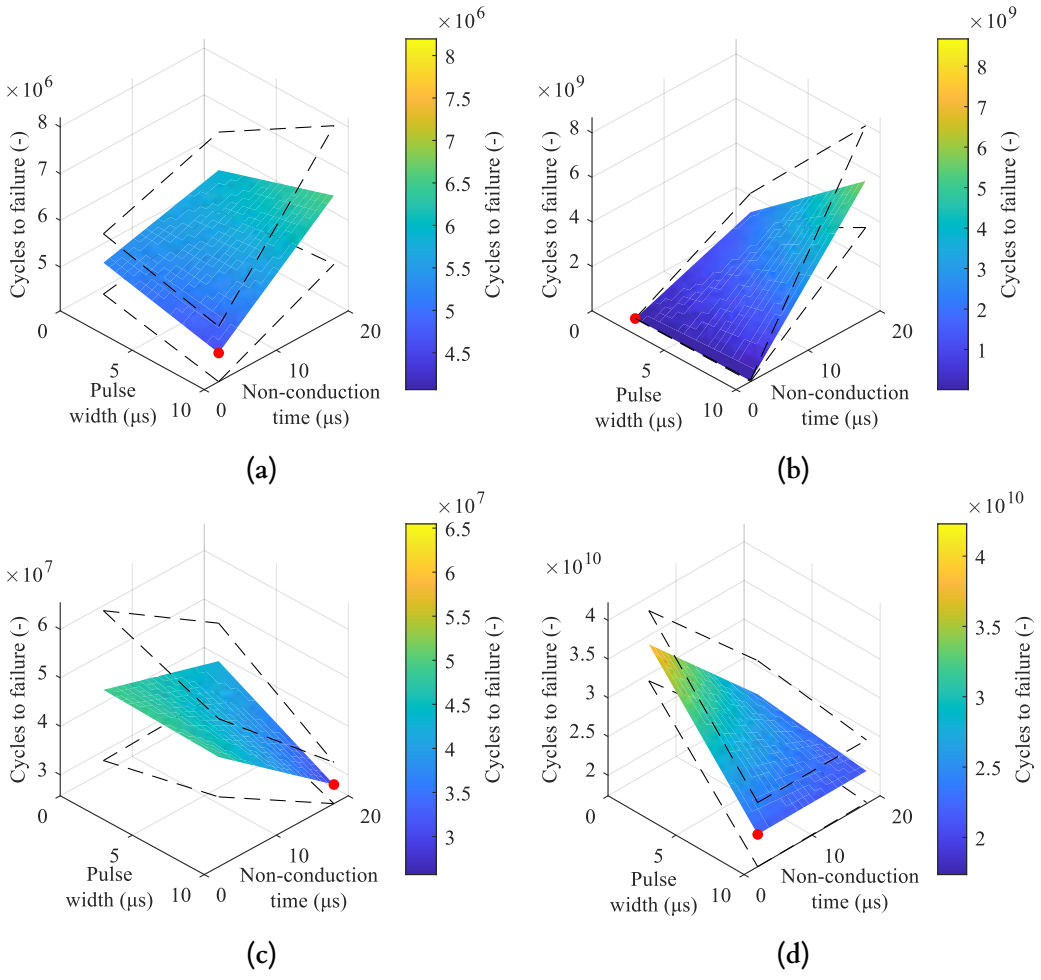

Figure 6.10: *Experimental cycles to failure results depending on the pulse width and non-conduction time of the electrical ageing tests represented by the scale parameter of the Weibull distribution (considering 63.2% probability) and confidence intervals with 90% probability, being the endurance value marked with a red dot (a) SW at* $t_r = 21$ ns*, (b) CRW at* $t_r = 21$ ns*, (c) SW at* $t_r = 458$ ns*, and (d) CRW at* $t_r = 458$ ns.

To assess whether the inconsistencies in the results could be linked to the assumed negligible effect of overshoot and frequency, the relationship between cycles to failure and these parameters was analysed. Figure 6.11 shows that cycles to failure do not follow a clear trend with peak-peak voltage. The samples subjected to the highest overshoot

did not always exhibit the shortest lifetimes. The same was also observed between the four samples tested in the same ageing point. This suggests that the overshoot did not significantly impact the results.

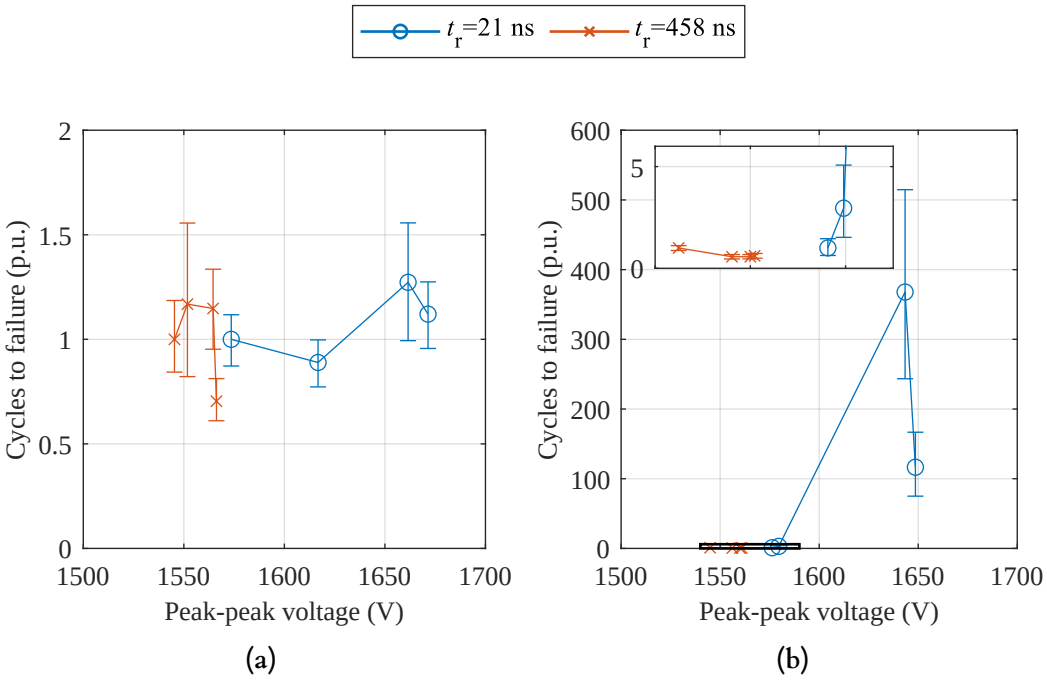

Figure 6.11: *Experimental cycles to failure results represented by the p.u value of the scale parameter of the Weibull distribution (considering 63.2% probability and normalised to the lowest peak-peak voltage level) and confidence intervals with 90% probability depending on the test peak-peak voltage of the electrical ageing tests (mean value of the 4 tested samples) (a) SW, and (b) CRW.*

Frequency dependence was evaluated in Figure 6.12, where the cycles to failure follow a consistent trend with the frequency. Interestingly, the results for low rise time levels followed a power law trend similar to those reported in the literature for lower frequency ranges (5-30 kHz) [51]. This indicates that the second assumption, no endurance impact above 35 kHz, may not hold. Consequently, further validation is needed by comparing frequencies at constant duty cycles.

Lastly, the observed variability in the results may be due to sample handling practices. As noted in [51], handling samples with bare hands can increase experimental variability on endurance tests. Future tests should ensure the use of gloves to minimise contamination and improve repeatability.

In summary, two key conclusions can be drawn: (1) a decrease in the rise time unconditionally reduces the endurance of the SW and CRW insulations, and (2) the most critical conditions typically occur under high pulse widths and low non-conduction durations. However, these trends are influenced by both the rise time level and the insulation type. To improve the robustness of the conclusions, a third level should be

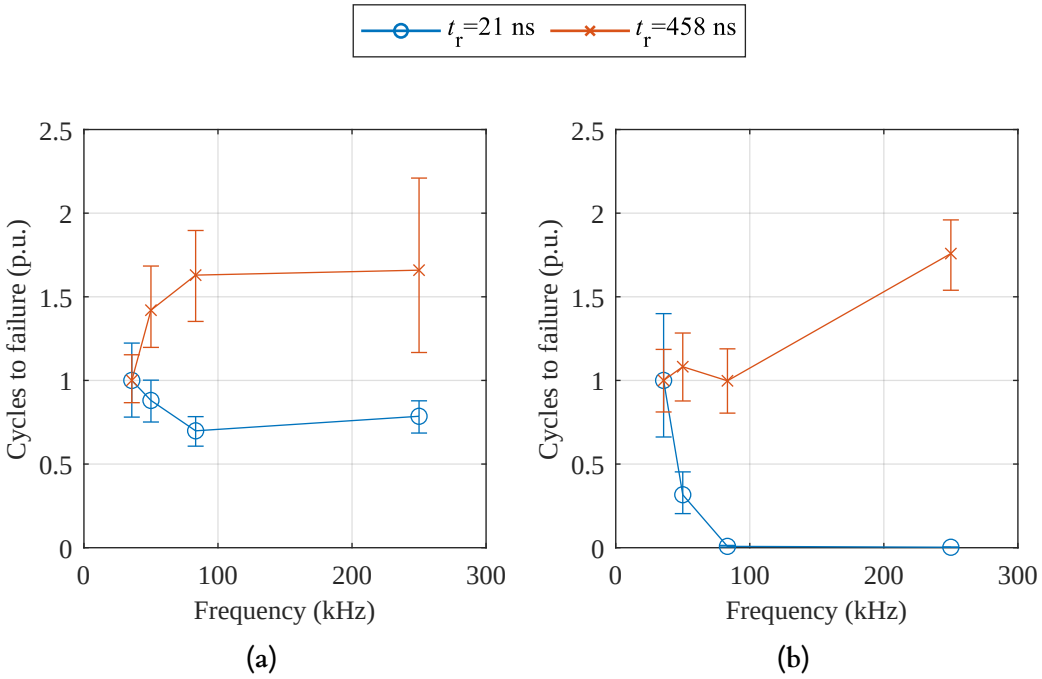

Figure 6.12: *Experimental cycles to failure results represented by the p.u value of the scale parameter of the Weibull distribution (considering 63.2% probability and normalised to the lowest peak-peak voltage level) and confidence intervals with 90% probability depending on the test frequency of the electrical ageing tests (a) SW, and (b) CRW.*

added to the DoE, frequency effects should be evaluated using constant duty cycles, and consistent handling procedures must be adopted. Additionally, measuring the PDIV and the RPDIV in the same test conditions could give valuable insights on the understanding of the effect of pulse width and the non-conduction duration individually and collectively.

6.1.3 Concluding Remarks

This section evaluates the key factors driving insulation ageing, focusing on thermal and electrical stress. Drawing from the literature and earlier findings, the ageing behaviour of stator insulation systems was compared under isothermal and thermomechanical thermal stress, while the combined influence of electrical waveforms parameters, i.e. rise time, pulse width, and non-conduction time, was assessed using DoE methodology.

In thermal ageing experiments, failures consistently occurred in the groundwall insulation. When exposed to equivalent peak temperatures, isothermal ageing led to shorter endurance times than thermomechanical ageing. No significant acceleration effect was observed for thermomechanical ageing over isothermal ageing, suggesting that the thermal cycles did not induce sufficient mechanical stress in the PA66-FG30 material. This contrasts with prior studies where larger thermal gradients and alternative materials (e.g., PI, PAI, PEI) resulted in pronounced mechanical fatigue. These findings highlight that the effectiveness of thermomechanical ageing as an accelerated testing method apparently

depends on both the insulation material and the applied temperature gradient. However, when conditions were defined by the same rms temperature, thermomechanical ageing proved more restrictive, likely due to intermittent exposure to higher temperatures.

Electrical ageing tests were conducted using a DoE approach, analysing endurance across varying rise times, pulse widths, and non-conduction durations for two insulation types: SW and CRW. Results indicated that shorter rise times consistently decreased insulation endurance, even though rise time did not directly influence PDIV according to the literature. This effect is most likely attributed to a reduced RPDIV. The interaction of pulse width and non-conduction time with endurance was more complex and depended on rise time and insulation type. At high rise times, longer pulse widths generally reduce endurance, particularly when combined with short non-conduction durations. For CRW, endurance improved with increased non-conduction time, aligning with theoretical expectations of reduced space charge and increased RPDIV. At low rise times, however, results were more variable and sometimes contradictory. Considering the most critical scenarios, cycles to failure degradation was generally most severe under high pulse widths and short non-conduction durations, although exceptions were observed depending on the rise time and the insulation material.

Overshoot and peak-peak voltage levels showed no clear impact on endurance. In contrast, frequency effects deviated from the initial assumption that frequencies above 35 kHz do not affect endurance, suggesting the need for further validation under controlled duty cycles. Future work should include a third DoE level, more stringent handling procedures, and co-measurement of PDIV and RPDIV to better understand the influence of waveform parameters on insulation degradation.

6.2 Insulation Health Diagnosis

As extensively discussed in previous sections, Type I insulation systems are intended to remain free of PD activity throughout their operational lifetime. Considerable research has thus focused on developing electric machines capable of operating without PD activity (Chapters 4 and 5). Nevertheless, maintaining a PD-free state presents difficulties due to inevitable insulation ageing. Indeed, thermal stress could cause a decrease in the (R)PDIV, as previously reported in [20, 74, 90, 119, 147, 149, 150, 154] (Section 6.1.1). Consequently, machines initially free from PD activity may still develop it later, potentially hastening insulation degradation and subsequent premature failure.

Periodic winding insulation health monitoring contributes to the prevention of unforeseen machine failures [172]. The following sections present an overview of widely employed monitoring techniques, with a particular focus on off-line methods, subsequently evaluating and comparing their effectiveness in determining the overall condition of stator insulation systems. The work developed in this section is supported by a conference proceeding presented on ICEM 2024 [23].

6.2.1 Overview of the Insulation Health Diagnosis Markers

Two main diagnostic methods commonly reported in the literature for monitoring insulation health are impedance spectroscopy and PD analysis (e.g.: PDIV measurements). Both techniques are widely utilised due to their non-destructive nature, making them suitable for regular insulation condition assessment [172–174].

Various health markers can be derived from impedance spectrum measurement. Changes in impedance spectrum patterns over the ageing process can reveal the deterioration state of the tested specimen [173]. Among these markers, resonance frequency (f_r) has previously been suggested as a potential marker of interturn insulation degradation [175–177], since it directly correlates with the increase in interturn capacitance caused by thermal ageing, decreasing by up to 3 MHz in the worst-case scenario.

In contrast, other researchers reported that impedance at frequencies above and below f_r has demonstrated higher sensitivity to changes in the insulation than f_r itself, with sensitivity differences up to three orders of magnitude [178]. Capacitance measurements have also been proposed as suitable health markers [179]. Specifically, thermal ageing studies on TPs have commonly reported increased interturn insulation capacitance [17, 90, 176, 180]. As reported in [17], an increase of approximately 20% in interturn capacitance could lead to a sufficiently reduced PDIV, thereby enabling the onset of PD activity. Groundwall insulation capacitance, on the other hand, typically decreases with ageing, exhibiting reductions from 12% [147] to as large as 30% prior to breakdown [181]. A comparable tendency in capacitance was also observed in phase-phase insulation measurements of impregnated motorettes [182].

To clarify how each insulation type influences impedance spectrum measurements, a simplified model for random-wound electric machines is presented in Figure 6.13. In this circuit, R_g and C_g represent the groundwall parameters, R_s and L_s are the equivalent resistance and inductance in each coil, and C_t is the interturn capacitance coupling [179]. Of these parameters, C_g and C_t depend solely on geometry and insulation dielectric properties, showing negligible frequency dependence. The model can be simplified based on frequency ranges, as summarised in the following points [179]:

- **Low Frequency (LF) range (below f_r):** The impedance of groundwall insulation dominates over winding impedance and mutual coupling between turns. Therefore, the simplified LF model (Figure 6.13 LF) relates impedance spectrum exclusively to groundwall parameters (R_g and C_g).
- **Medium frequency range (around f_r):** The effect of the winding parameters cannot be disregarded, and thus simplifications cannot be assumed. The winding inductance and resistance, and interturn and groundwall insulation capacitances affect the impedance spectrum. Accordingly, it is complex to relate the impedance spectrum to the insulation capacitances.
- **High Frequency (HF) range (above f_r):** The impedance of the winding branch (RL) increases, whereas the impedance of C_t branch decreases. The simplified HF

model (Figure 6.13 HF) relates the impedance spectrum to both interturn and groundwall capacitances.

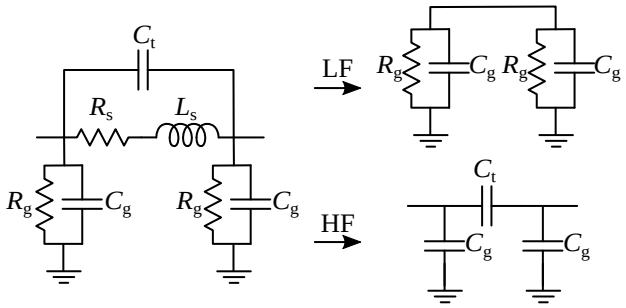

Figure 6.13: *LF and HF simplifications of the model for common-mode impedance spectrum interpretation based on [179].*

Among the parameters used to characterise PD activity, PDIV is commonly employed as a health indicator for insulation systems subjected to thermal ageing. Previous studies using thermally aged TPs have consistently observed a decrease in interturn PDIV with ageing, even when insulation breakdown does not occur [20, 48, 74, 119]. Similar reductions in interturn PDIV have been recorded in studies with impregnated motorettes [150, 154]. Nevertheless, consistent results for groundwall PDIV have not always been obtained, possibly due to variations arising from manufacturing defects [154]. [147] obtained more consistent results for the groundwall PDIV decrease with the increase in thermal ageing time, with an average decrease between 55-66% before failure.

Despite general agreement on the PDIV feasibility as a health marker, because of dispersion in measurement results, reliance on PDIV alone as an ageing marker could be problematic [147, 183, 184]. Consequently, some studies proposed PD energy (charge) as an alternative marker, given its significant changes approaching insulation failure [183].

Some research efforts have combined insulation capacitance with PDIV to assess insulation degradation, observing increased capacitance alongside reduced PDIV during ageing [17, 90, 147]. However, these analyses have typically focused only on interturn insulation samples, such as TPs or coils, excluding groundwall insulation. Furthermore, no comparative study evaluating the sensitivity of both methods as complete insulation system monitoring techniques, tested until failure, has been identified in the existing literature. Hence, further research is required to determine which method provides the most comprehensive assessment of the entire insulation system during ageing.

6.2.2 Experimental Comparison of Impedance Spectroscopy and Partial Discharge Analysis as Insulation Health Diagnosis Techniques

The current work builds on previous studies by extending the analysis up to the failure of complete windings presented in Section 3.1.3, considering interturn and groundwall insulations. It compares the sensitivity of impedance spectroscopy and PD measurements

as a health monitoring techniques for thermally aged electric machine winding insulation systems. To this end, during the thermal ageing experiments presented in Section 6.1.1, the CM impedance of the samples was also measured, as described in Section 3.4, in addition to the PDIV tests.

The condition of the interturn and groundwall insulation was assessed using various markers. Resonant frequency (f_r), the impedance below (at LF level) and above (at HF level) f_r, and parallel capacitance (C_p) were extracted from impedance spectroscopy. From the PD analysis, PDIV and PD charge were used. These markers were compared in terms of: (1) their ability to detect each insulation deterioration, (2) sensitivity to changes induced by ageing, and (3) capability to indicate proximity to breakdown, without specific tuning to each application.

To illustrate where the markers from impedance measurements were extracted, Figure 6.14 presents the impedance, phase, and parallel capacitance spectra of the sample aged isothermally at 230 °C. The corresponding spectra for the remaining samples are provided in Appendix E. Except for the samples thermomechanically aged at 200–260 °C, the measurements taken at the failure time during the PDIV test are also included, as they were carried out before those tests.

Figure 6.14 (a) reveals an increase in impedance at both LF and HF ranges with ageing. Impedance values at 10 kHz and 1 MHz showed the highest sensitivity, increasing by approximately 40% and 28%, respectively. Most of this increase occurred within the first 24 h, followed by a milder upward trend. Furthermore, f_r shifted by about 11% to higher frequencies, showing a similar trend to the phase evolution (Figure 6.14 (b)).

The changes in C_p (Figure 6.14 (c)) were also evident in both frequency ranges. At 10 kHz, C_p decreased by 28% during thermal deterioration of the groundwall insulation. At 1 MHz, the reduction reached 23%. These changes may be linked to variations in the interturn and groundwall insulation capacitances.

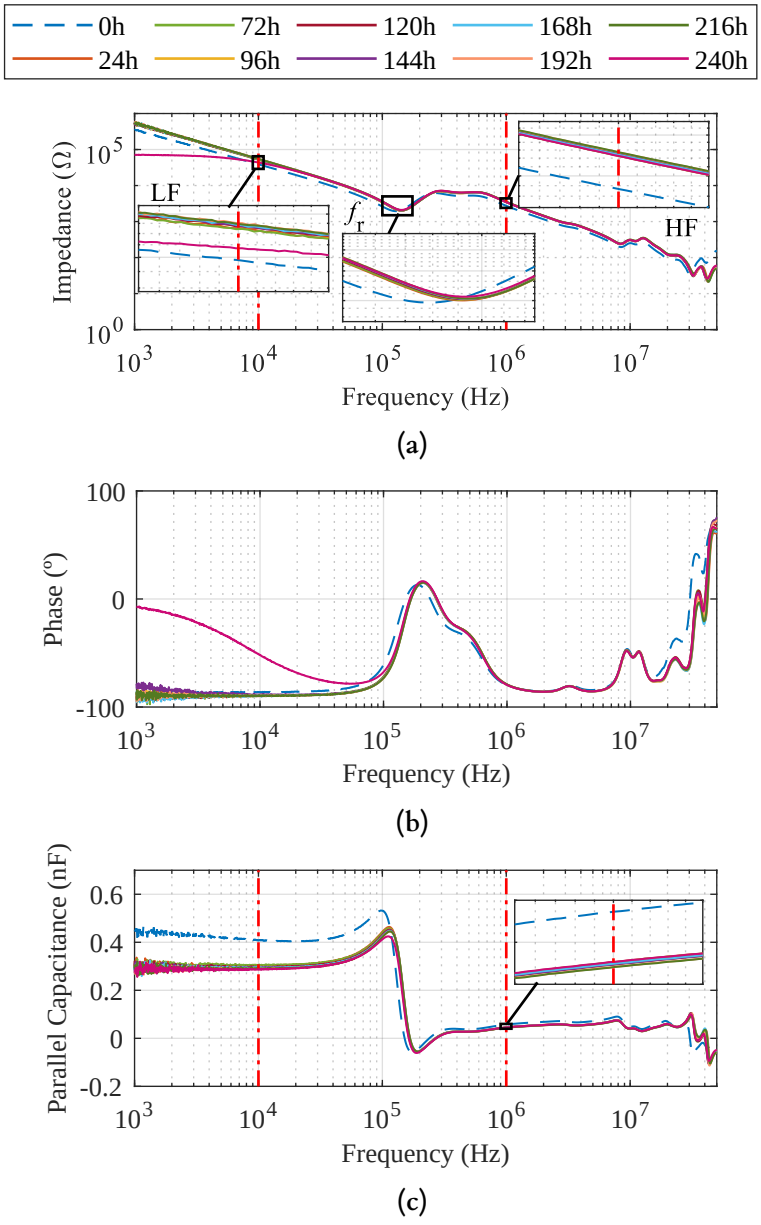

Figure 6.14: *Experimental CM impedance spectrum evolution during isothermal ageing at 230 °C (a) impedance, (b) phase, and (c) parallel capacitance.*

The PD markers were directly extracted from the PDIV measurement. These results were previously presented in Section 6.1.1, Figure 6.3. All in all, the following markers were evaluated:

- **PDIV:** Widely used in the literature [20, 48, 74, 119], in the current study, it was defined as the voltage level at which a PD charge equal to or grater than 0.05 nC was detected.
- **PD charge:** Shown to be promising in [183]. Here, it was defined as the highest charge recorded during the PDIV measurement.

- **Resonance frequency:** Used in [175–177]. For the current comparison, it was extracted from the impedance first peak as shown in Figure 6.14 (a), f_r rectangle.
- **Impedance at frequencies below and above f_r:** Proposed in [178]. At frequencies below f_r, it represents the groundwall insulation, following the simplification of LF range of Figure 6.13. Considering that the mayor change in this range for the current experiments was reported at 10 kHz, the impedance at 10 kHz ($Z_{10\,\mathrm{kHz}}$) was selected as marker (Figure 6.14, (a) LF rectangle).

  At frequencies above f_r, the impedance lies on the HF range of Figure 6.13, therefore, it considers the groundwall and interturn insulations. Given the changes at 1 MHz, the impedance at 1 MHz ($Z_{1\,\mathrm{MHz}}$) was selected as marker (Figure 6.14 (a), HF rectangle).
- **Parallel capacitance (C_p):** This marker was widely used [17, 90, 176, 180]. For the groundwall insulation (LF range), the average of C_p at 6, 18, 30 and 42 kHz (named as $C_p$mean) was proposed in [181]. These values are below f_r of the current results, and therefore, the C_p mean was used.

  At high frequencies, C_p at 1 MHz was selected, which showed most significant changes. As in the case of the HF range impedance, this marker also evaluates the interturn and groundwall insulations.

Figure 6.15 presents the evolution of the groundwall insulation markers ($Z_{10\,\mathrm{kHz}}$, $C_p$mean, PDIV, and PD charge) throughout ageing tests of all samples (presented in Table 3.3). Likewise, Figure 6.16 shows the markers related to interturn insulation (f_r, $Z_{1\,\mathrm{MHz}}$, C_p, PDIV, and PD charge). As previously mentioned, impedance-based markers reflect the condition of both insulations.

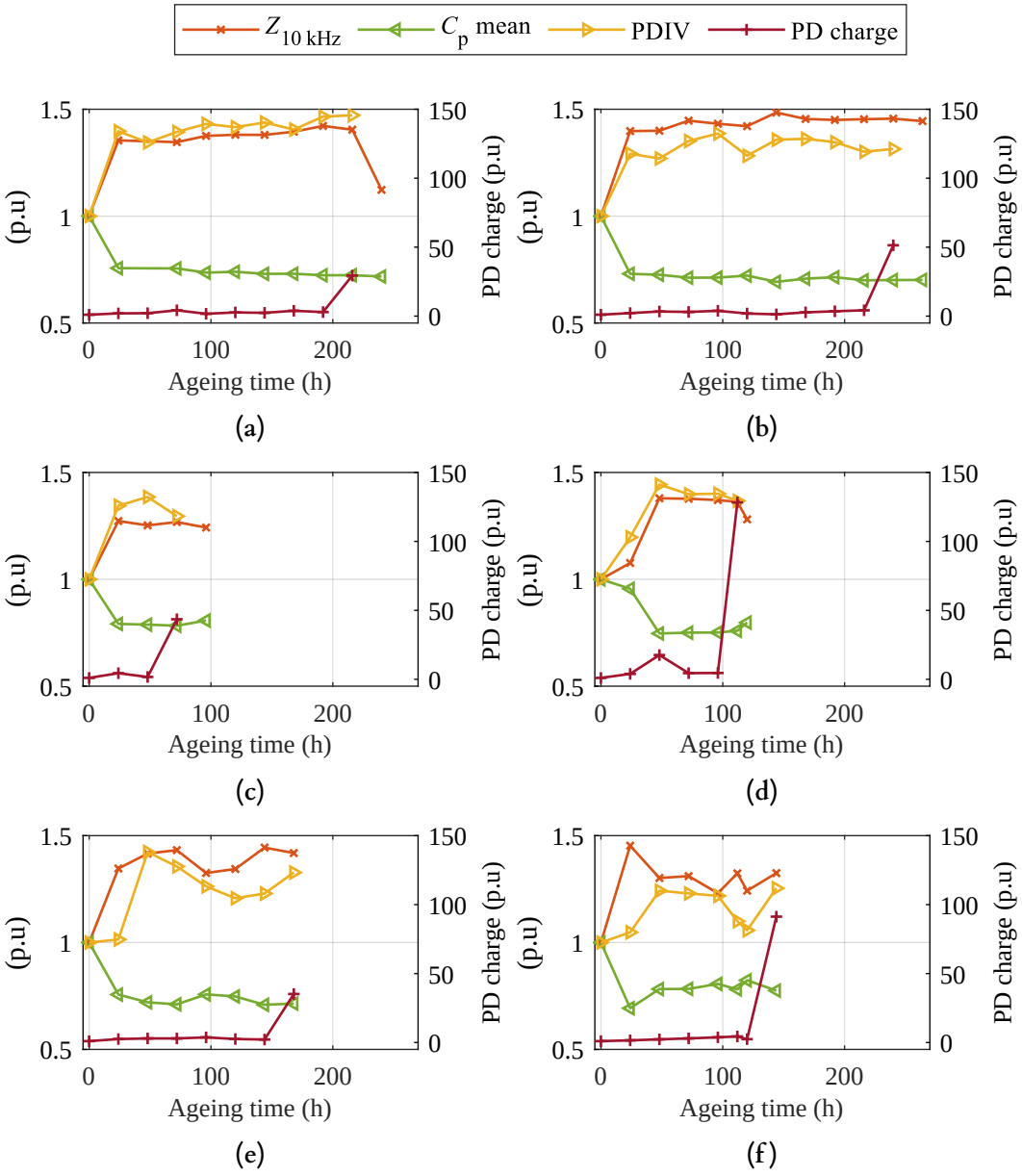

Figure 6.15: *Evolution of the markers of the groundwall insulation during thermal ageing experiments in p.u. referenced to the non-aged condition (a) isothermal 230 °C, (b) thermomechanical 200-230 °C, (c) isothermal 260 °C sample 1, (d) thermomechanical 200-260 °C sample 1, (e) isothermal 260 °C sample 2, and (f) thermomechanical 200-260 °C sample 2.*

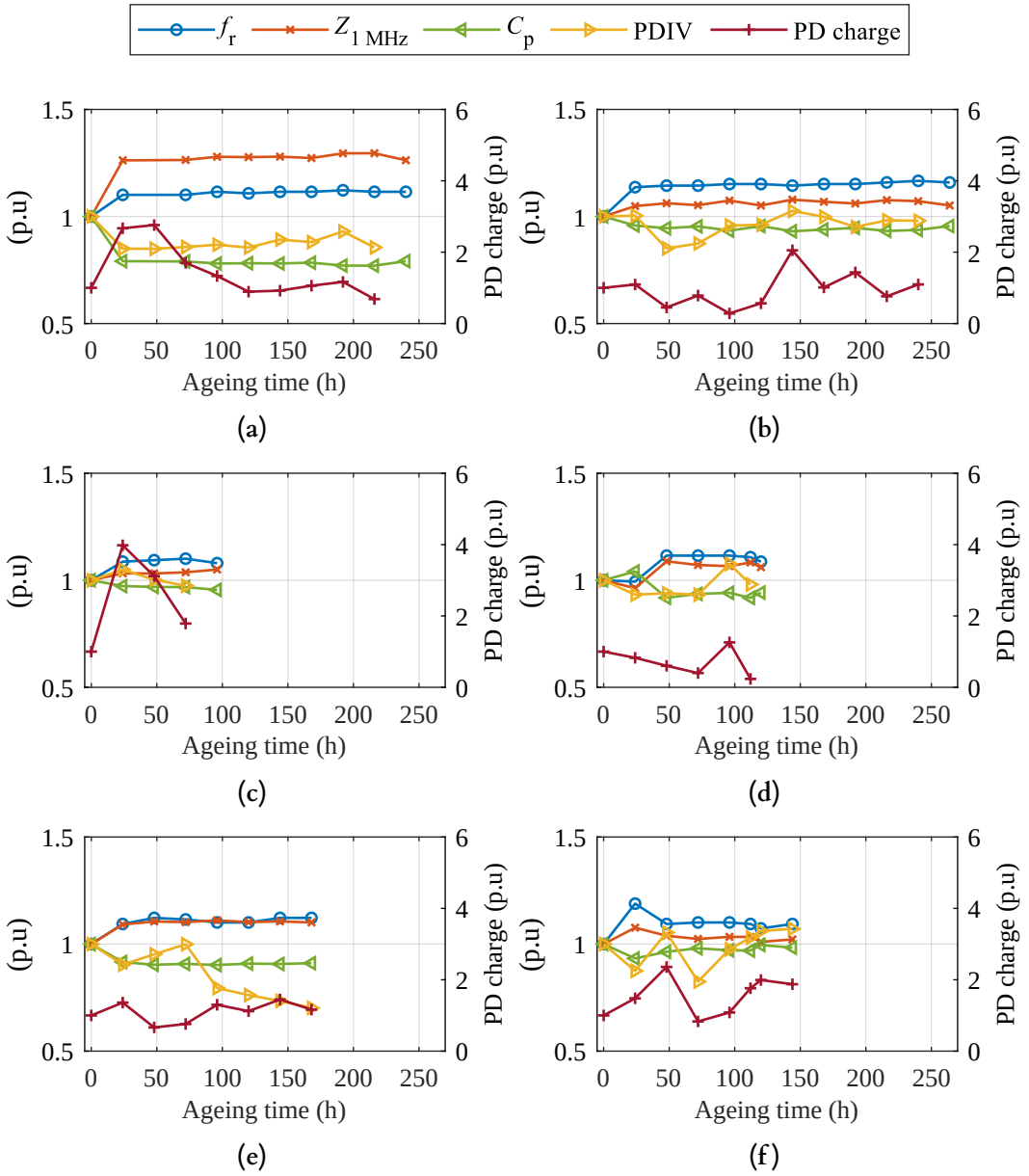

Figure 6.16: *Evolution of the markers of the interturn insulation during thermal ageing experiments in p.u. referenced to the non-aged condition (a) isothermal 230 °C, (b) thermomechanical 200-230 °C, (c) isothermal 260 °C sample 1, (d) thermomechanical 200-260 °C sample 1, (e) isothermal 260 °C sample 2, and (f) thermomechanical 200-260 °C sample 2.*

6.2.2.1 Resonance Frequency

The variation of f_r has been reported as an ageing marker for interturn insulation [175, 176], where reaching a critical variation indicates an approaching failure, with a maximum shift of 12% occurring without reaching the insulation breakdown. In contrast, in the present work (Figure 6.16) the f_r increased rapidly by around 8-13%, followed by a disregarded variation throughout the remainder of the ageing process for all samples,

except for samples 2 thermomechanically aged at 200–260 °C. In this case, f_r increased by 18% at the early stage, subsequently stabilising at 9–10%. The observed general trend of the samples was similar to the results reported in [173], where a sharp initial displacement was followed by a more gradual change.

Although the variation of f_r was noticeable, a critical threshold must be established for each specific application to assess ageing and indicate a potential failure [175]. This requirement represents a significant limitation for using f_r as a general marker. In fact, no clear shift was observed in f_r prior to breakdown when compared to the initial ageing stage. To the best of the author's knowledge, this phenomenon has not been analysed in previous studies, as samples were not tested until failure [173, 175–177].

The influence of parameters besides interturn insulation on f_r (Section 6.2) represents an additional limitation. This may hinder the identification of the specific insulation layer undergoing degradation and complicate the interpretation of ageing progression in interturn or groundwall insulation [179].

6.2.2.2 Impedance Below and Above Resonance Frequency

The impedance at frequencies around f_r was also proposed as an ageing marker in [178], who reported that values measured at $\pm$ 2% of f_r were 3 orders of magnitude more sensitive to ageing than f_r itself for interturn insulation evaluation.

Regarding interturn and groundwall insulation variation (Figure 6.16), the impedance at 1 MHz followed a trend similar to that of f_r, with an initial increase followed by stabilisation. Although the impedance at 1 MHz exhibited a rapid initial increase of about 28%, exceeding the f_r variation, for the sample subjected to isothermal ageing at 230 °C, the changes in the other samples remained below the 10%. This contrasts with the conclusions reported in [178], which indicated that impedance was more sensitive than f_r. Except for the mentioned sample, the sensitivity of the impedance at 1 MHz was comparable to or lower than that of f_r. These finding support the use of f_r as a sufficiently sensitive interturn ageing marker, in line with the conclusions of [177]. The impedance at 10 kHz depicted in Figure 6.15 (used to assess groundwall insulation) followed a similar trend to the 1 MHz results, with increases of approximately 30–45%.

As observed with f_r, the impedance did not exhibit a distinct shift immediately before breakdown. Thus, identifying proximity to failure remains difficult, even if a critical variation threshold were to be defined. Furthermore, while the impedance at LF allows for the specific evaluation of groundwall insulation, in the HF range it is not possible to separate the effects of interturn and groundwall insulation degradation.

6.2.2.3 Parallel Capacitance

Capacitance is one of the most frequently reported ageing markers [17, 90, 176, 180–182]. Interturn capacitance has been reported to increase by approximately 20% [17],

whereas the groundwall capacitance tends to decrease, with reductions ranging between 12–30% [147, 181].

To analyse the groundwall insulation variance, C_p mean was evaluated (Figure 6.15), which decreased by 21–31% at the initial ageing stages, maintaining a relatively stable value during the remaining hours until failure. This reduction was likely due to the deterioration of C_g prior to breakdown (see Section 6.2.1). A similar trend with changes limited to 12% was reported in [147], while [181] observed a 30% reduction just before failure, with a constantly decreasing trend.

At 1 MHz, C_p was 21% lower after isothermal ageing at 230 °C, but limited to 3–10% for the remaining samples (Figure 6.16). This variation likely results from a combination of C_t and C_g effects (see Section 6.2.1).

Multiple authors have reported the increase of interturn insulation capacitance during thermal ageing using TPs [17, 90, 176, 180]. Although this increase was not evident from C_p at 1 MHz, the simplifications shown in Figure 6.13 suggests that the difference between C_p at 1 MHz (5–23%, related to C_t and C_g) and at LF (20–30%, related to C_g) could indicate the influence of the C_t variation. That is, the increase in C_t may attenuate the decrease in C_g observed at LF, resulting in a less pronounced reduction at HF. Hence, detaching the ageing effect on interturn insulation could be achieved by calculating equation (6.2).

$$C_t = C_p(1\ \text{MHz}) - C_p\ \text{mean(LF)} \tag{6.2}$$

Table 6.3 summarises the estimated difference (in %) in C_t relative to the unaged condition (0 h) for all samples during early ageing stages (24–48 h). Except for the isothermal sample at 230 °C, the increase in C_t was estimated to be between 17–24%. These values are in good agreement with the literature, where interturn capacitance increases of approximately 20% were reported after thermal ageing [17, 180]. Indeed, although the actual PDIV measurement does not fully represent the ageing of the coils (since the coil wires were significantly more deteriorated than the routing sections due to heat accumulation Section 6.1.1), the observed decreasing trend in interturn PDIV (Figure 6.16) could reflect the C_t increase, as noted in [90].

When comparing isothermal and thermomechanical ageing, Section 6.1.1 concluded that the mechanical stress generated under thermomechanical conditions was not sufficient to accelerate the groundwall insulation degradation. However, the C_t differences presented in Table 6.3 suggest that mechanical stress was indeed induced in the winding wires. At a peak temperature of 230 °C, a higher C_t difference relative to the unaged condition was observed under thermomechanical ageing. A similar trend was observed when comparing the mean values of both samples subjected to peak temperatures of 260 °C. This finding aligns with the effect of thermomechanical ageing reported for winding wire coils in [74], which showed more severe degradation in thermomechanical aged samples. Even so, as discussed in Section 6.1.1, groundwall insulation was the limiting factor in the present

Table 6.3: *Estimated interturn capacitance difference after the initial ageing cycles (24–48 h) compared to the unaged sample (0 h) for all thermally aged samples (sam.) (%).*

	Isothermal ageing			Thermomechanical ageing		
	230 °C	260 °C		200–230 °C	200–260 °C	
	Sam. 1	Sam. 1	Sam. 2	Sam. 1	Sam. 1	Sam. 2
C_p (1 MHz)	-21	-3	-10	-6	-9	-7
C_p mean (LF)	-25	-21	-25	-27	-26	-31
C_t	4	18	15	21	17	24

samples, and the larger C_t variation, possibly indicating greater interturn degradation under thermomechanical conditions, did not result in reduced endurance.

When evaluating changes before failure, neither C_p mean nor C_p (1 MHz) exhibited a significant variation, and a critical threshold would need to be established for each application. Such limits must be determined through dedicated testing tailored to the final machine configuration, as recommended in [180]. Nevertheless, the stabilisation of the marker could hinder the correct identification of the failure proximity.

6.2.2.4 Partial Discharge Inception Voltage

PDIV is used as a marker in [20, 48, 74, 119]. Information about the insulation systems can be obtained depending on the measurement configuration [9]. A critical PDIV value should be defined as an end-of-life criterion for each application [9].

For interturn insulation, there is a general agreement that PDIV decreases over time [20, 48, 119, 175, 183]. This may be attributed to the decrease in the insulation thickness [119] and the increase in ε_r due to de-polymerisation and oxidation byproducts in the presence of organic compounds [90]. As a result, the electric field in the air may be intensified, increasing the probability of partial discharge initiation. However, there is a disparity in the reported PDIV reduction trends. While a relatively linear decrease of 20–40% was reported in [48, 119, 175], other works such as [20, 183] observed a reduction of around 10%, followed by stabilisation before breakdown. Notably, [183] is the only reference that extended the analysis until failure.

In the present study, as discussed in Section 6.1.1, the same ageing conditions could not be ensured in the routing compared to the coils, resulting in a more erratic interturn PDIV trend, although a decreasing tendency can be speculated. For instance, in the sample isothermally aged at 230 °C (Figure 6.16 (a)), the PDIV stabilised at around 16%, and did not vary following a trend similar to those in [20, 183]. The observed disparate in the trends may hinder the definition of a universal critical variation value. If PDIV stabilises prematurely, the established critical threshold might not be reached before insulation failure occurs.

Regarding the groundwall insulation, PDIV stabilised after an initial increase (Fig-

ure 6.15) and generally did not exhibit a significant change to indicate an imminent breakdown. As explained in Section 6.1.1, this increase could be attributed to the decrease in ε_r of the groundwall insulation, i.e., PA66-FG30. The observed capacitance decrease at LF supports this explanation, considering the direct relationship between permittivity and capacitance.

6.2.2.5 Partial Discharge Charge

PD charge was proposed as a marker in [183]. As discussed in Section 6.1.1, the PD charge for interturn insulation did not exhibit a significant variation (Figure 6.16). In contrast, [183] reported a clear increasing trend followed by stabilisation when PD charge was measured using a constant input voltage. For the current work, however, the PD charge was obtained from the PDIV measurement, where the input voltage level was not fixed. Although the PDIV voltage remained relatively stable throughout the tests, these small variations could introduce uncertainties in the observed evolution of the PD charge.

On the other hand, the results for groundwall insulation (Figure 6.15) were consistent with the trend described in [183]. In the present experiments, a clear stabilisation was observed at approximately twice the initial charge level. Additionally, a substantial increase in charge was recorded just before the breakdown, without a corresponding variation in the PDIV, as also noted in [183]. This increase occurred during the ageing cycle preceding the failed PDIV test. No such increase was observed for interturn insulation, which did not fail.

Taken together, these results suggest that PD charge might be a reliable marker for identifying imminent insulation failure. This information can be extracted from the PDIV measurement, enabling separate evaluation of each insulation system. While PD charge may not present a consistent trend throughout the ageing process, it has demonstrated its effectiveness as a marker for approaching failure, without requiring a defined critical threshold for each specific application.

6.2.3 Concluding Remarks

The work presented in this section compares impedance spectroscopy and PD measurements as a health monitoring techniques for thermally aged electric machine winding insulation systems. Complete windings were thermally aged until failure, and both the impedance spectrum and PD were periodically measured at ambient temperature. Based on these results, several markers proposed in the literature were evaluated (f_r, the impedance below and above f_r, and parallel capacitance from impedance spectroscopy, and PDIV and PD charge from PD measurements). These markers were compared considering: (1) detection of deterioration of interturn and groundwall insulations, (2) sensitivity to changes in the insulation due to ageing, and (3) ability to indicate a near breakdown with no adaptation to each specific application.

While markers obtained from impedance spectroscopy varied with ageing, they failed to show a significant distinction near the point of failure. Consequently, the stabilisation of these markers may impede the accurate identification of an approaching breakdown, even if a critical variation is experimentally defined for each application. Moreover, detaching the effect of interturn and groundwall insulations from other influencing factors could be challenging, particularly when using f_r. A possible solution was proposed in this study through the use of C_p to decouple the contributions of both insulations. Nonetheless, further investigation is required. For instance, the analysis could be extended to winding wire coil samples (as used in [74]), in which only the interturn insulation deteriorates. By comparing the capacitance evolution of these samples with that of complete winding under the same ageing conditions, it could be validated whether the proposed method for isolating interturn insulation deterioration via HF C_p is reliable.

PD analysis appeared to offer a more meaningful health diagnosis technique. Interturn and groundwall insulations could be assessed independently, depending on the measurement configuration. Additionally, PDIV provided valuable information regarding the PD-free working status of the electric machine, and the PD charge measured during testing could reveal an imminent failure.

Hence, the periodic monitoring of PDIV and PD charge could support more effective insulation maintenance decisions. This approach enables the identification of the specific insulation system affected and the urgency of any required intervention.

Future work on this investigation could include expanding the number of tested samples. Further analysis of the correlation between impedance evolution and PD activity during ageing may also provide valuable insights.

Chapter 7

Conclusions and Future Lines

Three and a half years have passed since the beginning of this PhD project. This period has allowed the development of sound conclusions. However, several challenges remain, along with opportunities for further research. This final chapter summarises the key findings and proposes potential directions for future work.

7.1 Conclusions

At the beginning of the PhD, several objectives and hypotheses were defined, shaping the workflow over the past few years. This section evaluates the level of fulfilment and validity of those initial aims.

The main goal of the PhD was to establish design tools and guidelines for developing robust and reliable insulation systems in electromobility drives based on WBG converters, with particular focus on insulation system behaviour under operating conditions and long-term endurance. This goal aligns with the structure of the document.

Chapter 2 provided the theoretical background necessary to understand the challenges posed by WBG converters on insulation system design, as well as the fundamentals of PD phenomena. Chapter 3 defined the sample configurations and detailed the experimental methodology applied throughout the work.

Focussing on PDIV under operating conditions, Chapter 4 presented a comprehensive analysis of the variables influencing this parameter, identifying the key factors require for accurate PDIV estimations. After reviewing the limitation of existing models in the literature, new accurate models were developed, particularly for interturn insulation, that require minimal resources, and no extensive simulation or experimental calibration.

Extending the analysis of the PDIV, Chapter 5 addressed the effect of winding manufacturing techniques and assembling stages on the insulation system, with a focus on groundwall insulation. It is also demonstrated the applicability of the models proposed in Chapter 4 for selecting optimal insulation thickness and material during machine design.

Finally, Chapter 6 focused on the long-term endurance of insulation systems under WBG converter operation. Thermal stress was evaluated through a comparison of isothermal and thermomechanical ageing, while electrical stress was analysed by studying the combined effects of waveform parameters. The chapter also examined the effectiveness of insulation health diagnostic markers based on impedance spectroscopy and PD analysis.

Overall, the main goal of the PhD can be considered accomplished at this stage. The following points discuss the fulfilment of the remaining objectives and the validation of the original hypotheses.

O1. Identify the most relevant environmental and electrical variables affecting the PDIV, and analyse their influence on the initiation of PD activity.

H1. *The use of WBG-based converters to supply the electric machines could affect the PDIV at the operating conditions.*

H2. *The exposure of the insulation to high humidity and temperature will worsen the PDIV at operating conditions*

The findings presented in Chapter 4 address **O1** by identifying temperature, humidity, and pressure as the most influential environmental parameters affecting

PDIV, with temperature confirmed as the dominant factor. Humidity was also shown to degrade PDIV under specific thermal conditions, thereby validating **H2**, which proposed the exposure to high humidity and temperature would negatively impact the insulation performance. Pressure demonstrated a U-shape influence on PDIV, although its practical relevance is limited in systems operating at atmospheric pressure.

Regarding electrical parameters, the analysis revealed that waveforms characteristics, including those typical of WBG-based converter, have limited effect on PDIV when overshoot is properly controlled. The literature presents contradictory finding on the role of rise time, yet most recent studies suggest that rise time does not directly impact PDIV. Instead, the associated overshoot caused by shorter rise times may affect the measured PDIV, making the peak-peak voltage the most relevant parameter. There is broader consensus on the increase in PDIV with shorter pulse widths when combined with short rise times. Nevertheless, most studies, along with the experimental results in this work, support the suitability of sinusoidal waveforms for evaluating insulation systems fed by pulsed voltage. These findings underscore the importance of managing overshoot in practical applications using WBG-based converters. These observations challenge the general assumption in **H1**.

In summary, the main conclusions related to this objective are: (1) temperature and humidity must be incorporated into PDIV estimation models, with pressure only considered when the application involves non-atmospheric conditions, and (2) sinusoidal waveforms remain valid for model development and validation, provided that overshoot is carefully controlled in real application.

O2. Develop models and procedures for estimating PDIV under representative operating conditions obtaining a mean error lower than 5%, with a particular focus on interturn insulation.

H3. *An accurate, fast and directly applicable PDIV model without parameter adjustment that considers most relevant factors affecting PDIV during operation would enable estimating the PDIV at the beginning of the electric machine lifetime when simulation and experimental resources are not available.*

H4. *By applying these models in the preliminary design stage of the insulation system could help to make consistent decisions regarding the required insulation system and material.*

By establishing and validating the Extended Dakin's and Extended parallel-plate models, Chapter 4 directly addresses **O2**. The novelty of these models lies in the extension of Dakin's and parallel-plate equations to account for temperature and/or humidity in the PDIV estimation, which, to the best of the author's knowledge, has not been previously addressed in the literature. For Extended Dakin's model, a new set of extensive experiments covering a wide range of environmental conditions, sample types, enamelled materials, and thicknesses was required to develop equations

grounded in experimental data. In the case of the Extended parallel-plate model, Dunbar's correction was incorporated to consider the effect of the temperature. The validity of this combination had not been previously demonstrated in the literature.

These models provide reliable PDIV estimations under representative operating conditions, particularly for interturn insulation systems. Notably, the Extended Dakin's model requires no parameter adjustment, relying solely on sample characteristics and environmental conditions, while achieving an accuracy comparable to more complex simulation-based approaches. This outcome validates **H3**, demonstrating that a fast and accurate model, without the need for empirical fitting and simulations, is capable of estimating PDIV at the beginning of the electric machine lifetime.

A comparative validation was performed against established FEM-based models employing Paschen's and Schumann's criteria, using a dataset of 140 samples tested across various temperatures and humidity levels. In the combined validation domain, the Extended Dakin's and Extended parallel-plate models exhibited mean errors of -5.3% and -2.5%, respectively, while FEM+Paschen's and FEM+Schumann's models yielded 1.7% and -12.6%. In terms of maximum error, the proposed models remained below 22%, compared to 26.1% and 38.6% for the FEM+Paschen's and FEM+Schumann's models, respectively. These results confirm that the proposed models offer comparable accuracy to existing methods while avoiding the need for simulations and parameter adjustments (in the case of the Extended Dakin's model).

A detailed comparison of computational efficiency highlighted the practical value of the proposed approaches. The Extended Dakin's and Extended parallel-plate approaches required only $0.25 \cdot 10^{-3}$s and $0.34 \cdot 10^{-3}$s per sample, respectively. In contrast, FEM+Paschen's and FEM+Schumann's models required 110.29 s and 155.75 s per sample. This corresponds to a computational cost reduction of over five orders of magnitude, making the proposed models particularly suitable for early-stage design applications.

These attributes directly support **H4**, as the models provide a practical tool for insulation performance evaluation during the design stage. Their simplicity and rapid computation allow designers to make consistent and informed decisions regarding material selection and insulation thickness without requiring simulation capabilities or extensive experimental characterisation.

In conclusion, the key finding supporting this objective are: (1) the proposed new models enable accurate and conservative PDIV prediction across a broad range of conditions, (2) their performance matches that of established by FEM-based methods with substantially lower computational cost, and (3) they facilitate early well-informed insulation design decisions without the need for simulation and experimentation resources.

O3. Evaluate the design and manufacturing factors affecting the insulation system of electric machines by validating and extending the practical applicability of the proposed PDIV estimation tools, and assessing the insulation system during manufacturing and assembling processes.

H5. *Different winding manufacturing techniques could affect the PD behaviour of the insulation system.*

H6. *The various weak points in the insulation system, whether identified during the design phase or not, could be successfully detected and addressed by consistently evaluating the PD behaviour throughout the assembly process of the electric machines.*

H7. *Fabrication tolerances associated with different processes can significantly influence the performance of the insulatin system, potentially reducing its reliability.*

The work developed in collaboration with two industrial companies presented in Chapter 5 contributes to fulfilling **O3** by evaluating key design and manufacturing factors, including the insulation performance of electric machines. This was achieved through the validation and practical application of the proposed PDIV estimation tools, alongside the systematic assessment of insulation behaviour through the manufacturing and assembly processes.

The comparative analysis between semi-automatic and needle winding machines, conducted together with the first industrial company, confirmed that both techniques yield consistent groundwall insulation quality. PDIV values differed by less than 5% across all configurations, with low variability between machines, indicating high repeatability and reliable manufacturing standards. These finding do not suggest a significant degradation of insulation due to the needle-winding process, although elevated discharge magnitudes observed at higher voltages warrant further investigation.

These findings partially support **H5**, highlighting that while both winding methods produce compliant insulation systems, subtle differences may affect long-term PD susceptibility of needle machines under electrical stress beyond the PDIV threshold. It must also be noted that the analysis was limited to (1) groundwall insulation evaluation, and (2) two winding techniques. Therefore, actual interturn defects should be evaluated in depth using impulse voltage PDIV measurements, and the conclusions drawn should not be generalised to all winding manufacturing methods, assessing individually additional techniques with due care.

A broader analysis of the machine development process, conducted with the second industrial partner, enabled the early detection of insulation weaknesses, notably in the thermistor area and inter-cap gaps of the initial prototypes. These weaknesses were successfully mitigated through targeted design modifications, including thermoretractable shielding and overlapping geometries, which enhanced insulation margins in the final product. Other potential solutions, such as varnishing or manual potting of the inter-cap gap, were evaluated and discarded due to limited

effectiveness. These results directly support **H6**, which proposed that various weak points can be effectively identified and resolved through systematic evaluation of PD behaviour during machine assembly.

Due to cap manufacturing tolerance issues affecting some final batch units, groundwall insulation was modified to ensure adequate phase-phase separation. The Extended Dakin's and Extended parallel-plate models were employed to predict groundwall PDIV for new material and thickness selections. Their predictions matched experimental values on simplified cap samples, with maximum errors of 4.6% and 11%, respectively. These results confirm their early-stage design practical applicability not only for interturn insulation but also for groundwall insulation, further supporting **H4**. The Extended Dakin's model proved particularly valuable due to its accuracy and independence from material-specific calibration. On this basis, a suitable cap material and insulation thickness were successfully defined in the early design stage.

Final system validation confirmed that all machines met the groundwall PDIV requirement of 1202 Vrms, withstanding 2000 Vrms for 120 seconds without failure. While potting introduced greater variability in TR300 resin caps, it enhanced overall insulation strength. Nylon 12 caps, ultimately selected for their superior manufacturing consistency, exhibited lower sensitivity to potting and did not reach insulation strength levels of TR300 resin. Nonetheless, the potting effectively reduced PD magnitudes for the units with Nylon 12 caps, which is a key factor for ensuring long-term ageing resistance.

The phase-phase insulation issues arising from the groundwall insulation cap manufacturing problems, along with the increased PDIV variability observed after potting, identified these processes as particularly sensitive, as they significantly affect the performance of the insulation system. These observations directly validate **H7**, which states that fabrication tolerances associated with different processes can significantly influence the performance of the insulatin system, potentially reducing its reliability.

In essence, the conclusions supporting this objective are: (1) the proposed models enable fast and accurate PDIV estimation to support design and material selection for groundwall insulation, (2) winding technique can influence PD behaviour slightly by increasing discharge magnitude at higher voltages, even when PDIV remains unchanged, and (3) consistent evaluation of PD behaviour throughout the assembly process allows for early detection and resolution of insulation issues, underscoring the importance of integrated validation during the final design definition.

O4. Identify, characterise, and assess the most critical stress factors that negatively impact the long-term endurance of insulation systems, by evaluating a set of insulation health monitoring markers.

H8. *The use of WBG-based converters and the high temperatures reached during operation will accelerate the ageing of the stator winding insulation system, reducing ultimately*

its endurance.

H9. *Developing endurance models that account for the most critical stress factors can help estimate the lifespan of the insulatin system under specific operating conditions, providing valuable support for insulation health diagnostics and preventive maintenance.*

H10. *By evaluating the insulation health during its lifetime could provide information regarding the proximity of insulation failure. This way, anticipated maintenance works could be performed, avoiding failure and ensuring reliable operation.*

Through the analysis of the thermal and electrical ageing mechanisms, Chapter 6 addresses, at least partially, **O4** by characterising the critical stress factors governing long-term insulation degradation and evaluating the effectiveness of selected health monitoring markers. Experimental results confirmed that high operational temperatures and specific waveform parameters typically of WBG-based converters, particularly the short rise times even when overshoot is controlled, accelerate insulation degradation. These findings directly support **H8**, which proposed that both WBG-induced electrical stress and thermal conditions negatively impact insulation endurance.

Ageing experiments conducted to complete windings under controlled isothermal and thermomechanical conditions revealed that failures occurred predominantly in the groundwall insulation. Under equivalent peak temperatures, isothermal ageing generally resulted in shorter endurance times. No significant acceleration effect from thermomechanical ageing was observed for PA66-FG30, contrasting with earlier studies involving materials like PI or PAI. These findings suggest that the effectiveness of thermal cycling depends strongly on the insulation material and the magnitude of the applied thermal gradients. Nonetheless, thermomechanical ageing proved more restrictive when compared at equal rms temperatures, refining assumptions regarding its universality as an acceleration method.

In parallel, electrical ageing experiments using a DoE approach for SW and CRW samples showed that shorter rise times consistently reduced endurance, likely due to lower RPDIV, despite no direct effect on PDIV could be considered. The interactions between pulse width, non-conduction duration, and rise time were found to be complex and insulation-type dependent. The most severe degradation typically occurred under high pulse widths and short non-conduction times, particularly for SW insulation. These results help clarify how waveform characteristics, such as those produced by fast-switching WBG devices, contribute to insulation wear, providing further confirmation of **H8**. Given the complexity of the results obtained from the electrical ageing experiments, it was not possible to further investigate **H9**.

To evaluate insulation health over time, Chapter 6 also compared PD analysis and impedance spectroscopy as diagnostic tools during thermal ageing. While several impedance-based markers (e.g., f_r, C_p) showed evolution with ageing, they did not provide clear indicators of imminent failure. Conversely, PD-based markers, such as

PDIV and discharge charge, demonstrated consistent sensitivity to degradation and more reliable anticipation of failure. These findings validate **H10**, supporting the use of PD measurements for insulation lifetime tracking and predictive maintenance strategies.

Accordingly, periodic monitoring of PDIV and PD charge emerges as a promising diagnostic approach to identify the affected insulation subsystem and determine the urgency of intervention. This enables condition-based maintenance, reducing the risk of unexpected failures and ensuring reliable operation throughout service life.

All in all, the conclusions supporting this objective are: (1) both thermal and electrical stress significantly reduce insulation endurance, especially under conditions representative of WBG operation, (2) degradation is dependent on waveform parameters and thermal cycling regime, with insulation material properties playing a central role, and (3) PD analysis, especially through PDIV and charge evolution, offers a more robust means of insulation health assessment compared to impedance spectroscopy.

7.2 Future Lines

Despite the general objectives of the PhD having been successfully addressed, the findings and conclusions are not exempt from limitations, which should be explored further in future investigations:

- **Extended validation of the proposed models for groundwall and phase-phase PDIV estimation:** The proposed models, particularly Extended Dakin's equation, demonstrated acceptable accuracy over 140 samples across a range of temperature and humidity levels. The extension of Extended Dakin's model for groundwall insulation also showed promising results at limited sample number at environmental conditions. A natural progression of this work is to extend the validation to further materials, including insulation papers, and environmental conditions. This would allow the Extended Dakin's model to become a general, fast, and easy-to-use tool for the full insulation system design of electric machines. Once a comprehensive PDIV model is defined, it could be integrated into interturn voltage models. This could enable prediction of the voltage each insulation system must withstand based on the applied bus voltage and drive system characteristics, allowing optimal material and thickness selection.
- **Dedicated investigation of RPDIV:** The main insulation parameter evaluated in this work for the design of the insulation system was the PDIV, emphasising how operation factors affect it and developing models to predict it. It is unfortunate that the study did not generally include RPDIV in this stage. During the electrical ageing experiments, it was observed that, in addition to PDIV, RPDIV has a significant effect on the endurance of the insulation, as it can be potentially more affected

by the WBG-based converter waveform parameters than the PDIV. Therefore, including models that can predict RPDIV in the design of the machines under operating environmental conditions could support even more reliable insulation system designs. Although the development of these types of models could be difficult due to the stochastic nature of PD activity, approaches using Volume-Time Theory model could be a suitable foundation.

- **Analysis of the interturn insulation in semi-automatic vs needle winding processes:** The comparison between the semi-automatic and needle winding manufacturing techniques was limited by the inability to measure interturn insulation performance on complete stators. The main PDIV measuring method used in the current study was the sinusoidal waveforms, which is not valid for the evaluation of interturn insulation on completely manufactured stators. This limited the comparison of the winding processes to the analysis of the groundwall and phase-phase insulations. Including interturn insulation in the analysis could finally validate the similarities between both techniques.

  Future work should assess interturn insulation either using pulse waveforms for the PDIV measurements, or by fabricating dedicated samples. For instance, the simplified samples used for cap material and thickness evaluation could be adapted to recreate interturn winding conditions by winding two wires in parallel. These samples could also allow investigation of key needle winding process parameters, such as tension, which may explain the observed differences in discharge magnitudes at high voltages.

  This extension to the interturn insulation analysis could also help clarify the origin of the charge level differences observed between semi-automatic and needle machines. A more detailed investigation of the frequency range of the measuring device, along with an evaluation of the resonance response of both machines, could whether the observed charge differences reflect a genuine variation or are the result of resonance phenomena.

- **Study of potting material and process improvements:** The negligible improvement of the Nylon 12 caps units after potting, compared to TR300 resin cap units, remains an open question. This could relate to the reduced potting volume in the Nylon 12 units, which requires further verification. Additionally, the variability introduced by the potting process, regardless of cap material, should be investigated. Process parameters should be better controlled and optimised to reduce variability and ensure consistent manufacturing quality.

- **Increase of the sample number and evaluation of mechanical properties of the insulation materials in thermal ageing tests and improve interturn insulation measuring:** The generalisability of the conclusions regarding the comparison between isothermal and thermomechanical ageing is subject to the limited number of samples utilized in the study. Increasing the number of samples, currently ongoing, would strengthen statistical confidence. Furthermore, analysis

of the mechanical properties of the PA66-FG30 groundwall material under thermal stress would help clarify whether thermomechanical cycling introduces significant additional stress. In particular, thermal strain and fatigue behaviour should be studied, as well as the combined mechanical effect of interturn-groundwall system and stator core.

Additionally, it was not possible to thoroughly evaluate interturn insulation degradation due to the lower thermal stress applied to the routing wires compared to those in the stator coils. Therefore, measuring the interturn insulation using impulse waveform-based equipment or employing alternative sample types, such as coils or motorettes, could help to further explore interturn insulation behaviour.

- **Further analysis of waveform parameters effect on the endurance:** While reducing rise time was clearly shown to decrease endurance, the combined influence of rise time, pulse width, and non-conduction duration remains complex. The chance of considering a negligible effect of the frequency beyond 35 kHz was questioned and remains opened, as it was not possible to isolate its effect due to variable duty cycles. Future experiments should analyse the possible effect of frequency, adjust the DoE parameters according to the obtained results, and consider to include a third level. These tests should be performed under strict handling conditions to reduce variability. Additionally, simultaneous measurements of PDIV and RPDIV under matching conditions could clarify the specific influence of waveform features on insulation degradation.

- **Development of endurance models accounting for thermal and electrical stresses:** As previously mentioned, the complexity of the electrical ageing results hindered the development of endurance models. Once the individual and combined effects of waveform parameters are clearly defined and confirmed, the next step should involve building a model based on those results. To achieve a comprehensive model, thermal parameters must also be included, with both isothermal and thermomechanical ageing conditions considered. This could be approached using a DoE methodology, although the increased number of variables would significantly extend the experimental campaign. An alternative strategy could involve a two-step modelling approach: first, thermally ageing insulation samples to different degradation levels, and then subjecting those same samples to electrical stress conditions analysed via DoE. In either case, a carefully planned and extensive experimental framework will be required.

  Another distinct option involves tracking the evolution of PDIV by incorporating changes in insulation thickness and relative permittivity during ageing. By defining a critical PDIV threshold, below which insulation should not operate as described in [9], the estimated PDIV over time could be systematically compared against this value. When the estimate approaches the threshold, maintenance actions could be scheduled. The PDIV estimation during ageing showed potential in the literature, where Dakin's equation and FEM+Schumann's models have been used to estimate

interturn PDIV at ambient conditions across various thermal ageing stages.

These efforts could be improved by estimating the degraded PDIV under operation conditions using the Extended Dakin's model developed in this work. Unlike the FEM+Schumann's model, which also enables operation-condition predictions, the extended Dakin's model avoids the need for simulations or parameter fitting. However, a major challenge lies in accurately estimating the evolution of insulation thickness and relative permittivity, as well as integrating the effect of electrical parameters. Furthermore, as observed in this work, groundwall PDIV may reach a plateau during thermal ageing, potentially limiting the applicability of this method to interturn insulation.

- **Online measurements to extend the analysis of the effectiveness of PD measurements as a diagnostic marker:** The comparison between impedance spectroscopy and PD-based markers positioned PD measurements as the preferable method to detect impending insulation failure. These measurements were conducted offline every 24 hours, successfully identifying failure in the ageing cycles prior to breakdown. It is imperative to acknowledge the temporal gap between the identification of impending failure and the actual breakdown to evaluate the necessity of maintenance and guarantee precise scheduling. This timing could not be evaluated in the current work.

  Extending the analysis to online measurements could help address this gap. Continuous monitoring of PD activity in aged samples would provide insights into how early the PD charge magnitude signals are approaching failure, continuing the work initiated here. This analysis could also examine the correlation between impedance spectroscopy and PD measurements in more detail.

  Further work should include other types of samples to more accurately assess interturn insulation. In the present study, interturn insulation was evaluated through the routing wires connecting coils of the same phase, where wires from all three phases were in contact. As the enamelled wire served as both interturn and phase-phase insulation, the phase-phase PD measurements were assumed to represent the interturn behaviour. However, the routing wires experienced significantly lower thermal ageing compared to the coils, limiting the ability to assess actual interturn degradation.

  To address this, alternative sample types such as coils, twisted pairs, or motorettes should be used. For example, the effectiveness of the PD charge magnitude as a degradation marker could be further evaluated during electrical ageing experiments by measuring PD activity in real time. Furthermore, the use of these samples could also support the separate evaluation of each insulatin system, allowing for a more precise analysis of the effectiveness of diagnostic markers across the complete insulation system.

- **Publish the work:** As previously stated, part of the work developed in Chapters 4 and 6 was published in a peer-reviewed journal and congress proceedings. The

remaining work, including the complete Extended Dakin's model development and validation, thermomechanical and isothermal ageing comparison, electrical factors effect on endurance, and the analysis of the effect of design and manufacturing factor on the insulation system was not yet published, efforts are underway to do so.

Appendix A

PDIV Results for the Derivation and Validation of Extended Dakin's Model

The development and validation of the Extended Dakin's models required extensive experimental data encompassing various insulation materials, thicknesses, and environmental conditions. This data was obtained through both in-house measurements and literature sources. This appendix compiles comprehensive information on the samples used to derive the Extended Dakin's temperature and Extended Dakin's absolute humidity models. Additionally, it provides details on the samples used for models validation, outlining any necessary assumptions and the corresponding estimated PDIV values.

A.1 Extended Dakin's Temperature Model

A.1.1 Model Derivation

This section describes the information regarding DT dataset. Table A.1 presents the PDIV measurement results, as outlined in Section 3.3.1, at 20, 100, and 180 °C for the samples listed in Table 3.1 (Section 3.1). The table includes the average, maximum, and minimum values obtained from three measured samples. These results were used to derive

the Extended Dakin's temperature equation and are graphically represented in Figure 4.19 in Section 4.3.2.1.

Table A.1: *In-house experimental average, maximum, and minimum PDIV (Vrms) results at 20, 100, and 180 °C for the Extended Dakin's temperature model derivation.*

Sample	20 °C			100 °C			180 °C		
name	Mean	Max	Min	Mean	Max	Min	Mean	Max	Min
PC1	713	726	696	614	621	608	543	548	537
PC2	805	819	797	727	749	707	638	651	616
PC3	954	957	953	838	884	798	746	775	718
PC4	800	813	792	754	768	742	711	714	707
PC5	912	926	891	862	875	856	817	824	810
PC6	997	1019	960	944	954	935	922	946	902
PC7	698	718	677	654	664	637	570	589	551
PC8	808	825	788	770	805	717	685	703	661
PC9	897	931	877	821	873	781	748	748	706
PC10	772	788	746	707	722	676	615	630	593
PC11	871	890	848	787	798	776	703	719	688
TP1	610	619	593	543	592	478	485	503	454
TP2	625	639	609	560	614	492	500	551	453
TP3	612	644	583	546	553	525	518	524	498
TP4	553	581	527	525	466	507	459	466	438

A.1.2 Model Validation

For the validation of the Extended Dakin's temperature model, obtaining measurements at multiple temperatures was preferred over measuring numerous samples at a single temperature. Consequently, a new dataset (VT) was generated, incorporating additional samples tested across a temperature range of 20–240 °C.

Table A.2 summarizes the specifications of additional in-house samples, experimental PDIV results, and PDIV estimations using the Extended Dakin's temperature model (equation 4.24). The relative humidity at ambient temperature was measured, while at higher temperatures, it was not controlled. For temperatures below 100 °C, the expected relative humidity was estimated using the equation provided in [73] for uncontrolled humidity conditions inside an oven, assuming an initial relative humidity of approximately 50%, consistent with actual conditions. For temperatures above 100 °C, the relative humidity was considered negligible under uncontrolled conditions [73]. The manufacturer provided all copper dimensions and the specific insulation thickness (t_{ins}) for PC samples, while the average t_{ins} for Grade 2 wires, as defined in [52], was used for TP. Additionally, the manufacturer supplied the relative permittivity ($\varepsilon_{r\,ins}$) measured at 1 kHz. Since these permittivity values were temperature-dependent, it was assumed to remain constant for a given temperature, regardless of RH.

Experimental data from the literature was also compared to the model. Twisted pair samples were used in all cases, and PDIV was measured with a sinusoidal waveform. Tables A.3, A.4, and A.5 set out the results published by D. Muto et al. [81], M. Gomez de la Calle et al. [122], and Y. Kikuchi et al. [70], respectively. In this latter case, the t_{ins} was not provided, and, as the wires were Grade 2, the average t_{ins} for this type was used. Additionally, PDIV measurements were carried out in the RH 30–80% range [70]. It should also be noted that results published by [81] were in terms of PDIV ratio to 25 °C value. Thus, the comparison of the model was also performed in those terms.

Table A.2: *Extended Dakin's temperature model validation sample specifications and PDIV results for validation (own measurements).*

Sample name	Material	Copper dimensions (mm)**	T(°C)	RH(%)	t_{ins} (μm)	ε_r (-)	PDIV$_{exp}$ (Vrms)	PDIV$_{est.}$ (Vrms)
VT1	PAI	3.460×1.600	20	52	100.0	4.424	891	853
VT2	PAI	3.460×1.600	20	59	144.6	4.424	927	990
VT3	PAI	3.460×1.600	20	62	152.8	4.424	1065	1013
VT4	PAI	3.460×1.600	20	58	153.6	4.424	1017	1015
VT5	PAI	3.460×1.600	20	63	161.8	4.424	1054	1037
VT6	PAI	3.460×1.600	20	62	157.0	4.424	1169	1024
VT7	PI	4.015×2.212	20	50	39.0	3.093	649	674
VT8	PI	4.015×2.212	20	50	54.0	3.093	799	769
VT9	PI+PAI	4.015×2.212	20	50	88.0	3.438	840	897
VT10	PI+PAI	4.015×2.212	20	50	66.0	3.438	821	799
VT11	PI+PAI	4.015×2.212	20	50	69.0	3.438	770	813
VT12	PI+PAI	4.015×2.212	20	50	71.0	3.889	783	783
VT13*	PE+PAI	0.850	20	50	36.3	4.258	617	575
VT14*	PE+PAI	1.000	20	50	39.0	4.258	620	592
VT15	PI	4.015×2.212	40	19	39.0	3.093	654	658
VT16	PI	4.015×2.212	40	19	80.0	3.093	823	883
VT17*	PE+PAI	0.850	40	19	35.0	4.258	592	553
VT18*	PI	0.900	40	19	37.0	3.093	636	644
VT19	PI	4.015×2.212	60	8	39.0	3.085	632	643
VT20	PI	4.015×2.212	60	8	80.0	3.085	794	865
VT21*	PE+PAI	0.850	60	8	35.0	4.251	563	539
VT22*	PI	0.900	60	8	37.0	3.085	612	629
VT23	PI	4.015×2.212	80	4	39.0	3.017	629	632
VT24	PI	4.015×2.212	80	4	80.0	3.017	802	853
VT25	PI	4.015×2.212	100	0	39.0	2.991	629	617
VT26	PI	4.015×2.212	100	0	80.0	2.991	802	835
VT27	PI	4.015×2.212	120	0	39.0	2.940	594	604
VT28	PI	4.015×2.212	120	0	80.0	2.940	781	819
VT29*	PE+PAI	0.850	140	0	35.0	4.036	512	488
VT30*	PI	0.900	140	0	37.0	2.931	519	573
VT31	PI	4.015×2.212	160	0	39.0	2.914	574	568
VT32	PI	4.015×2.212	160	0	80.0	2.914	748	775
VT33*	PE+PAI	0.850	160	0	35.0	4.069	490	469
VT34*	PI	0.900	160	0	37.0	2.914	498	555
VT35	PAI+PI	4.015×2.212	180	0	88.0	3.233	718	747

Table A.2 – Continued

Sample name	Material	Copper dimensions (mm)**	T(°C)	RH(%)	t_{ins} (μm)	$\varepsilon_{r\,ins}$ (-)	$PDIV_{exp}$ (Vrms)	$PDIV_{est}$ (Vrms)
VT36	PAI+PI	4.015×2.212	180	0	66.0	3.233	700	659
VT37	PAI+PI	4.015×2.212	180	0	59.0	3.233	620	628
VT38	PI	4.015×2.212	200	0	39.0	2.904	553	529
VT39	PI	4.015×2.212	200	0	80.0	2.904	714	725
VT40	PI+PAI	4.015×2.212	220	0	88.0	3.245	654	694
VT41	PI+PAI	4.015×2.212	220	0	66.0	3.245	647	610
VT42	PI+PAI	4.015×2.212	220	0	59.0	3.245	599	581
VT43*	PE+PAI	0.850	220	0	35.0	4.639	474	393
VT44*	PI	0.900	220	0	37.0	2.887	482	497
VT45	PAI	3.450×1.700	220	0	70.5	4.314	501	554
VT46	PAI	3.450×1.700	220	0	83.5	4.314	584	597
VT47	PAI	3.450×1.700	220	0	116.3	4.314	732	692
VT48	PI	3.450×1.700	220	0	63.0	2.887	685	630
VT49	PI	3.450×1.700	220	0	91.5	2.887	786	743
VT50	PI	3.450×1.700	220	0	100.0	2.887	879	773
VT51	PAI+CR	3.450×1.700	220	0	68.6	4.249	521	551
VT52	PAI+CR	3.450×1.700	220	0	82.1	4.249	614	597
VT53	PAI+CR	3.450×1.700	220	0	106.3	4.249	663	669
VT54	PAI+PI	3.450×1.700	220	0	67.0	3.678	619	581
VT55	PAI+PI	3.450×1.700	220	0	84.4	3.678	632	644
VT56	PI	4.015×2.212	240	0	39.0	2.878	540	488
VT57	PI	4.015×2.212	240	0	80.0	2.878	700	673
VT58	PI+PAI	4.015×2.212	240	0	88.0	3.250	604	665
VT59	PI+PAI	4.015×2.212	240	0	66.0	3.250	569	585
VT60	PI+PAI	4.015×2.212	240	0	59.0	3.250	570	556

* TP; ** ⌀ for TP and height×width for PC

Table A.3: *Extended Dakin's temperature model validation sample specifications and PDIV results for validation (D. Muto et al. [81]).*

Sample name	Material	Copper ∅ (mm)	T(°C)	RH(%)	t_{ins} (µm)	$\varepsilon_{r\,ins}$ (-)	$PDIV_{exp}$ (Vrms)	$PDIV_{est}$ (Vrms)
VT61	PAI	1.0	25	NP***	36.0	4.500	548	557
VT62	PEEK	1.0	25	NP	29.0	2.900	587	610
VT63	PEEK	1.0	25	NP	36.0	3.100	638	648
VT64	PPS	1.0	25	NP	46.0	3.200	746	707
VT65	PEEK/PPS	1.0	25	NP	72.0	3.200	940	847
VT66	PET	1.0	25	NP	107.0	3.600	1061	949
VT67**	PAI*	1.0	25	NP	30.0	2.911	100	100
VT68**	PAI	1.0	25	NP	30.0	3.751	100	100
VT69**	PEEK	1.0	25	NP	30.0	3.132	100	100
VT70**	PAI*	1.0	100	NP	30.0	2.855	92	91
VT71**	PAI	1.0	100	NP	30.0	3.890	90	89
VT72**	PEEK	1.0	100	NP	30.0	2.996	91	92
VT73**	PAI*	1.0	150	NP	30.0	2.924	87	83
VT74**	PAI	1.0	150	NP	30.0	3.995	84	81
VT75**	PEEK	1.0	150	NP	30.0	3.720	79	78
VT76**	PAI	1.0	180	NP	30.0	4.162	80	75
VT77**	PAI*	1.0	200	NP	30.0	3.037	81	75
VT78**	PAI	1.0	200	NP	30.0	4.232	76	72
VT79**	PEEK	1.0	200	NP	30.0	3.745	76	70
VT80**	PAI*	1.0	230	NP	30.0	3.107	79	69
VT81**	PAI	1.0	230	NP	30.0	4.346	78	66
VT82**	PEEK	1.0	230	NP	30.0	4.010	73	64

* PAI with improved $\varepsilon_{r\,ins}$; ** Ratio of PDIV to bases 25 °C in %; *** Not provided.

Table A.4: *Extended Dakin's temperature model validation sample specifications and PDIV results for validation (M. Gomez de la Calle et al. [122]).*

Sample name	Material	Copper ∅ (mm)	T(°C)	RH(%)	t_{ins} (μm)	$\varepsilon_{r\ ins}$ (-)	$PDIV_{exp}$ (Vrms)	$PDIV_{est}$ (Vrms)
VT83	NP**	0.4	25	36.5	16.0	4.530	416	400
VT84	NP	0.6	25	45.0	18.0	3.870	415	447
VT85	NP	0.6	25	44.0	30.0	3.990	542	543
VT86	NP	0.8	25	36.5	25.0	3.740	486	518
VT87	NP	1.0	25	34.0	30.0	4.090	492	538
VT88	NP	1.2	25	46.0	42.0	3.600	613	649
VT89	NP	1.8	25	32.0	43.0	3.560	639	658
VT90	NP	0.4	110	0.0	16.0	4.530*	363	350
VT91	NP	0.6	110	0.0	18.0	3.870*	394	394
VT92	NP	0.6	110	0.0	30.0	3.990*	496	482
VT93	NP	0.8	110	0.0	25.0	3.740*	447	459
VT94	NP	1.0	110	0.0	30.0	4.090*	493	477
VT95	NP	1.2	110	0.0	42.0	3.600*	587	580
VT96	NP	1.8	110	0.0	43.0	3.560*	602	589
VT97	NP	0.4	150	0.0	16.0	4.530*	367	326
VT98	NP	0.6	150	0.0	18.0	3.870*	410	367
VT99	NP	0.6	150	0.0	30.0	3.990*	499	451
VT100	NP	0.8	150	0.0	25.0	3.740*	459	429
VT101	NP	1.0	150	0.0	30.0	4.090*	486	446
VT102	NP	1.2	150	0.0	42.0	3.600*	583	545
VT103	NP	1.8	150	0.0	43.0	3.560*	583	553

* Ambient $\varepsilon_{r\ ins}$ was considered (as in [122]) as no data was provided; ** Not provided.

Table A.5: *Extended Dakin's temperature model validation sample specifications and PDIV results for validation (Y. Kikuchi et al. [70]).*

Sample name	Material	Copper ∅ (mm)	T(°C)	RH(%)	t_{ins} (µm)	$\varepsilon_{r\,ins}$ (-)	$PDIV_{exp}$ (Vrms)	$PDIV_{est}$ (Vrms)
VT104	PEI	1.4	30	30	42.8	4.020	721	622
VT105	PEI	1.4	30	40	42.8	4.089	699	617
VT106	PEI	1.4	30	60	42.8	4.197	678	611
VT107	PEI	1.4	30	80	42.8	4.334	654	603
VT108	PEI	1.4	60	30	42.8	3.912	698	605
VT109	PEI	1.4	60	40	42.8	4.008	681	599
VT110	PEI	1.4	60	60	42.8	4.161	668	590
VT111	PEI	1.4	60	80	42.8	4.270	668	584
VT112	PEI	1.4	80	30	42.8	3.823	688	595
VT113	PEI	1.4	80	40	42.8	3.986	684	585
VT114	PEI	1.4	80	60	42.8	4.155	690	575
VT115	PEI	1.4	80	80	42.8	4.300	695	567
VT116	PEI	1.4	30	30	42.8	3.919	684	628
VT117	PEI	1.4	30	40	42.8	3.994	673	623
VT118	PEI	1.4	30	60	42.8	4.104	646	616
VT119	PEI	1.4	30	80	42.8	4.261	640	607
VT120	PEI	1.4	60	30	42.8	3.907	648	606
VT121	PEI	1.4	60	40	42.8	4.020	665	599
VT122	PEI	1.4	60	60	42.8	4.163	664	590
VT123	PEI	1.4	60	80	42.8	4.298	653	582
VT124	PEI	1.4	80	30	42.8	3.803	676	596
VT125	PEI	1.4	80	40	42.8	3.960	683	586
VT126	PEI	1.4	80	60	42.8	4.130	687	576
VT127	PEI	1.4	80	80	42.8	4.272	679	568

A.2 Extended Dakin's Absolute Humidity Model

A.2.1 Model Derivation

Tables A.6, A.7, and A.8 present the PDIV measurement results for the DAH dataset, as outlined in Section 3.3.1, for relative humidity levels of 25%, 50%, and 65–75% at 30, 55, and 80 °C, respectively. The measurements were conducted on the samples listed in Table 3.1 (Section 3.1). Each table provides the average, maximum, and minimum PDIV values obtained from three measured samples. These results were subsequently used to develop the Extended Dakin's absolute humidity equation and are presented graphically in Figure 4.21 in Section 4.3.2.2.

Table A.6: *Experimental average, maximum, and minimum PDIV (Vrms) results at 25, 50, and 75% relative humidity levels at 30 °C for the Extended Dakin's absolute humidity model derivation.*

Sample name	25%			50%			75%		
	Mean	Max	Min	Mean	Max	Min	Mean	Max	Min
PC1	691	710	672	674	687	664	670	679	659
PC2	805	814	796	789	803	768	751	774	738
PC3	988	1003	971	943	955	924	906	939	881
PC4	793	799	788	783	788	780	763	764	760
PC5	931	939	916	904	920	888	879	904	865
PC6	991	998	981	996	1024	975	961	967	948
PC7	707	754	682	674	691	646	667	681	655
PC8	836	848	829	811	826	795	800	818	771
PC9	910	939	877	889	921	869	857	881	837
PC10	782	807	753	762	784	725	742	775	713
PC11	875	888	850	840	862	807	823	850	808
TP1	664	674	655	621	623	620	594	595	593
TP2	678	698	658	622	644	601	590	599	577

Table A.7: *Experimental average, maximum, and minimum PDIV (Vrms) results at 25, 50, and 75% relative humidity levels at 55 °C for the Extended Dakin's absolute humidity model derivation.*

Sample name	25%			50%			75%		
	Mean	Max	Min	Mean	Max	Min	Mean	Max	Min
PC1	669	686	659	651	660	640	653	656	648
PC2	779	795	767	759	765	757	744	753	729
PC3	930	950	904	887	893	882	852	869	830
PC4	802	822	781	768	788	754	760	793	728
PC5	925	928	922	878	897	847	851	881	799
PC6	1008	1021	997	950	983	926	907	944	855
PC7	692	698	683	667	691	648	658	662	655
PC8	802	826	789	776	800	757	787	795	783
PC9	892	900	877	857	885	841	824	834	803
PC10	733	741	724	724	726	720	728	784	675
PC11	858	880	833	832	863	796	806	832	783
TP1	637	640	635	617	617	617	584	589	578
TP2	629	634	626	613	635	601	565	617	511

Table A.8: *Experimental average, maximum, and minimum PDIV (Vrms) results at 25, 50, and 65% relative humidity levels at 80 °C for the Extended Dakin's absolute humidity model derivation.*

Sample	25%			50%			65%		
Sample name	Mean	Max	Min	Mean	Max	Min	Mean	Max	Min
PC1	683	689	674	643	656	632	651	659	644
PC2	778	795	751	684	702	667	735	752	725
PC3	902	912	885	860	881	838	831	839	820
PC4	788	811	773	781	818	748	755	769	746
PC5	906	916	894	874	880	864	832	850	803
PC6	972	1005	951	889	923	845	926	952	885
PC7	663	705	627	679	699	666	676	697	644
PC8	796	807	777	757	784	734	761	779	740
PC9	854	866	842	819	846	803	833	845	823
PC10	724	746	701	700	717	670	703	725	678
PC11	824	834	811	811	826	791	758	788	721
TP1	630	643	623	630	656	609	612	636	574
TP2	628	642	612	627	654	608	576	610	542

A.2.2 Model Validation

Similar to the validation approach for the Extended Dakin's temperature model, obtaining measurements across multiple temperatures and humidity levels was prioritised over measuring numerous samples at a single condition. Consequently, a new dataset was generated, referred to as VAH dataset. Unlike VT dataset, VAH dataset focused on measurements below 100 °C with defined relative humidity values.

The own measurements of samples VT1–VT24 from Table A.2 were included. Table A.9 presents the updated PDIV estimations using the Extended Dakin's absolute humidity model (equation (4.27)).

Experimental data from the literature was also compared to the model. In C. He et al. [141], PC samples were used, whereas all other experiments were conducted with TP samples. PDIV was measured using a sinusoidal waveform. Tables A.10, A.11, A.12,A.13, A.14, and A.15 compile the validation data from Y. Kikuchi et al. [70], S. Matsumoto et al. [97], A. Rumi et al. [86], Y. Ji et al. [94], H. Naderiallaf et al. [87], and C. He et al. [141], respectively.

For Y. Kikuchi et al. [70], A. Rumi et al. [86], and Y. Ji et al. [94], the specific insulation thickness was not provided. However, since the use of Grade 2 wires was specified, the average insulation thickness for Grade 2 wires was assumed. In all cases except for Y. Kikuchi et al. [70], relative permittivity values for specific temperatures and relative humidity levels were not provided, so they were kept constant across different conditions. A. Rumi et al. [86] and H. Naderiallaf et al. [87] explicitly stated that no significant variation in relative permittivity was observed in their samples.

Table A.9: *Extended Dakin's absolute humidity model validation sample specifications and PDIV results for validation (own measurements).*

Sample name	Material	Copper dimensions (mm)**	T(°C)	RH(%)	t_{ins} (µm)	$\varepsilon_{r\,ins}$ (-)	$PDIV_{exp}$ (Vrms)	$PDIV_{est}$ (Vrms)
VAH1	PAI	3.460×1.600	20	52	100.0	4.424	891	834
VAH2	PAI	3.460×1.600	20	59	144.6	4.424	927	963
VAH3	PAI	3.460×1.600	20	62	152.8	4.424	1065	984
VAH4	PAI	3.460×1.600	20	58	153.6	4.424	1017	986
VAH5	PAI	3.460×1.600	20	63	161.8	4.424	1054	1006
VAH6	PAI	3.460×1.600	20	62	157.0	4.424	1169	994
VAH7	PI	4.015×2.212	20	50	39.0	3.093	649	663
VAH8	PI	4.015×2.212	20	50	54.0	3.093	799	753
VAH9	PI+PAI	4.015×2.212	20	50	88.0	3.438	840	876
VAH10	PI+PAI	4.015×2.212	20	50	66.0	3.438	821	782
VAH11	PI+PAI	4.015×2.212	20	50	69.0	3.438	770	796
VAH12	PI+PAI	4.015×2.212	20	50	71.0	3.889	783	767
VAH13*	PE+PAI	0.850	20	50	36.3	4.258	617	568
VAH14*	PE+PAI	1.000	20	50	39.0	4.258	620	584
VAH15	PI	4.015×2.212	40	19	39.0	3.093	654	663
VAH16	PI	4.015×2.212	40	19	80.0	3.093	823	879
VAH17*	PE+PAI	0.850	40	19	35.0	4.258	592	560
VAH18*	PI	0.900	40	19	37.0	3.093	636	649
VAH19	PI	4.015×2.212	60	8	39.0	3.085	632	663
VAH20	PI	4.015×2.212	60	8	80.0	3.085	794	880
VAH21*	PE+PAI	0.850	60	8	35.0	4.251	563	560
VAH22*	PI	0.900	60	8	37.0	3.085	612	650
VAH23	PI	4.015×2.212	80	4	39.0	3.017	629	669
VAH24	PI	4.015×2.212	80	4	80.0	3.017	802	887

* TP; ** ⌀ for TP and height×width for PC.

In several studies, although the insulation material was identified, the specific relative permittivity value was not provided. In such cases, the following ambient temperature values were assumed:

- **S. Matsumoto et al. [97]:** The ambient temperature value for PE, as specified by the manufacturer of the samples in Table 3.1, was used.
- **A. Rumi et al. [86]:** The ambient temperature value for PEI+PAI, as specified by the manufacturer (Table 3.2), was used, assuming a composition of 72% PEI and 28% PAI.
- **C. He et al. [141]:** The ambient temperature value for PAI, as specified by the manufacturer (Table 3.2), was used. For PEEK, the 25 °C, 50% RH value specified in [81] was applied.

Table A.10: *Extended Dakin's absolute humidity model validation sample specifications and PDIV results for validation (Y. Kikuchi et al. [70]).*

Sample name	Material	Copper ∅ (mm)	T(°C)	RH(%)	t_{ins} (µm)	$\varepsilon_{r\,ins}$ (-)	$PDIV_{exp}$ (Vrms)	$PDIV_{est}$ (Vrms)
VAH25	PEI	1.4	30	30	42.8	4.020	721	622
VAH26	PEI	1.4	30	40	42.8	4.089	699	617
VAH27	PEI	1.4	30	60	42.8	4.197	678	611
VAH28	PEI	1.4	30	80	42.8	4.334	654	603
VAH29	PEI	1.4	60	30	42.8	3.912	698	605
VAH30	PEI	1.4	60	40	42.8	4.008	681	599
VAH31	PEI	1.4	60	60	42.8	4.161	668	590
VAH32	PEI	1.4	60	80	42.8	4.270	668	584
VAH33	PEI	1.4	80	30	42.8	3.823	688	595
VAH34	PEI	1.4	80	40	42.8	3.986	684	585
VAH35	PEI	1.4	80	60	42.8	4.155	690	575
VAH36	PEI	1.4	80	80	42.8	4.300	695	567
VAH37	PEI	1.4	30	30	42.8	3.919	684	628
VAH38	PEI	1.4	30	40	42.8	3.994	673	623
VAH39	PEI	1.4	30	60	42.8	4.104	646	616
VAH40	PEI	1.4	30	80	42.8	4.261	640	607
VAH41	PEI	1.4	60	30	42.8	3.907	648	606
VAH42	PEI	1.4	60	40	42.8	4.020	665	599
VAH43	PEI	1.4	60	60	42.8	4.163	664	590
VAH44	PEI	1.4	60	80	42.8	4.298	653	582
VAH45	PEI	1.4	80	30	42.8	3.803	676	596
VAH46	PEI	1.4	80	40	42.8	3.960	683	586
VAH47	PEI	1.4	80	60	42.8	4.130	687	576
VAH48	PEI	1.4	80	80	42.8	4.272	679	568

Table A.11: *Extended Dakin's absolute humidity model validation sample specifications and PDIV results for validation (S. Matsumoto et al. [97]).*

Sample name	Material	Copper ∅ (mm)	T(°C)	RH(%)	t_{ins} (µm)	$\varepsilon_{r\,ins}^{\star}$ (-)	$PDIV_{exp}$ (Vrms)	$PDIV_{est}$ (Vrms)
VAH49	PE	1	22	41	25.0	4.196	629	493
VAH50	PE	1	22	50	25.0	4.196	596	493
VAH51	PE	1	22	57	25.0	4.196	576	494
VAH52	PE	1	22	67	25.0	4.196	555	494

* Ambient $\varepsilon_{r\,ins}$ was considered, as no data was provided.

Table A.12: *Extended Dakin's absolute humidity model validation sample specifications and PDIV results for validation (A. Rumi et al. [86]).*

Sample name	Material	Copper ∅ (mm)	T(°C)	RH(%)	t_{ins} (µm)	$\varepsilon_{r\,ins}$* (-)	$PDIV_{exp}$ (Vrms)	$PDIV_{est}$ (Vrms)
VAH53	PEI+PAI	0.63	25	20	31.00	3.956	593	549
VAH54	PEI+PAI	0.63	25	50	31.00	3.956	561	550
VAH55	PEI+PAI	0.63	25	95	31.00	3.956	558	551
VAH56	PEI+PAI	0.63	50	25	31.00	3.956	550	551
VAH57	PEI+PAI	0.63	50	50	31.00	3.956	537	553
VAH58	PEI+PAI	0.63	50	95	31.00	3.956	523	557
VAH59	PEI+PAI	0.63	70	20	31.00	3.956	558	553
VAH60	PEI+PAI	0.63	70	50	31.00	3.956	549	558
VAH61	PEI+PAI	0.63	70	90	31.00	3.956	529	560
VAH62	PEI+PAI	0.63	90	20	31.00	3.956	585	557
VAH63	PEI+PAI	0.63	90	90	31.00	3.956	609	548

* Ambient $\varepsilon_{r\,ins}$ was considered, as specified in [86].

Table A.13: *Extended Dakin's absolute humidity model validation sample specifications and PDIV results for validation (Y. Ji et al. [94]).*

Sample name	Material	Copper ∅ (mm)	T(°C)	RH(%)	t_{ins} (µm)	$\varepsilon_{r\,ins}$* (-)	$PDIV_{exp}$ (Vrms)	$PDIV_{est}$ (Vrms)
VAH64	PEI	0.63	30	30	31	3.4	577	583
VAH65	PEI	0.63	30	45	31	3.4	560	584
VAH66	PEI	0.63	30	60	31	3.4	568	584
VAH67	PEI	0.63	30	75	31	3.4	595	585
VAH68	PEI	0.63	30	90	31	3.4	642	585
VAH69	PEI	0.63	60	30	31	3.4	558	586
VAH70	PEI	0.63	60	45	31	3.4	573	587
VAH71	PEI	0.63	60	60	31	3.4	585	588
VAH72	PEI	0.63	60	75	31	3.4	629	589
VAH73	PEI	0.63	60	90	31	3.4	643	589
VAH74	PEI	0.63	90	30	31	3.4	576	589
VAH75	PEI	0.63	90	45	31	3.4	613	588
VAH76	PEI	0.63	90	60	31	3.4	637	584
VAH77	PEI	0.63	90	75	31	3.4	654	577
VAH78	PEI	0.63	90	90	31	3.4	668	569

* Ambient $\varepsilon_{r\,ins}$ was considered.

Table A.14: *Extended Dakin's absolute humidity model validation sample specifications and PDIV results for validation (H. Naderiallaf et al. [87]).*

Sample name	Material	Copper ∅ (mm)	T(°C)	RH(%)	t_{ins} (μm)	$\varepsilon_{r\,ins}$* (-)	$PDIV_{exp}$ (Vrms)	$PDIV_{est}$ (Vrms)
VAH79	PEI+PAI	0.556	25	30	28.5	4.310	590	514
VAH80	PEI+PAI	0.556	25	40	28.5	4.310	570	514
VAH81	PEI+PAI	0.556	25	50	28.5	4.310	567	514
VAH82	PEI+PAI	0.556	25	60	28.5	4.310	556	515
VAH83	PEI+PAI	0.556	25	70	28.5	4.310	552	515
VAH84	PEI+PAI	0.556	25	80	28.5	4.310	541	515
VAH85	PEI+PAI	0.556	25	90	28.5	4.310	535	516
VAH86	PEI+PAI	0.556	40	20	28.5	4.310	583	514
VAH87	PEI+PAI	0.556	40	30	28.5	4.310	578	515
VAH88	PEI+PAI	0.556	40	40	28.5	4.310	562	516
VAH89	PEI+PAI	0.556	40	50	28.5	4.310	559	516
VAH90	PEI+PAI	0.556	40	60	28.5	4.310	550	517
VAH91	PEI+PAI	0.556	40	70	28.5	4.310	532	518
VAH92	PEI+PAI	0.556	40	80	28.5	4.310	530	519
VAH93	PEI+PAI	0.556	40	90	28.5	4.310	528	519
VAH94	PEI+PAI	0.556	60	20	28.5	4.310	569	517
VAH95	PEI+PAI	0.556	60	30	28.5	4.310	561	518
VAH96	PEI+PAI	0.556	60	40	28.5	4.310	559	520
VAH97	PEI+PAI	0.556	60	50	28.5	4.310	558	522
VAH98	PEI+PAI	0.556	60	60	28.5	4.310	556	523
VAH99	PEI+PAI	0.556	60	70	28.5	4.310	556	524
VAH100	PEI+PAI	0.556	60	80	28.5	4.310	553	525
VAH101	PEI+PAI	0.556	60	90	28.5	4.310	542	526
VAH102	PEI+PAI	0.556	90	20	28.5	4.310	555	524
VAH103	PEI+PAI	0.556	90	30	28.5	4.310	556	527
VAH104	PEI+PAI	0.556	90	40	28.5	4.310	579	529
VAH105	PEI+PAI	0.556	90	50	28.5	4.310	610	530
VAH106	PEI+PAI	0.556	90	60	28.5	4.310	614	530
VAH107	PEI+PAI	0.556	90	70	28.5	4.310	615	530
VAH108	PEI+PAI	0.556	90	80	28.5	4.310	618	528
VAH109	PEI+PAI	0.556	90	90	28.5	4.310	622	525

* Ambient $\varepsilon_{r\,ins}$ was considered, as reported in [87].

Table A.15: *Extended Dakin's absolute humidity model validation sample specifications and PDIV results for validation (C. He et al. [141]).*

Sample name	Material	Copper dimensions (mm)	T(°C)	RH(%)	t_{ins} (μm)	$\varepsilon_{r\,ins}$* (-)	$PDIV_{exp}$ (Vrms)	$PDIV_{est}$ (Vrms)
VAH110	PEEK	NP	25	55	100	3.067	1106	962
VAH111	PEEK	NP	25	80	100	3.067	1033	960
VAH112	PEEK	NP	25	98	100	3.067	815	959
VAH113	PEEK	NP	25	55	130	3.067	1203	1066
VAH114	PEEK	NP	25	80	130	3.067	1182	1063
VAH115	PEEK	NP	25	98	130	3.067	863	1061
VAH116	PAI	NP	25	55	100	4.424	932	833
VAH117	PAI	NP	25	80	100	4.424	878	832
VAH118	PAI	NP	25	98	100	4.424	867	832

* Ambient $\varepsilon_{r\,ins}$ was considered; ** Not provided.

Appendix B

Definition and Results of PDIV for the Comparison of the Models

This appendix outlines the implementation procedures for the Extended parallel-plate, FEM+Paschen's, and FEM+Schumann's models. In each case, the optimal Townsend's secondary ionisation coefficient (γ) or Schumann's constant (K_{Sch}) values were selected based on literature data. To ensure a fair comparison with the Extended Dakin's model, literature-reported values were used without adjustment. While calibrating γ or K_{Sch} for each sample based on experimental data would minimize error, this approach was intentionally avoided to maintain the model's general applicability. Lastly, the predicted PDIV values for each sample using each model are also provided.

B.1 PDIV Modelling Based on Extended Parallel-Plate Model

The prediction of the PDIV using Extended parallel-plate is simply based on the application of equation (4.21) adjusting the parameters (T, t_{ins}, and $\varepsilon_{\text{r ins}}$) of each sample. The critical factor in accurately estimating PDIV using Extended parallel-plate model is the definition of the γ value. As discussed in Section 4.2.2.1, there is no consensus in the literature regarding its value, with multiple proposals available.

To minimize error associated with γ selection, three approaches were evaluated. The first assigned γ based on the insulation material of each validation sample (as detailed in Section 4.3.3), using values from Table 4.4 in Section 4.2.2.1. If no literature-reported

value was available for a given material, $\gamma = 0.0078$ was applied, as recommended by [122] for generic enamel materials. The second approach used a fixed $\gamma = 0.0078$ for all materials, following the same reference. The third approach set $\gamma = 0.0025$, the generic value for twisted pairs proposed by [68]. Neither temperature nor relative humidity dependence was considered. Previous studies [122, 126] suggest that maintaining a constant γ across temperatures does not significantly impact prediction accuracy. Additionally, no studies have been found investigating the effect of relative humidity on γ.

Figure B.1 presents the error distributions for different γ values. Errors were first analysed separately for samples used in the VT dataset (Figure B.1 (a), Appendix A.1) and those used in the VAH dataset (Figure B.1 (b), Appendix A.2). In the first dataset, most samples had temperatures above 100 °C with constant relative humidity for those below 100 °C (around 50%), whereas in the second, all samples were below 100 °C with varying humidity levels.

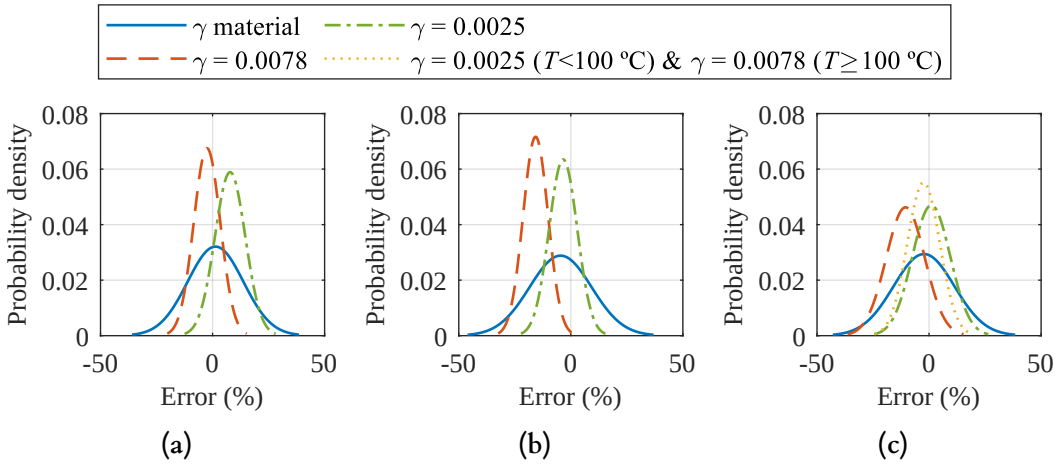

Figure B.1: *Comparison of the error distributions for different γ selection approaches in the Extended parallel-plate model implementation (a) using only the dataset from the Extended Dakin's temperature model validation, (b) using only the dataset from the Extended Dakin's absolute humidity model validation, and (c) combining both datasets.*

The results indicate that assigning γ based on material yielded the least accurate predictions in both cases. When most samples had temperatures above 100 °C (Figure B.1 (a)), $\gamma = 0.0025$ and $\gamma = 0.0078$ produced similar mean and maximum errors, but $\gamma = 0.0078$ offers a more conservative prediction. For temperatures below 100 °C (Figure B.1 (b)), $\gamma = 0.0025$ resulted in lower mean and maximum errors. These findings suggest that using $\gamma = 0.0078$ for temperatures above 100 °C and $\gamma = 0.0025$ for temperatures below 100 °C minimizes prediction error. This approach was implemented as the fourth method in the comparison of the whole temperature and relative humidity range of all validation samples.

Figure B.1 (c) presents error distributions for all validation samples (Section 4.3.3). Again, the worst performance occurred when γ was material-dependent, producing the highest error spread. Among the remaining cases, the best results were achieved by using

$\gamma = 0.0025$ for temperatures below 100 °C and $\gamma = 0.0078$ for those at or above 100 °C. This combination minimized the mean error and kept the maximum error within 24%, making it the selected approach for model comparisons.

Finally, although PC samples were not included in the comparison in Section 4.3.3 due to the lack of exact geometric values required for FEM simulations, an additional evaluation was conducted to ensure that the conclusions drawn from TP samples are also valid for PC samples when using the Extended parallel-plate model. The entire dataset used to develop the Extended Dakin's model was analysed using the Extended parallel-plate model. Figure B.2 compares the application of the Extended parallel-plate model considering only TP samples and including both TP and PC samples. The results show that including the PC samples does not lead to a significant difference in the mean error, deviation, or maximum error. Therefore, the Extended parallel-plate model was validated for accurate PDIV estimation in both sample types.

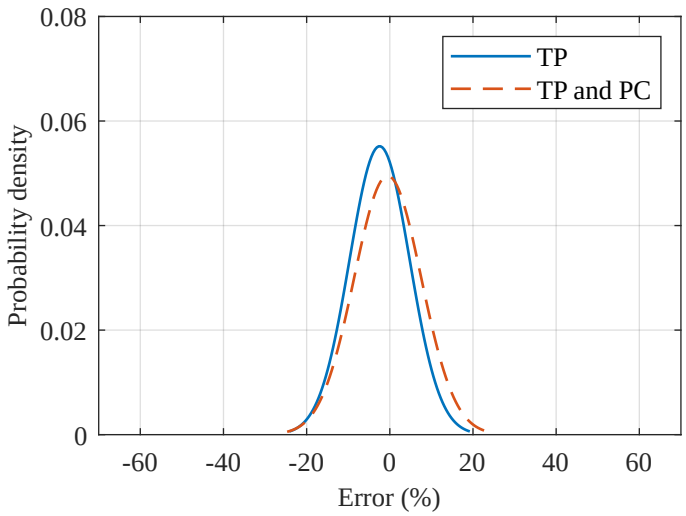

Figure B.2: *Comparison of the error distributions obtained with the Extended parallel-plate equation ($\gamma = 0.0025$ at $T < 100$ °C and $\gamma = 0.0078$ at $T \geq 100$ °C) for Extended Dakin's model complete validation dataset considering only TP samples, or TP and PC samples.*

B.2 PDIV Modelling Based on FEM Simulations and Paschen's or Schumann's Criteria

To replicate the FEM-based models using Paschen's or Schuman's criteria, the primary references were the doctoral theses of L. Lusuardi [32] and M. Gomez de la Calle [30], along with journal articles [87] and [151] by H. Naderiallaf.

Both methods begin with FEM simulations to determine the electric field distribution and field line lengths. However, each employs a distinct post-processing approach to estimate PDIV, as they are based on different gas breakdown mechanisms, as discussed in

Section 4.2. The following sections outline the procedures for extracting electric field lines and subsequently estimating PDIV using each criterion, demonstrated through the analysis of a single sample.

B.2.1 Calculation of Electric Field Line Length and Level Using FEM Simulations

The model geometry followed the configuration shown in Figure 4.15 (a) for round conductors, with a schematic representation in Figure B.3 (a). Air was assigned as the surrounding medium (Domain), while conductors were modelled as perfect conductors. The insulation region was defined with the specific relative permittivity for each sample. The spacing between wires was minimized to 0.0009 mm to avoid meshing issues. The copper diameter and insulation thickness were adjusted to match the specifications of each sample. A base voltage of 1 V was applied to the HV conductor, while the GND conductor was set to 0 V.

Figure B.3 (b) illustrates the mesh definition. A refined mesh was applied in the air region where PD occurs to ensure the accuracy of the prediction. A null relaxation was set between the wires to enhance mesh density. A 2D grid, shown in yellow in Figure B.3 (c), was used to output results. This grid, located in the area of interest, was divided into 600 horizontal and 300 vertical sections, providing a balance between computational efficiency and accuracy. The x and y coordinates, electric field values (E), and relative permittivity at each grid point were saved in a .txt file for post-processing.

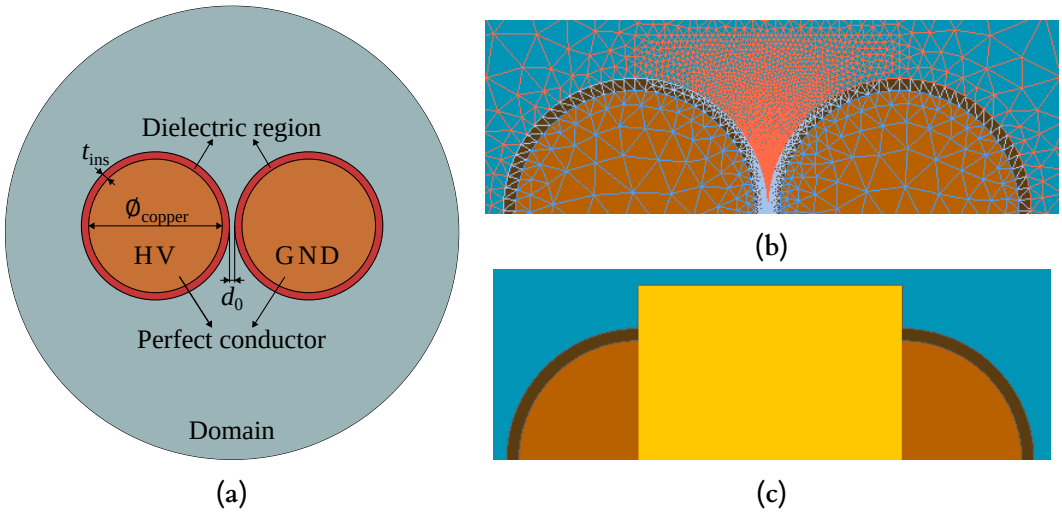

Figure B.3: *FEM model definition (a) schematic representation of the specific geometry, (b) simulated mesh example, and (c) 2D grid area to obtain the simulation results.*

Once the electrostatic simulation results were obtained in the 2D grid, they were processed in MATLAB to generate the V_0-d curve following these steps (Figure B.4):

1. **Filter relevant data:** Since partial discharges occur in the air, only the electric field data in the air region was retained. Electric field values from copper and insulation

were removed by discarding points with null electric field values (copper) and those with relative permittivity values different from 1 (insulation).

2. **Extract electric field contours:** The electric field data in the air region was structured into a matrix along with the corresponding x and y coordinates. The MATLAB function *contour* was used to compute the contours of the electric field lines, generating a matrix containing the x and y coordinates along with the respective electric field values for constant electric field lines.

3. **Calculate electric field line lengths:** The contour matrix was processed using the MATLAB function *contourlengths*, which determines the length of each contour line by summing the segment lengths between consecutive vertices. This provided the length of each electric field line and its corresponding electric field value, forming the E-d curve.

4. **Convert E-d to V_0-d:** Each electric field value was multiplied by its corresponding field line length to derive the V_0-d curve.

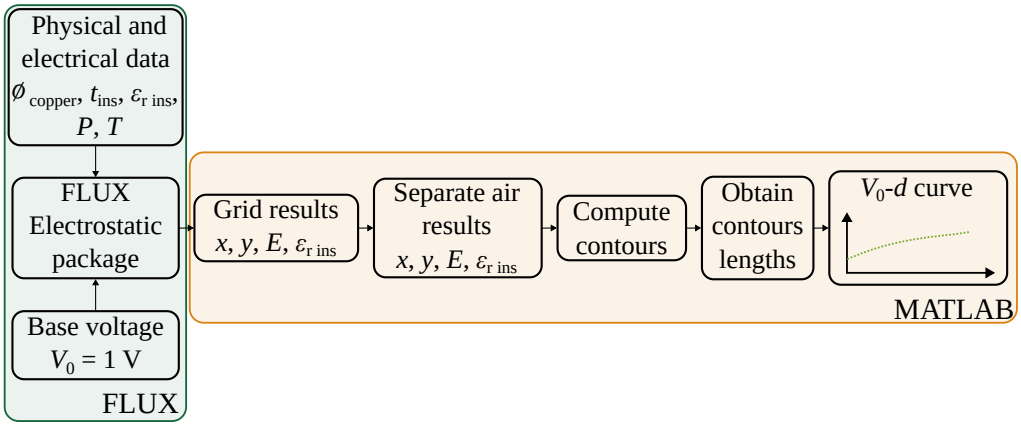

Figure B.4: *Flow chart to obtain the V_0-d curve based on FEM simulations based on [30].*

B.2.2 Paschen's Criteria Application

After obtaining the electric field lines, PDIV estimation based on Paschen's criteria was implemented in MATLAB, following the algorithm illustrated in Figure B.5, adapted from [30].

The V_0-d curve from FEM simulations was scaled to the evaluated voltage using V/V_0, where V is the tested voltage and V_0 is the base FEM simulation voltage (starting from $V = 300$ V). Simultaneously, Paschen's curve was defined using equation (2.17), incorporating the Dunbar correction for temperature dependence. The A and B constants (for air: $A = 12$ Torr^{-1}cm^{-1} and $B = 365$ V Torr^{-1}cm^{-1} ([30]) were converted to Pa^{-1}m^{-1} by dividing them by 1.33322. The adapted V-d curve was then compared with Paschen's curve. If they were not tangent, V was increased by 10 V, and the

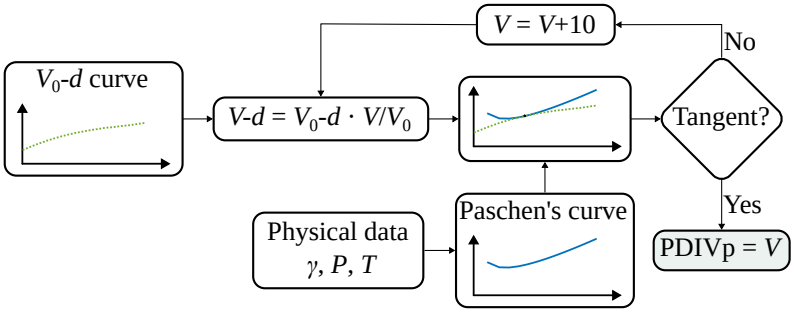

Figure B.5: *Flow chart of the algorithm to obtain Paschen's criteria based PDIV estimation using FEM simulation results based on [30].*

process repeated until either tangency was achieved or a point on the V-d curve surpasses Paschen's curve. The corresponding voltage was then identified as the peak PDIV value.

To validate the model, results were compared with those from M. Gomez de la Calle [30] at 25 °C and 150 °C. The validation samples (VT83–VT89 at 25 °C and VT97–VT103 at 150 °C, listed in Table A.4, Appendix A) used a γ value of 0.0078 [30]. As shown in Figure B.6, while exact values were not reproduced for all samples, the mean absolute error at 25 °C (3.77%) closely matches the 2.35% reported in [30], while at 150 °C, the error (3.76%) is comparable to the 7.05% reported. The maximum error observed across the temperature range (9.04% at 25 °C) is also consistent with [30] (11.05% at 150 °C), confirming the accurate implementation of the FEM+Paschen's model.

To determine the optimal γ value for this model, the same methodology used in the Extended parallel-plate model was applied. Figure B.7 compares error distributions for different γ values, with (a) showing results for VT dataset (Appendix A.1) and (b) for VAH dataset (Appendix A.2).

As observed in the Extended parallel-plate model, assigning γ based on material resulted in the least accurate predictions. When most samples had temperatures above 100 °C (Figure B.7 (a)), both $\gamma = 0.0025$ and $\gamma = 0.0078$ produced similar mean errors, but $\gamma = 0.0078$ showed a higher probability density at the mean error and a lower maximum error. For temperatures below 100 °C (Figure B.7 (b)), $\gamma = 0.0025$ yielded lower mean and maximum errors. These findings confirm that using $\gamma = 0.0078$ for temperatures above 100 °C and $\gamma = 0.0025$ for temperatures below 100 °C provides the most accurate predictions.

Figure B.7 (c) presents the error distributions for all validation samples (Section 4.3.3). Consistent with the Extended parallel-plate model, the best performance was achieved by applying $\gamma = 0.0025$ below 100 °C and $\gamma = 0.0078$ at or above 100 °C. This combination minimized the mean error while keeping the maximum error within 25%, making it the preferred approach for model comparison.

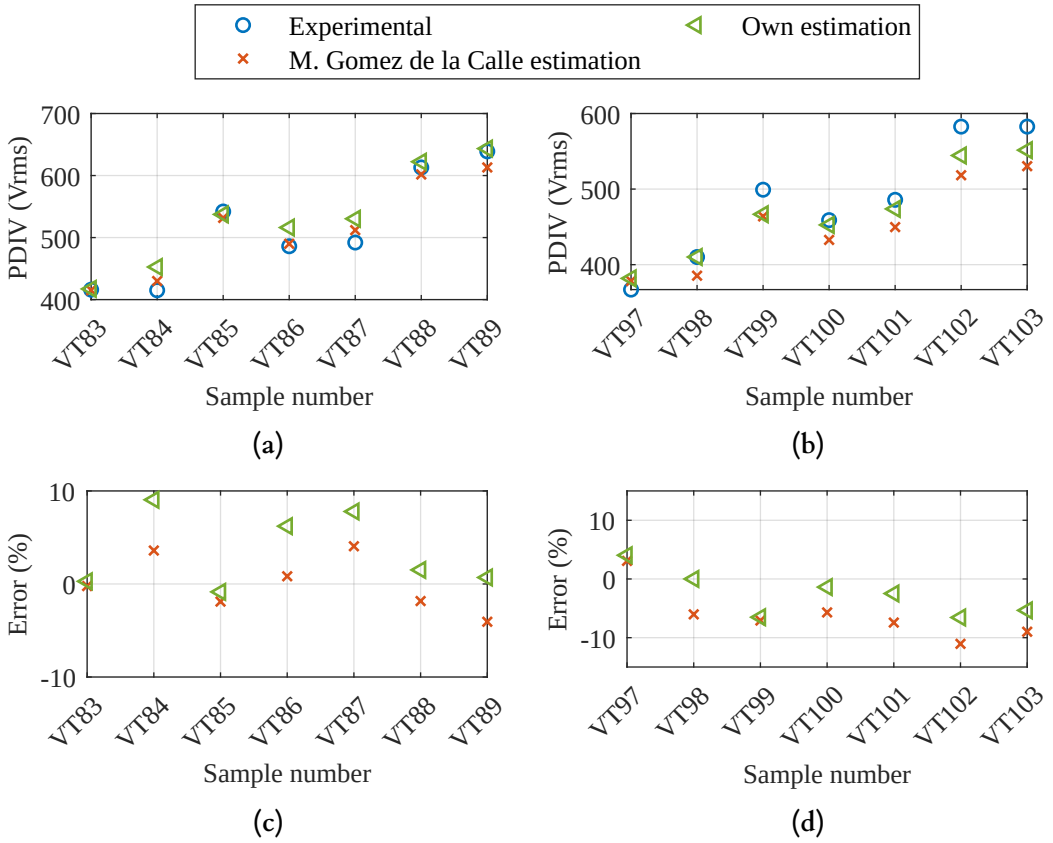

Figure B.6: *Comparison of M. Gomez de la Calle [30] experimental, and own and M. Gomez de la Calle [30] estimation PDIV results obtained using FEM+Paschen's criterion model obtained using FEM+Paschen's criterion model (a) PDIV at 25 °C, (b) PDIV at 150 °C, (c) model error at 25 °C, and (d) model error at 150 °C.*

B.2.3 Schumann's Criteria Application

After obtaining the electric field lines, PDIV estimation based on Schumann's criteria was implemented in MATLAB, following the algorithm illustrated in Figure B.8, adapted from [30].

The process starts by loading the electric field (E) values and field line lengths (d) from FEM simulations. The E values are then scaled to the evaluated voltage using V/V_0, where V is the tested voltage and V_0 is the base FEM simulation voltage (starting from $V = 300V$). Then, input data is prepared to compute the effective ionisation coefficient ($\bar{\alpha}$) using BOLSIG-, a software that utilizes the LXCat [185] database to determine ionisation (α) and attachment (η) coefficients, essential for obtaining $\bar{\alpha}$ and evaluating Schumann's criterion (equation (2.23)). The required input parameters include [151]:

- **Temperature of the gas:** The specific temperature of the air was set in K.
- **Air composition definition (in % or p.u):** The air composition at a given temperature and relative humidity was calculated following [32, 151]. The standard

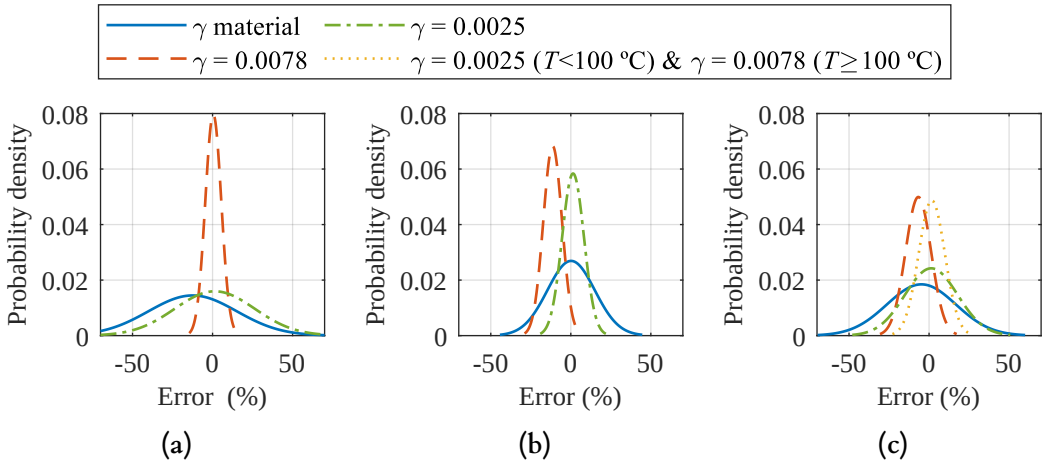

Figure B.7: *Comparison of the error distributions for different γ selection approaches in the FEM+Paschen's model implementation (a) using only VT dataset, (b) using only VAH dataset, and (c) combining both datasets.*

dry air mixture at 20 °C was considered as 78.08% nitrogen (N_2), 20.95% oxygen (O_2), 0.93% argon (Ar), and 0.04% carbon dioxide (CO_2). For moist air, the molar concentration of water (H_2O) was determined using equation (B.1), where 0.622 represents the ratio of the molar masses of water and air, and pH_2O is the vapour pressure of water (Pa), given by equation (B.2) (RH in p.u and t_{amb} in °C).

$$x_{H_2O} = 0.622 \frac{p_{H_2O}}{p - p_{H_2O}} \tag{B.1}$$

$$p_{H_2O} = 611\ RH\ 10^{7.4\left(\frac{t_{amb}}{t_{amb}+237}\right)} \tag{B.2}$$

With x_{H_2O} determined, the concentrations of the remaining air components were computed using equation (B.3).

$$x_{i_{moist}} = x_{i_{dry}} (1 - x_{H_2O}) \tag{B.3}$$

- **Reduced electric field for ionisation parameters calculation (in Townsend):** For each of the field lines obtained from FLUX, the reduced electric field was computed as E/n, where n is the gas number density (m^{-3}), obtained from the ideal gas law (equation (B.4)) [76]. Here, P represents gas pressure (Pa), T is gas temperature (K), and k_B is Boltzmann's constant (1.380649×10^{-23} J/K). To express E/n in Townsend, the electric field (E in V/m obtained from FLUX) was multiplied by 10^{21}.

$$n = \frac{P}{k_B\ T} \tag{B.4}$$

In addition to these inputs, ionisation reactions for N_2, O_2, Ar, CO_2, and H_2O were considered, obtained from the LXCat database [185], as specified in [32].

Using these parameters, the air ionisation (α) and attachment (η) coefficients were computed by multiplying n with the output values of α/n and η/n from BOLSIG-. With these values, the effective ionisation coefficient $\bar{\alpha}$ was obtained using equation (2.8), and Schumann's criterion was evaluated through equation (2.23). If none of the field lines met the criterion, meaning that $(\alpha - \eta)d < K_{\text{Sch}}$ (where d is the electric field line length), the voltage V was increased by 10 V, and the process was repeated. The iteration continued until at least one field line satisfied $(\alpha - \eta)d \geq K_{\text{Sch}}$, at which point the corresponding voltage was identified as the peak PDIV value.

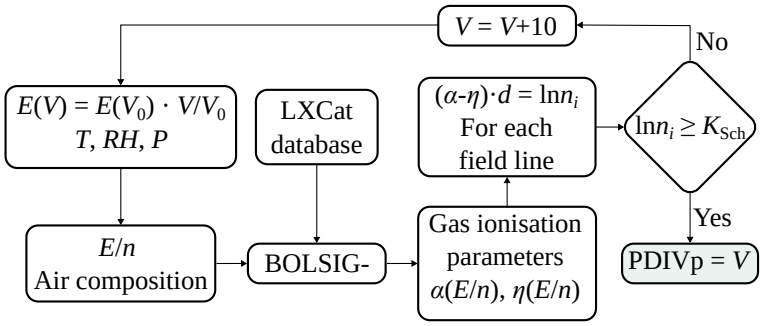

Figure B.8: *Flow chart of the algorithm to obtain Schumann's criteria based PDIV estimation using FEM simulation results based on [30].*

To verify the accuracy of the FEM+Schumann's model implementation, the results were compared with those reported by M. Gomez de la Calle [30], following the same validation approach as for the FEM+Paschen's model. The same samples were analysed, using $K_{\text{Sch}} = 5.98$, as in [30].

As shown in Figure B.9, while the exact values were not reproduced for all samples, the mean absolute error at 25 °C (3.67%) closely aligns with the 4.19% reported in [30]. At 150 °C, the error (8.37%) is comparable to the 7.16% reported. The maximum deviation across the temperature range (12.18% at 150 °C) is also consistent with [30] (11.77% at 150 °C). These results confirm the correct implementation of the FEM+Schumann's model for use in the comparisons presented in Section 4.3.3.

For determining the K_{Sch} value for each sample, literature values were used, as summarized in Table 4.5, following the same approach as in the previously implemented models. Since all validation samples were measured using AC sinusoidal voltages, the influence of waveform on K_{Sch} was disregarded. Similarly, pressure effects were not considered. Given that all samples were twisted pairs, only the values proposed for this configuration were selected. Therefore, two approaches were evaluated. The first approach applied $K_{\text{Sch}} = 5.98$, as proposed in [121] for various enamelled materials. The second approach utilized equations from [87], which define K_{Sch} based on RH and temperature for PEI+PAI insulation. If no equation was available for a specific RH and temperature condition, $K_{\text{Sch}} = 5.98$ was used.

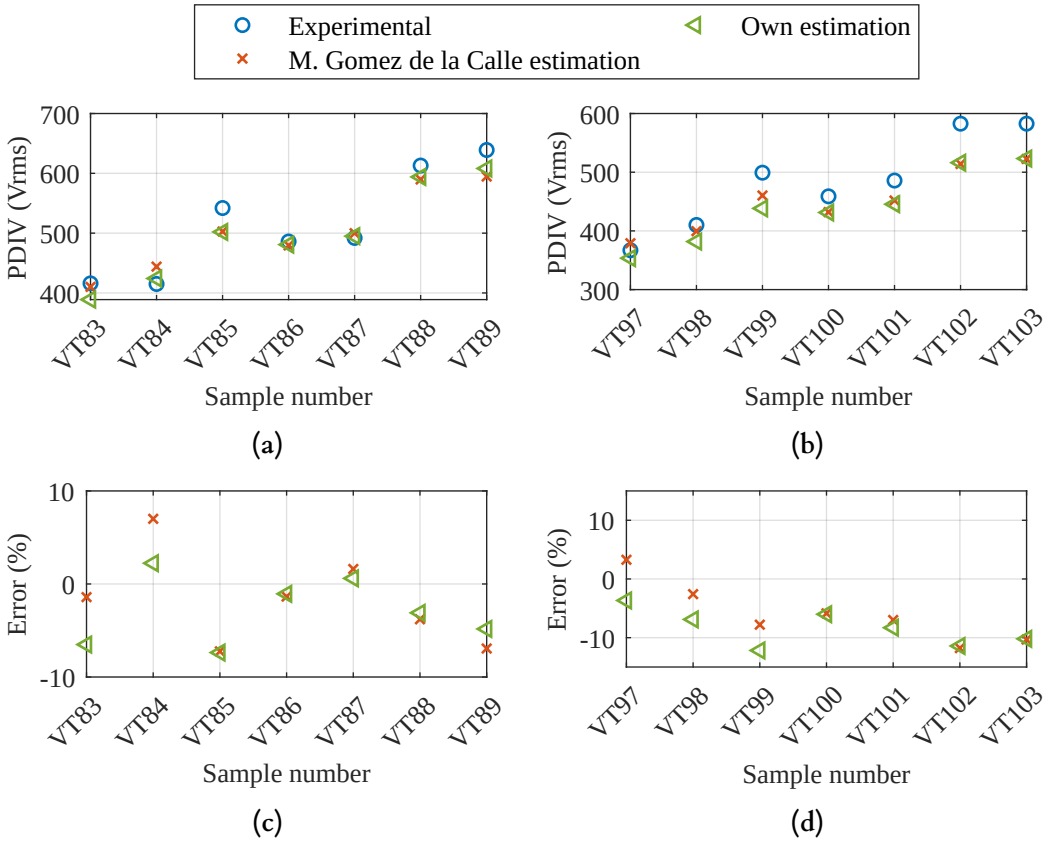

Figure B.9: *Comparison of M. Gomez de la Calle [30] experimental, and own and M. Gomez de la Calle [30] estimation PDIV results obtained using FEM+Schumann's criterion model (a) PDIV at 25 °C, (b) PDIV at 150 °C, (c) model error at 25 °C, and (d) model error at 150 °C.*

Both approaches were tested separately on the datasets for the Extended Dakin's temperature model (Appendix A.1) and the Extended Dakin's absolute humidity model (Appendix A.2) validations. Figure B.10 compares the results for VT dataset (a), VAH dataset (b), and the combined dataset (c). In all cases, using $K_{\text{Sch}} = 5.98$ yielded the best results, producing the lowest mean error with the highest probability density and the smallest maximum error. Consequently, $K_{\text{Sch}} = 5.98$ was used for model comparisons in Section 4.3.3.

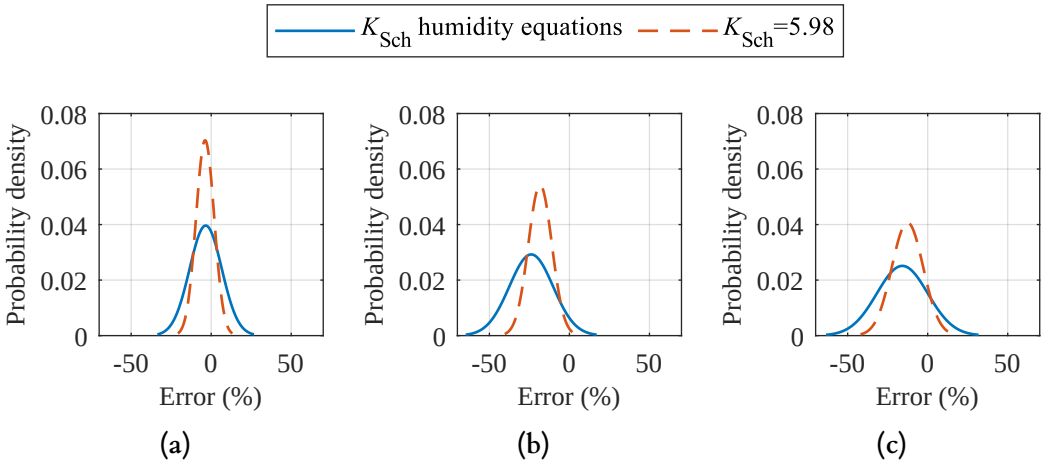

Figure B.10: *Comparison of the error distributions for different K_{Sch} selection approaches in the FEM+Schumann's model implementation (a) using only VT dataset, (b) using only VAH dataset, and (c) combining both datasets.*

B.3 Results of the PDIV Predictions with Different Models

Table B.1 compiles the results obtained with each model (ED: Extended Dakin's, PP: Extended parallel-plate, FP: FEM+Paschen's, and FS: FEM+Schumann's) described in Section 4.3 for VT dataset and VAH dataset. Further details on each sample are provided in Appendix A.

Table B.1: *Parameters, and experimental (exp) and predicted results obtained in the comparison of the models conducted in Section 4.3.3 (ED: Extended Dakin's, PP: Extended parallel-plate, FP: FEM+Paschen's, and FS: FEM+Schumann's) using VT and VAH datasets.*

Sample name	T(°C)	RH(%)	t_{ins} (μm)	$\varepsilon_{r\,ins}$ (-)	$PDIV_{exp}$ (Vrms)	$PDIV_{ED}$ (Vrms)	$PDIV_{PP}$ (Vrms)	$PDIV_{FP}$ (Vrms)	$PDIV_{FS}$ (Vrms)
VT13	20	50	36.3	4.258	617	568	611	651	530
VT14	20	50	39.0	4.258	620	584	627	658	544
VT17	40	19	35.0	4.258	592	560	590	615	509
VT18	40	19	37.0	3.093	636	649	678	707	594
VT21	60	8	35.0	4.251	564	560	578	601	502
VT22	60	8	37.0	3.085	612	650	662	693	580
VT29	140	0	35.0	4.036	513	485	476	502	474
VT30	140	0	37.0	2.931	519	570	547	566	530
VT33	160	0	35.0	4.069	490	467	467	488	460
VT34	160	0	37.0	2.914	498	552	538	559	523
VT43	220	0	35.0	4.639	474	389	431	453	424
VT44	220	0	37.0	2.887	482	493	514	537	502
VT61	25	50	36.0	4.500	548	554	594	615	516
VT62	25	50	29.0	2.900	587	605	644	665	552
VT63	25	50	36.0	3.100	638	642	683	707	594

Table B.1 – Continued

Sample name	T(°C)	RH(%)	t_{ins} (μm)	$\varepsilon_{r\,ins}$ (-)	$PDIV_{exp}$ (Vrms)	$PDIV_{ED}$ (Vrms)	$PDIV_{PP}$ (Vrms)	$PDIV_{FP}$ (Vrms)	$PDIV_{FS}$ (Vrms)
VT64	25	50	46.0	3.200	746	698	746	785	658
VT65	25	50	72.0	3.200	941	832	917	969	827
VT66	25	50	107.0	3.600	1061	928	1057	1153	990
VT67	25	50	30.0	2.911	100	100	100	100	100
VT68	25	50	30.0	3.751	100	100	100	100	100
VT69	25	50	30.0	3.132	100	100	100	100	100
VT70	100	0	30.0	2.855	92	92	81	82	93
VT71	100	0	30.0	3.890	90	89	80	78	89
VT72	100	0	30.0	2.996	91	93	82	81	92
VT73	150	0	30.0	2.924	87	84	77	77	86
VT74	150	0	30.0	3.995	84	81	76	74	86
VT75	150	0	30.0	3.720	80	78	73	73	83
VT76	180	0	30.0	4.162	80	75	73	73	84
VT77	200	0	30.0	3.037	81	75	73	74	83
VT78	200	0	30.0	4.232	76	71	72	71	81
VT79	200	0	30.0	3.745	76	70	70	70	79
VT80	230	0	30.0	3.107	79	69	71	72	80
VT81	230	0	30.0	4.346	78	66	70	67	78
VT82	230	0	30.0	4.010	73	64	67	67	76
VT83	25	37	16.0	4.530	416	401	470	488	389
VT84	25	45	18.0	3.870	415	448	504	523	424
VT85	25	44	30.0	3.990	542	541	582	608	502
VT86	25	37	25.0	3.740	486	516	560	594	481
VT87	25	34	30.0	4.090	492	535	577	615	495
VT88	25	46	42.0	3.600	613	643	684	707	594
VT89	25	32	43.0	3.560	639	651	694	721	608
VT90	110	0	16.0	4.530	363	349	378	389	361
VT91	110	0	18.0	3.870	394	392	404	417	389
VT92	110	0	30.0	3.990	496	480	465	488	460
VT93	110	0	25.0	3.740	447	457	448	474	438
VT94	110	0	30.0	4.090	493	475	462	495	460
VT95	110	0	42.0	3.600	587	578	546	566	537
VT96	110	0	43.0	3.560	602	587	553	573	544
VT97	150	0	16.0	4.530	367	324	370	382	354
VT98	150	0	18.0	3.870	410	365	394	410	382
VT99	150	0	30.0	3.990	499	449	451	467	438
VT100	150	0	25.0	3.740	459	426	435	453	431
VAH25	30	30	42.8	4.020	721	620	655	672	573
VAH26	30	40	42.8	4.089	699	616	651	679	559
VAH27	30	60	42.8	4.197	678	610	645	686	573
VAH28	30	80	42.8	4.334	654	603	637	665	559
VAH29	60	30	42.8	3.912	698	628	639	665	559
VAH30	60	40	42.8	4.008	681	623	633	651	544
VAH31	60	60	42.8	4.161	668	614	624	665	537
VAH32	60	80	42.8	4.270	668	609	619	651	530
VAH33	80	30	42.8	3.823	688	634	631	658	537
VAH34	80	40	42.8	3.986	684	624	621	636	523
VAH35	80	60	42.8	4.155	690	612	612	643	509
VAH36	80	80	42.8	4.300	695	601	604	629	495

Table B.1 – Continued

Sample name	T(°C)	RH(%)	t_{ins} (μm)	$\varepsilon_{r\,ins}$ (-)	$PDIV_{exp}$ (Vrms)	$PDIV_{ED}$ (Vrms)	$PDIV_{PP}$ (Vrms)	$PDIV_{FP}$ (Vrms)	$PDIV_{FS}$ (Vrms)
VAH37	30	30	42.8	3.919	684	626	662	693	587
VAH38	30	40	42.8	3.994	673	621	657	679	573
VAH39	30	60	42.8	4.104	646	615	650	672	559
VAH40	30	80	42.8	4.261	640	607	641	672	566
VAH41	60	30	42.8	3.907	648	628	639	665	559
VAH42	60	40	42.8	4.020	665	622	632	651	544
VAH43	60	60	42.8	4.163	664	614	624	658	537
VAH44	60	80	42.8	4.298	653	607	617	643	530
VAH45	80	30	42.8	3.803	676	635	632	665	530
VAH46	80	40	42.8	3.960	683	625	622	643	530
VAH47	80	60	42.8	4.130	687	613	613	643	502
VAH48	80	80	42.8	4.272	679	602	606	636	495
VAH49	22	41	25.0	4.196	629	493	542	566	460
VAH50	22	50	25.0	4.196	596	493	542	566	460
VAH51	22	57	25.0	4.196	576	494	542	566	460
VAH52	22	67	25.0	4.196	555	494	542	566	460
VAH53	25	20	31.0	3.956	593	549	590	622	509
VAH54	25	50	31.0	3.956	561	550	590	622	509
VAH55	25	95	31.0	3.956	558	551	590	622	509
VAH56	50	25	31.0	3.956	550	551	574	601	495
VAH57	50	50	31.0	3.956	537	553	574	601	495
VAH58	50	95	31.0	3.956	523	557	574	601	488
VAH59	70	20	31.0	3.956	558	553	563	594	481
VAH60	70	50	31.0	3.956	549	558	563	594	474
VAH61	70	90	31.0	3.956	529	560	563	594	467
VAH62	90	20	31.0	3.956	585	557	553	580	467
VAH63	90	90	31.0	3.956	609	548	553	580	403
VAH64	30	30	31.0	3.400	577	583	619	651	537
VAH65	30	45	31.0	3.400	560	584	619	651	530
VAH66	30	60	31.0	3.400	568	584	619	651	530
VAH67	30	75	31.0	3.400	595	585	619	651	530
VAH68	30	90	31.0	3.400	642	585	619	651	530
VAH69	60	30	31.0	3.400	558	586	598	629	509
VAH70	60	45	31.0	3.400	573	587	598	629	509
VAH71	60	60	31.0	3.400	585	588	598	629	509
VAH72	60	75	31.0	3.400	629	589	598	629	502
VAH73	60	90	31.0	3.400	643	589	598	629	502
VAH74	90	30	31.0	3.400	576	589	581	608	481
VAH75	90	45	31.0	3.400	613	588	581	608	474
VAH76	90	60	31.0	3.400	637	584	581	608	460
VAH77	90	75	31.0	3.400	654	577	581	608	445
VAH78	90	90	31.0	3.400	668	569	581	608	417
VAH79	25	30	28.5	4.310	590	514	558	587	481
VAH80	25	40	28.5	4.310	570	514	558	587	481
VAH81	25	50	28.5	4.310	567	514	558	587	481
VAH82	25	60	28.5	4.310	556	515	558	587	481
VAH83	25	70	28.5	4.310	552	515	558	587	481
VAH84	25	80	28.5	4.310	541	515	558	587	481
VAH85	25	90	28.5	4.310	535	516	558	587	481

Table B.1 – Continued

Sample name	T(°C)	RH(%)	t_{ins} (μm)	$\varepsilon_{r\,ins}$ (-)	$PDIV_{exp}$ (Vrms)	$PDIV_{ED}$ (Vrms)	$PDIV_{PP}$ (Vrms)	$PDIV_{FP}$ (Vrms)	$PDIV_{FS}$ (Vrms)
VAH86	40	20	28.5	4.310	583	514	549	580	474
VAH87	40	30	28.5	4.310	578	515	549	580	474
VAH88	40	40	28.5	4.310	562	516	549	580	474
VAH89	40	50	28.5	4.310	559	516	549	580	474
VAH90	40	60	28.5	4.310	550	517	549	580	474
VAH91	40	70	28.5	4.310	532	518	549	580	474
VAH92	40	80	28.5	4.310	530	519	549	580	474
VAH93	40	90	28.5	4.310	528	519	549	580	474
VAH94	60	20	28.5	4.310	569	517	539	573	460
VAH95	60	30	28.5	4.310	561	518	539	573	460
VAH96	60	40	28.5	4.310	559	520	539	573	460
VAH97	60	50	28.5	4.310	558	522	539	573	460
VAH98	60	60	28.5	4.310	557	523	539	573	460
VAH99	60	70	28.5	4.310	556	524	539	573	460
VAH100	60	80	28.5	4.310	553	525	539	573	453
VAH101	60	90	28.5	4.310	542	526	539	573	453
VAH102	90	20	28.5	4.310	555	524	526	552	445
VAH103	90	30	28.5	4.310	557	527	526	552	438
VAH104	90	40	28.5	4.310	579	529	526	552	431
VAH105	90	50	28.5	4.310	610	530	526	552	424
VAH106	90	60	28.5	4.310	615	530	526	552	417
VAH107	90	70	28.5	4.310	615	530	526	552	410
VAH108	90	80	28.5	4.310	618	528	526	552	403
VAH109	90	90	28.5	4.310	622	525	526	552	382

Appendix C

PD Patterns of Semi-Automatic and Needle Machines

This appendix collects the PD patterns of Samples 2 and 3 of semi-automatic (Figures C.1 and C.2) and needle (Figures C.3 and C.4) machines that are discussed in Section 5.1.3.

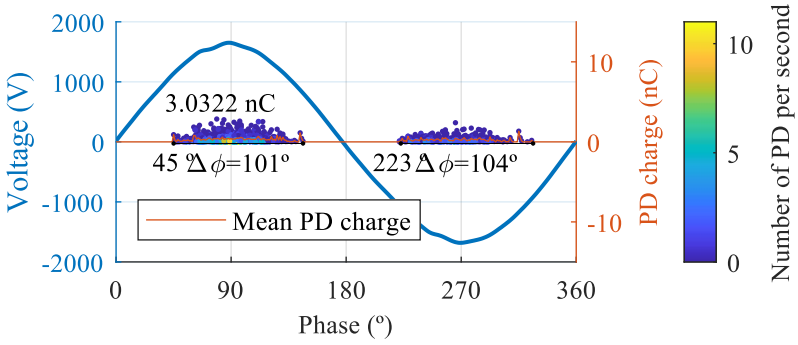
2000
1000
0
-1000
-2000
Voltage (V)
3.0322 nC
45 Δϕ=101°
223 Δϕ=104°
Mean PD charge
10
0
-10
PD charge (nC)
10
5
0
Number of PD per second
0
90
180
270
360
Phase (°)

(a)

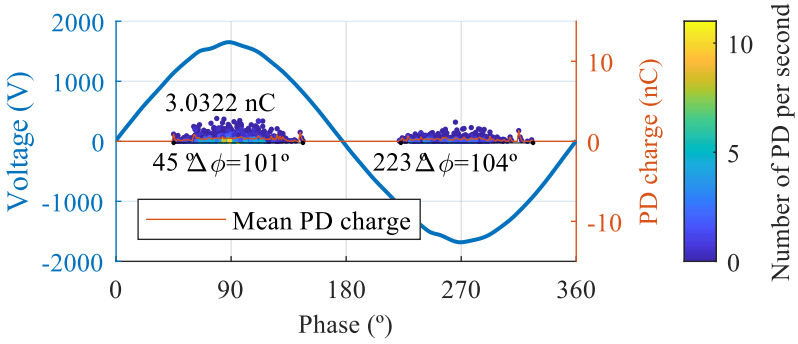
2000
1000
0
-1000
-2000
Voltage (V)
3.0322 nC
45 Δϕ=101°
223 Δϕ=104°
Mean PD charge
10
0
-10
PD charge (nC)
10
5
0
Number of PD per second
0
90
180
270
360
Phase (°)

(b)

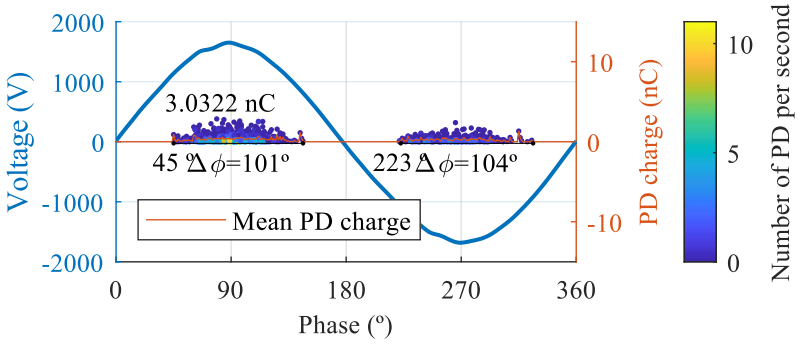
2000
1000
0
-1000
-2000
Voltage (V)
3.0322 nC
45 Δϕ=101°
223 Δϕ=104°
Mean PD charge
10
0
-10
PD charge (nC)
10
5
0
Number of PD per second
0
90
180
270
360
Phase (°)

(c)

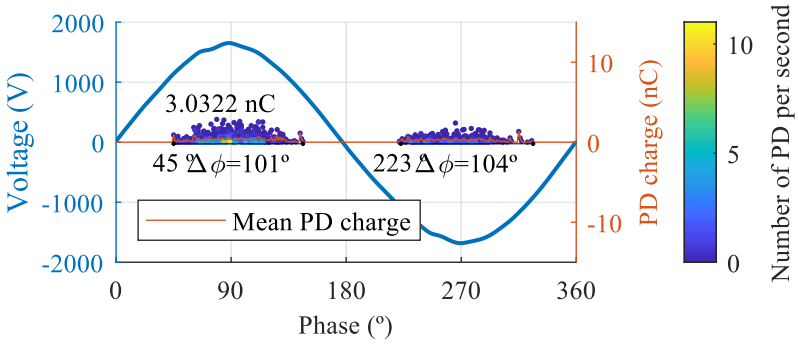
2000
1000
0
-1000
-2000
Voltage (V)
3.0322 nC
45 Δϕ=101°
223 Δϕ=104°
Mean PD charge
10
0
-10
PD charge (nC)
10
5
0
Number of PD per second
0
90
180
270
360
Phase (°)

(d)

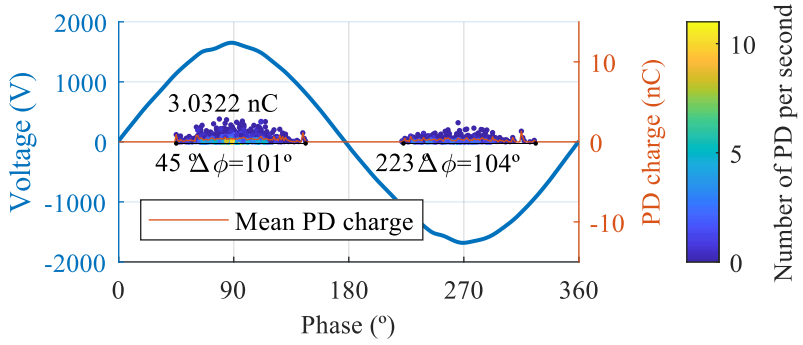

(e)

Figure C.1: *Groundwall insulation PD patterns (UVW to HV, stator to GND) of semi-automatic machine sample 2 (a) 1300 Vrms, (b) 1400 Vrms, (c) 1500 Vrms, (d) 1600 Vrms, and (e) 1700 Vrms.*

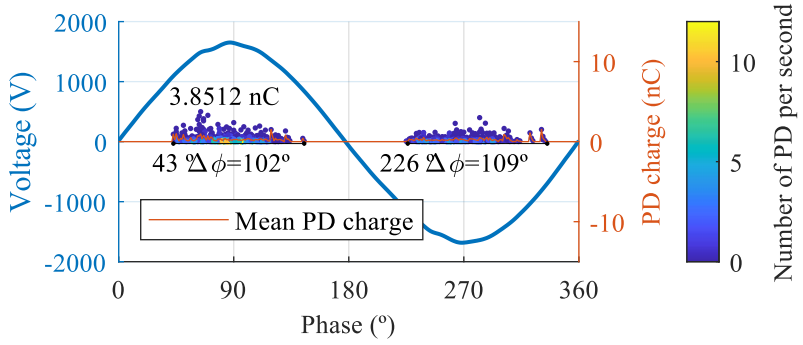

(a)

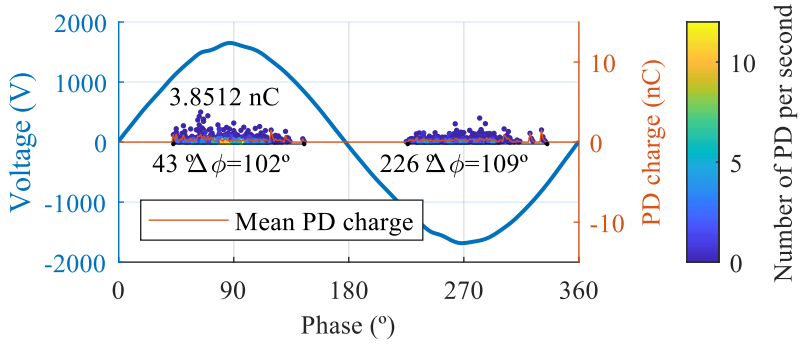

(b)

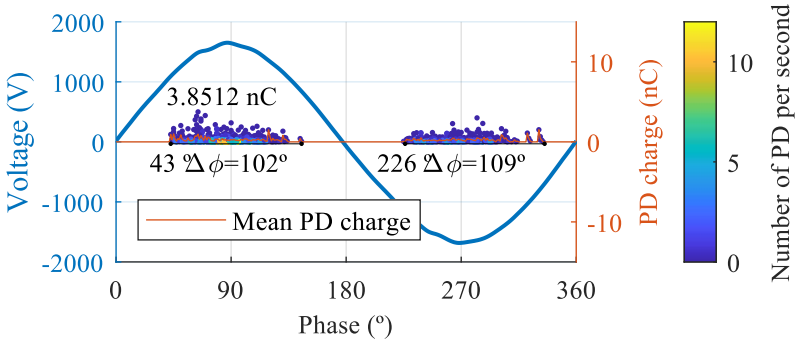

(c)

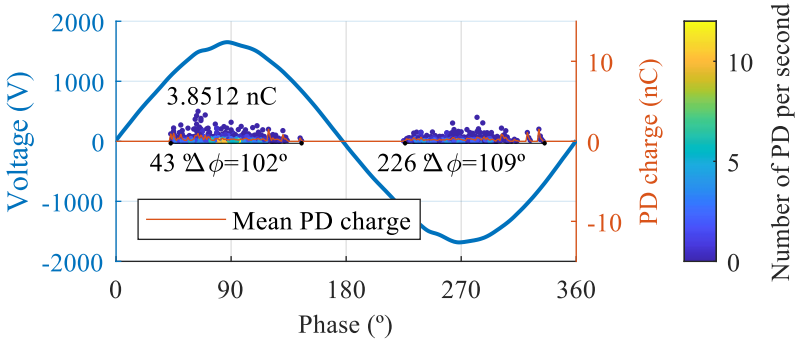

(d)

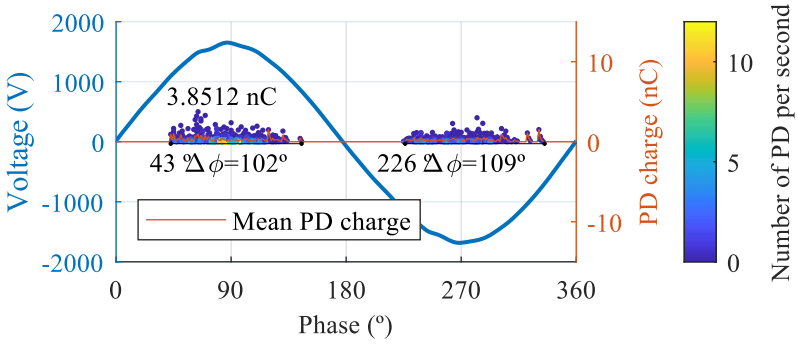

(e)

Figure C.2: *Groundwall insulation PD patterns (UVW to HV, stator to GND) of semi-automatic machine sample 3 (a) 1300 Vrms, (b) 1400 Vrms, (c) 1500 Vrms, (d) 1600 Vrms, and (e) 1700 Vrms.*

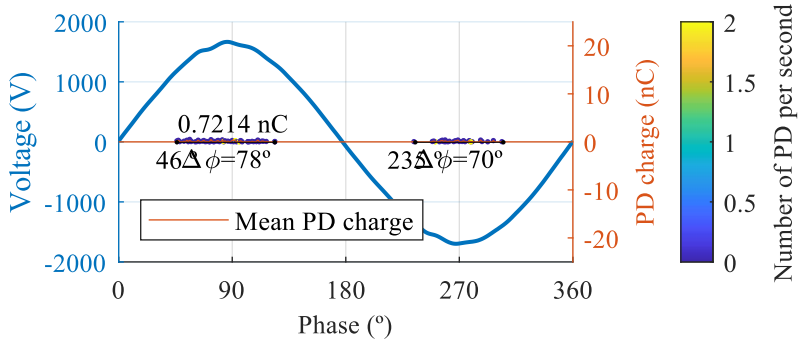
Voltage (V)
PD charge (nC)
Number of PD per second
Phase (°)
0.7214 nC
46 Δϕ=78°
Mean PD charge

(a)

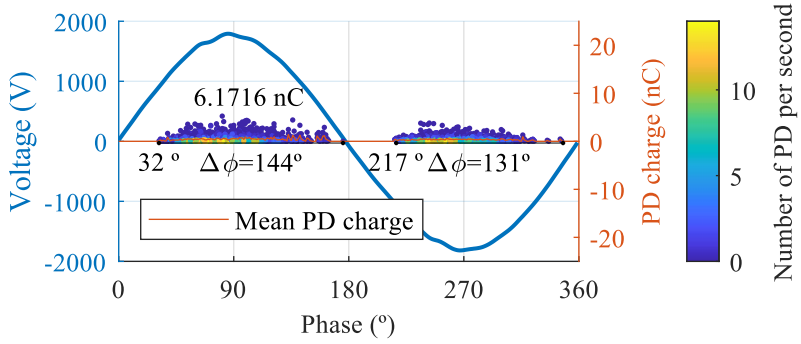
Voltage (V)
PD charge (nC)
Number of PD per second
Phase (°)
6.1716 nC
32 ° Δϕ=144°
217 ° Δϕ=131°
Mean PD charge

(b)

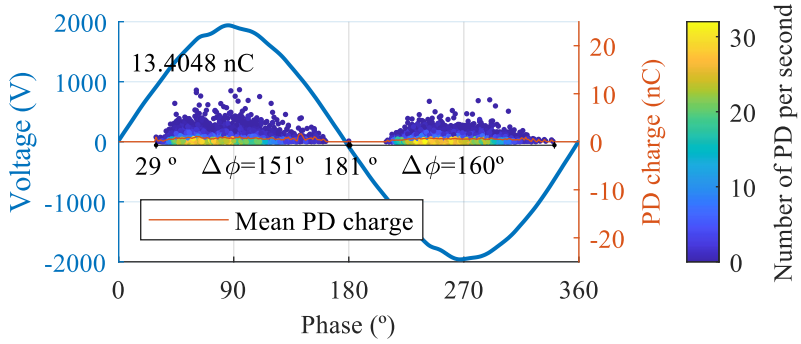
Voltage (V)
PD charge (nC)
Number of PD per second
Phase (°)
13.4048 nC
29 ° Δϕ=151°
181 ° Δϕ=160°
Mean PD charge

(c)

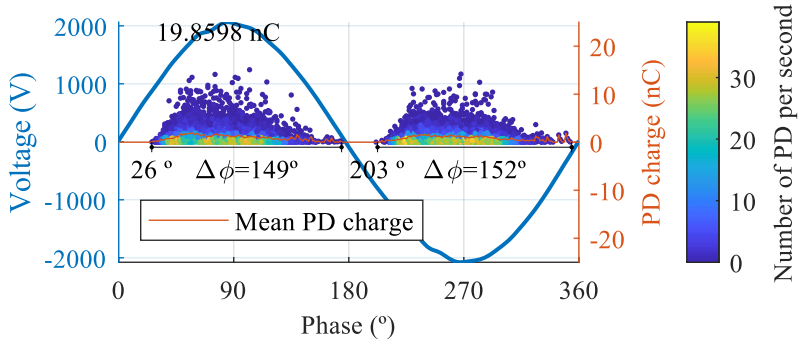
Voltage (V)
PD charge (nC)
Number of PD per second
Phase (°)
19.8598 nC
26 ° Δϕ=149°
203 ° Δϕ=152°
Mean PD charge

(d)

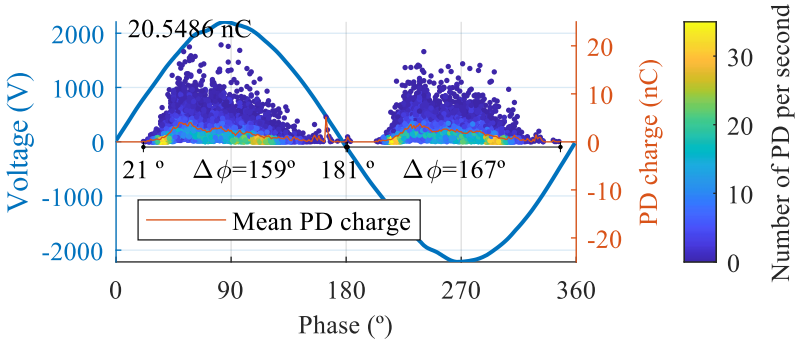

(e)

Figure C.3: *Groundwall insulation PD patterns (UVW to HV, stator to GND) of needle machine sample 2 (a) 1300 Vrms, (b) 1400 Vrms, (c) 1500 Vrms, (d) 1600 Vrms, and (e) 1700 Vrms.*

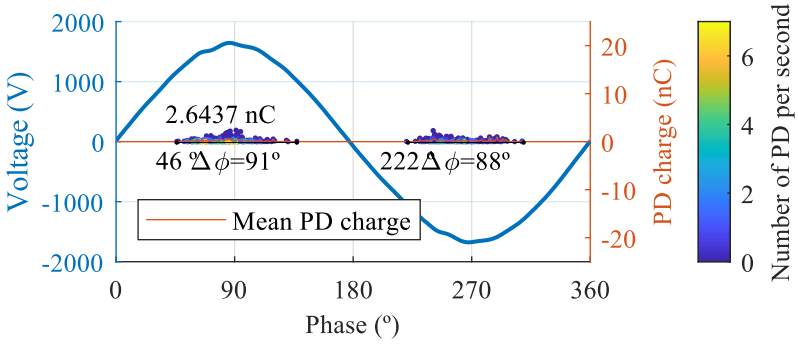

(a)

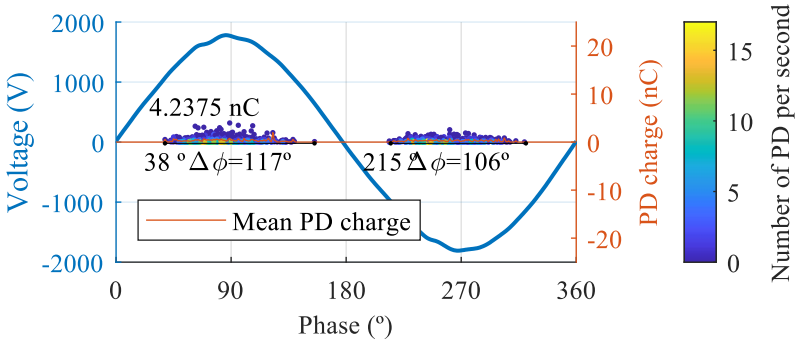

(b)

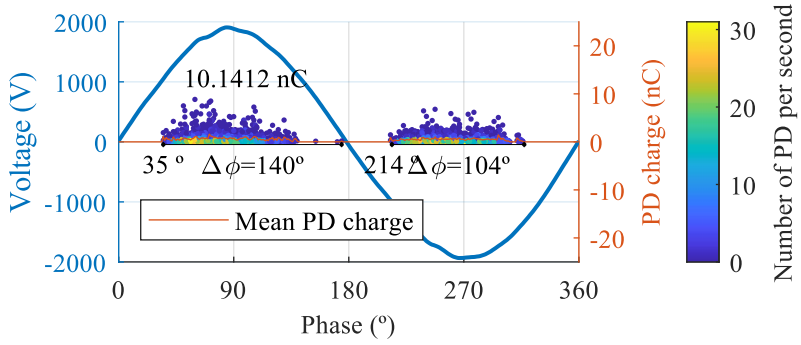

(c)

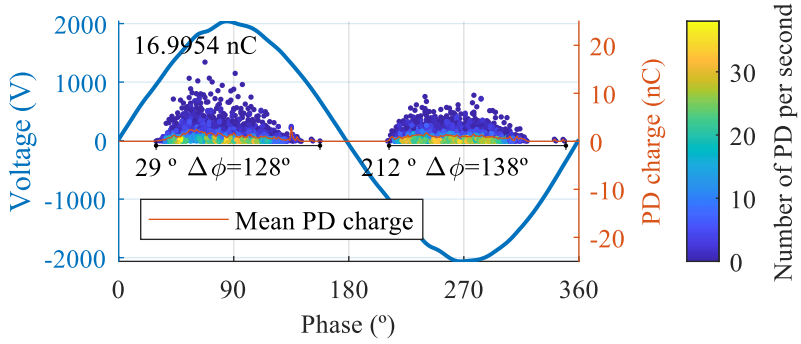

(d)

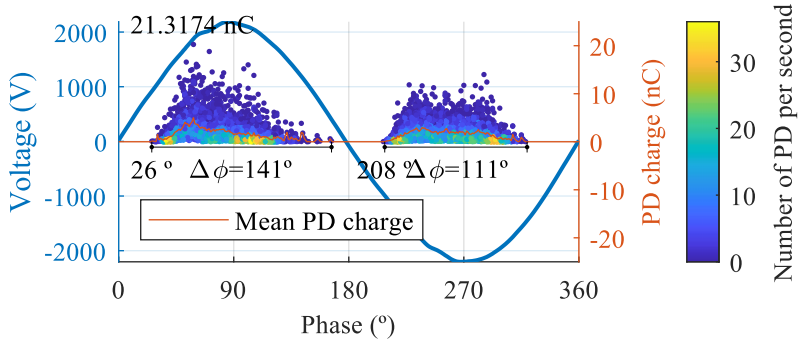

(e)

Figure C.4: *Groundwall insulation PD patterns (UVW to HV, stator to GND) of needle machine sample 3 (a) 1300 Vrms, (b) 1400 Vrms, (c) 1500 Vrms, (d) 1600 Vrms, and (e) 1700 Vrms.*

Appendix D

Electrical Ageing Experiments Results

This appendix collects the numerical results of the electrical ageing tests conducted on the samples defined in Section 3.1.3 as described in Section 3.5.2 for SW samples (Table D.1) and CRW samples (Table D.2). The analysis of these results is presented in Section 6.1.2.

Table D.1: *Experimental results for the 3-factor 2-level DoE electrical ageing experiments for SW samples post processed using the Weibull distribution (considering 63.2% probability) of 4 tested samples.*

No.	t_r (ns)	t_w (µs)	t_{nc} (µs)	Cycles to failure (-)			
				α	β	Lower 90% conf. int.	Upper 90% conf. int.
1	21	2	2	5263427	7.14	4591678	5882356
2	21	2	18	5897507	6.15	5033516	6709441
3	21	10	2	4680663	6.93	4066317	5248836
4	21	10	18	6698761	3.94	5229900	8194587
5	458	2	2	49152592	2.77	34570156	65463682
6	458	2	18	42067524	5.11	35475550	49884402
7	458	10	2	48275409	5.23	40073967	56178367
8	458	10	18	29624634	6.08	25684508	34169193

α: scale parameter; β: shape parameter.

Table D.2: *Experimental results for the 3-factor 2-level DoE electrical ageing experiments for CRW samples post processed using the Weibull distribution (considering 63.2% probability) of 4 tested samples.*

No.	t_r **(ns)**	t_w **(µs)**	t_{nc} **(µs)**	**Cycles to failure (-)**			
				α	β	Lower 90% conf. int.	Upper 90% conf. int.
1	21	2	2	16843732	2.11	10624616	24512636
2	21	2	18	1961866674	2.21	1263016157	2808039925
3	21	10	2	49780961	1.47	25628826	85475074
4	21	10	18	6195679940	2.36	4100878177	8669864291
5	458	2	2	37938190942	7.32	33208780362	42282388906
6	458	2	18	23343083117	4.65	18926142304	27690650662
7	458	10	2	21528014591	4.53	17359566923	25651210317
8	458	10	18	21576361832	4.66	17508417545	25577384234

α: scale parameter; β: shape parameter.

Appendix E

Impedance Spectrum Results During Thermal Ageing Experiments

Experimental CM impedance spectrum evolution during thermal ageing conducted on the samples defined in Section 3.1.3 as described in Section 3.5.1 are presented in Figures E.1, E.2, E.3, E.4, and E.5. The analysis of these results is presented in Section 6.2.2.

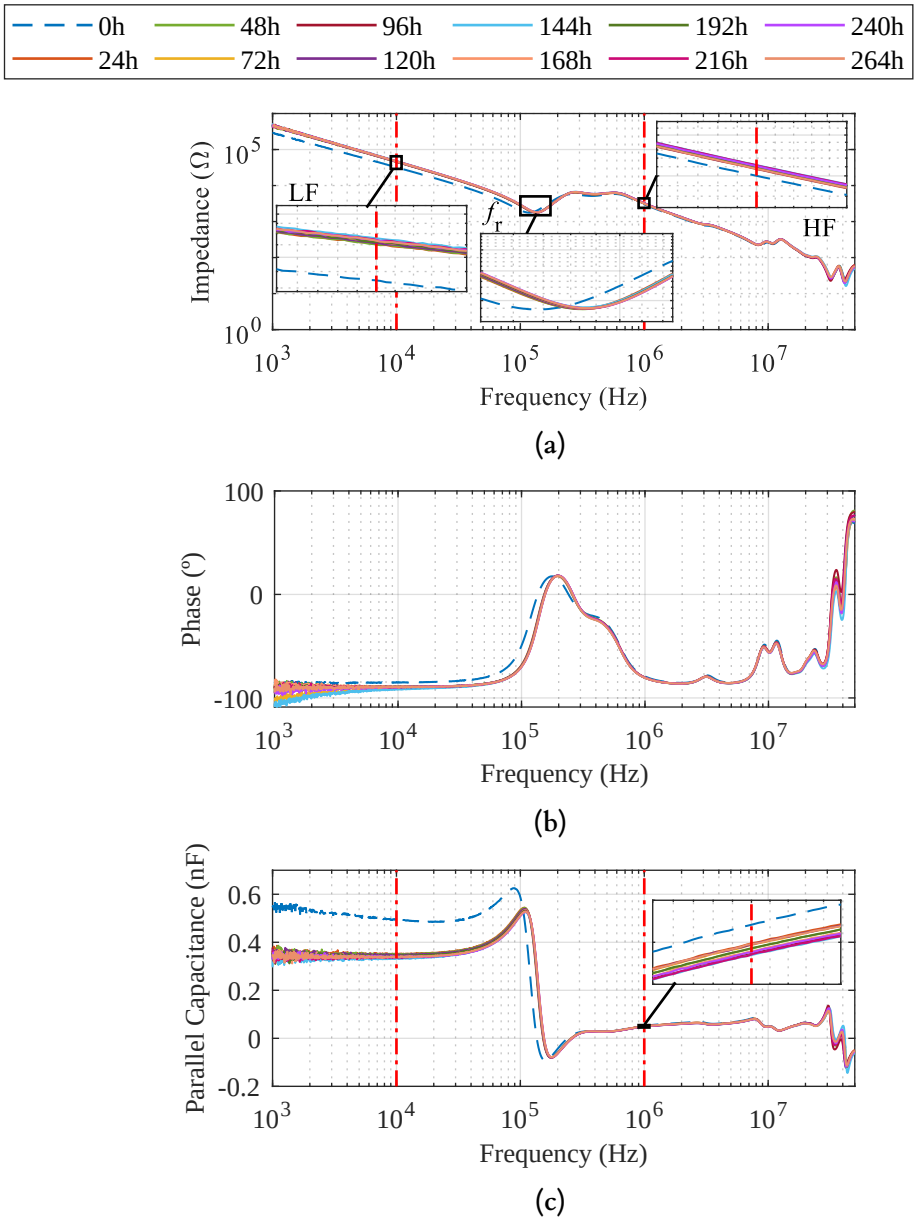

Figure E.1: *Experimental CM impedance spectrum evolution during thermomechanical ageing at 200-230 °C (a) impedance, (b) phase, and (c) parallel capacitance. (LF: Low Frequency; HF: High Frequency; f_r: resonance frequency).*

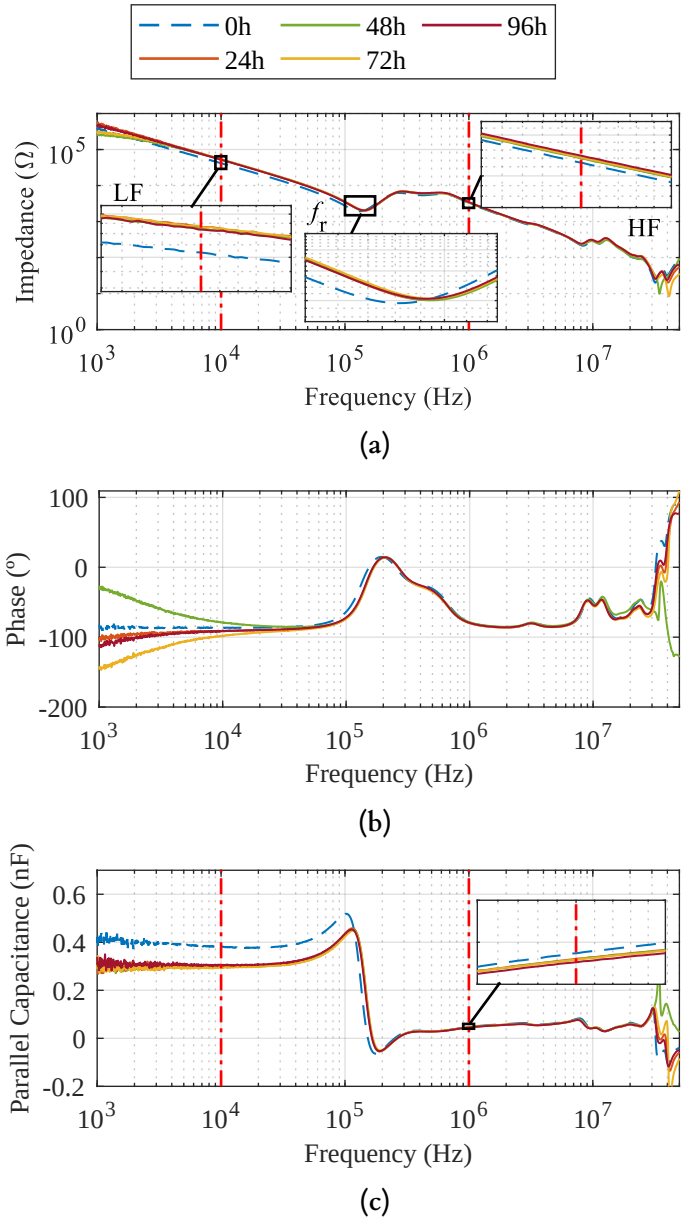

Figure E.2: *Experimental CM impedance spectrum evolution during isothermal ageing at 260 °C of sample 1 (a) impedance, (b) phase, and (c) parallel capacitance. (LF: Low Frequency; HF: High Frequency; f_r: resonance frequency).*

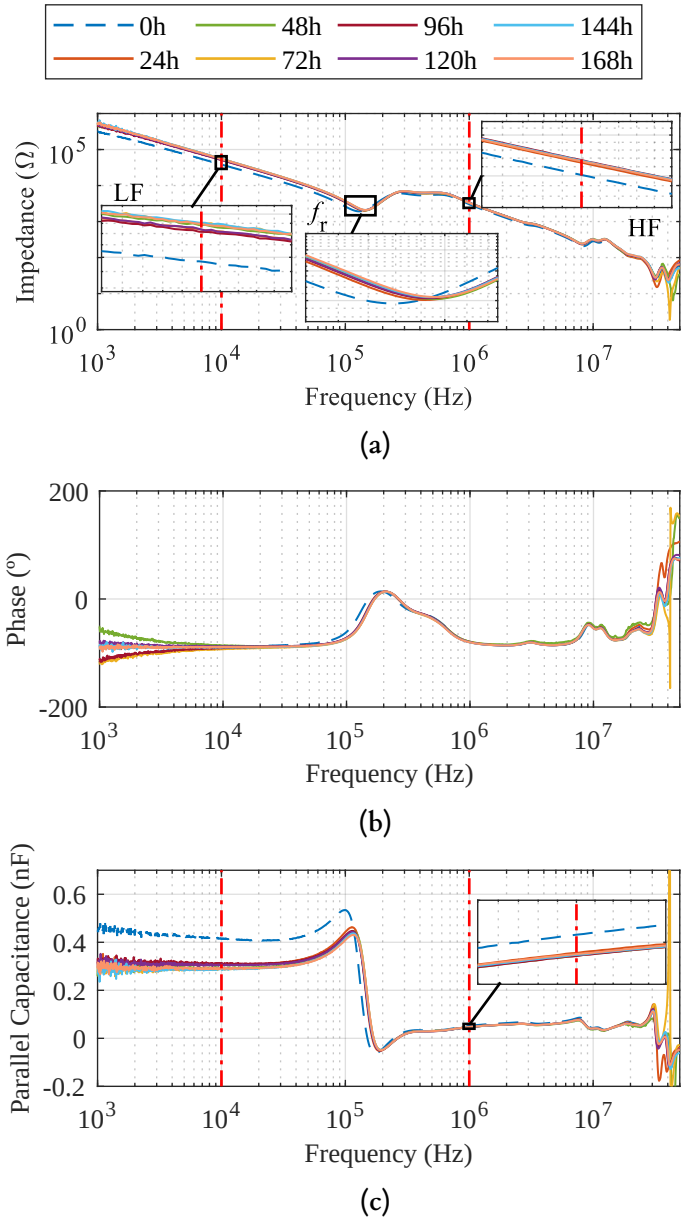

Figure E.3: *Experimental CM impedance spectrum evolution during isothermal ageing at 260 °C of sample 2 (a) impedance, (b) phase, and (c) parallel capacitance. (LF: Low Frequency; HF: High Frequency; f_r: resonance frequency).*

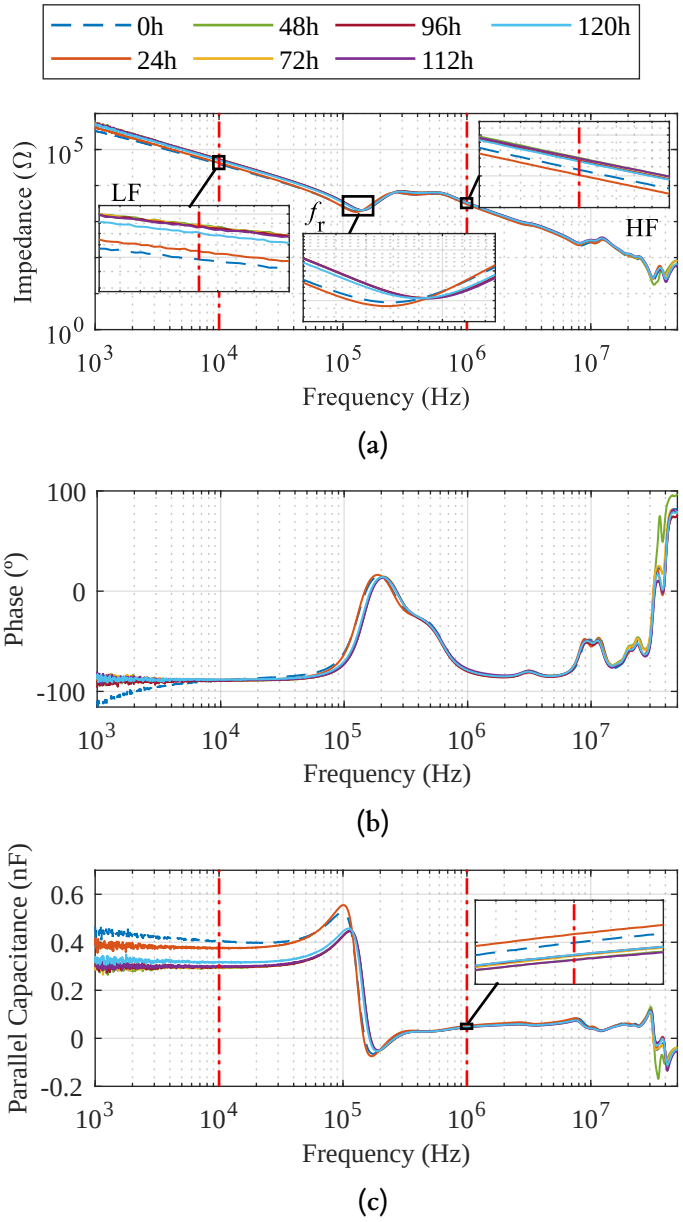

Figure E.4: *Experimental CM impedance spectrum evolution during thermomechanical ageing at 200-260 °C of sample 1 (a) impedance, (b) phase, and (c) parallel capacitance. (LF: Low Frequency; HF: High Frequency; f_r: resonance frequency).*

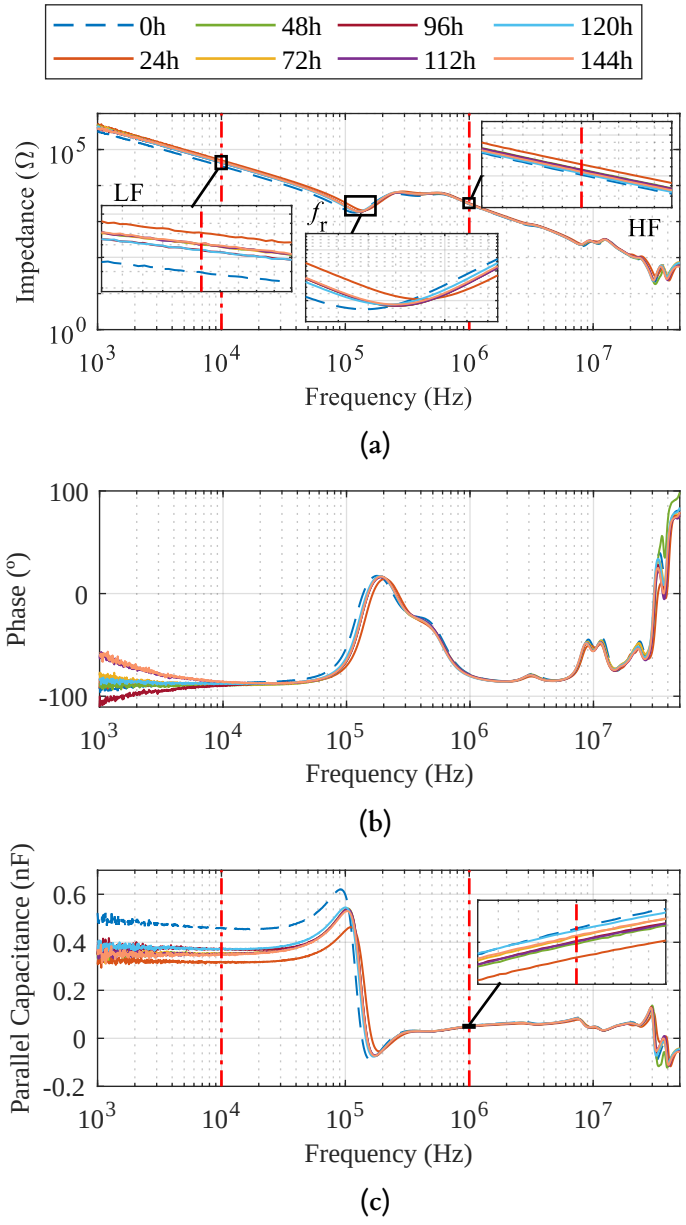

Figure E.5: *Experimental CM impedance spectrum evolution during thermomechanical ageing at 200-260 °C of sample 2 (a) impedance, (b) phase, and (c) parallel capacitance. (LF: Low Frequency; HF: High Frequency; f_r: resonance frequency).*

Bibliography

[1] E. Commission, "European green deal: Commission proposes transformation of eu economy and society to meet climate ambitions," 2021.

[2] A. Joshi, "Review of vehicle engine efficiency and emissions," *SAE Technical Paper*, no. 2021-01-0575, 2021.

[3] H. El Hadraoui, M. Zegrari, A. Chebak, O. Laayati, and N. Guennouni, "A multi-criteria analysis and trends of electric motors for electric vehicles," *World Electric Vehicle Journal*, vol. 13, no. 4, 2022.

[4] B. Laszlo, "Introduction to the fundamental technologies of power density - Power management - Technical articles - TI E2E support forums," 2020. Accessed: 28-Apr-2025.

[5] A. K. Morya, M. C. Gardner, B. Anvari, L. Liu, A. G. Yepes, J. Doval-Gandoy, and H. A. Toliyat, "Wide bandgap devices in ac electric drives: Opportunities and challenges," *IEEE Transactions on Transportation Electrification*, vol. 5, no. 1, pp. 3–20, 2019.

[6] D. Han, Y. Li, and B. Sarlioglu, "Analysis of sic based power electronic inverters for high speed machines," in *2015 IEEE Applied Power Electronics Conference and Exposition (APEC)*, pp. 304–310, 2015.

[7] A. Carlsson, V. Josefsson, S. Nategh, A. Boglietti, and R. Arvidsson, "Insulation system design for 800 v traction motors used in e-mobility applications," in *2022 International Conference on Electrical Machines (ICEM)*, pp. 1321–1326, 2022.

[8] J. He, H. Chen, R. Katebi, N. Weise, and N. A. Demerdash, "Mitigation of uneven surge voltage stress on stator windings of induction motors fed by sic-mosfet-based adjustable speed drives," in *2017 IEEE International Electric Machines and Drives Conference (IEMDC)*, pp. 1–7, 2017.

[9] "Iec 60034-18-41: Rotating electrical machines - part 18-41: Partial discharge free electrical insulation systems (type i) used in rotating electrical machines fed from voltage converters - qualification and quality control tests," 2014. First edition.

[10] M. J. Scott, J. Brockman, B. Hu, L. Fu, L. Xu, J. Wang, and R. Darbali Zamora, "Reflected wave phenomenon in motor drive systems using wide bandgap devices," in *2014 IEEE Workshop on Wide Bandgap Power Devices and Applications*, pp. 164–168, 2014.

[11] A. Selema, M. N. Ibrahim, and P. Sergeant, "Electrical machines winding technology: Latest advancements for transportation electrification," *Machines*, vol. 10, no. 7, 2022.

[12] A. Morya and H. A. Toliyat, "Insulation design for wide bandgap (wbg) device based voltage source converter fed motors," in *2017 IEEE 5th Workshop on Wide Bandgap Power Devices and Applications (WiPDA)*, pp. 74–79, 2017.

[13] R. Hemmati, F. Wu, and A. El-Refaie, "Survey of insulation systems in electrical machines," in *2019 IEEE International Electric Machines & Drives Conference (IEMDC)*, pp. 2069–2076, 2019.

[14] V. Grau and R. W. De Doncker, "The effects of steep voltage slopes on insulation systems of coil windings caused by next generation power semiconductor devices," in *2019 IEEE Electrical Insulation Conference (EIC)*, pp. 26–29, 2019.

[15] M. Florkowski, B. Florkowska, and P. Zydron, "Partial discharges in insulating systems of low voltage electric motors fed by power electronics—twisted-pair samples evaluation," *Energies*, vol. 12, no. 5, 2019.

[16] F. Guastavino, A. Dardano, A. Ratto, and E. Torello, "Electrical aging test on twisted pair specimens under different environmental conditions," *Annual Report - Conference on Electrical Insulation and Dielectric Phenomena, CEIDP*, pp. 81–84, 2009.

[17] S. Savin, S. Ait-Amar, and D. Roger, "Turn-to-turn capacitance variations correlated to pdiv for ac motors monitoring," *IEEE Transactions on Dielectrics and Electrical Insulation*, vol. 20, no. 1, pp. 34–41, 2013.

[18] X. Liu, T. Zhang, Y. Bai, X. Ding, and Y. Wang, "Effects of accelerated repetitive impulse voltage aging on performance of model stator insulation of wind turbine generator," *IEEE Transactions on Dielectrics and Electrical Insulation*, vol. 21, no. 4, pp. 1506–1515, 2014.

[19] R. Succi, T. Han, and A. Cavallini, "An investigation on the dielectric properties of thermally-aged kapton and its capability to withstand partial discharges," in *2019 IEEE Conference on Electrical Insulation and Dielectric Phenomena (CEIDP)*, pp. 381–384, 2019.

[20] F. Guastavino, L. Briano, F. Gallesi, and E. Torello, "Effect of thermal stress over the partial discharge inception voltage on twisted pairs," in *2020 IEEE Conference on Electrical Insulation and Dielectric Phenomena (CEIDP)*, pp. 366–368, 2020.

[21] L. Elorza Azpiazu, G. Almandoz, A. Egea, G. Ugalde, and X. Badiola, "Study of partial discharge inception voltage in inverter fed electric motor insulation systems," *Applied Sciences*, vol. 13, no. 4, 2023.

[22] L. E. Azpiazu, A. Egea, G. Almandoz, G. Ugalde, and I. Sarasola, "Experimental-based model for turn-to-turn pdiv prediction dependent on temperature," in *2024 International Conference on Electrical Machines (ICEM)*, pp. 1–7, 2024.

[23] L. E. Azpiazu, Y. Moreno, A. Egea, G. Almandoz, and A. A. Rebollo, "Comparison of impedance spectroscopy and partial discharge analysis as insulation health diagnosis techniques," in *2024 International Conference on Electrical Machines (ICEM)*, pp. 1–7, 2024.

[24] I. López, E. Ibarra, A. Matallana, J. Andreu, and I. Kortabarria, "Next generation electric drives for HEV/EV propulsion systems: Technology, trends and challenges," *Renewable and Sustainable Energy Reviews*, vol. 114, no. April 2018, p. 109336, 2019.

[25] C. A. Rivera, G. Ugalde, J. Poza, F. Garramiola, and X. Badiola, "Less rare-earth electromagnetic design for a high-performance permanent magnet motor," *Applied Sciences (Switzerland)*, vol. 12, 4 2022.

[26] G. C. Stone, I. Culbert, E. A. Boulter, and H. Dhirani, *Electrical Insulation for Rotating Machines*. Wiley, 2014.

[27] P. Stenzel, J. Richnow, J. Franke, and C. Endisch, "Impact of the needle winding technology on the operational behavior of an asynchronous machine," in *2015 5th International Electric Drives Production Conference (EDPC)*, pp. 1–8, 2015.

[28] P. Stenzel, P. Dollinger, J. Richnow, and J. Franke, "Innovative needle winding method using curved wire guide in order to significantly increase the copper fill factor," in *2014 17th International Conference on Electrical Machines and Systems (ICEMS)*, pp. 3047–3053, 2014.

[29] I. Automation, "Needle winding technology," 2025. Accessed: 28-Apr-2025.

[30] M. Gómez and D. Calle, *Partial Discharge Inception Voltage in Turn-To-Turn Insulation Systems : Modelling and Uncertainties*. PhD thesis, Universidad Carlos III de Madrid, 2021.

[31] CGTrader, "Hairpin winding 3d model," 2025. Accessed: 28-Apr-2025.

[32] L. Lusuardi, *Towards a partial discharge free insulation system for the More Electrical Transportation*. PhD thesis, Alma Mater Studiorum - Università di Bologna, 2020.

[33] T. Dimier, M. Cossale, and T. Wellerdieck, "Comparison of stator winding technologies for high-speed motors in electric propulsion systems," in *2020 International Conference on Electrical Machines (ICEM)*, vol. 1, pp. 2406–2412, 2020.

[34] J. Seefried, A. Riedel, A. Kühl, and J. Franke, "Challenges and solutions for contacting insulated litz wire structures in the context of electromechanical engineering," in *Production at the Leading Edge of Technology*, pp. 466–475, Springer International Publishing, 2022.

[35] P. Shams Ghahfarokhi, A. Podgornovs, A. J. M. Cardoso, A. Kallaste, A. Belahcen, and T. Vaimann, "Hairpin windings for electric vehicle motors: Modeling and investigation of ac loss-mitigating approaches," *Machines*, vol. 10, no. 11, 2022.

[36] C.-L. Lin, H.-M. Dai, C.-H. Chao, S. Wei, and C.-F. Yang, "Drivetrain and powertrain thermal analyses of a tesla model 3 electric vehicle," *Sensors and Materials*, 2023.

[37] EVSpecifications, "2022 tesla model 3 performance awd - specifications," 2025. Accessed: 28-Apr-2025.

[38] I. Husain, B. Ozpineci, M. S. Islam, E. Gurpinar, G. J. Su, W. Yu, S. Chowdhury, L. Xue, D. Rahman, and R. Sahu, "Electric Drive Technology Trends, Challenges, and Opportunities for Future Electric Vehicles," *Proceedings of the IEEE*, vol. 109, no. 6, pp. 1039–1059, 2021.

[39] G. Scelba, D. Camuglia, G. De Donato, S. Vaschetto, A. Cavagnino, and E. Agamloh, "On the Effects of Ultra-High Switching Frequency on PWM-Inverter-Fed Induction Motors," *ECCE 2020 - IEEE Energy Conversion Congress and Exposition*, pp. 3823–3830, 2020.

[40] D. Han, S. Li, W. Lee, and B. Sarlioglu, "Adoption of wide bandgap technology in hybrid/electric vehicles-opportunities and challenges," *2017 IEEE Transportation and Electrification Conference and Expo, ITEC 2017*, vol. 3, pp. 561–566, 2017.

[41] D. D'Amato, J. Loncarski, V. G. Monopoli, F. Cupertino, L. P. Di Noia, and A. Del Pizzo, "Impact of PWM Voltage Waveforms in High-Speed Drives: A Survey on High-Frequency Motor Models and Partial Discharge Phenomenon," *Energies*, vol. 15, no. 4, 2022.

[42] P. Yi, P. K. S. Murthy, and L. Wei, "Performance evaluation of SiC MOSFETs with long power cable and induction motor," *ECCE 2016 - IEEE Energy Conversion Congress and Exposition, Proceedings*, 2016.

[43] R. S. Ferreira and A. C. Ferreira, "Transient voltage distribution in induction motor stator windings using finite elements method," in *IECON 2018 - 44th Annual Conference of the IEEE Industrial Electronics Society*, pp. 737–742, 2018.

[44] Y. Moreno, G. Almandoz, A. Egea, B. Arribas, and A. Urdangarin, "Analysis of permanent magnet motors in high frequency—a review," *Applied Sciences*, vol. 11, no. 14, 2021.

[45] C. Petrarca, A. Maffucci, V. Tucci, and M. Vitelli, "Analysis of the voltage distribution in a motor stator winding subjected to steep-fronted surge voltages by means of a multiconductor lossy transmission line model," *IEEE Transactions on Energy Conversion*, vol. 19, no. 1, pp. 7–17, 2004.

[46] X. Ju, Y. Zhang, Z. Xue, Y. Cheng, and S. Cui, "Moving towards the reliability-oriented design of hairpin winding for ev traction machines driven by sic inverter," *CES Transactions on Electrical Machines and Systems*, vol. 9, pp. 26–35, 3 2025.

[47] A. Saha and M. Ghassemi, "A review of electrical insulation challenges for electrical powertrain components in the future more and all electric aircraft under low-pressure conditions," 2024.

[48] A. Rumi, L. Lusuardi, A. Cavallini, M. Pastura, D. Barater, and S. Nuzzo, "Partial Discharges in Electrical Machines for the More Electrical Aircraft. Part III: Preventing Partial Discharges," *IEEE Access*, vol. 9, pp. 30113–30123, 2021.

[49] "Iec 60270: High-voltage test techniques - partial discharge measurements," 2000. Amendment 1:2015.

[50] B. Gaussens, M. Bailoni, and S. Nategh, "Advanced insulation and wire wrap systems for 800v+ next gen e-motors," 2022.

[51] M. Szczepanski, *Development of methods allowing the test and the comparison of low-voltage motors insulation systems running under partial discharges (fed by inverter)*. PhD thesis, Univ. Paul Sabatier - Toulouse III PhD Thesis, 2019.

[52] "Iec 60317-0-1: Specifications for particular types of winding wires - part 0-1: General requirements - enamelled round copper wire," 2013. Fourth edition.

[53] "Iec 60317-0-2: Specifications for particular types of winding wires - part 0-2: General requirements - enamelled rectangular copper wire," 2020. Fourth edition.

[54] "Iec 60050-212: International electrotechnical vocabulary (iev) - part 212: Electrical insulating solids, liquids and gases," 2010. Second edition.

[55] D. J. Griffiths, *INTRODUCTION TO ELECTRODYNAMICS*. Pearson, 2013.

[56] K. C. Kao, *Dielectric Phenomena in Solids*. Elsevier Academic Press, 2004.

[57] R. P. Deshpande, *Capacitors*. McGraw-Hill Education, 2015.

[58] "Iec 60216-1: Electrical insulating materials - thermal endurance properties - part 1: Ageing procedures and evaluation of test results," 2013. Sixth edition.

[59] "Iec 60034-18-31: Rotating electrical machines - part 18-31: Functional evaluation of insulation systems - test procedures for form-wound windings - thermal evaluation and classification," 2012. Second edition.

[60] S. Rahmanzadeh and M. S. Pishvaee, "Electron radar search algorithm: a novel developed meta-heuristic algorithm," *Soft Computing*, vol. 24, no. 11, pp. 8443–8465, 2020.

[61] G. C. Stone, A. Cavallini, G. Behrmann, and C. A. Serafino, *PRACTICAL PARTIAL DISCHARGE MEASUREMENT ON ELECTRICAL EQUIPMENT*. Wiley, 8 2023.

[62] J. Lehr and P. Ron, *Electrical Breakdown in Gases*. John Wiley & Sons, Inc, 2017.

[63] N. Hayakawa, F. Shimizu, and H. Okubo, "Estimation of partial discharge inception voltage of magnet wires under inverter surge voltage by volume-time theory," *IEEE Transactions on Dielectrics and Electrical Insulation*, vol. 19, no. 2, pp. 550–557, 2012.

[64] J. Kuffel and P. Kuffel, *High Voltage Engineering Fundamentals, 2nd Edition*. Newnes, 2000.

[65] E. Gockenbach, *High Voltage Engineering*. Springer Handbooks, 2021.

[66] E. Sili, F. Koliatene, and J. P. Cambronne, "Pressure and temperature effects on the paschen curve," *Annual Report - Conference on Electrical Insulation and Dielectric Phenomena, CEIDP*, pp. 464–467, 2011.

[67] E. Sili and J. P. Cambronne, "A New Empirical Expression of the Breakdown Voltage for Combined Variations of Temperature and Pressure," *International Journal of Aerospace and Mechanical Engineering*, vol. 6, no. 3, pp. 611–616, 2012.

[68] R. Färber, Y. Lu, M. Balmelli, O. Self, and C. M. Franck, "Static breakdown threshold modeling of quasi-uniform gas gaps with a focus on the pdiv of contacting enameled wire," *Journal of Physics D: Applied Physics*, vol. 56, 2023.

[69] "Iec 60172: Test procedure for the determination of the temperature index of enamelled and tape wrapped winding wires," 2020. Second edition.

[70] Y. Kikuchi, T. Murata, Y. Uozumi, N. Fukumoto, M. Nagata, Y. Wakimoto, and T. Yoshimitsu, "Effects of ambient humidity and temperature on partial discharge characteristics of conventional and nanocomposite enameled magnet wires," *IEEE Transactions on Dielectrics and Electrical Insulation*, vol. 15, pp. 1617–1625, 2008.

[71] N. A. Driendl, F. A. Pauli, and K. Hameyer, "Characterization of insulation material parameters in low-voltage electrical machines," 2022 International Conference on Electrical Machines (ICEM), 2022.

[72] OMICRON LAB, "Bode 100 User Manual," 2023.

[73] T. Kaji, H. Asai, H. Kojima, and N. Hayakawa, "Combined effect of temperature and humidity on partial discharge inception voltage of magnet wires under inverter-surge voltage," in *IEEJ Transactions on Fundamentals and Materials*, vol. 139, pp. 30–37, IEEE, 2019.

[74] L. Lusuardi, A. Cavallini, V. Madonna, P. Giangrande, and M. Galea, "Unconventional accelerated thermal ageing test for traction electric motors in vehicles," in *2020 IEEE Electrical Insulation Conference, EIC 2020*, no. 807081, pp. 212–216, 2020.

[75] E. Unicrom, "Variación de la resistencia de un material con la temperatura," 2025. Accessed: 28-Apr-2025.

[76] L. Lusuardi, A. Rumi, A. Cavallini, D. Barater, and S. Nuzzo, "Partial discharge phenomena in electrical machines for the more electrical aircraft. part ii: Impact of reduced pressures and wide bandgap devices," *IEEE Access*, vol. 9, pp. 27485–27495, 2021.

[77] "Iec 62539: Guide for the statistical analysis of electrical insulation breakdown data," 2007. First edition.

[78] C. Abadie, T. Billard, and T. Lebey, "Partial Discharges in Motor Fed by Inverter: From Detection to Winding Configuration," *IEEE Transactions on Industry Applications*, vol. 55, no. 2, pp. 1332–1341, 2019.

[79] D. R. Meyer, A. Cavallini, L. lusuardi, D. Barater, G. Pietrini, and A. Soldati, "Influence of impulse voltage repetition frequency on RPDIV in partial vacuum," *IEEE Transactions on Dielectrics and Electrical Insulation*, vol. 25, no. 3, pp. 873–882, 2018.

[80] W. Hassan, G. A. Hussain, F. Mahmood, S. Amin, and M. Lehtonen, "Effects of environmental factors on partial discharge activity and estimation of insulation lifetime in electrical machines," *IEEE Access*, vol. 8, pp. 108491–108502, 2020.

[81] D. Muto, M. Oya, T. Aoi, and T. Ueno, "A study on partial discharge phenomena of winding wires," *Furukawa Review*, no. 45, pp. 13–21, 2014.

[82] Y. Zenda, S. Takenouchi, M. Kozako, M. Hikita, T. Okamoto, S. Jintong, A. Izumi, and K. Karasawa, "Effect of Temperature on RPDIV of Enamel Twisted Pair under Repetitive Impulse Voltage Application with Different Rise Time," *Annual Report - Conference on Electrical Insulation and Dielectric Phenomena, CEIDP*, vol. 2021-Decem, pp. 603–606, 2021.

[83] T. G. Aakre, E. Ildstad, and S. Hvidsten, "Partial discharge inception voltage of voids enclosed in epoxy/mica versus voltage frequency and temperature," *IEEE Transactions on Dielectrics and Electrical Insulation*, vol. 27, no. 1, pp. 214–221, 2020.

[84] N. Driendl, F. Pauli, and K. Hameyer, "Influence of ambient conditions on the qualification tests of the interturn insulation in low-voltage electrical machines," *IEEE Transactions on Industrial Electronics*, vol. 69, pp. 7807–7816, 2022.

[85] Y. Kikuchi, T. Murata, N. Fukumoto, M. Nagata, Y. Wakimoto, and T. Yoshimitsu, "Investigation of partial discharge with twisted enameled wires in atmospheric

humid air by optical emission spectroscopy," *IEEE Transactions on Dielectrics and Electrical Insulation*, vol. 17, no. 3, pp. 839–845, 2010.

[86] A. Rumi, A. Cavallini, and L. lusuardi, "Impact of WBG Converter Voltage Rise-Time and Switching Frequency on the PDIV of Twisted Pairs," *Proceedings of the 2020 IEEE 3rd International Conference on Dielectrics, ICD 2020*, pp. 902–905, 2020.

[87] H. Naderiallaf, Y. Ji, P. Giangrande, and M. Galea, "Modeling humidity impact on pdiv for turn-to-turn insulation of inverter-fed motors at different temperatures," *IEEE Transactions on Dielectrics and Electrical Insulation*, pp. 1–10, 2023.

[88] R. Färber, O. Šefl, and C. M. Franck, "On the influence of humidity on the breakdown strength of air—with a case study on the pdiv of contacting enameled wire pairs," *Journal of Physics D: Applied Physics*, vol. 7, 2024.

[89] P. Wang, P. Li, Y. Li, A. Cavallini, Q. Zhang, and J. Zhang, "Influence of ambient humidity on pdiv and endurance of inverter-fed motor insulation," *2019 IEEE Electrical Insulation Conference, EIC 2019*, pp. 201–204, 2019.

[90] H. Naderiallaf, P. Giangrande, and M. Galea, "Investigating the effect of waveform characteristics on pdev, pdiv and rpdiv for glass fibre insulated wire," in *2022 International Conference on Electrical Machines (ICEM)*, pp. 1327–1333, 2022.

[91] Y. Ji, P. Giangrande, W. Zhao, G. Buticchi, and P. Zhang, "Combined effect of short rise time and relative humidity on the partial discharge inception mechanism in rotating electrical machines insulation," *IEEE Transactions on Dielectrics and Electrical Insulation*, 2024.

[92] M. Radmilović-Radjenović, B. Radjenović, Ž. Nikitović, Š. Matejčik, and M. Klas, "The humidity effect on the breakdown voltage characteristics and the transport parameters of air," *Nuclear Instruments and Methods in Physics Research, Section B: Beam Interactions with Materials and Atoms*, vol. 279, pp. 103–105, 2012.

[93] N. Yanagita, T. Kato, T. Rokunohe, T. Iwata, H. Kojima, N. Hayakawa, and H. Okubo, "Development of a partial discharge inception calculation model of a nonuniform air gap considering the effect of humidity," *Electrical Engineering in Japan (English translation of Denki Gakkai Ronbunshi)*, vol. 186, pp. 1–9, 2014.

[94] Y. Ji, P. Giangrande, W. Zhao, V. Madonna, H. Zhang, J. Li, and M. Galea, "Investigation on combined effect of humidity–temperature on partial discharge through dielectric performance evaluation," *IET Science, Measurement and Technology*, vol. 17, pp. 37–46, 2023.

[95] T. Wakimoto, H. Kojima, and N. Hayakawa, "Measurement and evaluation of partial discharge inception voltage for enameled rectangular wires under ac voltage," *IEEE Transactions on Dielectrics and Electrical Insulation*, vol. 23, pp. 3566–3574, 12 2016.

[96] Y. Kikuchi, T. Okuda, J. Matsusue, Y. Nishimura, F. Yamada, and T. Nakamura, "F1 partial discharge characteristics in twisted enameled wires under high repetition voltage pulses generated by a sic-mosfet inverter power supply," 2023.

[97] S. Matsumoto, N. N. Nam, D. Nagaba, and T. Ogiya, "Partial discharge characteristics of twisted magnet wire under high frequency AC voltage," *Proceedings of the International Symposium on Electrical Insulating Materials*, pp. 57–60, 2014.

[98] D. Fabiani, G. C. Montanari, A. Cavallini, and G. Mazzanti, "Relation between space charge accumulation and partial discharge activity in enameled wires under PWM-like voltage waveforms," *IEEE Transactions on Dielectrics and Electrical Insulation*, vol. 11, no. 3, pp. 393–405, 2004.

[99] G. C. Montanari and P. Seri, "About the definition of pdiv and rpdiv in designing insulation systems for rotating machines controlled by inverters," in *2018 IEEE Electrical Insulation Conference (EIC)*, pp. 554–557, 2018.

[100] P. Wang, H. Xu, J. Wang, W. Zhou, and A. Cavallini, "The influence of repetitive square wave voltage rise time on partial discharge inception voltage," *Annual Report - Conference on Electrical Insulation and Dielectric Phenomena, CEIDP*, vol. 2016-Decem, pp. 759–762, 2016.

[101] H. Naderiallaf, P. Giangrande, and M. Galea, "Characterization of pdiv, pdev, and rpdiv in insulated wires under unipolar repetitive square wave excitations for inverter-fed motors," *IEEE Access*, vol. 11, pp. 51047–51063, 2023.

[102] Z. Wei, H. You, and P. Fu, "Twisted Pairs Under Single Voltage Pulses Generated by Silicon-Carbide Devices," *IEEE Transactions on Transportation Electrification*, vol. 8, no. 2, pp. 1674–1683, 2022.

[103] Z. Wei, H. You, B. Hu, R. Na, and J. Wang, "Partial discharge behavior on twisted pair under ultra-short rise time square-wave excitations," in *2019 IEEE Electrical Insulation Conference (EIC)*, pp. 493–496, 2019.

[104] A. Cavallini, E. Lindell, G. C. Montanari, and M. Tozzi, "Inception of partial discharges under repetitive square voltages: Effect of voltage waveform and repetition rate on pdiv and rpdiv," in *2010 Annual Report Conference on Electrical Insulation and Dielectic Phenomena*, pp. 1–4, 2010.

[105] Y. Yang, X. Bai, Y. Lei, and K. Liu, "Voltage rise rate-related generalised probabilistic lifetime model of turn-to-turn insulation in inverter-fed motors," *High Voltage*, pp. 1–10, 2023.

[106] P. Wang, A. Cavallini, and G. C. Montanari, "The influence of square wave voltage duty cycle on PD behavior," *Annual Report - Conference on Electrical Insulation and Dielectric Phenomena, CEIDP*, vol. 2015-Decem, pp. 338–341, 2015.

[107] P. Wang, N. Yang, C. Zheng, and Y. Li, "Effect of repetitive impulsive and square wave voltage frequency on partial discharge features," *Proceedings of the IEEE International Conference on Properties and Applications of Dielectric Materials*, vol. 2018-May, pp. 152–155, 2018.

[108] H. Naderiallaf, P. Giangrande, and M. Galea, "Impact of unipolar repetitive square wave voltage rise time and frequency on (rpdiv-pdiv) and (pdiv-pdev)," 2023.

[109] P. Wang, A. Cavallini, and G. C. Montanari, "The influence of impulsive voltage frequency on PD features in turn insulation of inverter-fed motors," *2014 IEEE Conference on Electrical Insulation and Dielectric Phenomena, CEIDP 2014*, pp. 35–38, 2014.

[110] C. Pan, K. Wu, G. Chen, Y. Gao, M. Florkowski, Z. Lv, and J. Tang, "Understanding Partial Discharge Behavior from the Memory Effect Induced by Residual Charges: A Review," *IEEE Transactions on Dielectrics and Electrical Insulation*, vol. 27, no. 6, pp. 1951–1965, 2020.

[111] L. lusuardi, A. Cavallini, and M. Degano, "The impact of impulsive voltage waveforms on the electrical insulation of actuators for more electrical aircraft (mea)," in *IECON 2017 - 43rd Annual Conference of the IEEE Industrial Electronics Society*, pp. 4414–4418, 2017.

[112] A. Rauscher, S. Kalamkar, and C. Endisch, "Impact of high voltage waveform on partial discharge inception in electrical machines," in *IEEE International Symposium on Industrial Electronics*, Institute of Electrical and Electronics Engineers Inc., 2024.

[113] B. Hu, Z. Wei, H. You, R. Na, R. Liu, H. Xiong, P. Fu, J. Zhang, and J. Wang, "A Partial Discharge Study of Medium-Voltage Motor Winding Insulation Under Two-Level Voltage Pulses With High Dv/Dt," *IEEE Open Journal of Power Electronics*, vol. 2, no. February, pp. 225–235, 2021.

[114] A. Rumi and A. Cavallini, "The influence of short-width sic pulses on the partial discharge inception voltage of turn-turn insulation," *2022 IEEE Conference on Electrical Insulation and Dielectric Phenomena (CEIDP)*, pp. 447–450, 2022.

[115] L. Benmamas, P. Teste, E. Odic, G. Krebs, and T. Hamiti, "Contribution to the analysis of PWM inverter parameters influence on the partial discharge inception voltage," *IEEE Transactions on Dielectrics and Electrical Insulation*, vol. 26, no. 1, pp. 146–152, 2019.

[116] J. He, G. Wu, B. Gao, and J. Wu, "Study on aging characteristics for inverter-fed traction motor inter-turn insulation based on analysis of dielectric characteristic parameters," *Annual Report - Conference on Electrical Insulation and Dielectric Phenomena, CEIDP*, pp. 81–84, 2007.

[117] K. Sandip Garud and M.-Y. Lee, "Thermal management characteristics of electric vehicle driving motor with oil spray cooling based on spray locations and oil types," *Applied Thermal Engineering*, vol. 248, p. 123234, 2024.

[118] C. Abadie, *On-line non-intrusive partial discharges detection in aeronautical systems*. PhD thesis, Université Toulouse 3 Paul Sabatier, 2017.

[119] M. Szczepanski, L. Fetouhi, M. Sabatou, S. Dreuilhe, S. Pin, C. Van de Steen, and G. Belijar, "How does pdiv change during isothermal aging of magnet wire," in *2022 IEEE Electrical Insulation Conference (EIC)*, pp. 266–271, 2022.

[120] L. Benmamas, P. Teste, G. Krebs, E. Odic, F. Vangraefschepe, and T. Hamiti, "Contribution to partial discharge analysis in inverter-fed motor windings for automotive application," in *2017 IEEE Electrical Insulation Conference (EIC)*, pp. 348–351, 2017.

[121] L. Lusuardi, A. Cavallini, M. G. D. Calle, and G. Robles, "Insulation Design of Low Voltage Electrical Motors Fed by PWM Inverters," *IEEE Electrical Insulation Magazine*, vol. 35, no. 3, pp. 7–15, 2019.

[122] M. Gómez de la Calle, J. M. Martínez-tarifa, S. Member, Á. Manuel, G. Solanilla, G. Robles, and S. Member, "Uncertainty Sources in the Estimation of the Partial Discharge Inception Voltage in Turn-to-Turn Insulation Systems," *IEEE Access*, vol. 8, 2020.

[123] T. W. Dakin, H. M. Philofsky, and W. C. Divens, "Effect of electric discharges on the breakdown of solid insulation," *Transactions of the American Institute of Electrical Engineers, Part I: Communication and Electronics*, vol. 73, no. 2, pp. 155–162, 1954.

[124] "As50881h: Wiring aerospace vehicle," 2023. Revised 13 January 2023.

[125] M. C. Halleck, "Calculation of Corona-Starting Voltage in Air-Solid Dielectric Systems," *Transactions of the American Institute of Electrical Engineers. Part III: Power Apparatus and Systems*, vol. 75, no. 3, pp. 211–216, 1956.

[126] P. Collin, D. Malec, and Y. Lefevre, "About the relevance of using paschen's criterion for partial discharges inception voltage (pdiv) estimation when designing the electrical insulation system of inverter fed motors," in *2019 IEEE Electrical Insulation Conference (EIC)*, pp. 513–516, 2019.

[127] V. Madonna, P. Giangrande, W. Zhao, G. Buticchi, H. Zhang, C. Gerada, and M. Galea, "Reliability vs. performances of electrical machines: Partial discharges issue," in *2019 IEEE Workshop on Electrical Machines Design, Control and Diagnosis (WEMDCD)*, vol. 1, pp. 77–82, 2019.

[128] S. Duchesne, G. Parent, J. Moenecley, and D. Roger, "Prediction of pdiv in motor coils using finite element method," in *2016 IEEE International Conference on Dielectrics (ICD)*, vol. 2, pp. 638–641, 2016.

[129] Y. Kemari, C. V. d. Steen, G. Belijar, L. Laudebat, S. Diaham, Z. Valdez-Nava, and C. Abadie, "A townsend's secondary ionization coefficient estimation method for partial discharge inception voltage prediction for insulating polymers," in *2022 IEEE 4th International Conference on Dielectrics (ICD)*, pp. 226–229, 2022.

[130] H. Naderiallaf, M. Degano, and S. Member, "Modeling air pressure impact on pdiv for rectangular wire turn-to-turn insulation of inverter-fed motors under different voltage waveform excitations," *IEEE Access*, vol. 12, pp. 176232–176246, 2024.

[131] H. Naderiallaf, Y. Ji, P. Giangrande, and M. Galea, "Air pressure impact on the avalanche size for turn-to-turn insulation of inverter-fed motors," *IEEE Transactions on Dielectrics and Electrical Insulation*, vol. 31, pp. 85–94, 2024.

[132] H. Naderiallaf, Y. Ji, P. Giangrande, and M. Galea, "Temperature impact on pdiv for turn-to-turn insulation of inverter-fed motors: From ground level to cruising altitude," *IEEE Transactions on Dielectrics and Electrical Insulation*, vol. 31, pp. 1044–1053, 2024.

[133] J. Gao, A. Rumi, Y. He, and A. Cavallini, "Towards a holistic approach to inverter-fed machine design: Fem-based pdiv prediction of complete windings," *IEEE Transactions on Dielectrics and Electrical Insulation*, vol. PP, p. 1, 2023.

[134] Y. Y. Lau, Y. Liu, and R. K. Parker, "Electron emission: From the Fowler-Nordheim relation to the Child-Langmuir law," *Physics of Plasmas*, vol. 1, no. 6, pp. 2082–2085, 1994.

[135] K. Ito, T. Shibata, and T. Kawasaki, "Development of High Voltage Wire for New Structure Motor in Full Hybrid Vehicle," *SAE International Journal of Alternative Powertrains*, vol. 5, no. 2, pp. 272–277, 2016.

[136] N. Driendl, F. Pauli, and K. Hameyer, "Modeling of partial discharge processes in winding insulation of low-voltage electrical machines supplied by high du/dt inverters," in *IECON 2019 - 45th Annual Conference of the IEEE Industrial Electronics Society*, vol. 1, pp. 7102–7107, 2019.

[137] F. Pauli, N. Driendl, and K. Hameyer, "Study on temperature dependence of partial discharge in low voltage traction drives," in *2019 IEEE Workshop on Electrical Machines Design, Control and Diagnosis (WEMDCD)*, IEEE, 2019.

[138] C. V. D. Steen, "Partial discharge detection , experimental-simulation comparison and actual limits," in *Electrical Insulation Conference*, pp. 537–541, 2020.

[139] O. Calculator, "Absolute humidity calculator," 2025. Accessed: 28-Apr-2025.

[140] AcademiaLab, "Presión de vapor del agua," 2025. Accessed: 28-Apr-2025.

[141] C. He, M. Beltle, S. Tenbohlen, T. Hubert, S. Schmidt, and J. Schneider, "Partial discharge characteristic of hairpin windings for inverter-fed motors," in *ICD 2022 - IEEE 2022 4th International Conference on Dielectrics, Proceedings*, pp. 49–52, 2022.

[142] Y. M. Lafuente, *High Frequency Analysis of Permanent Magnet Motors*. PhD thesis, Mondragon Unibertsitatea, Hernani, May 2024. Supervised by Dr. Gaizka Almandoz Larralde and Dr. Aritz Egea Caceres.

[143] S. Böhler, "Pd seminar," 2024. Seminar conducted at Mondragon Unibertsitatea.

[144] "Iec 60034-27-1: Rotating electrical machines - part 27-1: Off-line partial discharge measurements on the winding insulation," 2017. First edition.

[145] V. Madonna, P. Giangrande, and M. Galea, "Weibull Distribution and Geometrical Size Factor for Evaluating the Thermal Life of Electrical Machines' Insulation," *IECON Proceedings (Industrial Electronics Conference)*, vol. 2020-Octob, pp. 1114–1119, 2020.

[146] F. Guastavino, G. Coletti, and E. Torello, "Medium term aging characterization of enamelled wires for high frequency applications," *IEEE Transactions on Dielectrics and Electrical Insulation*, vol. 12, no. 3, pp. 524–529, 2005.

[147] J. M. Gonzalez, L. K. Rodrigues, F. Beza-Florentin, C. Butnaru, M. Mikula, A. Neves, and J. V. Sarrico, "A methodology for accelerated thermal aging of an automotive hairpin stator," *IEEE Transactions on Dielectrics and Electrical Insulation*, 2025.

[148] K. Alkhalid, J. Wang, P. Fu, D. Schweickart, and D. Grosjean, "Temperature impact on partial discharge induced aging of aviation wires under high dv/dt voltage excitations," in *2023 IEEE Workshop on Power Electronics for Aerospace Applications, PEASA 2023*, pp. 1–5, IEEE, 2023.

[149] A. Rumi, J. G. Marinelli, and A. Cavallini, "Converter stress impact on thermally aged resin for low-voltage machines," *Annual Report - Conference on Electrical Insulation and Dielectric Phenomena, CEIDP*, vol. 2021-Decem, pp. 40–43, 2021.

[150] F. Loubeau, P. Rain, A. Durieux, and F. L. Strat, "Partial discharge behavior of motorettes under different aging conditions," in *2018 IEEE 2nd International Conference on Dielectrics, ICD 2018*, pp. 1–4, IEEE, 2018.

[151] H. Naderiallaf, M. Degano, and C. Gerada, "Pdiv modelling for rectangular wire turn-to-turn insulation of inverter-fed motors through thermal ageing," *IEEE Transactions on Dielectrics and Electrical Insulation*, vol. PP, p. 1, 2023.

[152] A. Rumi, J. G. Marinelli, and A. Cavallini, "Converter stress impact on thermally aged resin for low-voltage machines," *Annual Report - Conference on Electrical Insulation and Dielectric Phenomena, CEIDP*, vol. 2021-Decem, pp. 40–43, 2021.

[153] Y. Wang, J. Pan, H. Tang, Y. He, and Q. Wang, "Partial discharge characteristics of electrical aircraft machine winding after thermal aging," in *2022 IEEE International Conference on High Voltage Engineering and Applications, ICHVE 2022*, pp. 1–4, IEEE, 2022.

[154] A. J. Samarakoon, T. Tallerico, B. Wolhaupter, T. Balachandran, and K. Haran, "Partial discharge investigation of electric machine winding due to thermo-mechanical stresses for electric aircraft propulsion," in *2023 IEEE International Electric Machines & Drives Conference (IEMDC)*, pp. 1–6, IEEE, 2023.

[155] L. Stahl and P. Werle, "Investigations on different polymers used for insulation in e-mobility applications," *2023 IEEE Electrical Insulation Conference, EIC 2023*, pp. 1–4, 2023.

[156] L. Stahl, B. Özdemir, J. Torres, and P. Werle, "Pdiv and ac breakdown behavior of magnet wire in different embedded media," in *Proceedings of the 2024 IEEE 5th International Conference on Dielectrics, ICD 2024*, Institute of Electrical and Electronics Engineers Inc., 2024.

[157] L. Stahl, J. Torres, and P. Werle, "Novel testing method on insulation materials used for e-mobility," 23rd International Symposium on High Voltage Engineering (ISH 2023), 8 2023.

[158] P. Plastics, "Thermal properties of plastic materials," 2025. Accessed: 24-Apr-2025.

[159] WHM Group, "Pa66 gf30 black datasheet," 2023. Accessed: 11-Jun-2025.

[160] L. A. Pilato and M. J. Michno, *Advanced Composite Materials*. Springer-Verlag Berlin Heidelberg, 1st ed., 1994. Accessed: 2025-06-11.

[161] S. Diaham, M.-L. Locatelli, T. Lebey, and S. Dinculescu, "Dielectric and thermal properties of polyamide-imide (pai) films," 2009. Accessed: 2025-06-11.

[162] F. Alvarez-Gonzalez, D. Hewitt, A. Griffo, J. Wang, M. Diab, and X. Yuan, "Design of Experiments for Stator Windings Insulation Degradation under High dv/dt and High Switching Frequency," in *ECCE 2020 - IEEE Energy Conversion Congress and Exposition*, no. 978, pp. 789–795, 2020.

[163] F. Guastavino, A. Ratto, S. Squarcia, and E. Torello, "Electro-thermal aging tests on different kinds of enamelled wires," in *Proceedings of the 2010 IEEE International Conference on Solid Dielectrics, ICSD 2010*, pp. 1–4, 2010.

[164] F. Guastavino, G. Coletti, A. Ratto, and E. Torello, "Electrical ageing test on conventional and nanocomposite enamels: PD patterns analysis," *2009 IEEE Electrical Insulation Conference, EIC 2009*, no. June, pp. 537–541, 2009.

[165] M. S. Moonesan, S. H. Jayaram, and E. A. Cherney, "Study on form-wound machine turn insulation subjected to unipolar and bipolar square waves," *IEEE Transactions on Dielectrics and Electrical Insulation*, vol. 23, no. 6, pp. 3242–3248, 2016.

[166] P. Wang, G. C. Montanari, and A. Cavallini, "Partial discharge phenomenology and induced aging behavior in rotating machines controlled by power electronics," *IEEE Transactions on Industrial Electronics*, vol. 61, pp. 7105–7112, 12 2014.

[167] P. Wang, Z. Changjiang, Y. Li, Y. Lei, and A. Cavallini, "The pd and endurance features of enameled wires at short repetitive impulsive voltages," 6 2018.

[168] P. Wang, A. Cavallini, and G. C. Montanari, "The effect of impulsive voltage rise time on insulation endurance of inverter-fed motors," IEEE, 2015.

[169] P. Wang, W. Zhou, K. Wang, J. Li, Q. Zhou, and Y. Lei, "Comparison of pd characteristics for inverter-fed motor insulation under sinusoidal and repetitive square wave voltage conditions," *Gaodianya Jishu/High Voltage Engineering*, vol. 42, pp. 3895–3900, 2016.

[170] T. Liu, Y. Xiao, Y. Lu, X. Huang, Q. Li, and Z. Wang, "Effect of voltage frequency on surface discharge characteristics and aging process," in *2017 IEEE Electrical Insulation Conference, EIC 2017*, no. June, pp. 463–466, 2017.

[171] A. Rumi and A. Cavallini, "Turn-to-turn converter stress impact on the lifetime of rotating machines," in *Annual Report - Conference on Electrical Insulation and Dielectric Phenomena, CEIDP*, Institute of Electrical and Electronics Engineers Inc., 2023.

[172] V. N. Höpner and V. E. Wilhelm, "Insulation life span of low-voltage electric motors—A survey," *Energies*, vol. 14, no. 6, pp. 1–32, 2021.

[173] P. A. Panagiotou, E. J. Stone, J. Muhlthaler, A. Reeh, A. Lambourne, and G. W. Jewell, "Thermal Degradation Profile of Concentrated Stator Winding Insulation by Impedance Spectroscopy," in *Proceedings of the 2023 IEEE 14th International Symposium on Diagnostics for Electrical Machines, Power Electronics and Drives, SDEMPED 2023*, no. Project 51689, pp. 554–560, 2023.

[174] J. E. Ruiz-Sarrio, J. A. Antonino-Daviu, A. Navarro-Navarro, and V. Biot-Monterde, "A Review of Broadband Frequency Techniques for Insulation Monitoring and Diagnosis in Rotating Electrical Machines," *IEEE Transactions on Industry Applications*, vol. PP, pp. 1–11, 2024.

[175] S. Savin, S. Ait-Amar, and D. Roger, "Organic enameled wire aging monitoring based on impedance spectrum analysis," in *Annual Report - Conference on Electrical Insulation and Dielectric Phenomena, CEIDP*, pp. 874–877, 2012.

[176] M. Toudji, S. Duchesne, and G. Parent, "Predictive diagnostic based on HF modeling of electrical machines windings," in *2019 IEEE International Electric Machines and Drives Conference, IEMDC 2019*, pp. 901–906, 2019.

[177] S. Ait-Amar, D. Roger, and S. Savin, "Aging monitoring of electrical machines using winding high frequency equivalent circuits," *Open Physics*, vol. 17, pp. 670–677, 1 2019.

[178] N. J. Jameson, M. H. Azarian, M. Pecht, K. Wang, and X. Aidong, "Electromagnetic coil equivalent circuit model sensitivity analysis for impedance-based insulation

health monitoring," in *2017 Prognostics and System Health Management Conference (PHM-Harbin)*, pp. 1–6, IEEE, jul 2017.

[179] D. Zheng, G. Lu, and P. Zhang, "A Noninvasive Interturn Insulation Condition Monitoring Method Based on the Common-Mode Impedance Spectrum of Inverter-Fed Machines," *IEEE Transactions on Industry Applications*, vol. 57, no. 5, pp. 4786–4795, 2021.

[180] V. Madonna, P. Giangrande, L. Lusuardi, A. Cavallini, C. Gerada, and M. Galea, "Thermal Overload and Insulation Aging of Short Duty Cycle, Aerospace Motors," *IEEE Transactions on Industrial Electronics*, vol. 67, no. 4, pp. 2618–2629, 2019.

[181] I. Tsyokhla, A. Griffo, J. Wang, and S. Member, "On - Line Condition Monitoring for Diagnosis and Prognosis of Insulation Degradation of Inverter - fed Machines," *IEEE Transactions on Industrial Electronics*, vol. PP, no. 1, p. 1, 2018.

[182] Z. Huang, A. Reinap, and M. Alakula, "Dielectric properties modeling and measurement of single tooth coil insulation system under accelerated degradation test," in *Proceedings - 2016 22nd International Conference on Electrical Machines, ICEM 2016*, pp. 2698–2703, 2016.

[183] M. Szczepanski, L. Fetouhi, M. Sabatou, S. Pin, and G. Belijar, "PD energy as a marker of low-voltage insulation aging," *2021 Electrical Insulation Conference, EIC 2021*, pp. 377–380, 2021.

[184] C. He, S. Tenbohlen, and M. Beltle, "Ageing analysis of hairpin windings in inverter-fed motor under pwm voltage," *Energies*, vol. 18, p. 1376, 3 2025.

[185] LXCat, "Plasma data exchange project," 2009. Accessed: 24-Apr-2024.